



## UvA-DARE (Digital Academic Repository)

### Exploring the implications of hadronic particle acceleration in X-ray binaries

Kantzas, D.

**Publication date**

2022

**Document Version**

Final published version

[Link to publication](#)

**Citation for published version (APA):**

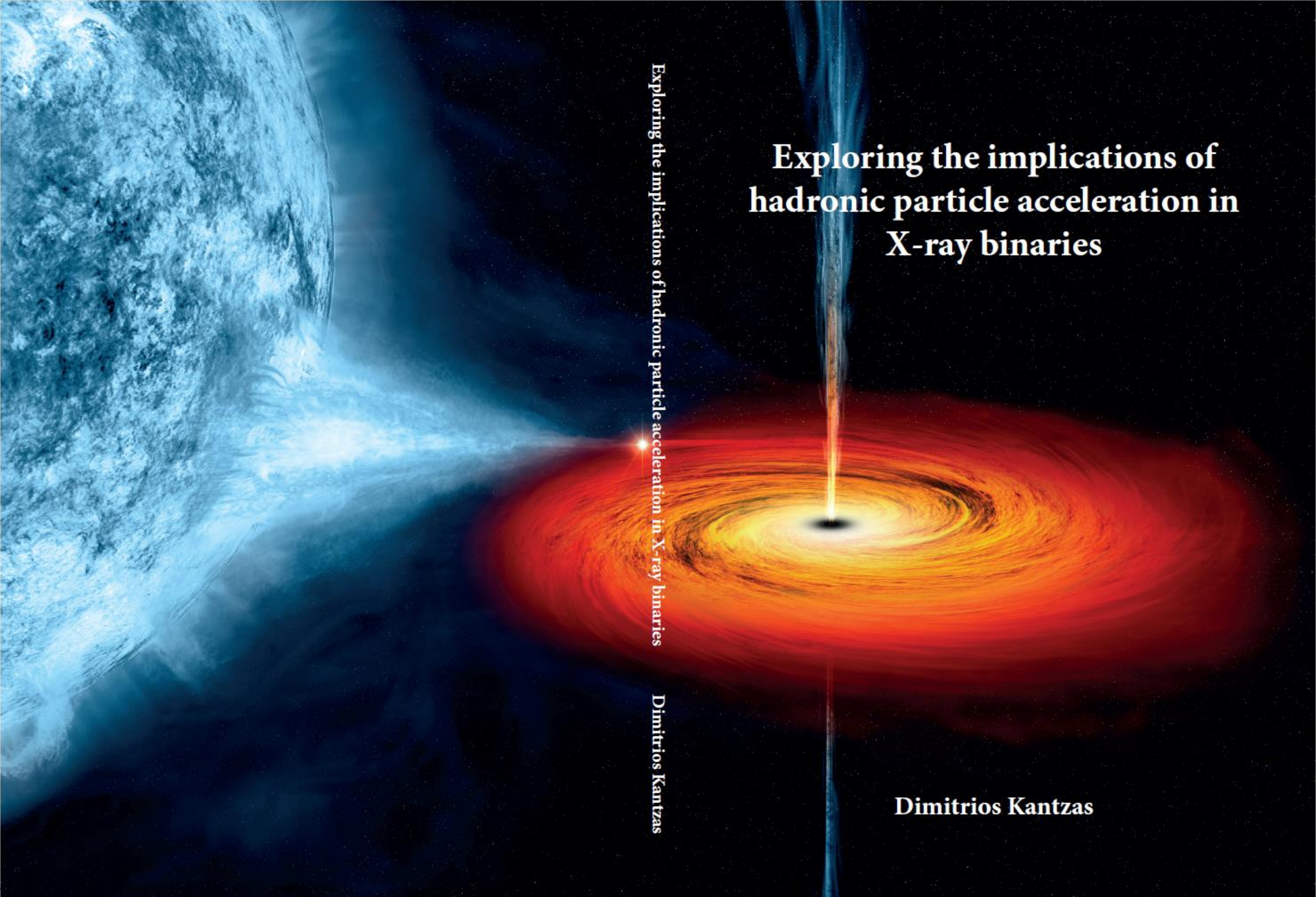
Kantzas, D. (2022). *Exploring the implications of hadronic particle acceleration in X-ray binaries*. [Thesis, fully internal, Universiteit van Amsterdam].

**General rights**

It is not permitted to download or to forward/distribute the text or part of it without the consent of the author(s) and/or copyright holder(s), other than for strictly personal, individual use, unless the work is under an open content license (like Creative Commons).

**Disclaimer/Complaints regulations**

If you believe that digital publication of certain material infringes any of your rights or (privacy) interests, please let the Library know, stating your reasons. In case of a legitimate complaint, the Library will make the material inaccessible and/or remove it from the website. Please Ask the Library: <https://uba.uva.nl/en/contact>, or a letter to: Library of the University of Amsterdam, Secretariat, Singel 425, 1012 WP Amsterdam, The Netherlands. You will be contacted as soon as possible.



**Exploring the implications of  
hadronic particle acceleration in  
X-ray binaries**

Exploring the implications of hadronic particle acceleration in X-ray binaries

Dimitrios Kantzas

Dimitrios Kantzas

Exploring the implications of  
hadronic particle acceleration in  
X-ray binaries

DIMITRIOS KANTZAS



© 2022, Dimitrios Kantzas  
contact: [d.kantzas@uva.nl](mailto:d.kantzas@uva.nl)

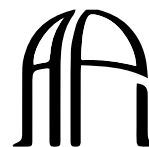
Exploring the implications of hadronic particle acceleration in X-ray binaries  
Thesis, Anton Pannekoek Institute, Universiteit van Amsterdam

Cover Image Credit: NASA/CXC/M.Weiss  
Printed by Ipskamp

ISBN: 978-94-6421-833-6



UNIVERSITY OF AMSTERDAM



ANTON PANNEKOEK  
INSTITUTE

The research included in this thesis was carried out at the Anton Pannekoek Institute for Astronomy (API) of the University of Amsterdam. It was supported by the Netherlands Research School for Astronomy (NOVA). Support was occasionally provided by the Leids Kerkhoven-Bosscha Fonds (LKBF).



# Exploring the implications of hadronic particle acceleration in X-ray binaries

ACADEMISCH PROEFSCHRIFT

ter verkrijging van de graad van doctor  
aan de Universiteit van Amsterdam  
op gezag van de Rector Magnificus  
prof. dr. ir. P.P.C.C. Verbeek  
ten overstaan van een door het College voor Promoties ingestelde  
commissie, in het openbaar te verdedigen in de Aula der  
Universiteit  
op woensdag 5 oktober 2022, te 11.00 uur

door

**Dimitrios Kantzas**

geboren te Griekenland

**Promotiecommissie:**

*Promotor:* prof. dr. S. B. Markoff Universiteit van Amsterdam  
*Copromotor:* dr. J. Vink Universiteit van Amsterdam

*Overige leden:* prof. dr. J. A. Hinton Max Planck Institute for Nuclear Physics  
dr. M. Petropoulou National and Kapodistrian University of Athens  
dr. D. Gaggero University of Valencia  
prof. dr. A.L. Watts Universiteit van Amsterdam  
prof. dr. G. Bertone Universiteit van Amsterdam  
prof. dr. R.A.M.J. Wijers Universiteit van Amsterdam  
dr. N.D. Degenaar Universiteit van Amsterdam

Faculteit der Natuurwetenschappen, Wiskunde en Informatica



*To my parents*



# Contents

<b>1</b>	<b>Introduction</b>	<b>1</b>
1.1	Cosmic Rays: a long-standing mystery . . . . .	1
1.1.1	Cosmic ray spectrum . . . . .	3
1.1.2	Cosmic ray composition . . . . .	3
1.1.3	Cosmic ray sources . . . . .	5
1.2	X-ray binaries . . . . .	7
1.2.1	Black hole X-ray binaries . . . . .	8
1.2.2	XRB classification . . . . .	9
1.3	Relativistic jets from BHXBs . . . . .	12
1.4	Particle acceleration . . . . .	15
1.4.1	Diffusive shock acceleration . . . . .	16
1.4.2	Magnetic reconnection . . . . .	17
1.4.3	CR propagation . . . . .	18
1.5	Non-thermal radiative processes . . . . .	19
1.5.1	Leptonic processes . . . . .	19
1.5.2	Hadronic processes . . . . .	21
1.6	The effect of losses on the accelerated particles . . . . .	28
1.7	Ground-based gamma-ray astronomy . . . . .	29
1.8	Thesis outline . . . . .	31
<b>2</b>	<b>A new lepto-hadronic model applied to the first simultaneous multiwavelength data set for Cygnus X-1</b>	<b>33</b>
2.1	Introduction . . . . .	35
2.2	Observations and Data Extraction . . . . .	38

2.2.1	Very Large Array (VLA)	38
2.2.2	NORthern Extended Millimeter Array (NOEMA)	40
2.2.3	<i>XMM-Newton</i>	40
2.2.4	<i>NuSTAR</i>	40
2.2.5	<i>INTEGRAL</i>	41
2.3	Model Details	41
2.3.1	Dynamical Quantities	41
2.3.2	Particle distributions	43
2.3.3	Radiative Processes	45
2.3.4	Corona model	49
2.4	Results	49
2.4.1	Plasma quantities	50
2.4.2	Best fits to the multiwavelength spectrum	51
2.4.3	GeV-TeV spectrum	51
2.5	Discussion	57
2.5.1	Comparison with previous works	59
2.5.2	Perspective for CTA, HAWC, and LHAASO	59
2.6	Summary and Conclusions	61
<b>3</b>	<b>The prototype X-ray binary GX 339–4: using TeV <math>\gamma</math>-rays to assess LMXBs as Galactic cosmic ray accelerators</b>	<b>65</b>
3.1	Introduction	66
3.2	GX 339–4	68
3.2.1	Observational constraints in the hard state	68
3.2.2	Observational data	69
3.3	Modelling	70
3.3.1	Jet properties	70
3.3.2	Particle acceleration	71
3.3.3	Radiative Processes	72
3.3.4	Accretion disc and thermal corona	73
3.4	Results	73
3.5	Discussion	78
3.5.1	Multi-wavelength spectrum and jet dynamics	78
3.5.2	Particle distributions	81
3.5.3	Non-thermal proton power	81
3.5.4	$\gamma$ -ray attenuation on the optical/IR emission	84
3.5.5	$\gamma$ -rays from BHXBs	84
3.6	Summary and Conclusions	88
	Appendix 3.A Proton characteristic timescales	89
<b>4</b>	<b>Exploring neutrino and cosmic ray production in X-ray binary jets</b>	

<b>using multi-wavelength case studies</b>	<b>91</b>
4.1 Introduction . . . . .	93
4.2 Neutrinos from BHXB jets . . . . .	95
4.2.1 Jet dynamics and particle acceleration . . . . .	96
4.2.2 Lepto-Hadronic Processes . . . . .	97
4.2.3 Electromagnetic spectrum . . . . .	98
4.3 Intrinsic neutrino emission . . . . .	98
4.3.1 Neutrino emission from Cyg X-1 . . . . .	98
4.3.2 Neutrino emission from GX 339-4 . . . . .	99
4.3.3 Neutrino rates . . . . .	100
4.3.4 Contribution from all known BHXBs . . . . .	102
4.4 Diffuse secondary emission . . . . .	104
4.4.1 BHXBs as CR sources . . . . .	104
4.4.2 Diffuse gamma-ray and neutrino emission from BHXBs . . . . .	107
4.5 Discussion . . . . .	108
4.5.1 Cyg X-1 and GX 339-4 as Galactic neutrino sources . . . . .	108
4.5.2 BHXBs as Galactic neutrino sources . . . . .	110
4.5.3 Gamma-ray emission counterpart . . . . .	111
4.5.4 BHXBs and the CR spectrum . . . . .	112
4.5.5 Diffuse gamma-ray and neutrino emission from BHXBs . . . . .	116
4.6 Summary and Conclusions . . . . .	116
Appendix 4.A Detected BHXBs . . . . .	118
Appendix 4.B Neutrino backgrounds . . . . .	122
4.B.1 Atmospheric neutrino background . . . . .	122
4.B.2 Astrophysical neutrino background . . . . .	122
4.B.3 Diffuse neutrino spectrum . . . . .	122
Appendix 4.C Contribution from individual sources . . . . .	123
Appendix 4.D Maximum CR energy from a high-mass BHXB . . . . .	123
<b>5 Exploring the role of composition and mass-loading on the properties of hadronic jets</b>	<b>127</b>
5.1 Introduction . . . . .	128
5.2 Magnetically accelerated steady-state jets . . . . .	131
5.2.1 Jet dynamical properties . . . . .	132
5.2.2 The acceleration region and particle acceleration . . . . .	135
5.2.3 Jet evolution and particle acceleration . . . . .	136
5.2.4 Radiative Processes . . . . .	136
5.3 Results for the steady-state jets . . . . .	138
5.3.1 Specific enthalpy and particle acceleration . . . . .	139
5.3.2 Total energy flux evolution for steady state jets . . . . .	141
5.3.3 Electromagnetic spectrum of steady state jets . . . . .	142

5.4	Mass loaded jets . . . . .	145
5.4.1	Mass loading region . . . . .	146
5.4.2	Jet segments beyond the mass loading region . . . . .	148
5.4.3	Particle acceleration and mass loaded jets . . . . .	149
5.5	Results for mass-loaded jets . . . . .	149
5.5.1	Total energy flux evolution for mass-loaded jets . . . . .	149
5.5.2	Electromagnetic spectra of steady state mass-loaded jets . . . . .	150
5.6	Discussion . . . . .	151
5.6.1	Steady state jets . . . . .	151
5.6.2	Mass-loaded jets – HadJet . . . . .	153
5.6.3	Total proton energy . . . . .	155
5.7	Summary and Conclusions . . . . .	157
Appendix 5.A	Specific enthalpy for a hard power law of accelerated particles	158
Appendix 5.B	All energy components plots . . . . .	158
Appendix 5.C	Artificial mass loss . . . . .	160
Appendix 5.D	Proton power . . . . .	161
<b>Bibliography</b>		<b>165</b>
<b>Contribution from co-authors</b>		<b>185</b>
<b>Publications</b>		<b>187</b>
<b>Samenvatting</b>		<b>189</b>
<b>Summary</b>		<b>195</b>
<b>Περίληψη</b>		<b>199</b>
<b>Acknowledgements</b>		<b>205</b>

## 1.1 Cosmic Rays: a long-standing mystery

Cosmic rays (CRs) are high energy particles discovered over a century ago. Since their initial discovery, the origin of CRs is highly debated. In 1909, Theodor Wulf used his electrometer (an instrument to detect charged particles) to compare the measured levels of radiation between the top and the bottom of the Eiffel Tower. If the radiation's origin was in Earth, as was commonly believed, the radiation would drop significantly at the peak of the Eiffel Tower at a height of 330 m. The radiation level was  $6 \text{ ions cm}^{-3}$  at sea level, and the predicted value was to drop to half at some distance of the order of 80 m (Longair 2011). The measured levels of radiation at the top of the Eiffel Tower instead were  $3.5 \text{ ions cm}^{-3}$  suggesting that its origin must be of extraterrestrial nature (Wulf 1909). The initial result of Theodor Wulf was initially rejected by the community but a few years later, in 1912, Victor Hess used Wulf's detector in a balloon flight at an altitude of 5300 m to conclude that *"the results of the observations seem most likely to be explained by the assumption that radiation of very high penetrating power enters from above into our atmosphere"* (Hess 1912). Victor Hess received the Nobel Prize in Physics in 1936 for his discovery.

More than 11 decades later, we have managed to observe the entire CR spectrum that spans more than 10 orders of magnitude in flux, and 10 orders of magnitude in energy. Numerous detectors have been used over the years, both ground-based and in orbit, but despite the intense searches there are still several significant open questions. The exact astrophysical source or sources of CRs have still not been unambiguously identified, and the exact physical mechanism responsible for the particle acceleration is highly debated.

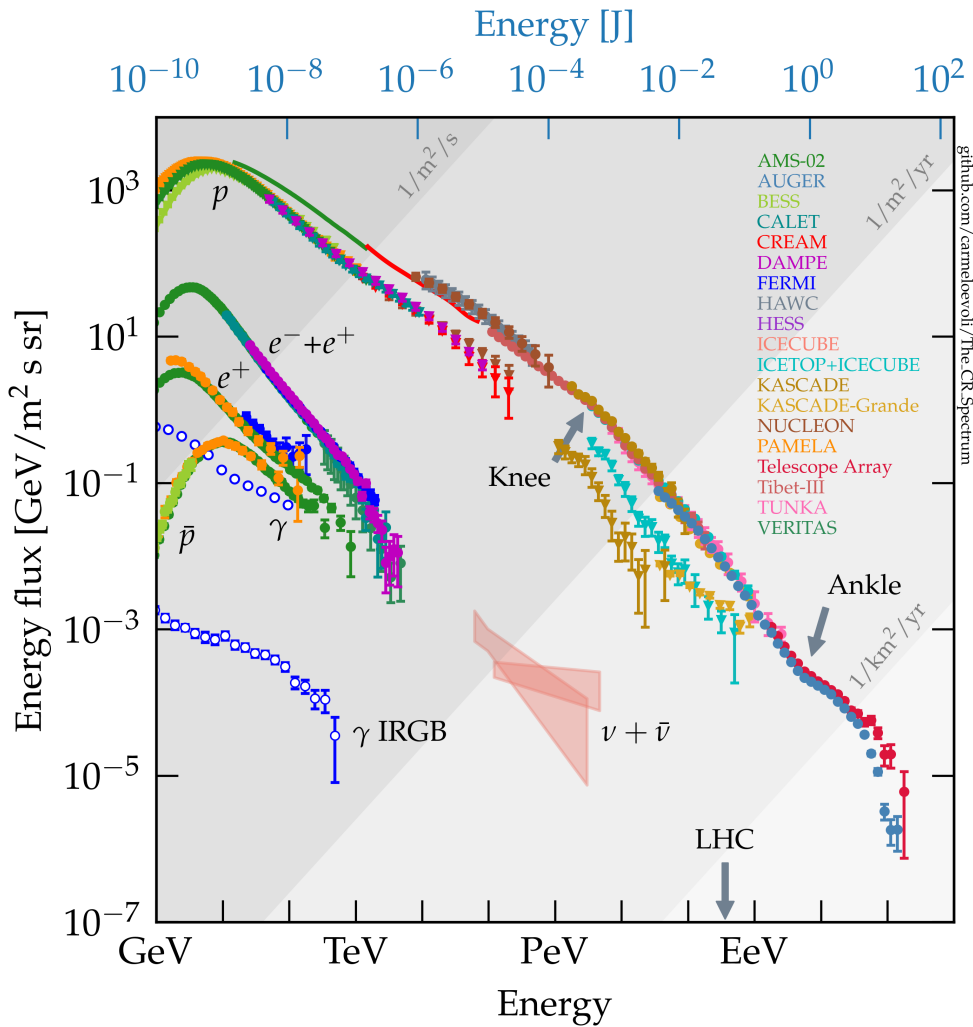


**Figure 1.1:** The CR spectrum as observed with various detectors shown in the legend. The CR spectrum covers more than 10 orders of magnitude in energy flux and extends between GeV and 100 EeV ( $10^{20}$  eV) in particle energy. The different components are indicated in the plot with protons ( $p$ ), electrons ( $e^-$ ), positrons ( $e^+$ ) and antiprotons ( $p^+$ ) dominating the CR spectrum in the GeV-to-TeV energy regime. Protons and heavier elements dominate the most energetic part of the spectrum. The data were compiled together by Evoli (2018).



### 1.1.1 Cosmic ray spectrum

Figure 1.1 shows the CR spectrum as a function of the particle energy, where the different colours correspond to different detectors, as shown in the legend. The low-energy regime of the spectrum at  $\sim 10^9$  eV (GeV) is mainly composed of protons with a detection flux greater than  $1 \text{ m}^{-2} \text{ s}^{-1}$  (Shikaze et al. 2007; Ahn et al. 2009; Yoon et al. 2011; Adriani et al. 2011; Aguilar et al. 2015b,a). In the low energy regime, we also detect electrons, positrons, and antiprotons (Aharonian et al. 2008a; Adriani et al. 2010, 2013; Aguilar et al. 2014b,a, 2016; DAMPE Collaboration et al. 2017; Adriani et al. 2018). The spectrum of electrons and positrons has a lower flux due to the solar wind in the GeV regime and extends up to TeV energies, whereas the proton spectrum extends up to the so-called “knee” at  $10^{15}$  eV (PeV). The detection flux at energies between TeV and PeV drops to  $1 \text{ m}^{-2} \text{ yr}^{-1}$ , and thus, the statistics are significantly reduced compared to the low-energy regime (Abbasi et al. 2013; Apel et al. 2013). The proton spectrum follows a single power law in energies up to the “knee” with a power-law index of  $s = 2.7$ , and then it softens to  $s = 3.1$  (Kulikov & Khristiansen 1959). A further spectral feature is evident at energies approximately  $10^{18}$  eV (EeV) where the spectrum hardens once more to  $s = 2.7$  (Bird et al. 1993). The detection rate at this energy regime is so low (of the order of  $1 \text{ km}^{-2} \text{ yr}^{-1}$ ) that  $\text{km}^2$  detectors are necessary, such as Pierre Auger Observatory in Argentina and the Telescope Array (TA) in the US (The Pierre Auger Collaboration et al. 2015 and Kawai et al. 2008, respectively).

### 1.1.2 Cosmic ray composition

Ground-based detectors enable us to measure the CR spectrum around and above the knee, however determining the exact composition of the cosmic rays is difficult. The main difficulty lies in the fact that we use indirect means to detect the CRs that enter the atmosphere and initiate hadronic showers, namely particle cascades that lead to stable secondary particles. However, to reconstruct the exact initial conditions of the incoming CR we require Monte Carlo simulations such as QGSJET-II (Kalmykov et al. 1997; Ostapchenko 2011), SIBYLL (Fletcher et al. 1994), Pythia (Sjöstrand et al. 2006), and Epos-LHC (Pierog & Werner 2008). In order for the Monte Carlo simulations to run efficiently some approximations must be made. To better constrain these approximations, data from experimental laboratories, such as the European Organization for Nuclear Research (CERN; from the French *Conseil Européen pour la Recherche Nucléaire* (European Council for Nuclear Research)) are used, but these laboratories operate at lower energies of the order of 3.5 TeV. The Monte Carlo simulations used to study the hadronic air-showers extrapolate to larger energies in order to reconstruct the initial conditions of the incoming CR. Such an extrapolation carries uncertainties that eventually make it almost impossible to derive

the exact composition of the CRs, especially at energies beyond EeV. In fact, different Monte Carlo simulations favour different CR compositions and further detections are required (Abbasi et al. 2010; Abu-Zayyad et al. 2013; Aab et al. 2014). Even between PeV and EeV the CR composition is not clear, but it is very likely that protons dominate in the PeV regime, whereas heavier elements start to dominate at greater energies (Aloisio et al. 2012; Buitink et al. 2016). The difference in CR composition at various energy regimes indicates that different sources must contribute in different part of the CR spectrum, and in fact, Galactic sources dominate up to the ankle and extragalactic CRs dominate in the energy regime beyond the ankle (see Section 1.1.3 for the CR origin). Understanding the composition of CRs is critically important in order to identify the sources from which the CRs originate.

In-situ measurements with detectors in orbit, on the other hand, allow for an accurate distinction on the CR mass, and hence, a well-defined CR composition. Proceeding on the pioneering work of space-borne missions, such as the Interplanetary Monitoring Platform (IMP; Garcia-Munoz et al. 1975) in the 1970s, the High-Energy Astronomy Observatory (HEAO-3; Binns et al. 1988) in the 1980s, the Advanced Composition Explorer (ACE; Stone et al. 1998) in the 2000s that made the first attempts for in-situ detection of CRs, the calorimetric instruments of the CALorimetric Electron Telescope (CALET; Adriani et al. 2019) onboard the International Space Station (ISS) and the Dark Matter Particle Explorer (DAMPE; Chang et al. 2017) recently measured the electron and positron CR spectra up to the TeV regime. The other CR detector onboard ISS, namely the Alpha Magnetic Spectrometer (AMS-02; Aguilar et al. 2013), and most importantly the Payload for Antimatter Matter Exploration and Light-nuclei Astrophysics (PAMELA; Picozza et al. 2007) were the first to show the positron excess in the GeV energy range, where the electron spectrum does not show the same feature. This result was initially interpreted as a dark matter signature (Picozza et al. 2007), but along with the latest  $\gamma$ -ray observations of pulsars wind nebulae (see, e.g., Abdo et al. 2010), it indicates the importance of propagation of CRs in the interstellar medium (see Section 1.4.3). Finally, a significant contribution to our understanding of the CR spectrum at low energies, below GeV, has come from the Voyager 1 and 2 missions. In 2012 and in 2018, Voyager 1 and Voyager 2, respectively, crossed the heliosheath to continue their journey in the very local interstellar medium (Gurnett et al. 2013; Stone et al. 2019, respectively). Both missions proved once more that the CR spectrum is modulated by the solar wind and were the first to detect the Galactic CRs in-situ with no contamination from the solar energetic particles (SEPs). However, the Voyager missions are only able to detect particles of energies up to 100 MeV as a result of the size of their detectors.

### 1.1.3 Cosmic ray sources

Decades of studies have established that the CR sources are not only from outside the solar system, but also from outside our Galaxy. CRs will remain confined in their acceleration sites, and will only escape when the size of the acceleration site is approximately equal to the gyroradius of the accelerating particles (Hillas 1984)

$$r_{\perp} = \frac{E}{ZeB}, \quad (1.1)$$

where  $E$  is the total energy of the accelerating particle,  $Z$  is the atomic number and  $B$  is the strength of the magnetic field of the acceleration site. This requirement, also known as the Hillas criterion, allows for an order of magnitude estimate of the maximum energy of the CRs in a given source of size  $R$

$$E \leq Z \left( \frac{B}{1 \mu\text{G}} \right) \left( \frac{R}{1 \text{pc}} \right) \text{PeV}. \quad (1.2)$$

Starting from the largest CR energies of the order of EeV, both Pierre Auger and TA suggest a bipolar anomaly on the sky that points away from the Galactic plane, which indicates an extragalactic origin of these highly energetic CRs (The Pierre Auger Observatory et al. 2017; Abbasi et al. 2020; Tinyakov et al. 2021). Several astrophysical systems, in agreement to Hillas criterion, are suggested to have the capacity to accelerate CRs to these energies. The relativistic outflows launched by active galactic nuclei (AGN; Protheroe & Kazanas 1983; Rachen & Biermann 1993; Aharonian et al. 2002; Murase et al. 2012; Petropoulou et al. 2015; Rodrigues et al. 2018) and the  $\gamma$ -ray bursts (GRBs; Levinson & Eichler 1993; Waxman 1995; Piran 2005; Mészáros 2006; Metzger et al. 2011; Hümmer et al. 2012; Berezhinsky 2013; Murase & Ioka 2013; Petropoulou et al. 2014; Tamborra & Ando 2015), are dominated by strong magnetic fields that force CRs to accelerate to high energies through various acceleration mechanisms (see Section 1.4). These two classes though cannot explain the entire CR spectrum as well as the rest of the observational constraints, such as the  $\gamma$ -ray and neutrino spectra (see Section 1.5.2), and further sources are needed. Starburst galaxies (Fields & Prodanović 2010; Ackermann et al. 2012; Murase et al. 2013; Tamborra et al. 2014; Peretti et al. 2019, 2020; Ajello et al. 2020; Ambrosone et al. 2021; Roth et al. 2021), galaxy clusters (Völk & Atoyan 1999; Perkins et al. 2006; Blasi et al. 2007b), mergers of compact objects (Takami et al. 2014; Kotera & Silk 2016; Rodrigues et al. 2019), and tidal disruption events (TDEs; Farrar & Gruzinov 2009; Wang & Liu 2016; Alves Batista & Silk 2017; Guépin et al. 2018; De Colle & Lu 2020; Stein et al. 2021) may be some additional extragalactic CR sources that contribute to the total observed extragalactic CR spectrum.

For decades, Supernovae (SNe) and young Supernova Remnants (SNRs) have been suggested being the dominant Galactic CR sources. Baade & Zwicky (1934) were the first to suggest that SNe could be the main CR sources based on energetic arguments,

which are outlined as follows. The CR power measured on Earth is of the order of  $10^{41} \text{ erg s}^{-1}$  (Gurnett et al. 2013). A SN explosion releases energy that reaches approximately,  $10^{53} \text{ erg}$  with thermal neutrinos carrying the vast majority of 99 per cent of that energy (Hirata et al. 1987). If the SN rate is of the order of 1 to 3 per year that results in an energy rate of the order of  $10^{42} \text{ erg s}^{-1}$ , a factor of 10 larger than the CR power we measure. Assuming a reasonable efficiency factor of 10 per cent for the accelerated CRs leads to the conclusion that SNe could potentially explain the entire CR spectrum from GeV up to PeV energies.

When CRs are accelerated to energies of the order of PeV, they interact with the surrounding medium producing  $\gamma$ -rays with energy approximately 10 per cent of the individual CR's energy, namely of the order of 1 to 100 TeV (see Section 1.5.2 for a more detailed description of these phenomena). Consequently, if SNe and young SNRs accelerated CRs up to PeV, then we should have detected TeV and hundreds of TeV  $\gamma$ -rays from these sources. Both direct and indirect  $\gamma$ -ray observations, such as those conducted with *Fermi* and the High Energy Stereoscopic System (H.E.S.S.) respectively, indicate that SNe emit very steep  $\gamma$ -ray spectra that sometimes show a cutoff at energies smaller than 100s of TeV. Figure 1.2 shows the  $\gamma$ -ray spectra of three historical SNRs, Cas A (Albert et al. 2007; Ahnen et al. 2017b), SN 1006 (Abramowski et al. 2011), and Tycho (Archambault et al. 2017), as well as some “famous” SNRs candidate sources for CR acceleration, HESS J1640-465 (HESS et al. 2014), RX J1713.7-3946 (Aharonian et al. 2007b), HESS J1731-347 (Abramowski et al. 2011), and Vela Jr (Aharonian et al. 2007a). All sources show very steep spectra with spectral index between -2.5 to -3.0, which implies that the parent protons cannot exceed far beyond 100s of TeV. If SNRs cannot accelerate CRs far beyond a few hundreds of TeV, then new Galactic sources capable of accelerating particles to high energy are needed, in order to contribute to or dominate the CR spectrum

The view that new Galactic sources are required to accelerate particles to high energy is in good agreement with the recent TeV-to-PeV observations of the ground-based detectors Large High Altitude Air Shower Observatory (LHAASO; Cao et al. 2021a), Tibet AS $_{\gamma}$  (Amenomori et al. 2021) and the High Altitude Water Cherenkov (HAWC; Albert et al. 2020). These facilities have recently managed to detect several Galactic sources that emit up to PeV  $\gamma$ -ray, but none of them coincide with an SN or SNR. Apart from the very-well known  $\gamma$ -ray emitter Crab nebula (Aharonian et al. 2006a; Forot et al. 2008; Abdo et al. 2009; Amenomori et al. 2019), and the recently discovered Cygnus cocoon (Bartoli et al. 2014, 2015; Ackermann et al. 2018; Aharonian et al. 2019), the rest of the sources remain unknown, though some of them could possibly coincide with pulsar halos. The need for further CR accelerators, has led several authors in the past to consider the Galactic jets of X-ray binaries (XRBs) likely acceleration sites, but this scenario stalled for several years (Heinz & Sunyaev 2002; Distefano et al. 2002; Romero et al. 2003; Fender et al. 2005; Cooper et al. 2020). In this work, I revisit the hadronic acceleration scenario in Galactic jets and examine

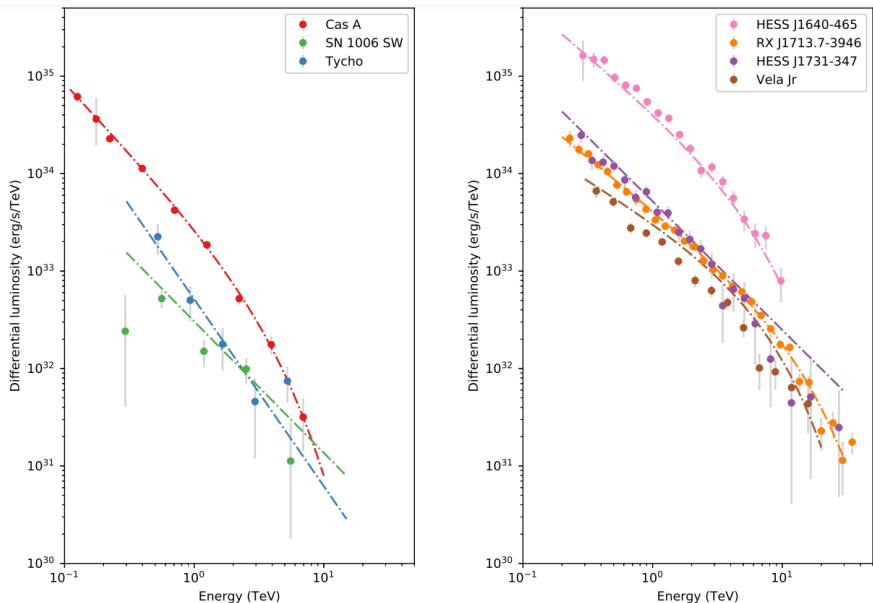


**Figure 1.2:** The  $\gamma$ -ray spectra of historical (*left*) and some additional famous SNRs (*right*) that show very steep spectra at energies below 10 TeV. The lack of TeV-to-PeV  $\gamma$ -ray emission from these sources supports the need for another class of PeV CR accelerators, known as PeVatrons. See text for references. The figure is from Aharonian et al. (2019).

the implications for such an acceleration to the detected electromagnetic spectra. In the following section I introduce the main characteristics of XRBs before discussing the likely radiative mechanisms occurring inside the jets.

## 1.2 X-ray binaries

Half of the stars in galaxies are in binary systems (see, e.g., Illarionov & Sunyaev 1975; Meurs & van den Heuvel 1989; Bhattacharya & van den Heuvel 1991). Many binary systems evolve into a phase where they emit most of their energy in the X-ray band, and thus are known as X-ray binaries (XRBs). XRBs consist of a compact object, such as a white dwarf, a neutron star or a black hole, and a donor star that feeds the compact object. In this work, I focus only on XRBs that harbour a black hole (BHXBs) since this class of XRBs is well known to launch relativistic jets during outbursts (see Section 1.3). The jets of XRBs shine across the entire broadband multiwavelength spectrum similar to AGN jets, making them likely CR acceleration sites. The major advantage of BHXB jets, however, is that they evolve on human-like timescales (see, e.g., Fender et al. 2004; Russell et al. 2006), so a better understanding

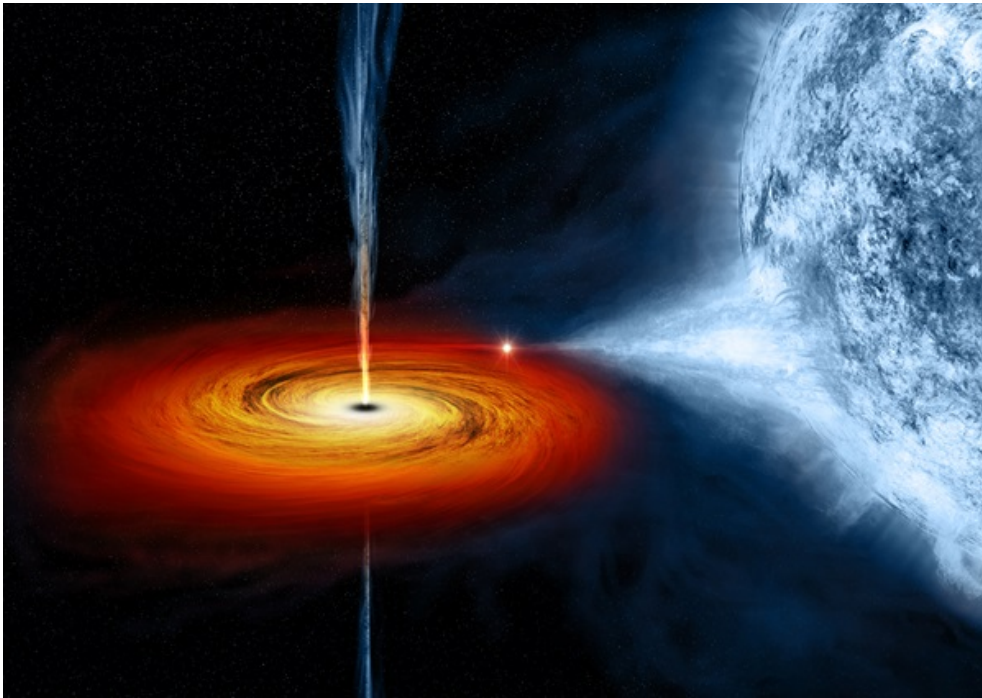


**Figure 1.3:** Illustration of the high-mass X-ray binary Cyg X-1. The central black hole accretes matter through an accretion disc that is fed by the stellar wind of the companion star, and launches two collimated relativistic outflows known as jets. Image Credit: NASA/Weiss.

of the small-scale jets in BHXBs can further our understating of the large-scale jets in AGN as well.

### 1.2.1 Black hole X-ray binaries

A black hole is a compact object with a gravitational potential so strong that nothing, not even light can escape. Black holes span a large mass range, from stellar mass black holes with masses a few times that of the Sun to supermassive black holes with masses millions or billions of times that of the Sun lying at the centres of galaxies. The first-ever (indirect) detection of a black hole occurred in the 1970s and is the prototypical case of Cygnus X-1 (Cyg X-1), a BHXB (Webster & Murrin 1972; Bolton 1972). Since the discovery of Cyg X-1,  $\sim 50$  more BHXBs have been detected in the Galaxy (Tetarenko et al. 2016b). Figure 1.3 shows an artist's impression of the morphology of Cyg X-1 that is common for the majority of BHXBs during outbursts. The main components of a BHXB are the central black hole and the companion star, which for this particular source is an O9.7Iab supergiant (Bolton 1972). The nature of the companion star leads to the classification of BHXBs between low- and high-mass

BHXBs (see below). Some additional components of a BHXB are the stellar wind, the accretion disc, and the relativistic collimated outflows, known as jets. These three components may vary with time during an outburst, but may also significantly differ between different XRBs.

## 1.2.2 XRB classification

BHXBs, and XRBs in general, are classified based on the nature of the companion star. When the donor's mass is approximately greater than a few to a few tens of solar masses, the binary is a high-mass BHXB. In the case where the mass of the donor star is of the order of a solar mass, then we talk about a low-mass BHXB. A further classification that applies to both low- and high-mass BHXBs is based on the spectral emission of the system, that evolves in time. When the X-ray band is dominated by a high and soft component, the system is in the soft state. When the X-ray emission becomes low but steep, the system is in the hard state (Remillard & McClintock 2006; Belloni 2010). This last classification is not very distinct because intermediate states have also been observed. I briefly expand on all the different classes in the following subsections.

### 1.2.2.1 High-mass BHXBs

There are several known high-mass BHXBs systems, with the most famous and well-studied ones being SS433 (Hillwig et al. 2004), Cyg X-1 (Orosz et al. 2011), and Cyg X-3 (Hanson et al. 2000; Vilhu et al. 2009). The companion star has a radius of the order of 10–30  $R_{\odot}$  and almost fills its Roche-lobe (Tauris & van den Heuvel 2006). The stellar wind of the companion star feeds the compact object with matter while the two bodies orbit each other with a period of the order of a few days.

### 1.2.2.2 Low-mass BHXBs

The orbital period of low-mass XRBs is usually smaller and of the order of a few hours to days. While the compact objects in high-mass systems are fed by the stellar wind of the companion star, the compact objects of low-mass XRBs are fed through overflow of the Roche-lobes (Tauris & van den Heuvel 2006). Low-mass XRBs are more abundant than high-mass XRBs, but it is not clear yet whether this is a natural result of the stellar evolution of binary systems or merely observational bias (see Sections 1.2.2.3 and 1.2.2.4). To date, there are tens of low-mass BHXBs and approximately twice as many with a neutron star (see, e.g., Tetarenko et al. 2016b), but recent population synthesis results suggest the existence of presumably  $10^5$  BHXBs (Pfahl et al. 2003; Yungelson et al. 2006; Olejak et al. 2020). Figure 1.4 shows an example of a high-mass (top) and a low-mass XRB (bottom). This particular figure is for a neutron star, but it would remain the same if the central compact object is a black hole, however

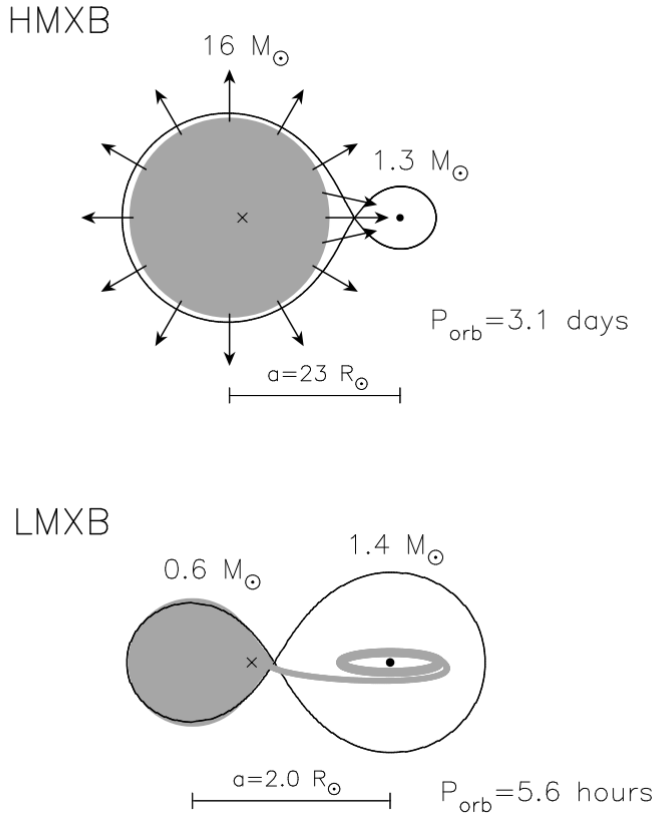


**Figure 1.4:** A characteristic example of a high-mass (*top*) and a low-mass (*bottom*) XRB. The compact objects of the systems are fed by a donor star that is 16 and 0.6 solar masses for the high-mass and low-mass XRB, respectively. While the compact object of the high-mass is fed by the stellar wind of the donor star, the compact object of the low-mass system is fed by Roche-lobe overflow. The figure is from Tauris & van den Heuvel (2006).

the mass of the black hole would have to be greater than  $\sim 5 M_{\odot}$  (Shaposhnikov & Titarchuk 2009; Abbott et al. 2021; The LIGO Scientific Collaboration et al. 2021).

### 1.2.2.3 Hard state

XRBs spend most of their time in quiescence, namely they remain too faint to be detected by current X-ray satellites. However, when they transit and undergo an outburst they rise from quiescence and their luminosity reaches approximately ten per cent of the Eddington luminosity  $L_{\text{Edd}} = 4\pi GM_{bh}m_p c / \sigma_T = 1.26 \times 10^{38} (M_{bh}/M_{\odot}) \text{ erg s}^{-1}$ , where  $M_{bh}$  is the mass of the black hole,  $G = 6.67 \times 10^{-8} \text{ cm}^3 \text{ g}^{-1} \text{ s}^{-2}$  is the gravita-



tional constant,  $m_p = 1.67 \times 10^{-24}$  g is the rest mass of the proton,  $c = 3 \times 10^{10}$  cm s $^{-1}$  is the speed of light,  $\sigma_T = 6.65 \times 10^{-25}$  cm $^2$  is the Thomson cross-section, and  $M_\odot = 1.989 \times 10^{33}$  g is the solar mass. In the hard state, the X-ray spectrum shows a power law in most of the cases, and is significantly harder than the rest of the outburst with a spectral index of 1.6–1.7 in the keV band. Whereas the entire outburst may last up to a few months, the so-called hard state lasts between a few weeks and some months (Fender et al. 2004, 2009; Russell et al. 2006; Belloni 2010).

The nature of this hard X-ray spectrum, as well as the physical mechanism responsible for the emission, are still debated. A few possible mechanisms have been suggested, the two leading mechanisms are; a thermal plasma of electrons known as corona (Sunyaev & Titarchuk 1980; Haardt & Maraschi 1993; Titarchuk 1994; Narayan & Yi 1994; Magdziarz & Zdziarski 1995; Del Santo et al. 2008; Reig & Kylafis 2015, 2021; Mastroserio et al. 2019), and relativistic outflows known as jets (see Section 1.3). The jets in particular are responsible for the non-thermal radio emission (Fender et al. 2000; Fender 2001; Fender et al. 2006), and in the last decade have also been connected to the  $\gamma$ -ray emission detected from a few BHXBs (Bosch-Ramon et al. 2008; Tavani et al. 2009; Zdziarski et al. 2012; Malyshev et al. 2013; Bodagheh et al. 2013; Pepe et al. 2015; Zanin et al. 2016).

#### 1.2.2.4 Soft state

When the source transits to the soft state, the X-ray spectrum transits from a hard power-law to a thermal-like bump. The spectrum is dominated by a multicolour black-body emission that is thought to originate in the accretion disc around the compact object (Shakura & Sunyaev 1973; Mitsuda et al. 1984). When the source returns to the hard state, the X-ray luminosity starts to drop. Usually low-mass BHXBs transit from the hard state to the soft, and back to the hard following a q-shaped diagram in a spectral hardness versus the X-ray luminosity plot (known as hardness-intensity diagram; HID). Figure 1.5 shows such an outburst for the prototypical low-mass BHXB, GX 339–4, as observed over the last three decades. Whereas low-mass BHXBs follow this normal behaviour (Fender et al. 2004; Belloni 2010), high-mass BHXBs on the other hand are persistent sources and spend most of their time in the hard state (Wilms et al. 2006; Rushton et al. 2012; Grinberg et al. 2013). During the soft state, we also detect the accretion disc wind in the Optical, the UV and the X-ray spectrum (Neilsen & Lee 2009; Ponti et al. 2012; Fabian 2012), a feature that has only recently been detected in the hard state as a result of better quality data (Muñoz-Darias et al. 2019; Kosenkov et al. 2020a).

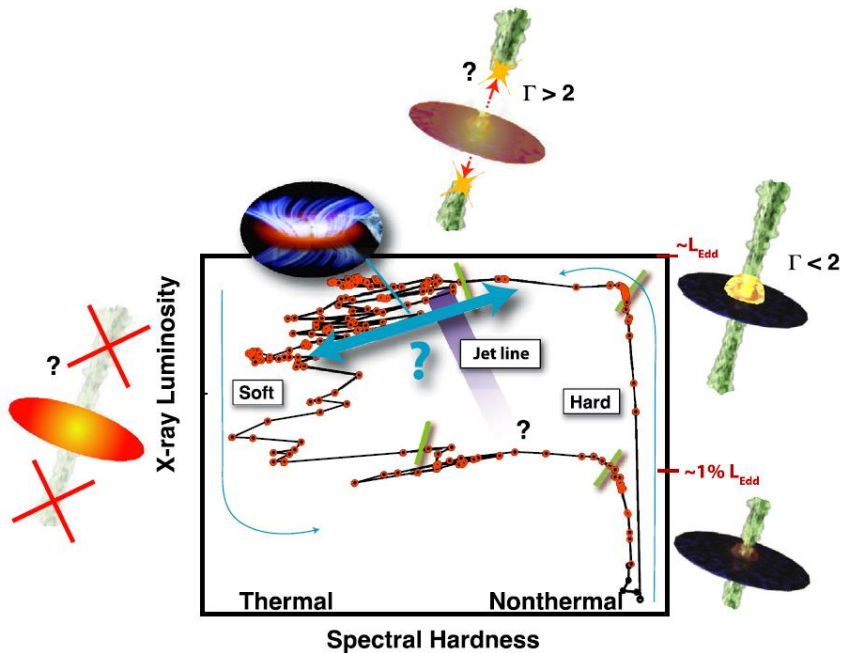


**Figure 1.5:** An outburst of an XRB based on the study case of GX 339–4. The system rises from quiescence to launch two relativistic jets in the so-called hard state. It then transits to the soft state, where the X-ray spectrum is dominated by the emission of a thermal disc. The system returns to the hard state before eventually decaying back to quiescence. The plot is from Romero et al. (2017).

### 1.3 Relativistic jets from BHXBs

Numerous astrophysical sources launch collimated outflows, known as jets, that nearly reach the speed of light and extend to large distances. Jets are composed of magnetic fields and particles that populate a broad distribution in energies. Among the first jets to be detected was the jet launched by the core of the galaxy M87. In 1918 Heber Curtis described the jet of M87 as a “*curious straight ray . . . apparently connected with the nucleus by a thin line of matter*” (Curtis 1918). Since 1922, when Edwin Hubble classified it as an extragalactic source, its nature remains unclear. In the post-war era, when significant advancements were made in radio astronomy, M87 was detected at 5 GHz (Baade & Minkowski 1954; Felten 1967) and since then, it has been detected across the entire electromagnetic spectrum up to TeV  $\gamma$ -rays (see, e.g., the recent multiwavelength campaign of The EHT MWL Science Working Group et al. 2021). Figure 1.6 shows the jets of M87 across the electromagnetic spectrum as detected by various telescopes. To date, there are thousands of AGN that hint

at the existence of relativistic jets (see, e.g., Ajello et al. 2020), but we still do not fully understand them. For instance, as I discuss later in this section, we still do not fully understand the launching mechanism nor the jet composition. The fact moreover that jets shine across the whole electromagnetic spectrum is consistent with efficient particle acceleration, but the exact acceleration mechanism remains unclear (see Section 1.4). Despite the detection of jets across the entire spectrum, we still do not have the sensitivity to resolve the exact site where the non-thermal radiation originates, and in particular, it is unclear whether it originates in the spine (the central region of a jet) or the sheath of the jets (the relativistic plasma embracing the spine). All the above open issues may also have a crucial impact on the contribution of jets to the CR spectrum beyond the knee, especially in the case of proton/ion-dominated composition. In this work, I focus on further understanding the hadronic acceleration in astrophysical jets and its implications on the electromagnetic and CR spectra.

Apart from AGN, relativistic jets are connected to further sources, such as GRBs (Band et al. 1993; Kouveliotou et al. 1993; Rhoads 1999; Sari et al. 1999; Piran 1999; Mészáros 2002; Kumar & Zhang 2015), TDEs (Zauderer et al. 2011; Cenko et al. 2012; Cendes et al. 2021), SNRs (Cobb et al. 2006; Pian et al. 2006; Soderberg et al. 2006, 2010; Margutti et al. 2014), and recently to pulsars (van den Eijnden et al. 2018, 2021) and XRBs. Mirabel & Rodríguez (1994) suggested the existence of a superluminous motion from GRS1915+105, a low-mass BHXB, the first superluminous motion to be reported in the Galaxy. Since the correlation of GRS1915+105 to a jet emission, it has been established that when BHXBs enter the hard state, they launch two relativistic jets that shine in the radio bands producing a flat radio spectrum (Blandford & Königl 1979; Fender et al. 2000). The jets might also be responsible for the X-ray spectrum detected during the hard state. In the early 2000s, Markoff et al. (2001, 2003) considered synchrotron radiation (see Section 1.5.1.1) as a viable scenario to explain the X-rays, this view was further supported by the simultaneous radio and X-ray observations of a number of BHXBs (Corbel et al. 2003; Merloni et al. 2003; Fender et al. 2004). An alternative view that could also explain the reflection signature off the accretion disc (Fabian et al. 1989) was inverse Compton scattering (see Section 1.5.1.2) in the jet-base (Maitra et al. 2009, 2011; Markoff et al. 2015; Connors et al. 2016), this view was further supported by recent X-ray timing analysis (see, e.g., Kara et al. 2019; Russell et al. 2020).

The relativistic jets of BHXBs share multiple similarities with their large-scale counterparts, namely the AGN jets. For both cases, the launching mechanism is heavily debated and could be due to the Blandford-Payne or Blandford-Znajek mechanism. In the former case, the jets are powered by the field lines anchored to the accretion disc that forms around the black hole (Blandford & Payne 1982), and in the latter case, the jets extract energy from the black-hole spin (Blandford & Znajek 1977). Jets that are launched by black holes can be mainly described by the mass of the black hole and hence are scale invariant (Falcke & Biermann 1995; Heinz &

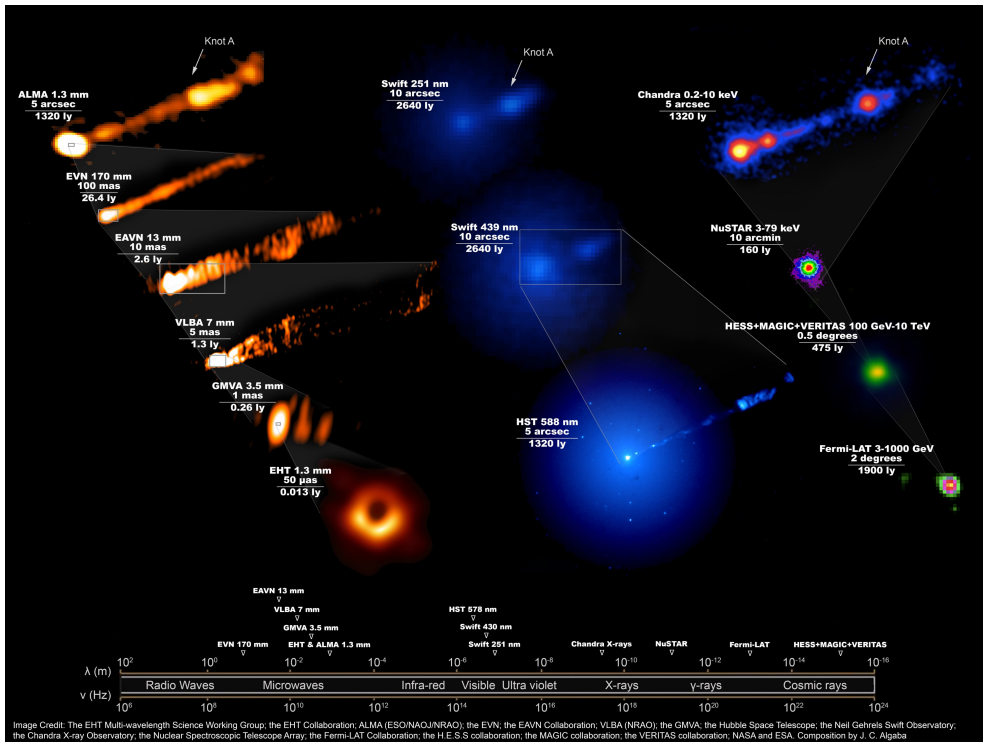


**Figure 1.6:** The multiwavelength view of M87. Different facilities that operate in different frequencies resolve the jets of M87 in various scales from radio bands (left) to  $\gamma$ -rays (right). Image Credit: The EHT Multi-wavelength Science Working Group; the EHT Collaboration; ALMA (ESO/NAOJ/NRAO); the EVN; the EAVN Collaboration; VLBA (NRAO); the GMVA; the Hubble Space Telescope; the Neil Gehrels Swift Observatory; the Chandra X-ray Observatory; the Nuclear Spectroscopic Telescope Array; the Fermi-LAT Collaboration; the H.E.S.S. collaboration; the MAGIC collaboration; the VERITAS collaboration; NASA and ESA. Composition by J. C. Algaba (The EHT MWL Science Working Group et al. 2021).

Sunyaev 2003; Merloni et al. 2003; Falcke et al. 2004; Plotkin et al. 2011). Both large and small-scale jets remain collimated up to distances of the order of  $10^9 r_g$ , where  $r_g = GM_{bh}/c^2 \simeq 1.5 \times 10^5 (M_{bh}/M_\odot)$  cm is the gravitational radius. Such a distance translates for an AGN jet to tens of kpc for a supermassive black hole in the centre of a galaxy, or hundreds of AU for a stellar-mass black hole. AGN jets are more powerful than small-scale jets because they may carry power of the order of  $10^{47}$  erg s $^{-1}$  for a billion solar mass black hole, which approaches the Eddington limit. Small-scale jets, on the other hand, may carry power of the order of  $10^{40}$  erg s $^{-1}$  for a ten solar mass black hole. The exact total jet power is hard to estimate and indirect means are used, such as observations of the termination shock that is used as a calorimeter (such as the case of Cyg X-1; Gallo et al. 2005). Even if BHXB jets are less energetic, they

have the advantage of transiting on human-like timescales, making them more suitable candidates to study the timing evolution of jets when they rise from quiescence and transition through an outburst cycle.

Despite observing astrophysical jets to be elongated and highly collimated outflows, the exact description of their dynamical conditions and their multiwavelength electromagnetic spectra is still challenging. Given these difficulties, multiple authors have assumed in the past that the location of the jet that is responsible for the non-thermal emission can be simplified to a spherical blob, known as the single-zone paradigm (Tavecchio et al. 1998; Mastichiadis & Kirk 1995, 2002; Marscher et al. 2008; Dimitrakoudis et al. 2012). Such an approximation has been very successful in explaining the timing properties of jetted sources, but has failed to interpret the entire multiwavelength spectrum from radio to X-rays/ $\gamma$ -rays. A very successful alternative is the so-called multi-zone approach, as initially described by Blandford & Königl (1979) and Hjellming & Johnston (1988). Later developments by Falcke & Biermann (1995), Markoff et al. (2001, 2005), Maitra et al. (2009), Vila & Romero (2010); Vila et al. (2012), Zdziarski et al. (2014b), Connors et al. (2016), Crumley et al. (2017), Lucchini et al. (2018, 2022) have shown that the multi-zone approach is in good agreement with the entire multiwavelength spectrum for both large-scale and Galactic jets.

To better understand the jet emission and dynamics, we need to better understand the jet composition as well. The two opposite launching mechanisms predict different jet content, at least at their bases. The Blandford-Znajek mechanism most likely leads to a leptonic jet content, whereas the Blandford-Payne mechanism favours a mixed composition of both electrons and protons. The Blandford-Znajek powered jets though may still allow for hadronic content if the jets are loaded further out along the length due to instabilities (see Chapter 5 for further details). In both cases, when particles are accelerated to high energy, they can produce  $\gamma$ -rays, but only the hadronic content can lead to the neutrino formation that is the smoking gun for CR sources, as I thoroughly explain below. In such a hadronic scenario, however, the jet power often exceeds the Eddington limit and the power required for the proton acceleration may exceed the jet reservoir. Such a problem has been puzzling the modelling community for quite some time now, challenging the paradigm that jets can contribute to the CR spectrum, and alternative scenarios are required (Böttcher et al. 2013; Zdziarski & Böttcher 2015; Liodakis & Petropoulou 2020).

## 1.4 Particle acceleration

Jets are among the most prominent candidates for particle acceleration up to energies that reach the ankle of the CR spectrum and beyond. The exact mechanism responsible for this acceleration is not clear yet and has been the subject of intense research

for decades. There are two different mechanisms that manage to reproduce the majority of the observational constraints, the diffusive shock acceleration (DSA) and magnetic reconnection. These are the two dominant mechanisms that I will expand on, there are however several more suggested mechanisms such as rotating magnetospheres (Rieger & Mannheim 2000), shear acceleration (Rieger & Duffy 2004, 2019; Liu et al. 2017; Rieger 2019), or acceleration due to turbulence (Pryadko & Petrosian 1997; Dmitruk et al. 2004; Petrosian 2012; Lazarian et al. 2012; Lynn et al. 2014; Comisso & Sironi 2018) that may dominate under different environmental conditions.

### 1.4.1 Diffusive shock acceleration

Based on the pioneering work of Fermi (Fermi 1949), when charged particles encounter a shock wave, they scatter back and forth multiple times to gain energy. In each shock crossing, the average energy gain of a relativistic particle is

$$\frac{\Delta E}{E} \simeq \frac{2}{3} \frac{\Delta u}{c}, \quad (1.3)$$

where  $E$  is the particle energy,  $\Delta E$  is the energy gain, and  $\Delta u = v_1 - v_2$  is the velocity difference between the upstream ( $v_1$ ) and the downstream ( $v_2$ ) regions of the shock wave. When a population of particles encounters the shock wave, they accelerate to high energies forming a distribution that scales as

$$N(E) \propto E^{-p}, \quad (1.4)$$

where  $p = (\chi + 2)/(\chi - 1)$  depends on the compression ratio of the shock wave  $\chi = v_1/v_2$ . For a strong shock wave where  $\chi \rightarrow 4 \Rightarrow p \simeq 2$ . The spectral index of  $p = 2$  is in good agreement with the radio spectrum we detect from particle accelerating sources, such as the BHB jets (see Section 1.5.1).

Using the Hillas criterion (Equation 1.2), we can estimate the timescale required for the particles to accelerate to energy  $E$  (Drury 1983; Jokipii 1987; Becker et al. 2006)

$$t_{\text{DSA}} = \frac{4E}{3f_{sc}ecB}, \quad (1.5)$$

where  $f_{sc}$  is an acceleration efficiency parameter (Aharonian 2002, 2004).

The DSA theory has thoroughly been tested, especially in the SNR acceleration paradigm, both in the linear and non-linear regimes (Axford et al. 1977; Bell 1978a,b, 2004; Achterberg 1983; Hillas 1984; Malkov 1997; Malkov & Drury 2001; Berezhko & Ellison 1999; Amato & Blasi 2005, 2006, 2009; Blasi et al. 2007a; Ptuskin et al. 2010; Caprioli 2012; Morlino & Caprioli 2012; Gabici & Aharonian 2014). Recent particle-in-cell simulations (PIC) that calculate the trajectories and energy gain of individual particles in an electromagnetic field from first principles, have shown that DSA is a

natural explanation for the formation of a power law of accelerated particles (Sironi & Spitkovsky 2009, 2011; Riquelme & Spitkovsky 2011; Caprioli & Spitkovsky 2013, 2014a,b,c; Park et al. 2015; Crumley et al. 2019) in agreement with multiwavelength observations of SNe and SNRs (Vink 2004, 2012; Patnaude et al. 2011; Raymond et al. 2011; Ackermann et al. 2011, 2013; Domček et al. 2021, and references above). Such state-of-the-art simulations have also successfully interpreted the magnetic amplification required to explain the CR acceleration up to larger energies (Bell 2004; Vink 2006, 2008). It is still not clear though if DSA is the dominant acceleration mechanism in jets as well, and hence further observations and spectral modelling can prove useful on finding the contribution of this mechanism in the acceleration of CRs in jets.

### 1.4.2 Magnetic reconnection

Whereas DSA manages to explain several observational constraints, such as the photon index of the non-thermal radio/IR observed spectrum, it struggles to sufficiently explain the particle acceleration in relativistic and strongly magnetised regions (Uzdensky 2011; Guo et al. 2014; Sironi & Spitkovsky 2014; Sironi et al. 2015; Kagan et al. 2015), and in fact, astrophysical jets are in principle characterised by strong magnetic fields. A promising alternative theory has managed to fill the gap in the last two to three decades, allowing for both highly magnetised environments and efficient particle acceleration.

When magnetic field lines of different polarity cancel out each other, particles gain energy due to magnetic reconnection. The average energy gain of the particles that are involved in a reconnecting region strongly depends on the magnetisation of the site that is defined as the Poynting flux over the total energy flux (Nokhrina et al. 2015)

$$\sigma = \frac{B^2}{4\pi(\rho c^2 + U_g + P_g)}, \quad (1.6)$$

where  $\rho$  is the mass density of the acceleration site,  $U_g$  is the intrinsic energy density and  $P_g$  is the gas pressure. PIC numerical simulations have shown that magnetic reconnection leads to particle power laws similar to DSA, namely

$$N(E) \propto E^{-p}, \quad (1.7)$$

where  $p$  ranges between harder values ( $p < 2$ ), but much softer as well ( $p \lesssim 4$ ) depending on the physical conditions of the source (Sironi & Spitkovsky 2014; Guo et al. 2014, 2016; Cerutti et al. 2014; Melzani et al. 2014; Sironi et al. 2015, 2016; Werner et al. 2015; Petropoulou et al. 2016, 2019; Petropoulou & Sironi 2018; Ball et al. 2018).

The time required for particles to reach the maximum energy in magnetic reconnection depends on the reconnection rate, which is  $r_{\text{rec}} = v_{\text{in}}/v_A$ , where  $v_{\text{in}}$  is the inflow velocity in the lab frame and  $v_A$  is the Alfvén velocity  $v_A = c\sqrt{\sigma/(1+\sigma)}$  (Sironi & Spitkovsky 2014; Petropoulou et al. 2019). For a collisionless plasma, such as astrophysical jets, the reconnection rate is of the order of  $r_{\text{rec}} \simeq 0.1$ , and hence the inflow velocity is  $v_{\text{in}} \simeq 0.1c$  (Sironi & Spitkovsky 2014). The inflow velocity also defines the electric field  $E_{\text{rec}}$  responsible for the particle acceleration, such that  $\mathbf{E}_{\text{rec}} = -\mathbf{v}_{\text{in}} \times \mathbf{B}/c \Rightarrow E_{\text{rec}} \simeq 0.1B$  (Uzdensky 2011; Kagan et al. 2015). The energy gain is

$$\left(\frac{dE}{dt}\right)_{\text{rec}} = ecE_{\text{rec}} \simeq 0.1ecB, \quad (1.8)$$

and therefore the acceleration timescale is

$$t_{\text{rec}} = \frac{E}{(dE/dt)_{\text{rec}}} = \frac{E}{0.1ecB}. \quad (1.9)$$

Besides the environmental conditions, a further significant difference between DSA and magnetic acceleration is the particle energy gain. For a relativistic and strongly magnetised flow, the acceleration timescale of magnetic reconnection is  $\propto E$  (see Equation 1.9). Whereas in the simple approximation, DSA leads to  $t_{\text{DSA}} \propto E$  (see Equation 1.5), PIC simulations of collisionless and relativistic shocks show a dependence of  $E \propto t_{\text{DSA}}^{1/2}$  (see, e.g., Plotnikov et al. 2011; Sironi et al. 2013), indicating that magnetic reconnection allows for a faster energy gain than DSA. Such a conclusion is not definite yet and strongly relies on the numerical restrictions PIC simulations have so far, but it is apparent that these different mechanisms allow for different acceleration properties, such as the particle acceleration efficiency and the slope.

Even though magnetic reconnection has proven useful in explaining the properties of the accelerated particles, the difficulty of comparing PIC simulations directly to observations make the development of semi-analytical models mandatory. In this work, I focus on better connecting the CR acceleration to the multiwavelength spectrum of non-thermal emitting sources and discuss the implication of both particle acceleration mechanisms on the detected spectra of BHXBs.

### 1.4.3 CR propagation

CRs are accelerated to high energies following some of the above mechanisms to form a non-thermal power law such that  $N \propto E^{-p}$ . When they escape to the interstellar (or intergalactic) medium, they propagate to reach Earth (Strong & Moskalenko 2001; Evoli et al. 2008; Vladimirov et al. 2011). Measurements of the local boron (B) to carbon (C) ratio in the 1–10 GeV/nucleon kinetic energy, show a power law that can be best explained with an index of  $\delta \simeq 0.6$  (see, e.g., Ptuskin 2012). The measured B/C



ratio measured by PAMELA and AMS-02 in larger energies above 100 GeV/nucleon, show a different slope of  $\delta = 0.4$  (Adriani et al. 2014; Génolini et al. 2019, respectively), suggesting that the propagation of CRs is energy dependent. The initial CR spectrum at the source is thus softened by a factor of  $\delta$ , namely,  $N \propto E^{-p-\delta}$  due to CR propagation. Combining the acceleration theory where  $p = 2 - 2.2$ , and the measured value of  $\delta = 0.4 - 0.6$ , we obtain a CR spectrum slope of  $s = 2.4 - 2.8$ , which in fact is the measured value of the CR spectrum up to the knee (see Section 1.1). This result favours once more the Galactic nature of the CRs up to the knee, and perhaps, even up to the ankle (see Section 1.1.3).

## 1.5 Non-thermal radiative processes

The exact jet composition is not clear, and two different scenarios are capable of explaining the current observations. First, a purely leptonic jet of electrons and positrons that are responsible for the non-thermal emission comprise the so-called leptonic models. In the leptonic scenario the existence of protons is not prohibited, and in fact protons may carry the majority of the jet kinetic energy. The leptonic population is mainly responsible for the non-thermal radiation. A second likely scenario is when the particle acceleration mechanism allows for equally efficient acceleration of both electrons and protons. In this so-called lepto-hadronic case, the accelerated protons contribute to the emitted radiation via a number of possible different radiative mechanisms that I describe below.

### 1.5.1 Leptonic processes

#### 1.5.1.1 Synchrotron radiation

The accelerated leptons (henceforth I may use the terms electrons and leptons interchangeably) of the jets, radiate away part of their energy due to their interaction with the magnetic field. This synchrotron radiation dominates the jet emission from the radio up to the IR/Optical, and sometimes even the X-ray spectrum, making it one of the most important radiative processes of jets.

An electron of energy  $E = \gamma m_e c^2$  that gyrates within a magnetic field of strength  $B$ , radiates part of its energy in a characteristic photon frequency (Blumenthal & Gould 1970; Rybicki & Lightman 2008)

$$\nu_c = \frac{3\gamma^2 e B \sin \alpha}{4\pi m_e c}, \quad (1.10)$$

where  $\alpha$  is the pitch angle. The power that an electron radiates away is proportional to its energy and the strength of the magnetic field, and is given by

$$P_{\text{syn}} = - \left( \frac{dE}{dt} \right)_{\text{syn}} = \frac{4}{3} \sigma_T c \beta^2 \gamma^2 U_B, \quad (1.11)$$

where  $U_B = B^2/8\pi$  is the magnetic energy density. The synchrotron loss timescale is

$$t_{\text{syn}} = \frac{E}{-(dE/dt)_{\text{syn}}} = \frac{6\pi m_e^2 c^3}{\sigma_T B^2 E \beta^2}. \quad (1.12)$$

In each jet segment, the accelerated electrons that follow a power-law as described by either Equation 1.4 or 1.7, radiate part of their power based on Equation 1.11, and all particles combined lead to an emitted spectrum that is a power-law as well. The slope of this emitted spectrum depends on the slope of the power law of the accelerated particles  $p$ , and in fact is equal to  $-(p-1)/2$ . Radio-to-IR observations of astrophysical sources, show a power-law in frequencies which corresponds to a slope of accelerated electrons close to  $2 - 2.2$ , similar to what we expect from the theory (see Section 1.4.1).

The overall synchrotron spectrum of BHXB jets is the convolution of two processes. First, the electron population of each jet segment radiates in a power law, as I describe above. This in fact is true in the optically thin regime, where the produced radiation escapes freely from the emitting region. The optical depth scales with the jet dynamical quantities, and the photon frequency where the optical depth transits from the optically thick to thin regime is (Ghisellini 2013)

$$\nu_t \propto \left( zKB^{(p+2)/2} \right)^{2/(p+4)}, \quad (1.13)$$

where  $z$  is the jet height and  $K$  is the normalisation factor of the accelerated particles. This particular frequency is known as the self-absorption frequency. For a Blandford-Königl (Blandford & Königl 1979) conical jet that constantly re-accelerates particles along its axis,  $B \propto z^{-1}$  and  $K \propto z^{-2}$  due to magnetic energy and particle number conservation along the jet. The self-absorption frequency then scales as  $\nu_t \propto z^{-1}$ , which means that the synchrotron radiation of the outer jet segments becomes optically thin to lower frequencies. The convolution of all jet segments leads to a flat spectrum in agreement with observations (Fender et al. 2000, 2009; Corbel & Fender 2002; Gandhi et al. 2011).

### 1.5.1.2 Inverse Compton scattering

A photon may scatter an electron and transfer part of its energy to the electron. We refer to this process as (direct) Compton scattering. In the case of a relativistic electron that carries more energy than the target photon, part of the electron's energy is transferred to the photon, and hence, we talk about the inverse process – namely the inverse Compton scattering (ICS).

When a relativistic electron of energy  $E$  scatters off of a photon field of energy density  $U_{\text{phot}}$ , it will lose part of its energy due to ICS. The power radiated away is

proportional to the energy of the electron and the energy density of the photon field similar to Equation 1.11, and is given by

$$P_{\text{ics}} = - \left( \frac{dE}{dt} \right)_{\text{ics}} = \frac{4}{3} \sigma_T c \beta^2 \gamma^2 U_{\text{phot}}. \quad (1.14)$$

When the target photons are those produced by synchrotron radiation, the process is known as synchrotron-self Compton (SSC) and the energy losses are

$$P_{\text{ssc}} = P_{\text{syn}} \frac{U_B}{U_{\text{phot}}}. \quad (1.15)$$

The time required for an electron to lose a significant part of its energy due to ICS, or in other words the ICS loss timescale, is

$$t_{\text{ics}} = \frac{E}{-(dE/dt)_{\text{ics}}} = \frac{3m_e^2 c^3}{4\sigma_T U_{\text{phot}} E \beta^2}. \quad (1.16)$$

The above Equations 1.14–1.16 hold in the Thomson regime, when the energy of the inbound photon is insignificant compared to the rest mass of the electron in its rest frame ( $\gamma\epsilon \ll m_e c^2$ , where  $\epsilon$  is the energy of the inbound photon). In the case where the energy of the photon becomes comparable to the electron rest energy, quantum electrodynamics effects require a more precise treatment that leads to the well-known Klein-Nishina regime (Klein & Nishina 1929). A semi-analytical approximations of this regime for astrophysical applications can be found in, e.g., Blumenthal & Gould 1970.

When a power law of accelerated electrons with a slope  $p$  upscatters a photon field to high energies, the resulting spectrum (of the upscattered photons) forms a power law as well, with a slope  $-(p - 1)/2$ , similar to the synchrotron radiation. The ICS process is a likely explanation of the GeV and TeV  $\gamma$ -rays detected by both extragalactic and Galactic jetted sources (Maraschi et al. 1992; Dermer & Schlickeiser 1993; Marcowith et al. 1995; Kaufman Bernadó & Mirabel 2002; Georganopoulos et al. 2002; Bosch-Ramon et al. 2006; Zdziarski et al. 2014b) if electrons of energy 1–100 TeV upscatter, for example, the cosmic microwave background (CMB) photons. There are multiple observations though in the same energy regime that favour the hadronic contribution due to the so-called pion bump, and some cases are further supported by the detection of high-energy astrophysical neutrinos (see below).

### 1.5.2 Hadronic processes

The need to explain some astrophysical observations via hadronic processes was evident even in the very early stages of  $\gamma$ -ray astronomy and high-energy CR observations. Shortly after the first observation of the CMB by Penzias and Wilson (Penzias & Wilson 1965), it became apparent that the CR spectrum will be suppressed due to

the inelastic interactions between the CRs and the CMB background (Greisen 1966; Zatsepin & Kuz'min 1966; Gould & Schröder 1966; Stecker 1968). The first observational hint for such a CR cutoff of the order of  $10^{20}$  eV (Linsley 1963), appeared in the 1970s, and was later established in the 1990s (Lawrence et al. 1991; Bird et al. 1995). The CR cutoff was finally confirmed at  $5\sigma$  confidence by, e.g., Abbasi et al. (2008) with almost two decades of High Resolution Fly's Eye (HiRes) experiment's data. The hadronic interactions are also vital in explaining the  $\gamma$ -ray spectra of several high-energy emitting sources we have been observing, such as SNRs (see, e.g., Morlino & Caprioli 2012; Gabici & Aharonian 2014) or AGN (see, e.g., Böttcher et al. 2013), the high-energy astrophysical neutrinos (Aartsen et al. 2013, 2018) and clearly the CR spectrum features like the aforementioned Greisen (1966); Zatsepin & Kuz'min (1966) (hereafter GZK) cutoff. In the following, I describe the two main channels of the hadronic processes that occur when accelerated protons interact with (i) the ambient thermal proton medium, and/or (ii) the ambient photon fields. We refer to the former as proton-proton (pp henceforth) interactions, and to the latter as proton-photon ( $p\gamma$  henceforth). I only focus on the accelerated protons and neglect heavier ions because I mainly focus on CR energies up to the knee, where protons dominate the spectrum. For hadronic interactions of heavier ions, I refer to the review of Kotera & Olinto (2011) and references therein.

### 1.5.2.1 Proton-proton collisions

When accelerated protons carry kinetic energy that is above the threshold for neutral pion production (see below) and interact with thermal protons from the ambient medium, they form charged and neutral pions

$$p + p \rightarrow p + p + \alpha\pi^0 + \beta(\pi^+ + \pi^-), \quad (1.17)$$

where  $\alpha$  and  $\beta$  are the multiplicities of the related products. The multiplicity depends on the energy of the colliding protons, and its exact numerical value is derived by Monte Carlo simulations. In this work I use the semi-analytical expressions of Kelner et al. (2006), as I discuss below. The charged pions decay into muons that further decay to secondary electrons, positrons, neutrinos and antineutrinos

$$\pi^+ \rightarrow \mu^+ + \nu_\mu, \quad \mu^+ \rightarrow e^+ + \nu_e + \bar{\nu}_\mu, \quad (1.18)$$

$$\pi^- \rightarrow \mu^- + \bar{\nu}_\mu, \quad \mu^- \rightarrow e^- + \bar{\nu}_e + \nu_\mu, \quad (1.19)$$

and the neutral pions decay into two  $\gamma$ -rays

$$\pi^0 \rightarrow \gamma + \gamma. \quad (1.20)$$

Morrison (1958) and Ginzburg & Syrovatskii (1964) were the first to discuss the need for interactions between CRs and the ambient medium in order to describe the

$\gamma$ -ray observations and the CR spectrum. Later calculations of (Stephens & Badhwar 1981; Dermer 1986; Berezhinsky 1991; Mannheim 1993; Mannheim & Schlickeiser 1994; Aharonian & Atoyan 2000; Blattnig et al. 2000) significantly furthered the field by introducing different approaches on the calculation of the cross-section and the distributions of the products of the pp collisions. The most up-to-date approximation for the cross-section is (Kafexhiu et al. 2014)

$$\sigma_{pp}(T_p) = \left[ 30.7 - 0.96 \log \left( \frac{T_p}{T_{\text{thr}}} \right) + 0.18 \log^2 \left( \frac{T_p}{T_{\text{thr}}} \right) \right] \times \left[ 1 - \left( \frac{T_{\text{thr}}}{T_p} \right)^{1.9} \right]^3 \text{ mb}, \quad (1.21)$$

where  $T_p$  is the proton kinetic energy in the laboratory frame,  $T_{\text{thr}} = 2m_\pi + m_\pi^2/2m_p \simeq 0.2797$  GeV is the threshold for this interaction to take place, and  $1 \text{ mb} = 10^{-27} \text{ cm}^2$ .

The above works led to the Monte Carlo algorithms, such as *Pythia* (Sjöstrand et al. 2006), *SIBYLL* (Fletcher et al. 1994), and *QGSJET* (Kalmykov et al. 1997; Ostapchenko 2011) that are still widely used not only to reconstruct the initial conditions of the inbound CRs and/or  $\gamma$ -rays, but also to examine the hadronic processes in astrophysical sources. Despite the precision, Monte Carlo simulations are relatively slow, making the comparison to the observational data slow. Kelner et al. (2006) were the first to parametrise the results of such simulations to produce accurate distributions of the products that can also be calculated relatively fast.

A power-law of accelerated protons, in particular, with an index of  $p$  and an exponential cutoff at the maximum attainable energy  $E_{\text{max}}$ , such that

$$J_p(E_p) = A E_p^{-p} \exp \left[ - \left( \frac{E_p}{E_{\text{max}}} \right)^\beta \right], \quad (1.22)$$

where  $A$  is the normalisation of the proton distribution,  $E_p$  is the energy of the relativistic proton, and  $\beta$  a factor between 1 and 2 (see, e.g., Lefa et al. 2012), will lead to a population of  $\gamma$ -rays via neutral pion decay that follows a spectrum

$$\frac{dN_\gamma}{dE_\gamma} = cn_H \int_{E_\gamma}^{\infty} \sigma_{pp}(E_p) J_p(E_p) F_\gamma \left( \frac{E_\gamma}{E_p}, E_p \right) \frac{dE_p}{E_p}, \quad (1.23)$$

where  $n_H$  is the number density of the target protons and  $F_\gamma$  is the produced  $\gamma$ -ray spectrum of each pp collision

$$F_\gamma(x, E_p) = B_\gamma \frac{\ln(x)}{x} \left( \frac{1 - x^{\beta_\gamma}}{1 + k_\gamma x^{\beta_\gamma} (1 - x^{\beta_\gamma})} \right) \times \left[ \frac{1}{\ln(x)} - \frac{4\beta_\gamma x^{\beta_\gamma}}{1 - x^{\beta_\gamma}} - \frac{4k_\gamma \beta_\gamma x^{\beta_\gamma} (1 - 2x^{\beta_\gamma})}{1 + k_\gamma x^{\beta_\gamma} (1 - x^{\beta_\gamma})} \right], \quad (1.24)$$

where  $x = E_\gamma/E_p$ , and

$$B_\gamma = 1.30 + 0.14 L + 0.011 L^2, \quad (1.25)$$

$$\beta_\gamma = \frac{1}{1.79 + 0.11 L + 0.008 L^2}, \quad (1.26)$$

$$k_\gamma = \frac{1}{0.801 + 0.049 L + 0.014 L^2}, \quad (1.27)$$

where  $L = \ln(E_p/1 \text{ TeV})$ .

The above resulting  $\gamma$ -ray spectrum is accurate only for  $E_p \gtrsim 0.1 \text{ TeV}$ . For proton energies less than this value, the photon spectrum is

$$\frac{dN_\gamma}{dE_\gamma} = 2 \int_{E_{\min}}^{\infty} \frac{q_\pi(E_\pi)}{\sqrt{E_\pi^2 - m_\pi^2 c^4}} dE_\pi, \quad (1.28)$$

where  $E_{\min} = E_\gamma + m_\pi^2 c^4/4E_\gamma$  and  $E_\pi$  is the neutral pion energy. In the above equation, the function  $q_\pi(E_\pi)$  is the distribution of the produced pions that is given by

$$q_\pi(E_\pi) = \tilde{n} \frac{cn_H}{K_\pi} \sigma_{pp} \left( m_p c^2 + \frac{E_\pi}{K_\pi} \right) J_p \left( m_p c^2 + \frac{E_\pi}{K_\pi} \right), \quad (1.29)$$

where  $K_\pi = \kappa/\tilde{n}$ ,  $\kappa \approx 0.17$  is the fraction of the proton energy released in the  $\gamma$ -rays, and  $\tilde{n}$  is the number of the produced pions. The parameter  $\tilde{n}$  depends on the power-law slope of the accelerated protons, and in fact,  $\tilde{n} = 1.10, 0.86, 0.91$  for  $p = 2, 2.5, 3$ .

Kelner et al. (2006) present similar prescriptions for the resulting distributions of secondary electrons  $e^-$ , muon neutrinos  $\nu_\mu$  and anti-neutrinos  $\bar{\nu}_\mu$  formed after the decay of charged pions and muons. In Figure 1.7 I show the distributions of  $\gamma$ -rays, secondary electrons and muon neutrinos derived from the above formulae. I assume  $p = 2.2$ , and a maximum energy of 60 TeV. The maximum energy of the secondary particles is the same as the maximum energy of protons, and the produced distributions show a power-law with an index same as that of the accelerated protons. The distribution of  $\gamma$ -rays is the so-called pion bump that is a natural result of the hadronic acceleration of the observed source. The distribution of secondary electrons I show here, is the injected one, and I do not account for cooling, which in fact might be important in astrophysical applications (see Section 1.6).

The timescale of pp interactions is derived by the mean-free path of this process assuming fully relativistic energies

$$t_{pp} = \frac{1}{K_{pp} \sigma_{pp} n_H c}, \quad (1.30)$$

and we see that it almost independent of the proton energy (the dependence of the cross-section on the proton energy is relatively small and in fact, an increase in the proton energy by even 7 orders of magnitude will merely lead to double the cross-section).

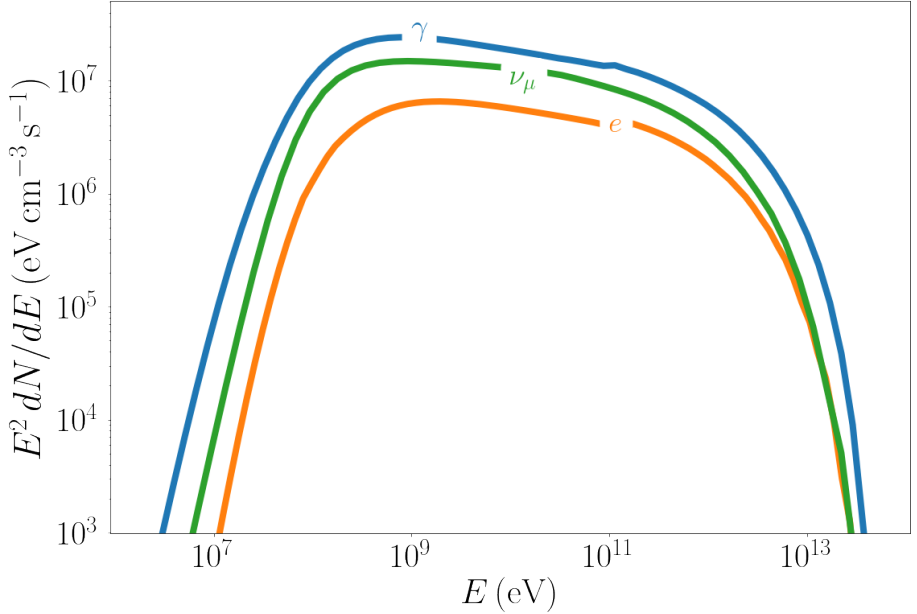


**Figure 1.7:** The products of pp collisions between accelerated protons that follow a power law in energies with an index  $p = 2.2$ , and cold protons. The protons populate a power law between 1 GeV and 60 TeV. The distributions of  $\gamma$ -rays ( $\gamma$ ), muon neutrinos ( $\nu_\mu$ ) and secondary electrons ( $e$ ) cutoff at the maximum energy of the accelerated protons.

### 1.5.2.2 Proton-photon collisions

The inelastic collisions between accelerated protons and target photons, unlike the ICS, lead to particle cascades similar to pp interactions. The  $p\gamma$  interactions also allow for a further channel, i.e., when pairs of electrons and positrons are directly produced. The energy requirement for this process to occur is such that the energy excess must be greater than  $\sim 1$  MeV, which is the rest mass of one electron and one positron. This process is known as Bethe-Heitler named after those who first studied it (Bethe & Heitler 1934). The pairs that are produced carry only a small fraction of the energy of the initial proton ( $< m_e/m_p$ ) consequently this process is often neglected (however see Petropoulou & Mastichiadis 2015). In this section, I do not expand on the Bethe-Heitler process, but I do account for it in the following chapters. The other channel of  $p\gamma$  is when the energy budget allows for the formation of pions, thus this process is known as photomeson interactions.

**Photomeson interactions** The interaction of an accelerated proton and a photon field initiates particle cascades similar to pp interactions, but in two main channels

$$p + \gamma \rightarrow p + \alpha\pi^0 + \beta(\pi^+ + \pi^-), \quad (1.31)$$

and

$$p + \gamma \rightarrow n + \pi^+ + \alpha\pi^0 + \beta(\pi^+ + \pi^-), \quad (1.32)$$

where  $\alpha$  and  $\beta$  are different compared to pp. For this process to occur, the energy of the accelerated proton must exceed the threshold of

$$E_{p,thr} \simeq 70 \left( \frac{\epsilon_\gamma}{1 \text{ eV}} \right)^{-1} \text{ PeV}, \quad (1.33)$$

where  $\epsilon_\gamma$  is the energy of the target photon. The produced pions further decay following Equations 1.18–1.20.

Greisen (1966) and Zatsepin & Kuz'min (1966) realised that this process is responsible for the high-energy cutoff of the CR spectrum when  $\sim 10^{20}$  eV CRs interact with the CMB photons.

Kelner & Aharonian (2008) were the first to produce semi-analytical expression to approximate the distributions of the secondary particles formed after decay. A similar proton power-law as above (Equation 1.22), leads to a spectrum of  $\gamma$ -rays

$$\frac{dN_\gamma}{dE_\gamma} = \int_{\eta_0}^{\infty} H(\eta, E_\gamma) d\eta, \quad (1.34)$$

where  $\eta = 4\epsilon_\gamma E_p / m_p^2 c^4$  and  $\eta_0 = 2m_\pi / m_p + m_\pi^2 / m_p^2 \simeq 0.313$ . The function  $H_\gamma$  in the above spectrum is

$$H(\eta, E_\gamma) = \frac{m_p^2 c^4}{4} \int_{E_\gamma}^{\infty} \frac{dE_p}{E_p^2} J_p(E_p) f_{ph} \left( \frac{\eta m_p^2 c^4}{4E_p} \right) \Phi_\gamma \left( \eta, \frac{E_\gamma}{E_p} \right), \quad (1.35)$$

where  $f_{ph}$  is the distribution of the target photon field. The function  $\Phi_\gamma$  includes the information about the cross-section of this process and depends on the energy range  $x = E_\gamma / E_p$ . In particular, when  $x_- < x < x_+$ ,

$$\Phi_\gamma(\eta, x) = B_\gamma \exp \left\{ -s_\gamma \left[ \ln \left( \frac{x}{x_-} \right) \right]^{\delta_\gamma} \right\} \times \left[ \ln \left( \frac{2}{1+y^2} \right) \right]^{2.5+0.4 \ln(\eta/\eta_0)}, \quad (1.36)$$

where

$$x_\pm = \frac{1}{2(1+\eta)} \left[ \eta + r^2 \pm \sqrt{(\eta - r^2 - 2r)(\eta - r^2 + 2r)} \right], \quad (1.37)$$

where  $r = m_\pi / m_p \simeq 0.146$ ,  $y = \frac{x - x_-}{x_+ - x_-}$ , and the quantities  $B_\gamma$ ,  $s_\gamma$  and  $\delta_\gamma$  are tabulated values that depend on the ratio  $\eta/\eta_0$ .



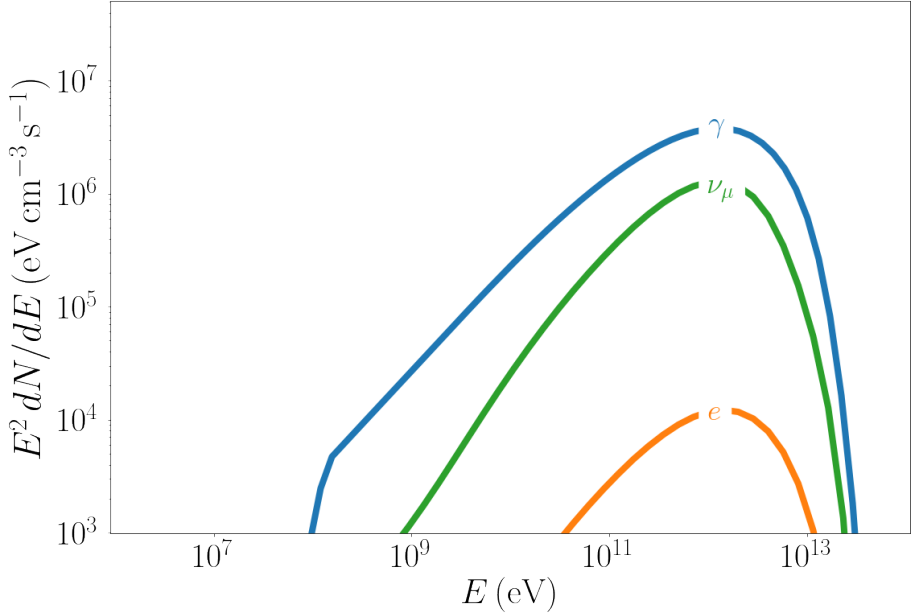


**Figure 1.8:** The products of  $p\gamma$  collisions between accelerated protons that form a power law in energies with an index  $p = 2.2$ , and a target photon field that forms a Gaussian distribution in the X-ray energy band.

In the energy range where  $x < x_-$ ,

$$\Phi_\gamma(\eta, x) = B_\gamma (\ln 2)^{2.5+0.4 \ln(\eta/\eta_0)}, \quad (1.38)$$

and in the energy range where  $x > x_+$ ,  $\Phi_\gamma = 0$ . Finally, Kelner & Aharonian (2008) provide similar formulae for the rest of the produced particles. In Figure 1.8, I show the produced distributions of  $\gamma$ -rays, muon neutrinos and electrons derived by the above calculations.

The timescale of photomeson losses is calculated by the mean free path of this process assuming a relativistic proton

$$t_{p\gamma} = \frac{1}{K_{p\gamma} \sigma_{p\gamma} f_{ph} c}, \quad (1.39)$$

where the cross-section is of the order of 0.2 mbarn (note that pp cross-section is of the order of 30 mbarn) and its full analytical expression is given by Blumenthal (1970) and Chodorowski et al. (1992).

## 1.6 The effect of losses on the accelerated particles

To capture the temporal evolution of a population of particles in a jet, we utilise the continuity equation (Fokker-Planck equation; Fokker 1914; Planck 1917)

$$\frac{\partial N}{\partial t} + \frac{\partial(\Gamma v_j N)}{\partial z} + \frac{\partial}{\partial E} \left( \frac{dE}{dt} N \right) - \frac{N}{\tau_{\text{esc}}} = Q, \quad (1.40)$$

that connects the radiative processes to the acceleration, the escape, and the diffusion/advection of particles. In the above equation,  $N$  is the number of particles that evolve with time  $t$ ,  $\Gamma v_j$  is the jet bulk velocity,  $z$  is the distance from the black hole along the jet,  $dE/dt$  is any (or the sum) of the radiative losses described above (e.g., Equation 1.11 and 1.14),  $t_{\text{esc}}$  is the characteristic escape timescale, and  $Q$  is the injection rate of particles in the acceleration site. All these quantities depend on the particle energy  $E$ , the time  $t$  and the height  $z$ . For simplicity, I incorporate the acceleration mechanism in the injection term  $Q$ , namely I assume that the injected particles follow a power law in energies resulting from some particle acceleration mechanism as described above. In the steady state case, and when the radiative losses occur on smaller timescales than the advection along the jet, the above equation may simplify to

$$\frac{\partial}{\partial E} \left( \frac{dE}{dt} N \right) - \frac{N}{\tau_{\text{esc}}} \simeq Q. \quad (1.41)$$

We can briefly examine the effect of the radiative losses on a distribution of particles  $N$  by computing their corresponding timescales. For the test case of a distribution of electrons that exists in a magnetic field of strength  $B$ , the above equation can be simplified to

$$\frac{N_e}{t_{\text{syn}}} - \frac{N_e}{t_{\text{esc}}} \simeq \dot{N}_0 E_e^{-p}, \quad (1.42)$$

where I assume that the injected electrons follow a power law in energies with an index  $p$ , and the synchrotron losses are described by their timescale  $t_{\text{syn}} = E_e/(dE_e/dt)$ . In the case of strong synchrotron losses, or in other words when  $t_{\text{syn}} \ll t_{\text{esc}}$

$$N_e \propto t_{\text{syn}} E_e^{-p} \propto E_e^{-(p+1)}, \quad (1.43)$$

which implies that the distribution of the accelerated electrons is eventually softened because of synchrotron losses. This result is very impactful to our understanding of the jet emission because in the case of a strong magnetic field, the observed spectrum provides the power-law slope of the cooled electrons, from which we then have to extract the initial  $p$ , which is consistent with the different acceleration mechanisms. Following the same approach, we can show that the ICS has the same effect on the spectrum of the accelerated electrons, and hence, on the observed spectrum. In both

cases, the observed spectrum follows a power law of  $-p/2$  instead of  $-(p-1)/2$  (see Section 1.5.1).

We do not expect such a spectral softening for the case of accelerated protons because firstly, the synchrotron and ICS losses of protons are suppressed by a factor of  $(m_e/m_p)^3$  and  $(m_e/m_p)^4$  respectively, and secondly, in the case of significant pp or p $\gamma$  collisions, as we see in Equations 1.30 and 1.39, respectively, the pp and p $\gamma$  collision timescales are almost energy independent, so  $N_p \propto E_p^{-p} t_{pp/p\gamma} \propto E_p^{-p}$ .

The synchrotron losses may be important in the case of the charged secondary particles though that are produced via pp or p $\gamma$  collisions. The distribution of secondary electrons/positrons in particular may be softened because of the above effect, and consequently, they may contribute to the observed spectrum. The secondary electrons, moreover, are produced via charged pion decay, and hence, in the case of a strong magnetic field, even the charged pions and/or muons may be softened before they decay to further particles (note that the lifetime of charged pions is 26 ns, and of muons is 2.2  $\mu$ s in their rest frame). The synchrotron losses for the populations of pions and muons are only important in the regime where

$$\left(\frac{B}{1\text{G}}\right) \left(\frac{E_p}{1\text{GeV}}\right) \ll \begin{cases} 7.8 \times 10^{11} \text{ for pions,} \\ 5.6 \times 10^{10} \text{ for muons.} \end{cases} \quad (1.44)$$

The above process is usually insignificant, and hence, Kelner et al. (2006) and Kelner & Aharonian (2008) provide the resulting electron and neutrino distributions in the approximation that the charged pions and muons decay before they lose any energy due to synchrotron radiation. It is not yet clear if the synchrotron radiation of pions and muons could potentially contribute to the observed spectrum because the exact value of the magnetic field and/or the maximum energy of the accelerated proton in the astrophysical sites are uncertain. In the extreme case though of a synchrotron timescale of pions and muons much shorter than the decay, the resulting spectra of the cooled pions, muons, and eventually, electrons, positrons and neutrinos are necessary (see, e.g., Rachen & Mészáros 1998; Mücke et al. 2003; Kashti & Waxman 2005; Lipari et al. 2007; Hümmer et al. 2010).

## 1.7 Ground-based gamma-ray astronomy

The identification of the Crab Nebula as a TeV source established the field of TeV astronomy in 1989 (Weekes et al. 1989). The 10m Imaging Atmospheric Cherenkov Telescope (IACT) of the Whipple Observatory in the US (Cawley et al. 1990), using the Monte Carlo simulations of Hillas (1985) to distinguish electromagnetic showers from the hadronic background, detected the Crab Nebula (Vacanti et al. 1991) as well as some extragalactic sources, such as Markarian 421 (Punch et al. 1992). After the pioneering work of the Whipple Observatory, the French Cherenkov Array at

Thémis (CAT) telescope (Barrau et al. 1998), the CANGAROO array of four 10 m IACTs in South Australia (Tanimori et al. 1998), and the High-Energy-Gamma-Ray Astronomy (HEGRA) in La Palma (Aharonian et al. 1999), were the first to employ stereoscopic imaging and to further observe the Crab Nebula. This technique was further developed and extended to lead to the current state-of-the-art IACTs of the Very Energetic Radiation Imaging Telescope Array System (VERITAS) with an array of four 12 m IACTs in the US (Vassiliev et al. 1999; Weekes et al. 2002; Holder et al. 2008), the two 17 m IACTs for the Major Atmospheric Gamma Imaging Cherenkov (MAGIC) Telescopes in La Palma (Baixeras 2003; Lorenz 2004), and H.E.S.S., an array of four 13 m IACTs and one 28 m telescope in Namibia (Hofmann et al. 2001; Hinton 2004).

Early attempts of a second technique, that of the water Cherenkov approach, failed to distinguish the purely electromagnetic showers originated in high-energy  $\gamma$ -rays from the hadronic background (see, e.g., CASA-MIA; Borione et al. 1994) until the construction of  $\sim 1 \text{ km}^2$  facilities. The Milagro collaboration, located in the US at an altitude of 2600 m above the sea level (Atkins et al. 2000, 2003), was the first water Cherenkov telescope to detect the Galactic diffuse emission (Atkins et al. 2005). The current state-of-the-art water Cherenkov facilities, such as the Tibet AS $_{\gamma}$  (Amenomori et al. 1999) in Tibet (4300 m above sea level), the HAWC (Abeysekara et al. 2013) in Mexico (4100 m above sea level), and LHAASO (Cao 2010) in China (4400 m above sea level) have significantly contributed to the TeV sky.

All the aforementioned facilities complement each other (see, e.g., Abdalla et al. 2021) and have firmly established TeV astronomy in recent years (Aharonian et al. 2008b; Hinton & Hofmann 2009; Hinton & Ruiz-Velasco 2020), leading to some prestigious awards, such as the Descartes Prize of the European Commission in 2006 and the Rossi Prize of the American Astronomical Society in 2010 to the H.E.S.S. collaboration, and extending the number of TeV emitters to more than 250 (based on the TeV source catalogue [tevcat](http://tevcat.uchicago.edu/)<sup>1</sup> and references therein, as of May 2022). The number of TeV sources may still be small compared to other energy bands (see, e.g., the GeV band as covered by *Fermi*/LAT; Abdollahi et al. 2020), but there are various sources of different a nature, as well as unidentified ones allowing for further investigation (see, e.g., Amenomori et al. 2021; Cao et al. 2021a). The detection and identification of TeV sources is crucial because the TeV regime provides valuable hints about particle acceleration, and consequently the CR sources that are still unidentified. The next generation facilities, such as the Cherenkov Telescope Array (CTA; Actis et al. 2011) and the Southern Wide-field Gamma-ray Observatory (SWGGO; Hinton & Collaboration 2022) will be very important in observing the night sky, detecting the sources that emit non-thermal radiation in the GeV-to-PeV regime, and finally identifying the CR sources. A facility, such as CTA, will also have the timing capacity for de-

---

<sup>1</sup><http://tevcat.uchicago.edu/>



**Figure 1.9:** An artist’s impression of the CTA, an array of three different-sized telescopes. Image Credit: Gabriel Pérez Diaz (IAC)/Marc-André Besel (CTAO)/ESO/ N. Risinger (skysurvey.org).

tecting transient events of Galactic and extragalactic origin. CTA will consist of two sites, one in the Northern and one in the Southern Hemisphere, on the island of La Palma in Spain and in the Atacama Desert in Chile, respectively. It will consist of three different sized telescopes, allowing the cover of the entire GeV-to-TeV spectrum, and will have a sensitivity that can be ten times greater than current ground-based  $\gamma$ -ray facilities. BHXBs are some of the Galactic sources that can potentially help to disentangle between the leptonic and the hadronic emission in the  $\gamma$ -ray regime, and finally assist to further understand the mechanisms behind the CR acceleration.

## 1.8 Thesis outline

Through this Ph.D. thesis, I focus on improving our understanding of particle acceleration in astrophysical jets launched by BHXBs. I focus on examining whether proton CRs can accelerate inside these Galactic jets, and what their signature on the electromagnetic spectrum would be in comparison to a leptonic origin, based on the processes discussed above. In the case of an efficient CR acceleration, I examine whether future  $\gamma$ -ray facilities like CTA can detect the TeV emission and hence if BHXBs can be potential CR candidate sources. Finally, to better connect the physical properties of the particle acceleration mechanisms, I develop an improved physical model of the jet kinematics based on the state-of-the-art numerical simulations, and connect the kinematics to the CR properties.

In Chapter 2, we present a new multi-zone, lepto-hadronic jet model in which CRs

are accelerated into a power-law similar to the non-thermal electrons. We compare the resulting multiwavelength spectrum of the newly developed model to a purely leptonic one, and test both models against the first simultaneous radio-to-X-ray data set obtained over a full orbital period of Cyg X–1 in 2016, via the CHOCBOX campaign (Cygnus X–1 Hard state Observations of a Complete Binary Orbit in X-rays; Uttley 2017). Using statistical means, such as the Markov Chain Monte Carlo (MCMC) method, we constrain the model parameters that allow for a more physical interpretation of the jet kinematics. To further constrain the jet model, we account for the non-simultaneous GeV observations and the polarisation measurements in the X-ray band. All these observational constraints allow us to discuss the properties of the accelerated CRs, such as the maximum attainable energy, and discuss if the predicted TeV flux could be detected by CTA and LHAASO.

In Chapter 3, we test the jet model we presented in Chapter 2 on the quasi-simultaneous radio-to-X-ray observations of a low-mass BHXB, GX 339–4, during a bright outburst in 2010. We constrain the jet kinematics using the MCMC method and discuss how we can interpret the prototypical behaviour of this particular source in terms of a broader population of low-mass BHXBs.

In Chapter 4, we present the predicted neutrino spectra and rates resulting in the aforementioned pp and p $\gamma$  hadronic processes for the Galactic jets of Cyg X–1 and GX 339–4. We use the electromagnetic conclusions we have derived in Chapter 2 and Chapter 3, to calculate the neutrino emission of not only the two prototypical sources, but also all 35 BHXB sources and candidate sources detected so far. We further expand this work to examine the contribution of a viable number of BHXB jets that reside in the Galactic plane on the CR spectrum detected on Earth. To do so, we utilise the most up-to-date CR propagation simulation DRAGON2, and finally calculate the contribution of BHXBs in the diffuse  $\gamma$ -ray and neutrino emissions with the numerical simulation HERMES.

Finally, in Chapter 5, we present a revised jet model in which we account for mass loading that occurs due to the instabilities grown in the interface between the jet sheath and its ambient medium. We develop this mass loading scenario based on current results of the state-of-the-art numerical general-relativity, magnetohydrodynamic (GRMHD) simulations that allow for a better understanding of jet physics. In this new jet model, the matter that entrains the jets is of lepto-hadronic nature, that due to energy dissipation, accelerates to high energies to lead to a  $\gamma$ -ray emission. We finally discuss how this mass-loading jet model can solve one of the long-standing open questions; how do CRs accelerate to high energies without violating the jet energy reservoir?

# A new lepto-hadronic model applied to the first simultaneous multiwavelength data set for Cygnus X–1

D. Kantzas, S. Markoff, T. Beuchert, M. Lucchini, A. Chhotray, C. Ceccobello, A. J. Tetarenko, J. C. A. Miller-Jones, M. Bremer, J. A. Garcia, V. Grinberg, P. Uttley & J. Wilms

*Monthly Notices of the Royal Astronomical Society, 2021, 500, 2, 2112-2126*

## *Abstract*

Cygnus X–1 is the first Galactic source confirmed to host an accreting black hole. It has been detected across the entire electromagnetic spectrum from radio to GeV  $\gamma$ -rays. The source’s radio through mid-infrared radiation is thought to originate from the relativistic jets. The observed high degree of linear polarisation in the MeV X-rays suggests that the relativistic jets dominate in this regime as well, whereas a hot accretion flow dominates the soft X-ray band. The origin of the GeV non-thermal emission is still debated, with both leptonic and hadronic scenarios deemed to be viable. In this work, we present results from a new semi-analytical, multi-zone jet model applied to the broad-band spectral energy distribution of Cygnus X–1 for both leptonic and hadronic scenarios. We try to break this degeneracy by fitting the first-ever high-quality, simultaneous multiwavelength data set obtained from the CHOCBOX campaign (Cygnus X–1 Hard state Observations of a Complete Binary Orbit in X-rays). Our model parameterises dynamical properties, such as the jet velocity profile, the magnetic field, and the energy density. Moreover, the model combines these dynamical properties with a self-consistent radiative transfer calculation including secondary cascades, both of leptonic and hadronic origin. We

conclude that sensitive TeV  $\gamma$ -ray telescopes like Cherenkov Telescope Array (CTA) will definitely answer the question of whether hadronic processes occur inside the relativistic jets of Cygnus X-1.



## 2.1 Introduction

Throughout the Universe, a significant fraction of accreting black holes are known to launch relativistic and collimated jets. Fundamental properties, such as the extent and power of these jets, scale essentially with the mass of the central black hole. While super-massive black holes (SMBHs) with  $M_{\text{BH}} \sim 10^6\text{--}10^9 M_{\odot}$  located at the centre of Active Galactic Nuclei (AGN) are able to power jets up to Mpc scales (e.g. Waggett et al. 1977), Galactic black holes ( $M_{\text{BH}} \sim \text{tens of } M_{\odot}$ ) hosted by X-ray binaries (XRBs) typically launch jets that remain collimated up to sub-pc scales (e.g. Mirabel & Rodriguez 1994; Hjellming & Rupen 1995; Mioduszewski et al. 2001; Gallo et al. 2005; Fender et al. 2006; Rushton et al. 2017; Russell et al. 2019).

AGN jets carry enough power to accelerate particles up to ultra-high energies of  $10^{19}$  eV and above (Aharonian 2000), which we detect as cosmic rays (CRs) on Earth. The exact acceleration mechanism is not known, but is likely related to diffusive shock acceleration (Axford 1969; Blandford & Ostriker 1978; Ellison et al. 1990; Rieger et al. 2007), magnetic re-connection (Spruit et al. 2001; Giannios 2010; Sironi et al. 2015), or shearing and instabilities at boundary layers between different velocities (Rieger & Duffy 2004; Liu et al. 2017).

The CR spectrum detected on Earth covers more than ten orders of magnitude in particle energy, from  $10^9$  to  $\sim 10^{21}$  eV. Two well-known characteristic spectral features of that spectrum are the so-called “knee” at  $10^{15}$  eV and the “ankle” at  $10^{18}$  eV (Kulikov & Khristiansen 1959; Bird et al. 1993, respectively). As shown by Hillas (1984), the maximum energy of the accelerated particles at a given magnetic field is limited by the size of the source due to confinement arguments. Accordingly, CRs above the ankle are likely of extragalactic origin whereas CRs below the knee are of Galactic origin. AGN jets are considered the most likely source of extragalactic CRs (e.g. Hillas 1984; Gaisser et al. 2016; Eichmann et al. 2018, and references therein). Supernovae and supernova remnants have been considered the dominant source of Galactic CRs for decades although questioned quite recently due to lack of  $\geq 100$  TeV observations (Aharonian et al. 2019). Hence, new candidate sources are needed.

Large AGN jets and small-scale XRB jets are (self-)similar in many regards. For example, they display similar non-thermal emission processes, suggesting that both classes are capable of accelerating particles to high energies regardless of their physical scales (e.g. Markoff et al. 2001; Bosch-Ramon et al. 2006; Zdziarski et al. 2012). Recent observations of hydrogen and helium emission lines from the jets of the accreting compact object SS 433 (Fabrika 2004), as well as the iron emission lines from the stellar-mass black hole candidate 4U 1630-47 (Díaz Trigo et al. 2013), provide indirect evidence of hadronic content of their jets. It is still not clear whether XRB jets can efficiently accelerate hadrons to high energy, but if so, they could also be potential Galactic CRs sources (see e.g. Heinz & Sunyaev 2002; Fender et al. 2005; Cooper et al. 2020).

The most striking evidence for particle acceleration inside Galactic jets comes from the non-thermal GeV radiation detected by the XRBs Cygnus X-1 (Cyg X-1) and Cygnus X-3 (Malyshev et al. 2013; Bodaghee et al. 2013; Zanin et al. 2016; Tavani et al. 2009). The jet-origin of the GeV emission is further favoured by the orbital modulation predicted, e.g. by Böttcher & Dermer (2005). Zdziarski et al. (2017) in fact detected an MeV–GeV modulation that likely originates from synchrotron self-Compton upscattering by particles accelerated in the compact black-hole-jet system of Cyg X-1 orbiting its companion star.

The exact nature of the non-thermal radiation is still unclear, with both leptonic and hadronic processes deemed to be viable. In the former case, a leptonic population is responsible for the overall electromagnetic spectrum from radio to  $\gamma$ -rays (e.g. Bosch-Ramon et al. 2006). In the latter case, the hadronic population reaches relativistic speeds as well and contributes equally, or even dominates, in the high energy regime of the spectrum. According to the Hillas criterion, particles can attain high-enough energy only if a strong magnetic field confines them in the acceleration region and provides enough power for particle acceleration. The power carried by accelerated protons has been claimed to exceed the Eddington luminosity in several cases making the hadronic model controversial (Zdziarski & Böttcher 2015). The hadronic channel, however, is the only possible way to explain the observed high and ultra-high energy CRs, as well as neutrinos through particle cascades (e.g. Mannheim & Schlickeiser 1994; Aharonian 2002).

The modelling of either of these radiative processes requires knowledge of the geometrical structure of the emitting region. Observations show jets that remain collimated up to large distances, following cylindrical or conical structures (e.g. Lister et al. 2013; Hada et al. 2016). However, for simplicity, spectral models often consider localized and spherical single-zone accelerating regions because they provide a good first-order approximation (e.g. Tavecchio et al. 1998; Mastichiadis & Kirk 2002; Marscher et al. 2008). In order to correctly factor in the observed jet geometry, we need to describe an accelerating and expanding outflow, and properly connect its physical properties with those of the accretion flow. Such inhomogeneous multi-zone jet models are able to self-consistently produce both the characteristic flat-to-inverted radio spectra observed in many compact jet systems, and the upscattered high-energy continuum (Blandford & Königl 1979; Hjellming & Johnston 1988).

Multiple groups have considered such multi-zone models in the past. For instance, Falcke & Biermann (1995) derived a simple model for the dynamical properties of a hydrodynamically driven, self-collimating jet, assumed to be powered by the accretion flow. This model was further developed with jet-intrinsic particle distributions and more detailed radiative calculations, and extended to XRBs by Markoff et al. (2001) and Markoff et al. (2005). The semi-analytical nature of this model has the great advantage that one can directly fit its physical parameters to data. Numerical simulations of the detailed magnetohydrodynamics of the jet flow, combined with radiative

transfer calculations, would be very computational expensive and time consuming for such a task.

In this work, we adopt the multi-zone leptonic model of Markoff et al. (2005) in its most recent version (Maitra et al. 2009; Crumley et al. 2017; Lucchini et al. 2018, 2019) and we further develop it by including hadronic interactions. This is the first hadronic multi-zone jet model for Galactic sources that additionally includes further improvements to the already implemented leptonic ones, such as pair cascades (Coppi & Blandford 1990; Böttcher & Schlickeiser 1997).

An ideal source to test our newly developed model, is one of the brightest and well-studied black-hole high-mass XRB, Cyg X-1 and its persistent jets (Stirling et al. 2001; Rushton et al. 2012). Along with the model, we present a new data set obtained by the CHOCBOX campaign (Cygnus X-1 Hard state Observations of a Complete Binary Orbit in X-rays: Uttley 2017). This campaign performed simultaneous observations with the satellite observatories *XMM-Newton*, *NuSTAR*, and *INTEGRAL*, which, together with the ground-based interferometers (NOEMA, VLA, and VLBA) provide the first multi-wavelength data set of that kind for Cyg X-1.

We also include the most recent X-ray polarisation information for Cyg X-1. Linear polarisation has been reported in the energy band below 200 keV but the polarisation fraction is strongly energy-dependent and does not exceed 10 per cent (Chauvin et al. 2018a,b). In contrast, the hard X-ray emission in the 0.4–2 MeV band is linearly polarised at a level of  $\sim 70$  per cent (Laurent et al. 2011; Jourdain et al. 2012; Rodriguez et al. 2015). Such a high polarisation fraction can only be explained as synchrotron emission from an ordered magnetic field, and places strong constraints on the modelling. In this work, we assume that the synchrotron radiation originates in the compact jets of Cyg X-1.

For this work, we adopt the updated distance and black-hole mass for Cyg X-1 of 2.22 kpc and  $21.4 M_{\odot}$ , respectively (Miller-Jones et al. 2021). The distance is in good agreement with the *Gaia* DR2 distance of  $2.38^{+0.20}_{-0.17}$  (Brown et al. 2018; Gandhi et al. 2019), which is about 30 per cent more distant than previously thought (Reid et al. 2011). The mass of the black hole was historically estimated to be between  $14.8 M_{\odot}$  (Orosz et al. 2011) and  $16 M_{\odot}$  (Ziółkowski 2014; Mastroserio et al. 2019), significantly lower than the updated value. The impact of the updated value of the mass of the black hole can be significant making the revision of modelling the source necessary. The jet inclination angle is  $27.5^{\circ}$ . The companion is a  $\sim 41 M_{\odot}$  star (Miller-Jones et al. 2021), which is about twice as massive as the foregoing estimate by Orosz et al. (2011). The spectral type of the companion star is O9.7 Iab (Bolton 1972). The binary separation is estimated to be  $\sim 3.7 \times 10^{12}$  cm (Miller et al. 2005) and the system orbital period is around 5.6 d (Webster & Murdin 1972).

This paper is organized as follows. We discuss the new observational data set of Cyg X-1 in Section 2.2 and our new lepto-hadronic model in Section 2.3. In Section 2.4 we present the results of our modelling. Finally, we outline in Section 2.5 the

significance of the results and summarize our work in Section 2.6.

## 2.2 Observations and Data Extraction

The bulk of the data we use to constrain the physical parameters of our model resulted from the CHOCBOX campaign (Uttley 2017). In particular, we select data within the time interval 2016 May 31 05:15:01.5 – 07:07:04.5 UTC, which provides simultaneous coverage by NOEMA, *XMM-Newton*, *NuSTAR*, and *INTEGRAL*.

In addition, we consider some supplemental, non-simultaneous, long-term averaged archival data. We use the mid-infrared data (Rahoui et al. 2011) to constrain physical properties of the donor star. We take into account a long-term 15-yr average MeV spectrum by *INTEGRAL* (Cangemi et al. 2021) as well as the publicly available GeV  $\gamma$ -ray spectrum from the *Fermi/LAT* collaboration (Zanin et al. 2016). The low flux and challenging detection techniques require averaging the data over longer timescales. Cangemi et al. (2021) are the first to average over all existing *INTEGRAL* data of Cyg X-1 in its hard state. The  $\gamma$ -ray spectrum we use here comprises data averaged over 7.5 yr, only during the hard state of Cyg X-1. Averaging thus provides the best-possible constraints to the MeV and GeV emission at the moment. While modelling, we do take into account the systematics arising from integrating over flux variations. We list all the data we use in this work in Table 2.1.

### 2.2.1 Very Large Array (VLA)

We observed Cyg X-1 with the Karl G. Jansky Very Large Array (VLA) on 2016 May 31, from 04:29–08:28 UT, under project code VLA/15B-236. The VLA observed in two subarrays, of 14 and 13 antennas spread approximately evenly over each of the three arms of the array, which was in its moderately-extended B configuration. The first subarray observed primarily in the Q-band, with two 1024-MHz basebands centred at 40.5 and 46.0 GHz, and the second observed primarily in the K-band, with the two 1024-MHz basebands centred at 20.9 and 25.8 GHz. Each subarray observed a single two-minute scan at a lower frequency (two 1024-MHz basebands centred at 5.25 and 7.45 GHz, and a single 1024-MHz baseband centred at 1.5 GHz, respectively) to characterise the broadband spectral behaviour. We used 3C 286 as the bandpass and delay calibrator, and to set the flux density scale, and we derived the complex gain solutions using the nearby extragalactic source J2015+3710.

We processed the data using the Common Astronomy Software Application (CASA; McMullin et al. 2007). The data were initially calibrated using the VLA CASA Calibration Pipeline (v4.5.3), and after some additional flagging to excise radio frequency interference, we imaged the target data using CASA version 4.5.2. The low elevation at the beginning of the run caused significant phase decorrelation and an increased system temperature. Although we were able to self-calibrate the data in phase down

**Table 2.1:** The observational multiwavelength data used in this work.

Observatory	log Frequency (Hz)	log Energy (eV)	Flux Density (mJy <sup>a</sup> )	References
VLA	10.32	-4.07	8.07 ± 0.03	This work
	10.61	-3.78	8.66 ± 0.10	
NOEMA	11.15	-3.24	6.87 ± 0.27	This work
<i>Spitzer</i>	12.97–13.77	-1.42–-0.61	54.57 at 10 <sup>13</sup> Hz	Rahoui et al. (2011)
<i>XMM-Newton</i>	16.86–18.38	2.48–4.0	0.07 at 3 keV	This work
			0.32 at 10 keV	
<i>NuSTAR</i>	17.87–19.28	3.49–4.89	0.54 at 3 keV	This work
			0.18 at 78 keV	
<i>INTEGRAL</i>	18.78–19.68	4.40–5.30	0.19 at 25 keV, 0.02 at 200 keV	This work
	19.73–20.90	5.35–6.52	0.01 at 225 keV, 10 <sup>-4</sup> at 3.3 MeV	
<i>Fermi/LAT</i>	22.43–24.43	8.05–10.05	7 × 10 <sup>-5</sup> at 0.1 GeV	Zanin et al. (2016)
			2 × 10 <sup>-9</sup> at 10 GeV	

<sup>a</sup>mJy = 10<sup>-26</sup> erg cm<sup>-2</sup> s<sup>-1</sup> Hz<sup>-1</sup>.

to a solution timescale of 2 minutes, the flux densities were still found to be biased low. We therefore restricted our images to the final 90 min of the run. Cygnus X-1 was significantly detected in all images, which were made with Briggs weighting, with a robust parameter of 1.

### 2.2.2 Northern Extended Millimeter Array (NOEMA)

The NOEMA observations of Cyg X-1 (project code: W15BQ, PI: Tetarenko) took place on 2016 May 31 (05:15:01-07:52:53.0 UT, MJD 57539.2188 – 57539.3284), in the 2 mm (tuning frequency of 140 GHz) band. These observations were made with the WideX correlator, to yield 1 base-band, with a total bandwidth of 3.6 GHz per polarisation. The array was in the 6ant-Special configuration (N02W12E04N11E10N07), with 6 antennas, spending 1.9 hrs on source during our observations. We used J2013+370 as a phase calibrator, 3C454.3 as a bandpass calibrator, and MWC349 as a flux calibrator. We performed phase only self-calibration on the data, with a solution interval of 45 seconds. The weather significantly degraded after 07:07 UT at NOEMA, therefore we do not include data after that time in our analysis. As CASA is unable to handle NOEMA data in its original format, flagging and calibration of the data were first performed in GILDAS<sup>1</sup> using standard procedures, then the data were exported to CASA<sup>2</sup> for imaging (with natural weighting to maximize sensitivity). The flux density of the source was measured by fitting a point source in the image plane (using the `imfit` task).

### 2.2.3 XMM-Newton

We consider the *XMM-Newton* observation ID 0745250501, which observed Cyg X-1 in timing mode using its EPIC-pn camera (Strüder et al. 2001) for a total of about 145 ks. First, we create calibrated and filtered event lists using the SAS v.16.1.0, which we further correct for X-ray loading and flag soft flare events. We consider only counts strictly simultaneous to the NOEMA observation time period resulting in a net exposure time of 3.5 ks. We use the filtered event lists to extract 0.3–10 keV spectra according to standard procedures.

### 2.2.4 NuSTAR

*NuSTAR* (Harrison et al. 2013) measures photons up to  $\sim 80$  keV by focusing hard X-rays on two focal-plane modules FPM A and FPM B. We extract data from within 3–78 keV with the standard *NuSTAR* Data Analysis Software NuSTARDAS-v.1.8.0 as part of HEASOFT-v.6.22.1. Due to the high flux of Cyg X-1, we extract source counts

---

<sup>1</sup><http://www.iram.fr/IRAMFR/GILDAS>

<sup>2</sup>To convert a NOEMA data set for use in CASA, we followed the procedures outlined at <https://www.iram.fr/IRAMFR/ARC/documents/filler/casa-gildas.pdf>.

from within a relatively large region of  $150''$  radius on both chips FPM A and FPM B, and background counts from a region of  $100''$  located off-source but close enough not prevent bias due to the spatial background dependence (Wik et al. 2014). To make sure to have simultaneous coverage with the observational time window of NOEMA, we define appropriate good-time intervals for the observation ID 30002150004, which results in a net exposure time of 1.9 ks each for FPM A and FPM B.

### 2.2.5 *INTEGRAL*

We extract the *INTEGRAL* Soft Gamma-Ray Imager (ISGRI; Lebrun et al. 2003) data with the *Off-line Scientific Analysis* (OSA) software v10.2 to match the simultaneous time interval as much as possible, resulting in the use of three science windows, 168500020010, 168500030010 and 168500040010 and 6.5 ks effective exposure time.

The state-resolved scientific products (images, light curves, and spectra) of the coded-mask instrument ISGRI were obtained with standard procedures. We extract spectra and images of Cyg X-1 on a single-science-window (scw) basis. For each scw, we construct a sky model including the brightest sources active in the field at the time of observation as found from the analysis of the full CHOCBOX *INTEGRAL* exposure, i.e. Cyg X-1, Cyg X-3, Cyg A, GRO J2058+42, KS 1947+300 and SAX J2103.5+4545.

## 2.3 Model Details

### 2.3.1 Dynamical Quantities

We describe the multi-zone jet model based on Markoff et al. (2005) and its extensions referenced above. In this section we summarize the major properties of the model and focus on our new extension of including the effect of hadronic particle acceleration and secondary production.

A fully self-consistent jet model should solve the force balance equations along the streamlines and perpendicular to them. This calculation would yield the radial profile and the acceleration profile describing a given jet configuration starting from a set of initial conditions. For simplicity we assume a fixed shape for the jet radial profile, based on observational evidence in AGN, which together with the longitudinal velocity profile then determines the profiles along the jet of the number density, and global magnetic field strength. Specifically, the cross-sectional radius  $R$  at any height  $z$  along the jet is given by

$$R(z) = R_0 + (z - z_0) \frac{\Gamma_0 \beta_0}{\Gamma_j \beta_j}, \quad (2.1)$$

where  $R_0$  is the radius of the jet base,  $z_0$  is the height of the jet base above the black hole,  $\beta_{0,j}$  and  $\beta_j$  are the bulk velocity of the plasma at the jet base and at height  $z$  respectively, and  $\Gamma$  is the corresponding Lorentz factor.

The solution of the Euler equation (Crumley et al. 2017)

$$\left\{ \Gamma_j \beta_j \frac{\Gamma_{\text{ad}} + \xi}{\Gamma_{\text{ad}} - 1} - \Gamma_{\text{ad}} \Gamma_j \beta_j - \frac{\Gamma_{\text{ad}}}{\Gamma_j \beta_j} + \frac{2(z - z_0) \Gamma_0 \beta_0 / (\Gamma_j \beta_j)}{R_0 \Gamma_j \beta_j + \Gamma_0 \beta_0 (z - z_0)} \right\} \times \frac{\partial \Gamma_j \beta_j}{\partial z} = \frac{2 \Gamma_0 \beta_0}{R_0 \Gamma_j \beta_j + \Gamma_0 \beta_0 (z - z_0)} \quad (2.2)$$

gives the velocity profile along the jet  $\Gamma_j(z)$ . In the above equation,  $\Gamma_{\text{ad}}$  is the adiabatic index of the flow (5/3 for a non-relativistic and 4/3 for a relativistic flow),

$$\xi = \left( \frac{\Gamma_j \beta_j}{\Gamma_0 \beta_0} \right)^{\Gamma_{\text{ad}} - 1}; \quad \Gamma_0 \beta_0 = \sqrt{\frac{\Gamma_{\text{ad}} (\Gamma_{\text{ad}} - 1)}{1 + 2 \Gamma_{\text{ad}} - \Gamma_{\text{ad}}^2}}. \quad (2.3)$$

Conservation of the particle number density results in;

$$n(z) = n_0 \left( \frac{\Gamma_j \beta_j}{\Gamma_0 \beta_0} \right)^{-1} \left( \frac{R}{R_0} \right)^{-2}, \quad (2.4)$$

where  $n_0$  is the differential number density at the jet base in  $\text{cm}^{-3} \text{erg}^{-1}$ . For a quasi-isothermal jet, which seems to be necessary to explain the flat/inverted spectrum, the internal energy density is given by (see Crumley et al. 2017):

$$U_j(z) = n_0 m_p c^2 \left( \frac{\Gamma_j \beta_j}{\Gamma_0 \beta_0} \right)^{-\Gamma_{\text{ad}}} \left( \frac{R}{R_0} \right)^{-2}, \quad (2.5)$$

where  $m_p c^2$  is the rest-frame energy of the protons that carry most of the kinetic energy. By assuming a fixed plasma beta parameter  $\beta = U_e / U_B$ , where  $U_e$  is the internal energy density of the electrons, and  $U_B$  the magnetic energy density, we can determine the profile of the magnetic field along the jet to be

$$B(z) = \sqrt{\frac{8\pi U_e(z)}{\beta}}, \quad (2.6)$$

where the energy density of the magnetic field is  $U_B = B^2 / 8\pi$ . For simplicity, we do not distinguish between toroidal and poloidal components but we assume that the field is tangled with a characteristic strength.

In addition to the jets, which include a thermal-dominated, corona-like region at their base, we incorporate a simple description for an additional thermal compact corona located around the black hole. We assume that a hot electron plasma of temperature  $T_{\text{cor}}$  is covering a radius  $R_{\text{cor}}$  and has an optical depth  $\tau_{\text{cor}}$ . These hot electrons inverse Compton upscatter the black body photons emitted by the accretion disc, while the thermal population in the jet base can upscatter both disc photons as well as synchrotron photons.



### 2.3.2 Particle distributions

Thermal electrons<sup>3</sup> are assumed to be directly injected into the jet base from the accreting inflow with a thermal Maxwell-Jüttner distribution, which reduces to the standard Maxwellian form in the non-relativistic case. Protons can be found in the jet base as well but they are entirely cold, and only carry the kinetic energy of the jet. The initial number density of the protons carried by the jet is defined as

$$n_0 = \frac{L_{\text{jet}}}{4\beta_{0,s}\Gamma_{0,s}c m_p c^2 \pi R_0^2}, \quad (2.7)$$

where half of the injected power  $L_{\text{jet}}$  goes into cold protons, while the other half is shared by the magnetic field and leptons, thus the factor  $1/4$ . We assume equal number density of electrons and protons. Further,  $\beta_{0,s}\Gamma_{0,s}c$  is the sound speed of a relativistic fluid with adiabatic index  $4/3$ . The total injected power  $L_{\text{jet}}$  is a free parameter of the model and is assumed to be proportional to the accretion energy  $\dot{M}c^2$ .

Once the particles propagate out some distance  $z_{\text{diss}}$  along the jet, a fitted parameter, we assume that a fixed fraction (10 per cent) of both leptons and hadrons are accelerated into a power-law with index  $p$  from this point onwards. We do not invoke any particular acceleration mechanism nor distinguish between acceleration or re-acceleration. We thus allow the power-law index  $p$  to be a free parameter in our model. Moreover, we assume constant particle acceleration beyond the particle acceleration region  $z_{\text{diss}}$ . Another free parameter is the acceleration efficiency  $f_{\text{sc}}$  (see e.g. Jokipii 1987; Aharonian 2004). Given this efficiency, the maximum energy achieved by the particles is calculated self-consistently along the jet by considering the main physical processes that limit the further acceleration of particles. The dominant cooling mechanisms are synchrotron radiation and inverse Compton scattering (ICS) for leptons, and escape from the source for hadrons. Adiabatic cooling is not relevant because the jets are actively collimated.

In order to calculate the particle distributions along the jets, we solve the continuity equation, which in energy phase space can be written in the general form:

$$\begin{aligned} & \frac{\partial N_i(E_i, t, z)}{\partial t} + \frac{\partial (\Gamma_j v_j N(E_i, t, z))}{\partial z} \\ & + \frac{\partial (b(E_i, t, z) N_i(E_i, t, z))}{\partial E_i} - \frac{N_i(E_i, t, z)}{\tau_{\text{esc}}(E_i, t, z)} = Q(E_i, t, z). \end{aligned} \quad (2.8)$$

The above equation describes the temporal evolution of the number density of the particle population  $i$ , i.e. electrons or protons. Since we assume a steady-state source, we

<sup>3</sup>We do not distinguish between electrons and positrons. The results in this work do not depend on the charge of the lepton.

neglect the first term on the left-hand side, making every quantity time-independent. We also neglect the effects of spallation and diffusion.

The second term on the left-hand side describes the propagation of particles along the jet. The third term expresses the radiative cooling of the particles, i.e. synchrotron radiation and ICS for leptons, as well as inelastic collisions for hadrons. The particles may escape the source within the timescale  $\tau_{\text{esc}}(E_i, t, z)$ , which in our treatment is only energy-dependent. Finally, the right-hand side describes the injection term, which is the sum of a Maxwell-Jüttner thermal distribution at low energies and a non-thermal power-law with an exponential cutoff at the self-consistently derived maximum energy. The non-thermal power-law is included only starting at the dissipation region  $z_{\text{diss}}$  where particle acceleration initiates.

Losses will dominate over acceleration above some particular energy  $E_{\text{max}}$  which can be self-consistently calculated – here for the leptonic case – by setting

$$\tau_{\text{acc}}^{-1}(E_{e,\text{max}}) = \tau_{\text{syn}}^{-1}(E_{e,\text{max}}) + \tau_{\text{ICS}}^{-1}(E_{e,\text{max}}) + \tau_{\text{esc}}^{-1}(E_{e,\text{max}}), \quad (2.9)$$

with the timescales for acceleration, synchrotron cooling, ICS cooling in the Thomson regime, and the escape of leptons, i.e.

1.  $\tau_{\text{acc}} = \frac{4E_e}{3f_{\text{sc}}ecB}$ ,
2.  $\tau_{\text{syn}} = \frac{6\pi m_e^2 c^3}{\sigma_{\text{T}} B^2 E_e \beta_e^2}$ ,
3.  $\tau_{\text{ICS}} = \tau_{\text{syn}} \frac{U_B}{u_{\text{rad}}}$ ,
4.  $\tau_{\text{esc}} = \frac{R}{\beta_e c}$ ,

respectively. Here,  $e$  is the electron charge,  $B$  the magnetic field of the jet at height  $z$  with radius  $R$ ,  $m_e$  the rest mass of the electron,  $c$  the speed of light,  $\sigma_{\text{T}}$  the Thomson cross-section,  $\beta_e$  the speed of the particle in units of  $c$ ,  $U_B = B^2/8\pi$  the energy density of the magnetic field,  $u_{\text{rad}}$  the energy density of the radiation field upscattered by the electrons.

Following the same approach, we calculate the maximum energy of protons in case of hadronic acceleration by setting

$$\tau_{\text{acc}}^{-1}(E_{p,\text{max}}) = \tau_{\text{syn}}^{-1}(E_{p,\text{max}}) + \tau_{\text{pp}}^{-1}(E_{p,\text{max}}) + \tau_{\text{p}\gamma}^{-1}(E_{p,\text{max}}) + \tau_{\text{esc}}^{-1}(E_{p,\text{max}}), \quad (2.10)$$

with the timescales for acceleration, synchrotron cooling, proton-proton collisions, proton-photon collisions, and the escape of protons, i.e.

1.  $\tau_{\text{acc}} = \frac{4E_p}{3f_{\text{sc}}ecB}$ ,

2.  $\tau_{\text{syn}} = \frac{6\pi m_p^2 c^3}{\sigma_T B^2 E_p \beta_p^2} \times \left(\frac{m_p}{m_e}\right)^2,$
3.  $\tau_{\text{pp}} = (K_{\text{pp}} \sigma_{\text{pp}} n_{\text{th}} c)^{-1},$
4.  $\tau_{p\gamma} = (K_{p\gamma} \sigma_{p\gamma} n_\gamma c)^{-1},$
5.  $\tau_{\text{esc}} = \frac{R}{\beta_p c}.$

Here,  $K_{\text{pp}}$  corresponds to the multiplicity (average number of secondary particles),  $\sigma_{\text{pp}}$  to the cross-section of this interaction, and  $n_{\text{th}}$  to the number density of the target particles (see Section 2.3.3.2). For proton-photon interactions between the accelerated protons and a photon field with number density  $n_\gamma$ , we consider the multiplicity  $K_{p\gamma}$  (Mannheim & Schlickeiser 1994). One can see that the proton-synchrotron timescale is approximately  $(m_p/m_e)^3$  times longer than the electron one.

The injection term becomes a power-law with an exponential cutoff beyond the particle acceleration region  $z_{\text{diss}}$ , i.e.

$$Q(E_i) = Q_0 E_i^{-p} \times \exp(-E_i/E_{i,\text{max}}), \quad (2.11)$$

where  $Q_0$  is a normalisation factor and  $p > 0$  is allowed to vary between 1.5 and 2.5, consistent with standard particle acceleration mechanisms. The power-law index is assumed to be equal for electrons and protons, which implies a common acceleration mechanism for both populations. Equation 2.11 is the less computationally-expensive form of the output of Particle-In-Cell (PIC) simulations where the thermal particle distribution leads to a self-consistent formation of a power-law of accelerated particles in time (e.g. Sironi & Spitkovsky 2009; Crumley et al. 2019, and references therein). We include further distributions of secondary pairs from hadronic processes and photon-photon annihilation (see below) into this injection term  $Q$ .

### 2.3.3 Radiative Processes

#### 2.3.3.1 Leptonic Processes

Electrons throughout the jet lose energy due to synchrotron and IC radiation. Before the particle acceleration region, even thermal electrons emit synchrotron radiation due to the relatively strong magnetic field. Beyond the particle acceleration region, the non-thermal leptonic process that dominates is the synchrotron radiation. For electron ICS we include photon fields from synchrotron radiation (synchrotron-self Compton – SSC), the disc around the black hole, and the companion star. We take into account the geometry of the companion star because, for high-mass XRBs like Cyg X-1, the size of the star is comparable to the size of the jet, especially for regions close to the compact object where the majority of the high energy radiation is likely

to originate. In particular, we calculate the photon field of the companion star as seen in the jet frame accounting for the Doppler boosting (each jet segment travels at a different Lorentz factor). All expressions for synchrotron radiation and ICS are taken from Blumenthal & Gould (1970) and Rybicki & Lightman (2008).

Furthermore, we include the full treatment of photon-photon annihilation and electromagnetic cascades (Coppi & Blandford 1990; Böttcher & Schlickeiser 1997). Depending on the number density of produced pairs, additional interactions between electrons and positrons can cause pair-annihilation leading to the production of  $\gamma$ -rays. This process can occur until the lepton energy budget becomes insufficient for further photon production. The photon fields we take into account are the same as for ICS. Finally, we add the produced pairs to the leptonic population, which are then cooled as described above.

### 2.3.3.2 Hadronic Processes

In the case where protons and/or ions are accelerated to relativistic energies in the jet, they can inelastically collide with thermal protons and photons inside the jet flow and produce secondary particles (Mannheim & Schlickeiser 1994). In the extension of our model, we therefore implement both proton-proton and proton-photon interactions. We use the full semi-analytical treatment of Kelner et al. (2006) and Kelner & Aharonian (2008) based on Monte-Carlo simulations (see below for more details).

**Proton-proton interactions** Collisions of non-thermal protons with thermal jet protons and stellar-wind protons (proton-proton collisions, pp, henceforth) lead to the production of  $\gamma$ -rays, secondary electrons, and neutrinos. The interactions responsible for the production of these particles can be described as

$$p + p \rightarrow p + p + \alpha\pi^0 + \beta(\pi^+ + \pi^-),$$

where  $\alpha$  and  $\beta$  are the collision energy-dependent multiplicity of the related products (see e.g. Romero et al. 2017). The charged pions decay as

$$\begin{aligned} \pi^+ &\rightarrow \mu^+ + \nu_\mu, & \mu^+ &\rightarrow e^+ + \nu_e + \bar{\nu}_\mu, \\ \pi^- &\rightarrow \mu^- + \bar{\nu}_\mu, & \mu^- &\rightarrow e^- + \bar{\nu}_e + \nu_\mu, \end{aligned}$$

and the neutral pions decay into two gamma-rays, i.e.

$$\pi^0 \rightarrow \gamma + \gamma.$$

In order for these interactions to occur, the energy of the accelerated proton has to exceed the threshold of  $E_{\text{th}} \simeq 1.22$  GeV (Mannheim & Schlickeiser 1994).

The lifetime of the produced mesons is well measured by laboratory experiments and short compared to the dynamical timescales of the jet. We can therefore assume instant decays. Consequently, the charged products do not radiatively lose energy

as they would in extreme environments of either very strong magnetic fields or very high energies (e.g. Mücke et al. 2003). The above statement can be parametrized as follows (e.g. Böttcher et al. 2013)

$$B\gamma_p \ll \begin{cases} 7.8 \times 10^{11} \text{ G for pions} \\ 5.6 \times 10^{10} \text{ G for muons,} \end{cases} \quad (2.12)$$

where  $B$  is the strength of the magnetic field in the jet rest frame and  $\gamma_p$  the Lorentz factor of the proton. Given that the highest value of the magnetic field is in the jet base ( $10^7$  G) and that hadronic interactions do not occur yet because particle acceleration occurs later, one can see that the above inequality is always satisfied.

In order to produce the distributions of stable products, we follow the semi-analytical approximation of Kelner et al. (2006). In particular, the differential number density of the  $\gamma$ -rays is given by the expression:

$$\frac{dn_\gamma(z, E_\gamma)}{dE_\gamma} = cn_{\text{targ}} \int_0^1 \sigma_{\text{pp}} \left( \frac{E_\gamma}{x} \right) n_p \left( z, \frac{E_\gamma}{x} \right) F_\gamma \left( x, \frac{E_\gamma}{x} \right) \frac{dx}{x}, \quad (2.13)$$

where  $E_\gamma$  is the energy of the  $\gamma$ -ray,  $n_{\text{targ}}$  is the number density of the thermal target protons,  $\sigma_{\text{pp}}$  is the cross section for pp collisions,  $n_p$  is the number density of the non-thermal protons,  $x = E_\gamma/E_p$  is the normalized photon energy with respect to initial proton energy and  $F_\gamma(x, E_\gamma/x)$  is the spectrum of  $\gamma$ -rays.

The cross section for pp interactions can be given by the semi-analytical expression

$$\begin{aligned} \sigma_{\text{pp}}(T_p) = & \left[ 30.7 - 0.96 \log \left( \frac{T_p}{T_{\text{thr}}} \right) + 0.18 \log^2 \left( \frac{T_p}{T_{\text{thr}}} \right) \right] \\ & \times \left[ 1 - \left( \frac{T_{\text{thr}}}{T_p} \right)^{1.9} \right]^3 \text{ mb,} \end{aligned} \quad (2.14)$$

where  $T_p$  is the proton kinetic energy in the laboratory frame and  $T_{\text{thr}} = 2m_\pi + m_\pi^2/2m_p \simeq 0.2797$  GeV the threshold kinetic energy for this interaction to take place (Kafexhiu et al. 2014). Kelner et al. (2006) provide semi-analytical calculations for the  $\gamma$ -ray spectrum as well as the other secondary particles.

For this work the target protons are the cold protons of the jet and protons emitted by the heavy companion star in the form of a homogeneous stellar wind. In particular, the companion star of Cyg X-1 is a blue supergiant that loses  $\sim 10^{-6} M_\odot \text{ yr}^{-1}$  in the form of stellar wind (Gies et al. 2008). We use the following expression to calculate the proton number density emitted by the companion

$$n_{\text{wind}}(z) = \frac{\dot{M}_\star}{4\pi(\alpha_\star^2 + z^2)v_{\text{wind}}m_p} \times \left[ 1 - \frac{R_\star}{\sqrt{\alpha_\star^2 + z^2}} \right]^{-\beta_{\text{wind}}} \quad (2.15)$$

(Grinberg et al. 2015), where  $\dot{M}_* = 4\pi\rho(r)v(r)$  is the mass-loss rate based on the radially-dependent mass density profile  $\rho(z)$ ,  $v_{\text{wind}}$  is the terminal velocity of the wind on the jet wall,  $\alpha_*^2$  is the distance of the massive star from the black hole,  $R_*$  is the radius of the massive star,  $z$  is the distance from the central black hole along the jet axis and  $\beta_{\text{wind}}$  is a free parameter used to improve the velocity profile of the wind found to be 1.6 (see e.g. Grinberg et al. 2015). From geometrical, filling-factor considerations, we assume that only 10 per cent of the wind protons take part in the pp process (see e.g. Pepe et al. 2015). Therefore, the total target number density (in  $\text{cm}^{-3}$ ) is given by:

$$n_{\text{targ}}(z) = 0.1n_{\text{wind}}(z) + n_{\text{p,cold}}(z). \quad (2.16)$$

**Proton-photon interactions** In addition to the pp interaction, inelastic collisions between non-thermal protons and photons occur in the jet ( $p\gamma$  henceforth). For this process we take into account the same photons fields as described above for leptonic ICS.

Depending on the centre-of-mass energy of the inelastic collision, we consider two processes: photopair and photomeson interactions. The photopair interaction is a  $p\gamma$  collision resulting in the production of an electron-positron pair

$$p + \gamma \rightarrow p + e^+ + e^-,$$

also called the Bethe-Heitler process. Alternatively, a  $p\gamma$  collision can result in the production of mesons, similarly to the pp interaction discussed above. The photomeson process can be written as

$$p + \gamma \rightarrow p + p + \alpha\pi^0 + \beta(\pi^+ + \pi^-).$$

The energy thresholds for photopair and photomeson processes to occur are:

$$E_{p,\text{thres}} = 4.8 \times 10^{14} / \epsilon_{\text{eV}} \text{ eV for photopair}, \quad (2.17)$$

$$E_{p,\text{thres}} = 7.1 \times 10^{16} / \epsilon_{\text{eV}} \text{ eV for photomeson}, \quad (2.18)$$

where  $\epsilon_{\text{eV}}$  is the energy of the target photon in eV. The photopair process has a lower energy threshold to occur. However, if the energy threshold for the photomeson process is met, then the energy loss of the proton is more significant compared to the photopair process, making the photomeson process dominant (Mannheim & Schlickeiser 1994).

Semi-analytical expressions for the distributions of stable secondary particles are provided by Kelner & Aharonian (2008). Secondary particles produced in the above processes can further interact within the jet before escaping. In this paper we do not add the secondary leptons to the primary leptonic population, but rather calculate their radiative processes and their relative contribution to the electromagnetic spectrum separately, for comparison.

### 2.3.4 Corona model

Along with the jet, we include an additional component in the form of a simple spherical corona surrounding the accretion disc. As discussed in section 2.4.2, this is necessary in order to match the X-ray emission of the source.

We assume that the electrons in the corona are thermal with a temperature  $T_{\text{cor}}$ , and that the entire corona is described by an optical depth  $\tau_{\text{cor}}$  and a radius  $R_{\text{cor}}$ . We define the number density of the injected electrons as:  $n_{e,\text{cor}} = \tau_{\text{cor}}/\sigma_{\text{T}}R_{\text{cor}}$ , where  $\sigma_{\text{T}}$  is the Thomson cross section. For the emission related to the corona, we only consider the disc photons as the source of seed photons for ICS, and we calculate the radiation energy density of the seed photons at the centre of the system. This means that the coronal radius  $R_{\text{cor}}$  effectively acts as a normalisation constant, rather than representing the exact physical radius of the X-ray emitting region.

## 2.4 Results

We perform simultaneous spectral fits of all data presented in Section 2.2 using the Interactive Spectral Interpretation System (ISIS; Houck & Denicola 2000). We explore the parameter space using a Markov Chain Monte Carlo (MCMC) method and its implementation via the `emcee` algorithm. In particular, we initiate 20 walkers per free parameter and perform  $\sim 10^4$  loops. The chains require a significant number of loops before they successfully converge, so we exclude the 50 per cent of the initial loops. We use the rest of the loops to derive the uncertainties of each free parameter (shown in Table 2.3. The fixed parameters including those of the donor star as assumed by Grinberg et al. (2015) are given in Table 2.2. The free parameters we allow to vary during the fitting are shown in Table 2.3. These are the injected power to the jet base  $L_{\text{jet}}$ , the radius of the jet base  $R_0$ , the location where the particle acceleration initiates  $z_{\text{diss}}$ , the plasma beta parameter  $\beta$ , the parameters for the disc, namely the innermost radius  $R_{\text{in,disc}}$  and the mass accretion rate in Eddington units ( $\dot{m} = \dot{M}c^2/L_{\text{Edd}}$ ), and the parameters of the corona, namely the temperature  $T_{\text{cor}}$ , the normalisation radius  $R_{\text{cor}}$  and the optical depth  $\tau_{\text{cor}}$ .

We present here the results of the best fits of our models. We choose one lepto-hadronic and one purely leptonic model to reproduce the MeV X-rays as jet synchrotron radiation, so as to explain the high degree of linear polarization (Laurent et al. 2011; Jourdain et al. 2012; Rodriguez et al. 2015; Cangemi et al. 2021). We achieve this by assuming that the non-thermal electrons accelerate in a hard power-law. We find that an index of  $p = 1.7$  provides sufficient results. We show two more models for comparison. One purely leptonic and one lepto-hadronic, with softer power-laws of  $p = 2.2$ . With such an assumption we fail to reproduce the MeV polarization as we show below.

**Table 2.2:** The fixed parameters of our models.

Parameter	Value	Description
$M_{\text{BH}} (M_{\odot})$	21.4	Mass of the black hole <sup>a</sup>
$\theta_{\text{incl}} (^{\circ})$	27.5	Viewing angle <sup>a</sup>
$D$ (kpc)	2.22	Distance of the source <sup>a</sup>
$N_H$ ( $10^{22} \text{ cm}^{-2}$ )	0.6	number column density
$h = z_0/R_0$	2	Initial jet height to radius ratio
$z_{\text{max}} (r_g)$	$10^8$	Maximum jet height <sup>b</sup>
$T_{\star} (K)$	$3.08 \times 10^4$	Temperature of the companion star <sup>a</sup>
$L_{\star} (\text{erg s}^{-1})$	$1.57 \times 10^{39}$	Luminosity of the companion star <sup>a</sup>
$a_{\star} (\text{cm})$	$3.7 \times 10^{12}$	Orbital separation distance <sup>a</sup>
$\dot{M}_{\star} (M_{\odot} \text{ yr}^{-1})$	$2.6 \times 10^{-6}$	Mass loss rate of the companion star <sup>c</sup>
$v_{\text{wind}} (\text{cm s}^{-1})$	$2.4 \times 10^8$	Velocity of the stellar wind <sup>c</sup>

<sup>a</sup>Miller-Jones et al. (2021),

<sup>b</sup>Tetarenko et al. (2019),

<sup>c</sup>similar to Grinberg et al. (2015).

### 2.4.1 Plasma quantities

The four different models presented here lead to different jet dynamical quantities, as we show in Table 2.3. The jet base radius varies between 2 and  $27 r_g$  and the region where the energy dissipates into particle acceleration varies between 15 and  $125 r_g$ . The two models with a hard injected particle distribution require a small value of plasma  $\beta$  compared to the softer models.

The best-fitting values for the injected power  $L_{\text{jet}}$  for the models with the hard power law ( $p = 1.7$ ), are comparable. Based on the jet-base radius  $R_0$  and the plasma  $\beta$ , we calculate the strength of the magnetic field along the jet. For all our models, we find relatively high magnetic field strengths at the jet base on the order of  $10^6 \text{ G}$ .

In Figure 2.1 we plot the energy density of various quantities along the jet axis for models the two models with  $p = 1.7$ . In particular, our fits are driven towards particle-dominated jets with the energy density of the protons dominating along the jet. Moreover, the energy density of the magnetic field is higher than the energy density of the (primary) electrons. We also show the energy density of the secondary pairs due to photon annihilation. We see that this process has its peak but still insignificant contribution in jet segments of high compactness, i.e. high photon number density at the jet base and in the particle acceleration region. The number density of the target photons drops significantly after the jet base, which suppresses the pair production.



At the particle acceleration region the compactness increases due to the non-thermal synchrotron and SSC photons. For the case of the lepto-hadronic model, we also show the energy density of secondary electrons from pp interactions, even though their energy density is more than five orders of magnitude lower than the rest.

### 2.4.2 Best fits to the multiwavelength spectrum

The combined data of Cyg X-1 presented in Section 2.2 result in a broad-band spectrum covering almost 15 orders of magnitude in photon frequency. We are able to reasonably fit all wavebands simultaneously with our model. Figures 2.2 and 2.3 show all four different model scenarios. The residuals are not always negligible, especially for the X-ray spectrum between  $10^{17}$  and  $10^{19}$  Hz. This is a natural consequence of our broad-band fit. The superb data coverage of the X-rays suggests a number of specific spectral features, e.g., due to relativistic reflection off the inner accretion disc, which our over-simplified model for the corona is not able to describe in detail. Such an in-depth treatment of all X-ray features is outside the scope of this work (see e.g., Tomsick et al. 2013; Duro et al. 2016; Parker et al. 2015; Basak et al. 2017).

We also take into account synchrotron-self absorption in the radio band and photoabsorption of X-ray photons with the column density  $N_H = 0.6 \times 10^{22} \text{ cm}^{-2}$  (Grinberg et al. 2015). The wind of the companion star could in principle attenuate the radio band even at inferior conjunction (when the companion star is behind the jet on the line of sight) examined here. Nevertheless, the 20 GHz radio emission originates from a region much further out in the jets than 10 times the separation of the system so this attenuation should be insignificant (see e.g. Szostek & Zdziarski 2007).

### 2.4.3 GeV-TeV spectrum

The lepto-hadronic model with  $p = 1.7$  is the only one that predicts significant TeV emission. In Figure 2.4 we plot the GeV to  $\sim$ PeV regime of its multiwavelength spectrum. For a comparison, we add the upper limits of the Major Atmospheric Gamma Imaging Cherenkov Telescopes - MAGIC (Ahnen et al. 2017a), the 3 and 5 yr sensitivity of the High-Altitude Water Cherenkov Observatory - HAWC (Abeysekara et al. 2013), and the predicted sensitivity of the Cherenkov Telescope Array - CTA (from [www.cta-observatory.org](http://www.cta-observatory.org)) and of the Large High Altitude Air Shower Observatory - LHAASO (Bai et al. 2019).

In the GeV range, we did not take into account photon annihilation due to the stellar photon field because the data we consider here are taken while the source was in the inferior conjunction. Further GeV observations will help to better understand the orbital modulation of Cyg X-1 as well in this domain.

Our evaluated spectrum above 0.1 TeV ( $10^{25}$  Hz) is dominated by the  $\gamma$ -rays produced via neutral pion decay from the hadronic collisions. The dominant process at

**Table 2.3:** The free parameters of the four models discussed in this paper that differ in the power-law index  $p$  of the accelerated particles. Before the double line, we show the fitted parameters and their uncertainties. Below, we show the evaluated quantities of the magnetic field, the total luminosity of the accelerated proton/electron population and the maximum energy of the protons/electrons at the particle acceleration region.

parameter	Lepto-hadronic models		Leptonic models		Description
	1.7	2.2	1.7	2.2	
$p$	1.7	2.2	1.7	2.2	Particle power-law index
$L_{\text{jet}}$ ( $10^{-4} L_{\text{Edd}}$ ) ( $\text{erg s}^{-1}$ )	$9_{-5}^{+26}$	$105_{-6}^{+360}$	$7.1_{-2.5}^{+3.4}$	$2.0_{-1.9}^{+2.1}$	Jet base injected power
$R_0$ ( $r_g$ )	$2.4_{-1.3}^{+7.0} \times 10^{36}$	$28.3_{-1.6}^{+97.1} \times 10^{36}$	$19.1_{-6.7}^{+9.2} \times 10^{35}$	$5.4_{-5.1}^{+5.7} \times 10^{35}$	Jet base radius
$z_{\text{diss}}$ ( $r_g$ )	$27_{-25}^{+29}$	$2^{+21}$	$3.1_{-1.1}^{+12.5}$	$3.1_{-1.1}^{+4.1}$	Particle acceleration region
$T_e$ (keV)	$81_{-15}^{+114}$	$15_{-4}^{+496}$	$64_{-14}^{+57}$	$125_{-45}^{+475}$	Jet base thermal electron temperature
$\beta$	$1762_{-1267}^{+3375}$	$711_{-703}^{+726}$	$756_{-726}^{+1530}$	$1114_{-1096}^{+1401}$	Plasma beta
$\dot{m}$ ( $10^{-3}$ )	$0.011_{-0.001}^{+0.529}$	$0.18_{-0.02}^{+0.89}$	$0.013_{-0.011}^{+0.332}$	$0.95_{-0.84}^{+0.97}$	Mass accretion rate
$R_{\text{in,disc}}$ ( $r_g$ )	$2.5_{-2.4}^{+15.9}$	$1.22_{-1.20}^{+1.25}$	$1.4_{-1.3}^{+1.5}$	$1.1_{-1.0}^{+1.2}$	Disc innermost radius
$T_{\text{cor}}$ (keV)	$19_{-17}^{+11}$	$3.1_{-1.1}^{+3.3}$	$6.3_{-4.3}^{+6.4}$	$3.1_{-1.1}^{+3.3}$	Corona temperature
$R_{\text{cor}}$ ( $r_g$ )	$90_{-10}^{+69}$	$89_{-9}^{+16}$	$105_{-14}^{+51}$	$81_{-1}^{+82}$	Corona normalisation radius
$T_{\text{cor}}$	$59_{-19}^{+60}$	$10_{-6}^{+38}$	$20_{-9}^{+41}$	$10_{-6}^{+9}$	Corona optical depth
$B_0$ (G)	$0.58_{-0.47}^{+0.32}$	$0.62_{-0.63}^{+0.63}$	$0.49_{-0.39}^{+0.50}$	$0.61_{-0.39}^{+6.30}$	Magnetic field at jet base
$B$ (G) @ $z_{\text{diss}}$	$1.8 \times 10^6$	$1.6 \times 10^6$	$1.6 \times 10^6$	$6.4 \times 10^5$	Magnetic field at particle acceleration region
$L_p$ ( $\text{erg s}^{-1}$ )	$9.1 \times 10^4$	$1.0 \times 10^6$	$1.6 \times 10^5$	$3.2 \times 10^4$	Accelerated proton power
$L_e$ ( $\text{erg s}^{-1}$ )	$4.3 \times 10^{38}$	$5.1 \times 10^{38}$	-	-	Accelerated electron power
$E_{p,\text{max}}$ (eV)	$1.3 \times 10^{36}$	$1.9 \times 10^{36}$	$2.1 \times 10^{36}$	$3.3 \times 10^{36}$	Proton maximum energy
$E_{e,\text{max}}$ (eV)	$2.7 \times 10^{15}$	$1.8 \times 10^{15}$	-	-	Electron maximum energy
$\chi^2 / \text{DoF}$	$6.1 \times 10^{10}$	$2.2 \times 10^{10}$	$3.3 \times 10^{10}$	$8.8 \times 10^{10}$	(primary) $\chi^2 / \text{degrees of freedom}$

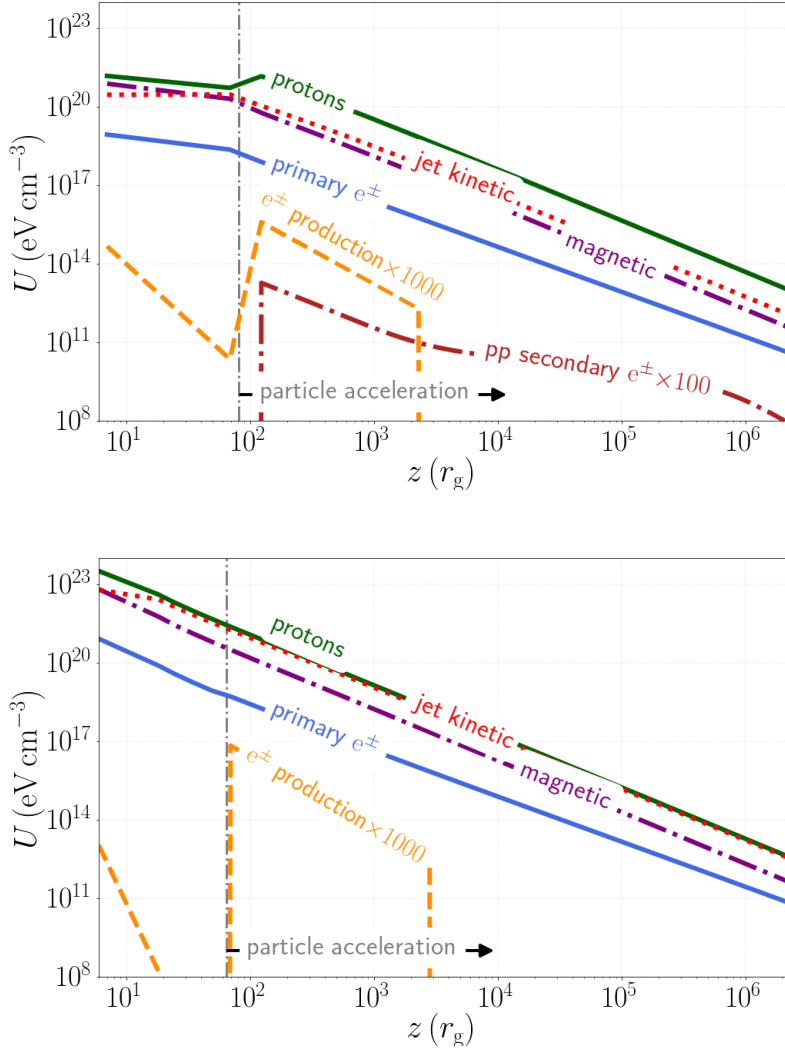


**Figure 2.1:** Contributions to the total energy density as a function of the distance along the jet for the model with a power-law index  $p = 1.7$ , for the lepto-hadronic case (*top*) and the purely leptonic case (*bottom*). The particle acceleration initiates at the vertical dot-dashed grey line. The jump in the proton energy density on the left plot is due to proton acceleration. We do not assume extraction of energy from other components to accelerate the particles. The proton and the jet kinetic energy density of the right plot coincide because no proton acceleration is taken into account. We stop to calculate the pair production after some distance because it has insignificant contribution.

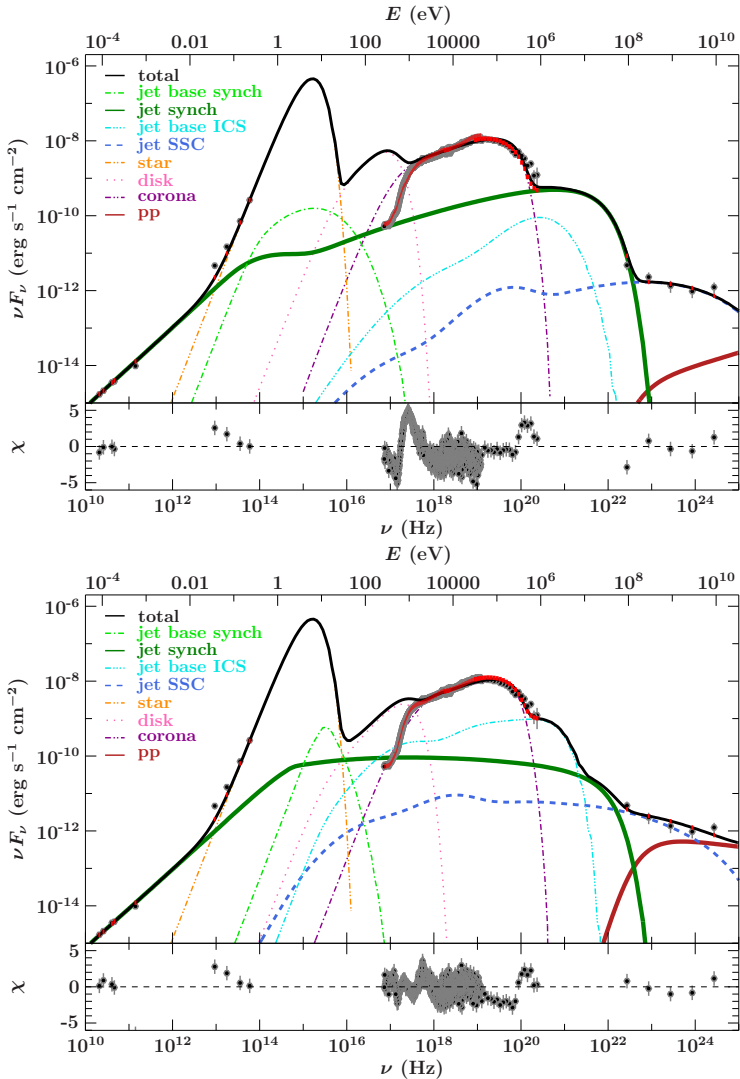


**Figure 2.2:** The best-fit multiwavelength spectrum of Cyg X-1 for the two lepto-hadronic scenarios with  $p = 1.7$  (*top*) and  $p = 2.2$  (*bottom*) and their  $\chi$  residuals. The solid black line shows the total unabsorbed spectrum. The absorbed spectrum that we fitted to the data in detector space is shown as solid red line. We also show some individual unabsorbed model components, i.e. the broadband radio-to- $\gamma$ -ray synchrotron spectrum from primary electrons (thick solid green line), the ICS spectrum ranging from eV to GeV (dashed dark blue line), the pp spectral component arising from the neutral pion decay (solid red line), disc photons upscattered in the thermal corona (dotted-dashed purple line), the black-body component emitted by the companion star (double-dotted-dashed orange line), and the multi-temperature thermal spectrum arising from the accretion disk (dotted magenta line). The dotted-dashed light green line shows the synchrotron radiation from thermal electrons and the triple-dotted-dashed light blue line shows the ICS from regions before the particle acceleration region. In the case where  $p = 1.7$  the jet-synchrotron dominates in the MeV band explaining the high degree of reported linear polarisation. In the soft case of  $p = 2.2$ , the fit does not explain the reported polarisation.

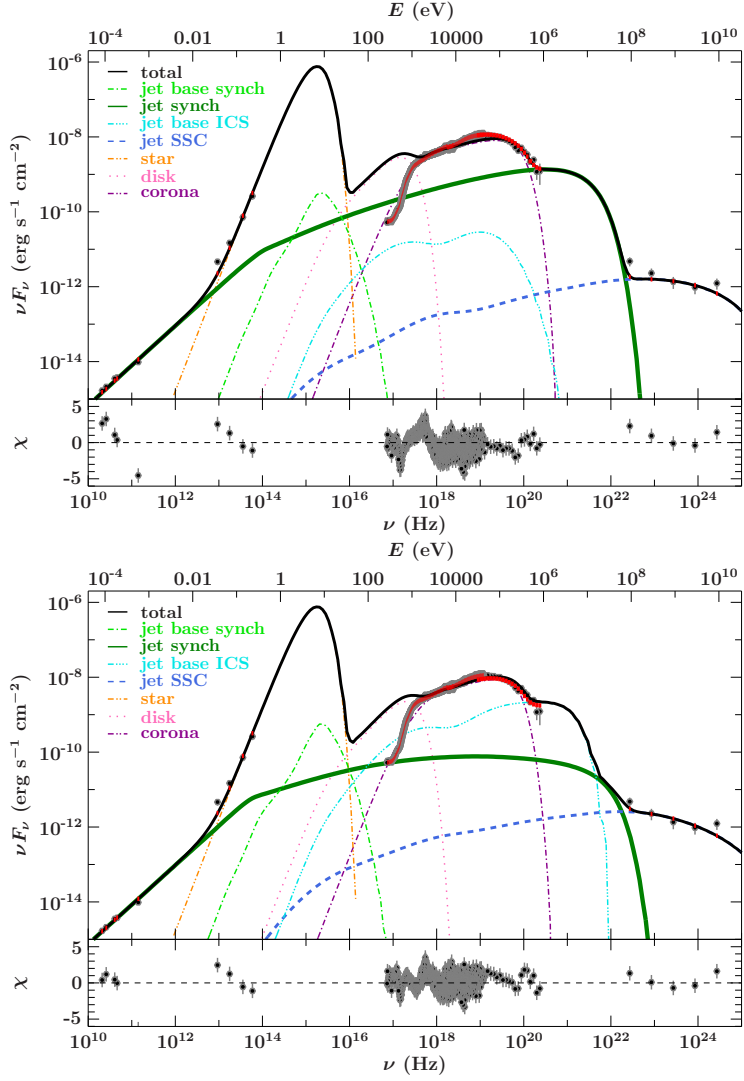


**Figure 2.3:** Similar to Figure 2.2 but for the two leptonic scenarios with  $p = 1.7$  (top) and  $p = 2.2$  (bottom).

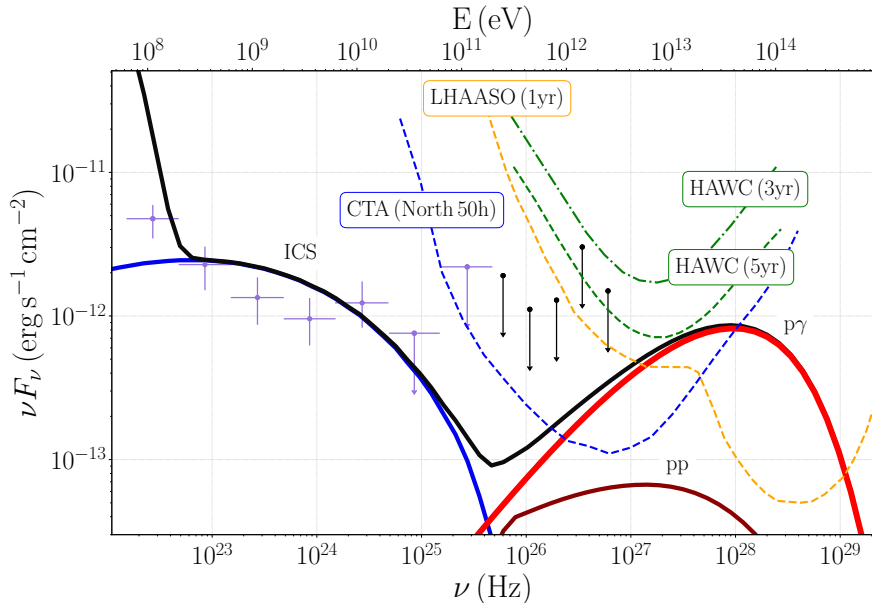


**Figure 2.4:** The GeV-to-TeV regime of the multiwavelength spectrum of Cyg X-1 for the leptohadronic scenario with  $p = 1.7$ . The black line shows the total spectrum. The ICS (solid dark blue) explains the *Fermi*/LAT (purple) data points in the GeV band. The neutral pion decay from  $p\gamma$  (thick light red) dominates the pp (dark red) and peaks in the TeV regime. Such emission will be detectable by future generation facilities, such as the CTA (dashed blue, adopted from [www.cta-observatory.org](http://www.cta-observatory.org)), and LHAASO (dashed orange, adopted from Bai et al. 2019). We also plot for comparison the upper limits of MAGIC (black upper limits) from Ahnen et al. (2017a), and the 3 (dot-dashed green) and 5 yr (dashed green) sensitivity of HAWC adopted from Abeyssekara et al. (2013).

the highest photon energies is the  $p\gamma$  interaction, between accelerated jet protons and the synchrotron MeV photons. The number density of other target photon fields is negligible compared to this MeV band in the jet rest frame. The flux levels predicted by our model are overall higher than the sensitivity limits of next-generation  $\gamma$ -ray telescopes. HAWC, LHAASO, and CTA will therefore be key for breaking further degeneracies within our model, and constraining important processes such as the  $p\gamma$  interactions in astrophysical jets.

For our discussion of the highest energies, we only consider the hard leptohadronic model ( $p = 1.7$ ), as the soft model ( $p = 2.2$ ) cannot explain the MeV polarisation. Neither leptonic model can produce any TeV emission via ICS because the electron scattering with GeV photons occurs deep in the Klein-Nishina regime. Thus, no further order scatters can occur inside the jets that would produce significant TeV radiation. A solid TeV detection would therefore rule out the leptonic models.

## 2.5 Discussion

A key open issue regarding Cyg X-1 is the polarised 0.4 – 2 MeV tail detected by *INTEGRAL* while the source is in the hard state (Laurent et al. 2011; Jourdain et al. 2012; Rodriguez et al. 2015; Cangemi et al. 2021). The above studies all independently conclude that the linear polarisation degree of the MeV emission is of the order of 50–70 per cent. While there is an overall agreement on the degree of polarisation, *INTEGRAL* does not have the spatial resolution to resolve the source, thus the integrated polarisation angle over the entire system does not provide constraining information on the detailed magnetic field geometry of the source.

Such high degree of polarisation, requires a structured and well-ordered magnetic field. High-resolution numerical simulations suggest that the wind of the accretion disc, which is associated to the corona, is very turbulent and could not explain such structured magnetic field (Chatterjee et al. 2019; Liska et al. 2017, 2020). Hence, jet-synchrotron is more likely to explain the MeV polarisation.

In this work, we take advantage of the new and unprecedented (in broadband simultaneity) CHOCBOX multi-wavelength data set to revisit the question of leptonic vs. hadronic processes, using a more sophisticated multi-zone approach. In particular we explore the consequences of taking the MeV polarisation as a ‘hard’ constraint, and the consequences for potential TeV  $\gamma$ -ray emission. We find that the only way to produce sufficient synchrotron flux to fit the MeV data is by assuming a hard power-law distribution of accelerated electrons with  $p = 1.7$ . If we assume a soft power-law with  $p = 2.2$  we fail to match this constraint.

These two different power-law indices of 1.7 and 2.2 are typically associated with different particle acceleration mechanisms. The hard particle spectrum ( $p = 1.7$ ) suggests second-order Fermi acceleration (e.g. Rieger et al. 2007) or magnetic reconnection (e.g. Biskamp 1996; Sironi & Spitkovsky 2014; Petropoulou & Sironi 2018 or Khiali et al. 2015 for the case of Cyg X-1 specifically). The softer injection value of  $p = 2.2$  is more suggestive of non-linear diffusive shock acceleration (e.g. Drury 1983; Malkov & Drury 2001; Caprioli 2012), but we show that the high degree of MeV polarisation cannot be attained. We find that the best fits to the data require a more efficient acceleration mechanism to be the dominant source of non-thermal particles. We note however that when we define the acceleration timescale to derive the maximum energy of the particles (see Equations 2.10 and 2.9), we use a simplified expression that is commonly used to describe first-order Fermi acceleration. In future work, we will include energy dependence to the acceleration timescale to explore in detail the different acceleration mechanisms.

Taking as a constraint the explanation of both the observed MeV spectrum and the GeV  $\gamma$ -rays, we require a generally high particle acceleration efficiency  $f_{sc}$ . For the models with a soft particle spectrum, we require a higher efficiency (0.1) as opposed to the models with the hard particle spectrum, where an acceleration efficiency of

0.01 is sufficient. This parameter also drives the maximum achievable energy of the particles. We find a maximum electron energy of 10–100 GeV (see Table 2.3) and proton energy of  $\sim 10^{15}$  eV. The high particle energies we find for both electrons and protons translate to a required high total power in particles, i.e.  $\sim 10^{36}$  erg s $^{-1}$  for electrons and  $\sim 10^{39}$  erg s $^{-1}$  for protons.

Independent measurements of the total kinetic jet power are useful to benchmark our fitted values for the total injected energy. One can estimate the jet power from the bubble-like structure located 5 pc from Cyg X-1 caused by the apparent interaction between the jet and the ISM. The mechanical power required to inflate such a bubble has been calculated to be of the order of  $10^{37}$  erg s $^{-1}$  (Gallo et al. 2005). It is, however, still debated whether the jet is solely evacuating this bubble, or whether other feedback channels, such as the companion star’s stellar wind, play a role. In that case, the jet power estimated by Gallo et al. (2005) would have to be considered as an upper limit (Sell et al. 2014). This estimate would lead to the exclusion of the lepto-hadronic model because of its exceeding jet power, while the purely leptonic model requires merely 10 percent of the estimated power. This large discrepancy (up to 3 orders of magnitude) driven by the inclusion/exclusion of hadronic processes is a well-known issue in the field (e.g. Bosch-Ramon et al. 2008; Zdziarski et al. 2012; Malyshev et al. 2013; Zdziarski et al. 2014a; Zhang et al. 2014; Pepe et al. 2015; Zdziarski et al. 2017; Beloborodov 2017; Fernández-Barral et al. 2017).

Most hadronic models show jet powers close to Eddington limit either for Galactic or extragalactic sources (Böttcher et al. 2013; Zdziarski & Böttcher 2015). However, there are a few possible ways of extracting further power from the system to the particles without violating other constraints. One possibility is a much more efficient dissipation of either magnetic or kinetic energy via particle acceleration, i.e. greater than 10 per cent. Another, perhaps more likely scenario is the one where the jets are launched by a magnetically dominated (MAD) accretion flow and a spinning black hole. In such systems, the jet can benefit from an efficient extraction of power both from the accretion disc and the black hole rotation (Blandford & Znajek 1977; Narayan et al. 2003; Tchekhovskoy et al. 2011). Alternatively, the total proton power can be reduced. One possibility is that the jets are predominantly leptonic up to when the bulk flow is accelerated to maximum velocity. The majority of protons are then mass-loaded further away from the launching point either by the wind of the accretion disc or of the companion star (Chatterjee et al. 2019; Perucho 2020). To calculate the total proton power in this work, we sum the proton power per segment along the jet. If we assume that protons accelerate only within a small part of the jet, then the total power could be significantly reduced (Pepe et al. 2015; Khiali et al. 2015; Abeysekara et al. 2018). Such assumptions would however only increase the free parameters of our model. Therefore, we decided to restrict ourselves to ‘standard’ assumptions for fitting the data, and to ease comparison with prior approaches.



### 2.5.1 Comparison with previous works

In Table 2.4 we present a schematic comparison between the main features of our new model and of a sample of similar works used to explain the multiwavelength spectrum of Cyg X–1. The models that we consider here are the following: Romero et al. 2014 (R14), Zdziarski et al. 2014a (Z14), Khiali et al. 2015 (K15), Pepe et al. 2015 (P15), and Zdziarski et al. 2017 (Z17).

It is generally agreed that the radio-to-FIR spectrum of Cyg X–1 is produced by its relativistic jets, and likely the GeV emission as well. Numerous studies dedicated to fitting high signal-to-noise X-ray spectra of Cyg X–1 invoke the presence of a corona with hot, thermal electrons to upscatter soft photons up to  $\sim 100$  keV energies, as this is standard for most XRB hard-state models (Tomsick et al. 2013; Duro et al. 2016; Parker et al. 2015; Basak et al. 2017; Walter & Xu 2017). Furthermore, the companion of Cyg X–1 is a high mass donor star, hence an additional black body (or even a more detailed stellar model) spectral component is required.

The key differences between approaches centre primarily on the nature of the particle acceleration in the jets, the role of the jets at high energies, and the level of detail in the modelling of the jet properties.

Constraining the contribution of the jets at high energies, and thus the total power requirements, hinges on the MeV polarisation and the  $\gamma$ -rays. Many of the prior works did not consider the MeV polarisation as a hard constraint. For those that did, R14 suggest that the synchrotron radiation from secondary electrons in the corona could explain the MeV tail. As we discussed above though, jet synchrotron is a more likely origin. Z14 explain the MeV flux as a result of jet synchrotron from primary electrons. They presented only a purely leptonic model and thus no TeV detection can be predicted. This choice thus places them in a regime with reasonable total jet powers. P15 manage to reproduce the MeV tail in a lepto-hadronic scenario with primary electron synchrotron radiation. This is similar to our lepto-hadronic model with  $p = 1.7$  but they use a much softer injected electron distribution. They manage to restrict the total proton power by making two assumptions discussed also above: first, protons are accelerated only from a minimum Lorentz factor of  $\gamma_{p,\min} = 100$  and second, the particle acceleration terminates at some distance from the jet base. None of these works though attempted to fit their free parameters to simultaneous data and perform statistical analysis, which may affect their conclusions.

### 2.5.2 Perspective for CTA, HAWC, and LHAASO

In Figure 2.4 we compare the results of the lepto-hadronic model with  $p = 1.7$  to the upper limits set by MAGIC after almost 100 hours of observations (Ahnen et al. 2017a). In addition, HAWC released its second catalog of TeV sources and a catalog of 9 Galactic sources after 1000 days of operation, but Cyg X–1 was not included

**Table 2.4:** Comparison between our results and previous works on reproducing the (multiwavelength) spectrum of Cyg X-1. When two models are discussed in a specific work, we separate them with a slash. cor-SYN stands for synchrotron radiation from a non-thermal corona, SYN for jet (primary) synchrotron radiation and (✓) stands for marginal detection. References included are: Romero et al. 2014 (R14), Zdziarski et al. 2014a (Z14), Khiali et al. 2015 (K15), Pepe et al. 2015 (P15) and Zdziarski et al. 2017 (Z17).

Features/model	Other works						This work	
	R14	Z14	K15	P15	Z17	Hadronic	Leptonic	
Power-law index <sup>a</sup>	2.2	1.4/2.5	1.8	2.0/2.4	2.2	1.7/2.2	1.7/2.2	
Corona presence	✓	✓	✗	✓	✓	✓	✓	
Hadronic processes	✓	✗	✓	✓	✗	✓	✗	
Simultaneous data	✗	✗	✗	✗	✗	✓	✓	
Statistical modelling/MCMC	✗	✗	✗	✗	✗	✓	✓	
MeV X-rays origin	cor-SYN	SYN/COM	SYN	SYN/COM	COM	SYN/COM	SYN/COM	
Explain MeV polarisation	✓	✓/✗	✗	✓/✗	✗	✓/✗	✓/✗	
CTA @ TeV prediction	✗	✗	✓	✓/✗	✗	✓	✗	
LHAASO @ 100 TeV prediction	✗	✗	(✓)	(✓/✗)	✗	✓	✗	

<sup>a</sup>accelerated particle power-law index:  $p: N(E) \propto E^{-p}$ .

in either of them (Abeysekara et al. 2017 and Abeysekara et al. 2020, respectively). Thus, we also plot the sensitivity predicted by the HAWC collaboration for 5 years of operation (Abeysekara et al. 2013).

We plot the predicted sensitivity of CTA for TeV  $\gamma$ -rays, as well as the sensitivity of LHAASO (Bai et al. 2019), which mostly focuses on  $\sim 100$  TeV. In the hadronic model with  $p = 1.7$ , the TeV emission is dominated by the  $p\gamma$  inelastic collisions between accelerated protons and synchrotron photons of the jet. The peak is at 20 TeV and the corresponding flux is expected to be  $2 \times 10^{-12}$  erg cm $^{-2}$  s $^{-1}$ , significantly above the predicted CTA sensitivity for 50 hours of observation from the north site. Moreover, the spectral index of this TeV emission is predicted to be positive and  $\sim 0.5$  for energies between 0.1–10 TeV (i.e.  $F_\nu \propto \nu^{0.5}$ ).

An interesting aspect of our model is that the photomeson interactions dominate the pp collisions. The energy threshold of pp inelastic collisions, in general, is lower than  $p\gamma$ . Nevertheless, the number density of the target protons from the thermal wind of the companion star within the jet is constant up to  $z \simeq a_*$  regardless of the physics of the jets (see equation 2.15). On the other hand, the number density of the target photons of  $p\gamma$  are highly model-dependent. For the hadronic models presented here the dominant target photons are the synchrotron photons of each jet segment. Consequently, in the case of the hard particle distribution ( $p = 1.7$ ) where the energy density of MeV photons is ten times higher than that of the soft particle distribution (see Figure 2.2), the  $p\gamma$  process dominates the TeV band.

Detection of TeV photons and a measurement of the spectral index of this emission by forthcoming very high-energy facilities could therefore give further insights into the acceleration mechanism. Finally, regardless of the spectral shape, the detection of Cyg X–1 from HAWC, and especially from CTA or LHAASO would exclude the possibility of purely leptonic jets for this source.

## 2.6 Summary and Conclusions

In this work, we present a new multi-zone jet model, based on the initial work of Markoff et al. (2005) and references above. We implement proton acceleration and inelastic hadronic collisions (proton-proton and proton-photon, Kelner et al. 2006; Kelner & Aharonian 2008, respectively). We include the distributions of secondary electrons and  $\gamma$ -rays produced through pion decay. We further improve the existing leptonic processes with more sophisticated pair-production calculations (Coppi & Blandford 1990; Böttcher & Schlickeiser 1997), as well as take into account the proper geometry of the companion star as seen in the jet rest frame. With such enhancements, we can make more accurate predictions of the high energy phenomena related to astrophysical jets, particularly the non-thermal emitted radiation.

Along with this new model, we present the first broadband, simultaneous data

set obtained by the CHOCBOX campaign for Cyg X-1 (Uttley 2017). This data set covers ten orders of magnitude in photon energy, from radio wavelengths to MeV X-rays. These bands are most susceptible to faster variability and hence simultaneous high-quality observations are beneficial to break model degeneracies.

The keV-to-MeV spectrum of Cyg X-1 exhibits significant evidence of linear polarisation. The keV spectrum shows low degree of linear polarisation (Chauvin et al. 2018b,a) but the 0.4 – 2 MeV is highly polarised at a level of 50 – 70 per cent (Laurent et al. 2011; Jourdain et al. 2012; Rodriguez et al. 2015; Cangemi et al. 2021). We interpret this high degree of linear polarisation in the MeV band as synchrotron radiation emitted by (primary) electrons accelerated inside the jets of Cyg X-1 in the presence of a highly ordered magnetic field. Such non-turbulent, dynamically dominant magnetic fields are most likely associated with astrophysical jets. To achieve the required MeV synchrotron flux, we must inject a hard power-law of accelerated electrons with index of  $p = 1.7$ .

We investigate the implications of the above assumptions for a purely leptonic and a lepto-hadronic scenario, performing statistical analyses to find the best fits to the CHOCBOX data set. Using an MCMC approach, we explore the parameter phase-space in order to constrain the parameters and minimize degeneracy. This paper is the first to compare a purely leptonic to a lepto-hadronic model for the case of XRB jets based on statistical analysis.

We find that the jet geometry does not significantly differ between the two compared scenarios; the main differences are the TeV radiation and the power requirements. Only the hadronic model is capable of producing significant TeV emission detectable by the next generation  $\gamma$ -ray telescopes of HAWC, LHAASO and CTA. Interestingly, we find that the dominant hadronic process is the proton-photon interaction. This scenario however requires near-Eddington power in the accelerated protons, using the most basic assumptions. We discuss ways around this issue but leave that for future work, in the case of a TeV detection. Such detection would be a game-changer for the field of XRBs, and support the possibility that Galactic CRs originate in more sources than only supernovae.

## Acknowledgements

We would like to thank the reviewer for the very helpful comments on improving the original manuscript. DK would like to thank Maria Petropoulou for fruitful discussions, and Ping Zhou and Thomas Russell for useful comments on the manuscript. DK, SM, ML, and AC were supported by the Netherlands Organisation for Scientific Research (NWO) VICI grant (no. 639.043.513). VG is supported through the Margarete von Wrangell fellowship by the ESF and the Ministry of Science, Research and the Arts Baden-Württemberg. JCAM-J is the re-

recipient of an Australian Research Council Future Fellowship (FT140101082), funded by the Australian government. This work is based on observations carried out under the project number W15BQ with the IRAM NOEMA Interferometer. IRAM is supported by INSU/CNRS (France), MPG (Germany) and IGN (Spain). This research made use of **ASTROPY** (<http://www.astropy.org>) a community-developed core **PYTHON** package for Astronomy (Astropy Collaboration et al. 2013; Price-Whelan et al. 2018), **MATPLOTLIB** (Hunter 2007), **NUMPY** (Oliphant 2006), **SCIPY** (Virtanen et al. 2020), **ISIS** functions (**ISISscripts**) provided by ECAP/Remeis observatory and MIT (<http://www.sternwarte.uni-erlangen.de/isis/>), and the CTA instrument response functions provided by the CTA Consortium and Observatory, see <https://www.cta-observatory.org/science/ctao-performance/> (version prod3b-v2) for more details.

## Data availability

The data underlying this article are available in Zenodo, at <https://dx.doi.org/10.5281/zenodo.4126910>



## The prototype X-ray binary GX 339–4: using TeV $\gamma$ -rays to assess LMXBs as Galactic cosmic ray accelerators

D. Kantzas, S. Markoff, M. Lucchini, C. Ceccobello, V. Grinberg, R. M. T. Connors  
& P. Uttley

*Monthly Notices of the Royal Astronomical Society, 2022, 510, 4, 5187–5198*

### *Abstract*

Since the discovery of cosmic rays (CRs) over a century ago, their origin remains an open question. Galactic CRs with energy up to the knee ( $10^{15}$  eV) are considered to originate from supernova remnants, but this scenario has recently been questioned due to lack of TeV  $\gamma$ -ray counterparts in many cases. Extragalactic CRs on the other hand, are thought to be associated with accelerated particles in the relativistic jets launched by supermassive accreting black holes at the center of galaxies. Scaled down versions of such jets have been detected in X-ray binaries hosting a stellar black hole (BHXBs). In this work, we investigate the possibility that the smaller-scale jets in transient outbursts of low-mass BHXBs could be sources of Galactic CRs. To better test this scenario, we model the entire electromagnetic spectrum of such sources focusing on the potential TeV regime, using the 'canonical' low-mass BHX B GX 339–4 as a benchmark. Taking into account both the leptonic radiative processes and the  $\gamma$ -rays produced via neutral pion decay from inelastic hadronic interactions, we predict the GeV and TeV  $\gamma$ -ray spectrum of GX 339–4 using lower-frequency emission as constraints. Based on this test-case of GX 339–4 we investigate whether other, nearby low-mass BHXBs could be detected by the next-generation very-high-energy  $\gamma$ -ray facility the Cherenkov Telescope Array, which would establish them as additional and numerous potential sources of CRs in the Galaxy.

### 3.1 Introduction

Accreting supermassive black holes located at the centres of galaxies are the most powerful engines in the Universe, and some of the most interesting laboratories to investigate the physics of extreme gravity. Of particular importance are those active galactic nuclei (AGN) that exhibit relativistic and collimated jets. The underlying physics that unites the accretion of black holes with the large scale jets is still an unanswered problem. These relativistic jets are considered powerful enough to accelerate particles to very high energy, making them likely a source of extragalactic cosmic rays (CRs) that reach energies of at least  $10^{19}$  eV (Hillas 1984; Abbasi et al. 2018; Perrone 2020).

CRs are elementary particles and/or atoms of extraterrestrial origin. The resulting CR spectrum covers ten orders of magnitudes in particle energy and shows two very well known characteristic spectral features where the slope changes. The first one is the ‘knee’ that is located around  $10^{15}$  eV, and the second feature is the ‘ankle’ that is located around  $10^{17}$  eV. Current models assume that CRs up to the knee are produced within the Milky Way, while CRs from above the ankle are of extragalactic origin (Hillas 1984; Drury 2012; Blasi 2013). Supernova remnants have long been considered the dominant source of Galactic CRs based on their size and measured magnetic fields (Hillas 1984; Völk et al. 2003; Vink 2012; Ackermann et al. 2013), but due to the lack of TeV  $\gamma$ -ray counterparts the debate is still open (Aharonian et al. 2019). Given the ability of AGN jets to accelerate cosmic rays, another promising alternative source could be the Galactic jets launched in X-ray binaries comprised of a stellar accreting black hole and a companion star (BHXBs; Mirabel & Rodriguez 1994; Fender 2001; McClintock et al. 2006). Such Galactic jets share the physical properties of AGN jets but on much smaller scales (Heinz & Sunyaev 2002; Romero et al. 2003; Romero & Orellana 2005; Fender et al. 2005; Romero & Vila 2008; Vila & Romero 2010; Vila et al. 2012; Pepe et al. 2015; Cooper et al. 2020; Kantzas et al. 2020).

The presence of jets in low mass BHXBs is transient, and is tightly connected to the properties of the accretion flow. In the so-called hard state, BHXBs display a flat or inverted radio-to-IR spectrum associated with jet synchrotron emission analogous to AGN jets (Blandford & Königl 1979; Hjellming & Johnston 1988; Falcke & Biermann 1995; Markoff et al. 2001; Fender et al. 2006; Corbel et al. 2003, 2012). BHXBs transit from quiescent to hard and soft states within ‘human-like’ timescales, hence we can observe the jet launching and jet quenching in real-time (see e.g. Russell et al. 2020). The dynamical timescales are roughly proportional to the mass of the black hole, so it would take typically millions of times longer to detect similar state transitions in AGN.

Accelerated particles in AGN jets are the source of the non-thermal radiation detected over the entire electromagnetic spectrum, from radio to TeV  $\gamma$ -rays (see e.g.



Tavecchio et al. 1998; Celotti et al. 2001; Aharonian 2004; Georganopoulos et al. 2006; Marscher et al. 2008; Ghisellini et al. 2009). However, the exact radiative mechanism has been under debate for a long time because it is tightly connected to the jet composition and the exact particle acceleration mechanism, which remain debated. Two scenarios are generally considered depending on the jet launching mechanism. First, a purely leptonic jet powered by the black hole spin (Blandford & Znajek 1977) may accelerate electrons/positrons that are responsible for the entire multi-wavelength spectrum (Maraschi et al. 1992; Dermer & Schlickeiser 1993; Levinson & Blandford 1995; Blandford & Levinson 1995; Marcowith et al. 1995; Böttcher & Schlickeiser 1997; Georganopoulos et al. 2002; Ghisellini et al. 2010). Second, a lepto-hadronic jet powered by the accretion disc (Blandford & Payne 1982; or which starts out leptonic and entrains hadronic mass) may accelerate leptons and baryons that contribute in different energy bands via different mechanisms (Mannheim 1993; Rachen & Biermann 1993; Mücke et al. 2003; Böttcher et al. 2013; Liodakis & Petropoulou 2020).

Recent GeV observations of the high-mass BHXBs Cygnus X-3 (Tavani et al. 2009) and Cygnus X-1 (Tavani et al. 2009; Malyshev et al. 2013; Zanin et al. 2016), and TeV observations of SS 433 (Abeysekara et al. 2018) suggest that some Galactic jets can accelerate particles to high energy. However, it is not known whether all BHXBs, especially the more abundant population of low-mass BHXBs can routinely produce  $\gamma$ -rays. Until now, only the high-mass BHXBs that are characterised by the presence of a strong stellar wind that interacts with the jet have been detected in the GeV and TeV bands (see e.g. Bodaghee et al. 2013). It is thus important to investigate whether the far more populous low-mass BHXBs can also produce  $\gamma$ -rays. In this work, we approach this question by studying the ‘canonical’ low-mass BHBX source GX 339-4, extending our previous work on the ‘canonical’ high-mass BHBX Cygnus X-1 (Kantzas et al. 2020). Similar to AGN jets, the emitting mechanism responsible for any  $\gamma$ -rays remains unclear, with both leptonic and hadronic processes considered feasible. We are also interested in exploring how the different composition scenarios may affect the jet dynamics and the interpretation of the jet properties.

In this work, we employ a multi-zone jet model to study the hadronic interactions within the jets, as well as the effect on the dynamics and the electromagnetic signature of low-mass BHBX jets. We examine the bright outburst of GX 339-4 in 2010 to model the radio-to-X-ray spectrum with the goal of predicting the TeV radiation originating in the jets. Using the case of GX 339-4 as a model, we assess the likelihood of other, closer low-mass BHXBs to be potential sources for the next generation  $\gamma$ -ray facilities, particularly the Cherenkov Telescope Array (CTA). Such TeV emission may be the signature of efficient CR acceleration inside the BHBX jets, and hence the entire Galactic population of BHBX jets may contribute to the Galactic CR spectrum.

In Section 3.2 we discuss the physical properties of GX 339-4 and its spectral behaviour. In Section 3.3 we describe the model we use to study the spectrum of GX 339-4. We present our results in Section 3.4, discuss their implication in Sec-

tion 3.5 and come to our final conclusions in Section 3.6.

## 3.2 GX 339–4

GX 339–4 is a ‘canonical’ low-mass BHXB discovered in 1973 (Markert et al. 1973). It undergoes outbursts every two-to-three years that last from a few weeks to months (Belloni et al. 1999; Corbel & Fender 2002; Corbel et al. 2003; Zdziarski et al. 2004; Homan et al. 2005; Belloni et al. 2006; Motta et al. 2009; Corbel et al. 2012). During outbursts, GX 339–4 rises out of quiescence and launches compact jets that contribute to the radio-to-optical spectrum as the source continues into the hard state (Corbel et al. 2000, 2003, 2012; Fender 2001; Corbel & Fender 2002; Fender et al. 2004; Homan et al. 2005; Casella et al. 2010; Gandhi et al. 2011). Such consistent, repetitive behaviour along with extensive and often simultaneous multiwavelength monitoring makes GX 339–4 a perfect target to better understand the properties of relativistic jets.

Although GX 339–4 is a well-studied source, its physical parameters are not well constrained because of the weakness of its companion star. Based on optical photometry the orbital period is estimated to be between 14.8 and 16.8 h (Callanan et al. 1992; Cowley et al. 2002, respectively). The inclination angle is still unknown but is constrained to  $< 60$  deg because of the lack of eclipsing (Cowley et al. 2002), and the lack of a detection of the companion star means the mass of the black hole is also uncertain. Various current estimates put the mass (in  $M_{\odot}$ ) between 4 and 16 (Shidatsu et al. 2011),  $5.8 \pm 0.8$  for an orbital period of 1.75 d (Hynes et al. 2003),  $> 7$  (Muñoz Darias et al. 2008) or 9.8 for a mass function of  $1.91 \pm 0.08 M_{\odot}$  (Heida et al. 2017). We adopt the most recent value of  $M_{\text{bh}} = 9.8 M_{\odot}$  of Heida et al. (2017). Hynes et al. (2004) set the distance of GX 339–4 higher than 6 kpc, and Zdziarski et al. (2004) derived a value of 8 kpc while Parker et al. (2016) found a distance of  $8 \pm 0.9$  kpc, which is the distance we adopt here.

### 3.2.1 Observational constraints in the hard state

GX 339–4 has been detected in the optical bands, but the origin of this emission is still not clear. Tetarenko et al. (2020) recently studied its multiwavelength emission and concluded that the optical emission in bright outbursts like the one of 2010 cannot originate exclusively from irradiation of the accretion disc, because unreasonable amounts of energy would be required. Thermal synchrotron emission from the base of the jets could then be considered a good candidate for the optical emission. On the other hand, GX 339–4 shows a flat spectrum in the radio with a spectral break in the IR band that corresponds to the transition of optically thick to optically thin synchrotron emission (Corbel & Fender 2002; Gandhi et al. 2011). Extrapolating the optically thin IR emission to the X-ray band, significantly underpredicts the optical

flux (Maitra et al. 2009; Gandhi et al. 2011; Tetarenko et al. 2019). Hence, if the optical emission originates in the jets, it must come from a different region compared to the IR (Markoff et al. 2003; Corbel et al. 2013).

Reflection features, including a broad iron emission line, are also evident in the X-ray spectrum of GX 339–4 (Nowak et al. 2002; García et al. 2015; Fürst et al. 2015; Parker et al. 2016; García et al. 2019; Dzielak et al. 2019). A jet synchrotron component that is beamed perpendicularly away from the accretion disc is very unlikely to produce significant relativistic reflection (Markoff & Nowak 2004; Reig & Kylafis 2021). Furthermore, Uttley et al. (2011) studied the energy-dependent time lags and found that the instabilities in the accretion disc may be responsible for driving the continuum variability on short and longer-than-second timescales. The large time-lags are due to the travel-time between the illuminating region and the disc where the X-rays are reprocessed, and can be only tens of gravitational radii at most. That indicates that the X-ray continuum should be governed by a single component, and a thermal corona close to the black hole could sufficiently explain it (but also see Mahmoud et al. 2019, for a two-component corona).

Based on these results, we approach the modelling assuming the most conservative case for the jet power: that the radio through IR up to the break is self-absorbed synchrotron from the extended jets, the optical emission is synchrotron emission from thermal particles at the base of the jets, and that the X-ray reflecting power-law is from a separate coronal region.

### 3.2.2 Observational data

In this work, we use archival quasi-simultaneous data to model the multiwavelength spectrum of GX 339–4 from radio to X-rays during the hard state of the 2010 outburst. We use the radio data obtained by the Australian Telescope Compact Array (ATCA) on MJD 55263 (Corbel et al. 2012), IR data obtained by the Wide-field Infrared Survey Explorer (WISE) on MJD 55266 (Gandhi et al. 2011), optical data obtained by the Small & Moderate Aperture Research Telescope System (SMARTS) on MJD 55263, and X-rays from the *Neil Gehrels Swift Observatory*/X-ray Telescope (*Swift*/XRT) on MJD 55262 (Corbel et al. 2012) and *Rossi X-ray Timing Explorer*/Proportional Counter Array (*RXTE*/PCA) on MJD 55263 (Corbel et al. 2012). We use the 0.5–4.0 keV XRT and the 3–45 keV PCA X-ray data. The IR data are not simultaneous and were obtained 3 days later, but we use them because they show a spectral break crucial for our interpretation of the whole spectrum (see below). There was no significant variability in this time, hence this is a decent assumption to combine these data (Corbel et al. 2012, 2013; Connors et al. 2019). We also use the upper-limits in the GeV band set by the *Fermi*/Large Area Telescope (LAT)  $\gamma$ -ray telescope during the 2010 outburst to further constrain the highest energy regime of the spectrum (Bodaghee et al. 2013). We provide the energy/frequency ranges and the corresponding flux

**Table 3.1:** The observational multiwavelength data we use in this work.

Observatory	log Frequency (Hz)		log Energy (eV)		Flux Density (mJy <sup>a</sup> )		Reference
ATCA	9.74	9.94	−4.64	−4.44	10.2 ± 0.1	11.3 ± 0.1	Corbel et al. 2012
WISE	13.13	13.41	−1.25	−0.97	87 ± 8	80 ± 7	Gandhi et al. 2011
	13.81	13.95	−0.57	−0.43	64 ± 5	55 ± 4	
SMARTS	14.25	14.40	−0.13	0.01	47 ± 5	50 ± 5	Buxton et al. 2012
	14.57	14.73	0.18	0.35	54 ± 5	92 ± 29	
<i>SWIFT</i> /RXT	17.08–18.0		2.7–3.7		0.2 at 3 keV		Corbel et al. 2012
<i>RXTE</i> /PCA	17.9–18.9		3.5–4.5		0.2 at 3 keV		Corbel et al. 2012

<sup>a</sup>1 mJy = 10<sup>−26</sup> erg cm<sup>−2</sup> s<sup>−1</sup> Hz<sup>−1</sup>.

density of all the data we use in Table 3.1.

### 3.3 Modelling

In this section, we briefly discuss our model, focusing on the interpretation of the free parameters we fit for. A more detailed description of the model can be found in Kantzas et al. (2020) and in Lucchini et al. (2022).

#### 3.3.1 Jet properties

We assume that two compact jets are launched by the accreting black hole with jet base radius  $R_0$ . The power injected into the jets in the comoving frame  $L_{\text{jet}}$  defines the number density of the cold (non-relativistic) protons in the plasma at the base of the jets as,

$$n_0 = \frac{L_{\text{jet}}}{2\beta_{0,s}\Gamma_{0,s}c\pi R_0^2(m_p c^2 + \langle\gamma_e\rangle m_e c^2(1 + 1/\beta))}, \quad (3.1)$$

where  $\beta_{0,s}\Gamma_{0,s}c$  is the comoving velocity of the plasma in the jet base assumed to be equal to the speed of sound in a relativistic fluid (Falcke & Biermann 1995; Markoff et al. 2008; Crumley et al. 2017; Lucchini et al. 2022),  $\beta = U_e/U_B$  is the plasma beta where  $U_e$  is the energy density of the electrons and  $U_B$  is the magnetic field energy density. For simplicity, we assume equal number density of electrons and protons, but we discuss the implication of this assumption in Section 3.5. We further assume that the electron population at the jet base is injected in a thermal Maxwell–Jüttner (MJ) distribution with a peak-energy of  $2.23 k_B T_e$ .

We vary the plasma beta at the jet base to define the strength of the magnetic field, which scales inversely with distance along the jet  $z$ . Assuming the electron enthalpy is not significant, we define the magnetisation of the jet as

$$\sigma = \frac{B_0^2}{4\pi n_0 m_p c^2}, \quad (3.2)$$

where  $B_0$  is the strength of the magnetic field at the jet base. We do not consider any particular magnetic field configuration (toroidal or poloidal) but merely describe the magnetic field by its total strength  $B$ .

### 3.3.2 Particle acceleration

At some distance  $z_{\text{diss}}$  along the jet axis, energy is dissipated into accelerating a fraction of the thermal particles into a non-thermal power-law. We assume that the accelerated particles carry a fixed fraction of the jet power, and in particular, we conservatively fix the power of the non-thermal leptons to be  $0.02 L_{\text{jet}}$  and of the protons to be  $0.05 L_{\text{jet}}$ .

We allow  $z_{\text{diss}}$  varying as a fitted parameter and, for the case of the leptonic populations, we assume constant re-acceleration along the jet, but we constrain the proton acceleration to occur only between  $z_{\text{diss}}$  and  $10 z_{\text{diss}}$  in order to limit the required power. Because the most compact part of the jet produces the non-thermal particles, this dissipation region also corresponds to the region where the synchrotron radiation breaks from flat/inverted due to self-absorption, to steep/optically thin. After predictions by Markoff et al. (2001), Corbel & Fender (2002) confirmed that this break typically falls in the NIR band during hard states, and we chose the epoch here because of high-quality observations by Gandhi et al. (2011) that could pinpoint the synchrotron break frequency to be  $4.6_{-2.0}^{+3.5} \times 10^{13}$  Hz. To match this frequency, we fix the particle acceleration region at  $2600 r_g$  from the black hole (see also Connors et al. 2019).

The accelerated particles follow a power-law in energy of the form

$$dn(E) \propto E^{-p} \times \exp(-E/E_{\text{max}}). \quad (3.3)$$

In principle, the power-law index  $p$  depends on the acceleration mechanism and may differ between electrons and protons, but we choose to use the same for both populations for simplicity.

In Equation 3.3,  $E_{\text{max}}$  is the maximum particle energy constrained by energy losses and/or escape. In this work, the maximum electron energy is limited by synchrotron losses and the maximum proton energy is limited by the lateral escape from the jet region. The maximum attainable energy is self-consistently calculated along the jet by equating the characteristic timescales of the losses to the acceleration timescale. The characteristic acceleration timescale  $t_{\text{acc}} = 4E/(3f_{\text{sc}}ecB)$  depends on the acceleration

efficiency parameter  $f_{\text{sc}}$  that we take to be close to maximum, namely  $f_{\text{sc}} = 0.01$  (Jokipii 1987; Aharonian 2004). We plot the characteristic timescales versus the particle kinetic energy for the population of the accelerated protons in Appendix 3.A.

The fractional number of accelerated particles with respect to the total number of particles  $f_{\text{nth}}$  depends on the acceleration mechanism as well. This number may not be constant along the jet. We parametrize the density of the accelerated particles following:

$$n_{\text{nth}} = n_{\text{th}} f_{\text{nth}} \left( \frac{\log_{10}(z_{\text{diss}})}{\log_{10}(z)} \right)^{f_{\text{pl}}}, \quad (3.4)$$

where  $f_{\text{pl}} > 0$  is a free parameter accounting for our ignorance about the exact nature of the dissipation.  $(n_{\text{nth}}) n_{\text{th}}$  is the number density of the (non-)thermal particles. The physical motivation behind such an assumption is the fact that it leads to the characteristic inverted spectrum between radio and optical wavelengths detected in BHXBs (see discussion in Lucchini et al. 2021).

The minimum energy of the accelerated particles depends on the injected distributions in the base. We assume that the minimum energy for accelerated protons is the rest mass energy ( $m_{\text{p}}c^2$ ). This choice is intended purely to limit the number of free parameters; we discuss its implication below. We take the peak of the MJ distribution  $2.23 k_{\text{B}}T_{\text{e}}$  to be the minimum energy of the accelerated electrons. We further define a heating parameter  $f_{\text{heat}}$

$$E_{\text{e,min}} = 2.23 f_{\text{heat}} k_{\text{B}}T_{\text{e}}. \quad (3.5)$$

The physical motivation behind this assumption is that along with the electron acceleration, some extra heating has been reported by numerical simulations (Sironi & Spitkovsky 2009; Gedalin et al. 2012; Plotnikov et al. 2013; Sironi et al. 2013; Sironi & Spitkovsky 2014; Melzani et al. 2014; Crumley et al. 2017). The value of this parameter is not well constrained, but we set it to be  $f_{\text{heat}} < 10$  (Sironi & Spitkovsky 2009, 2011; Crumley et al. 2019).

### 3.3.3 Radiative Processes

#### 3.3.3.1 Leptonic processes

Following Kantzas et al. (2020), the leptonic radiative processes we take into account are cyclo-synchrotron radiation and inverse Compton scattering (ICS), where the cyclo-synchrotron photons are further upscattered via the synchrotron-self Compton mechanism (SSC) along the jets. Further photon targets for the ICS are the disc photons. We also take into account a precise treatment of pair production due to photon annihilation and pair annihilation to electron-positron pairs (Coppi & Blandford 1990; Böttcher & Schlickeiser 1997).

### 3.3.3.2 Hadronic Processes

Accelerated protons interact with the bulk cold protons of the jet and, via proton-proton (pp) interactions, lead to pion production. Neutral pions decay into  $\gamma$ -rays and charged pions into secondary electrons and neutrinos via the muon decay channel (Mannheim & Schlickeiser 1994). Photomeson interactions between the accelerated protons and target photons ( $p\gamma$ ) lead to similar distributions of secondary particles. The target photons we consider here are: the thermal radiation of the accretion disc and the non-thermal radiation originating in the compact jet. Finally, we also account for photopair interactions that lead to the formation of pairs, after the inelastic collision between protons and photons. We use the semi-analytical formalism of Kelner et al. (2006) and Kelner & Aharonian (2008) for pp and  $p\gamma$  interactions, respectively. For the full description of the treatment of the cascades, see Kantzas et al. (2020). For the case of GX 339–4, no photon field is significant enough to attenuate the GeV and TeV emission (see also the discussion below).

### 3.3.4 Accretion disc and thermal corona

We assume a standard geometrically thin, optically thick accretion disc truncated at some innermost radius  $R_{\text{in}}$  with temperature  $T_{\text{in}}$  (Shakura & Sunyaev 1973; Frank et al. 2002). We describe the disc luminosity  $L_d$  in terms of Eddington luminosity  $L_{\text{Edd}} = 4\pi GM_{\text{bh}}m_{\text{p}}c/\sigma_{\text{T}}$ . We further assume the existence of a hot electron plasma of temperature  $T_{\text{cor}}$ , in a spherical region centred on the black hole, normalized by a radius  $R_{\text{cor}}$ , and of optical depth  $\tau_{\text{cor}} = n_e R_{\text{cor}} \sigma_{\text{T}}$ . These hot electrons upscatter the disc photons to higher energies. We require the existence of such a plasma to be able to model both the X-ray spectrum and properly account for the measured hard timing lags as mentioned in Section 3.1 (and see e.g. Connors et al. 2019, and discussion below).

## 3.4 Results

In this section, we present the results for the best fits of our model to the multi-wavelength spectrum of GX 339–4. We explore three different model scenarios: one purely leptonic, and two lepto-hadronic models. For the purely leptonic model, we assume that the non-thermal electrons follow a power-law with  $p = 2.2$  (Corbel & Fender 2002; Gandhi et al. 2011). For the two hadronic models, we explore both a soft ( $p = 2.2$ ) and a hard ( $p = 1.7$ ) particle power-law, respectively. For all models, we fix some common parameters as shown in Table 3.2. We choose the ratio between the height of the jet base and its radius to be constant and equal to 2 (Maitra et al. 2011; Crumley et al. 2017). The maximum height of the jet is fixed at a large enough value, so it does not influence the spectrum in the radio band via the self-absorption

**Table 3.2:** The fixed parameters of our models, see text for further discussion.

Parameter	Value	Description
$M_{\text{BH}} (M_{\odot})$	9.8	Mass of the black hole <sup>a</sup>
$\theta_{\text{incl}} (^{\circ})$	40	Inclination angle <sup>a</sup>
$D$ (kpc)	8	Distance of the source <sup>b</sup>
$h = z_0/R_0$	2	Initial jet height to radius ratio
$z_{\text{diss}} (r_{\text{g}})$	2600	Particle acceleration region <sup>c</sup>
$z_{\text{diss, max}} (z_{\text{diss}})$	10	Maximum proton acceleration region
$z_{\text{max}} (r_{\text{g}})$	$10^8$	Maximum jet height
$f_{\text{sc}}$	0.01	Particle acceleration efficiency parameter
$P_{\text{e}} (L_{\text{jet}})$	0.02	Power of non-thermal electrons
$P_{\text{p}} (L_{\text{jet}})$	0.05	Power of non-thermal protons
$R_{\text{in, disc}}$	$R_0$	Disc innermost radius (see Table 3.3)
$R_{\text{out, disc}} (r_{\text{g}})$	$10^5$	Disc outermost radius
$N_{\text{H}} (10^{22} \text{ cm}^{-2})$	0.6	Absorption coefficient <sup>d</sup>
$refl$	0.29	Reflection fraction <sup>e</sup>

<sup>a</sup>Heida et al. (2017),

<sup>b</sup>Parker et al. (2016)

<sup>c</sup>Gandhi et al. (2011),

<sup>d</sup>García et al. (2019),

<sup>e</sup>Magdziarz & Zdziarski (1995).

cutoff, and we choose the maximum reasonable particle acceleration efficiency parameter  $f_{\text{sc}} = 0.1$ , which results in maximum proton energies of the order of tens of TeV in the hadronic models. We tie the truncation radius of the thin accretion disc to the jet base radius to reduce model degeneracy because the disc does not contribute to the electromagnetic spectrum at all. We use the `tbabs` model to account for the neutral photoelectric absorption in the intergalactic medium, using the cross-sections by Verner et al. (1996) and the cosmic abundances by Wilms et al. (2000), where the absorption coefficient  $N_{\text{H}}$  sets the X-ray absorption column. We use the non-relativistic `reflect` function to treat in a simplified way the reflection detected in GX 339–4, parametrised primarily via the reflection fraction  $refl = \Omega/2\pi$ , which indicates the amplitude of the reflected spectrum (Magdziarz & Zdziarski 1995). We choose this simple model in order to minimize the free parameters used to describe



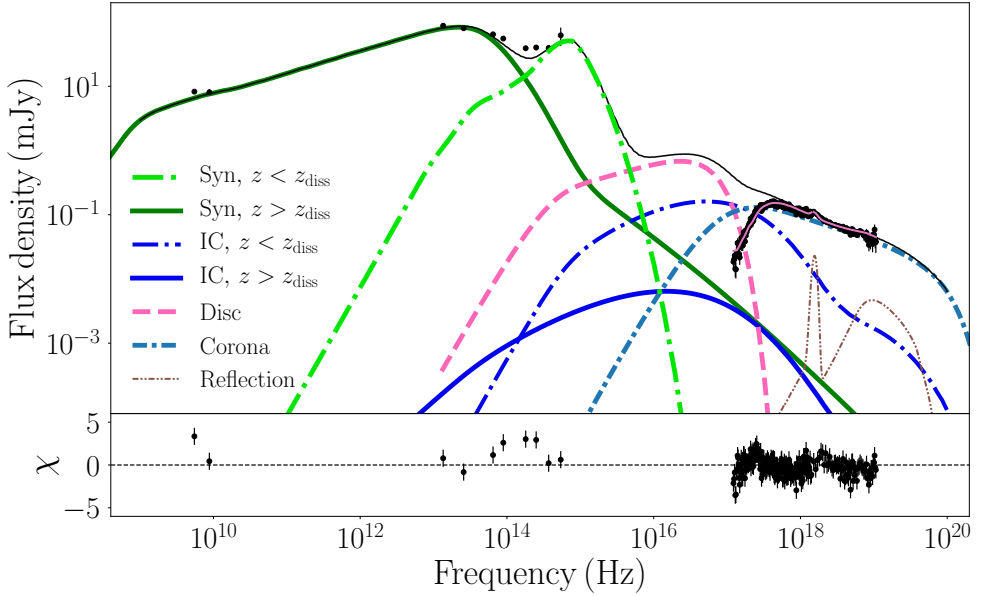


**Figure 3.1:** The best fit with the  $\chi$ -residuals of the multiwavelength spectrum of the 2010 outburst of GX 339–4 assuming a purely leptonic model. The solid black line shows the total intrinsic emission, the red line shows the X-ray absorbed emission, and the rest of the components are explained in the legend.

the X-ray spectrum, which is well-fit by a power law. Our focus is on constraining the jet physics that drives the  $\gamma$ -ray band, thus we retain most of the free parameters for that model.

We use the Interactive Spectral Interpretation System (ISIS; Houck & Denicola 2000) to forward fold the model into X-ray detector space, and to find the statistical best fit to the data presented in Section 3.2.2. We use the `emcee` function to explore the parameter space using a Markov Chain Monte Carlo (MCMC) method (Foreman-Mackey et al. 2013). We initiate 20 walkers per free parameter and perform  $10^4$  loops. We reject the first 50 per cent of the run as the “burn-in” period. We provide the  $1\sigma$  uncertainties in Table 3.3, along with the results of the best fit for each model.

In Figures 3.1–3.3 we show the best fits of the multi-wavelength spectrum of GX 339–4 for the three different models we explore. In Figure 3.1, we show the purely leptonic model, whereas in Figures 3.2 and 3.3 the results of the lepto-hadronic models.

The unique contribution of the hadronic processes can only be seen in the TeV  $\gamma$ -ray band because the purely leptonic model cannot produce significant emission at GeV and above. In Figures 3.4 and 3.5 we show the predicted GeV to 100 TeV  $\gamma$ -ray spectrum of GX 339–4. The primary-accelerated electrons dominate in the GeV

**Table 3.3:** Parameters for the three fitted models, distinguished via the power-law index of the accelerated electrons  $p_e$  and protons  $p_p$ . We show the free parameters and the  $1\sigma$  uncertainties as discussed in Section 3.3 before the double line. Below the double line are indicative evaluated quantities of the plasma magnetisation, the magnetic field, the total luminosity of the accelerated proton/electron population and the maximum energy of the protons/electrons at the particle acceleration region.

Parameter \ model	Leptonic	Hadronic soft	Hadronic hard
$p_e$	2.2	2.2	1.7
$p_p$	-	2.2	1.7
$L_{\text{jet}}$ ( $10^{-3} L_{\text{Edd}}$ ) ( $\times 10^{36} \text{ erg s}^{-1}$ )	$2.5_{-2}^{+5}$ $3_{-2}^{+6}$	$70^{+100}$ $90_{-83}^{+117}$	$50^{+60}$ $70_{-60}^{+70}$
$R_0(r_g)$	$100^{+100}$	$110^{+100}$	$90^{+90}$
$T_e$ (keV)	$1600_{-600}^{+2400}$	$2100_{-2000}^{+2300}$	$2000_{-1900}^{+2000}$
$f_{\text{pl}}$	$4_{-3}^{+5}$	$4_{-3}^{+5}$	$4_{-3}^{+5}$
$f_{\text{heat}}$	$5_{-5}^{+7}$	$8_{-6}^{+9}$	$7_{-6}^{+9}$
$\beta$	$0.2_{-0.1}^{+1.5}$	$0.2_{-0.1}^{+0.4}$	$0.04^{+0.04}$
$L_d$ ( $10^{-3} L_{\text{Edd}}$ )	$5_{-4}^{+9}$	$23_{-22}^{+24}$	$2^{+3}$
$T_{\text{cor}}$ (keV)	$170_{-100}^{+200}$	$55^{+350}$	$60_{-50}^{+70}$
$R_{\text{cor}}$ ( $r_g$ )	$300_{-200}^{+300}$	$160_{-155}^{+460}$	$460_{-440}^{+470}$
$\tau_{\text{cor}}$	$0.6_{-0.4}^{+0.6}$	$0.7_{-0.6}^{+0.8}$	$0.7^{+0.7}$
$\chi^2/\text{DoF}$	250/233	240.8/233	190/233
$\sigma$	1.7	0.03	0.1
$B_0$ (G)	$2 \times 10^5$	$1 \times 10^6$	$2 \times 10^5$
$B$ (G)@ $z_{\text{diss}}$	$1 \times 10^4$	$6 \times 10^3$	$1 \times 10^4$
$E_{p,\text{max}}$ (eV)	-	$2.8 \times 10^{13}$	$2.7 \times 10^{13}$
$E_{e,\text{max}}$ (eV)	$1 \times 10^8$	$5.2 \times 10^{10}$	$5.3 \times 10^{10}$

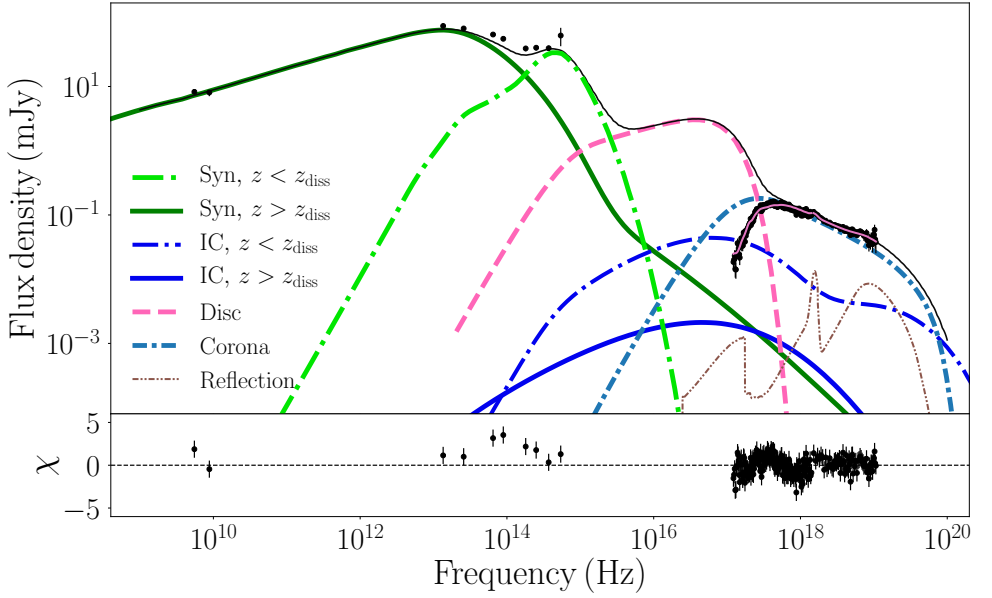


**Figure 3.2:** Similar to Figure 3.1 but for the lepto-hadronic model with  $p_e = 2.2$  and  $p_p = 2.2$  power-law index.

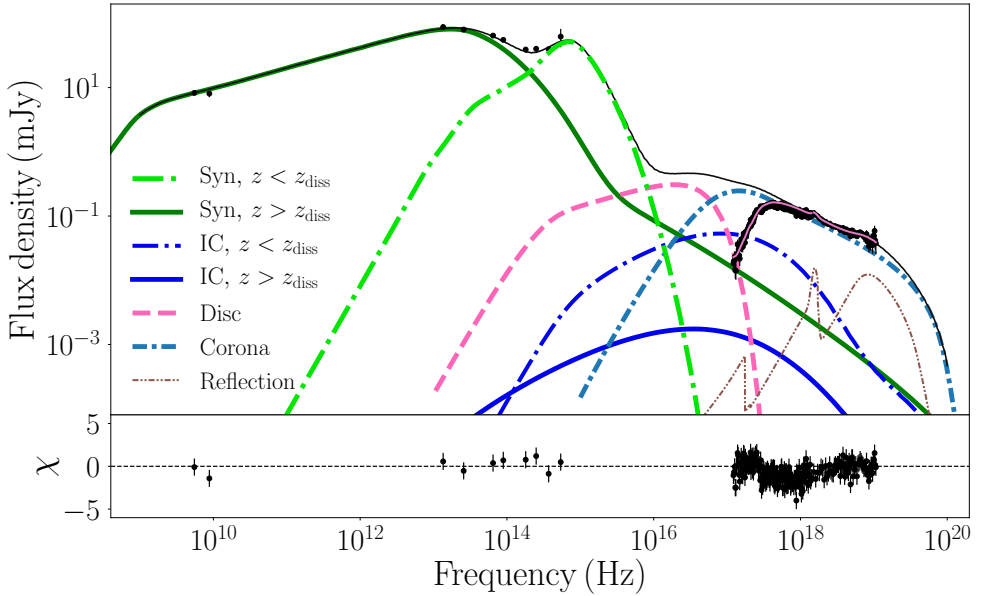


**Figure 3.3:** Similar to Figure 3.1 but for the lepto-hadronic model with  $p_e = 1.7$  and  $p_p = 1.7$  power-law index.

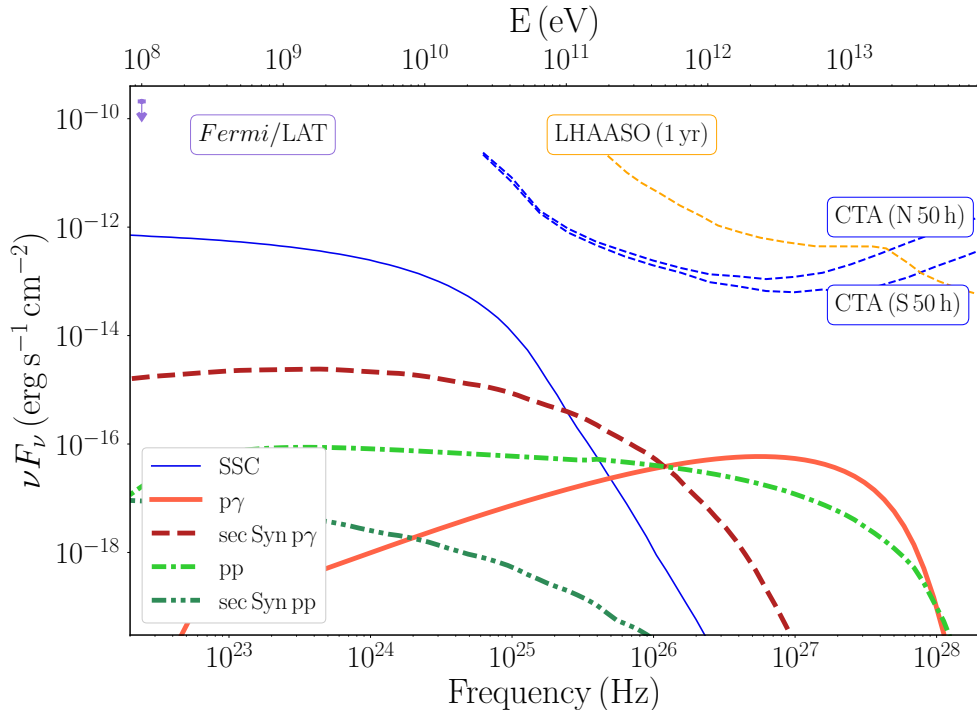


**Figure 3.4:** The  $\gamma$ -ray spectrum for the lepto-hadronic model with  $p_e = 2.2$  and  $p_p = 2.2$  power-law index. We compare the predicted spectrum to the *Fermi*/LAT upper limits of the 2010 outburst (Bodaghee et al. 2013), the sensitivity of LHAASO after one year of operation (Bai et al. 2019), and the predicted 50-hour sensitivity of the North and South site of CTA (from [www.cta-observatory.org](http://www.cta-observatory.org)). The solid red line shows the pion bump from  $p\gamma$ , the dashed red line shows the synchrotron radiation from secondary leptons from  $p\gamma$ , the dash-dotted green line shows the pion bump from  $pp$  interactions, and the dash-double dotted line shows the synchrotron radiation from secondary leptons from  $pp$ .

regime via SSC. The hadronic processes dominate in the TeV energy band, in particular, the neutral pion decay from both  $pp$  and  $p\gamma$  collisions as well as the synchrotron radiation of secondary pairs from the latter. Because we set the acceleration efficiency parameter  $f_{sc}$  to a high value, the protons are able to achieve high energies of the order of  $\sim 10^{13}$  eV, producing  $\gamma$ -rays of the order of TeV.

## 3.5 Discussion

### 3.5.1 Multi-wavelength spectrum and jet dynamics

Our results with our new lepto-hadronic multi-zone jet model confirm earlier results that stratified jets can self-consistently reproduce the radio-to-X-ray spectrum, to-

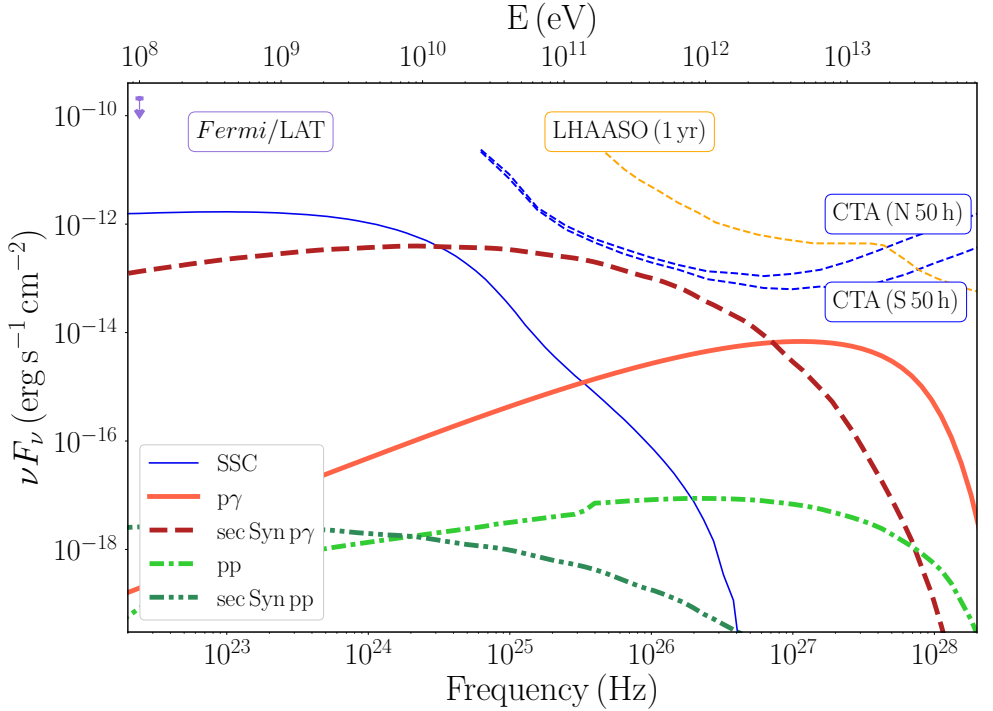


**Figure 3.5:** Similar to Figure 3.4 but for the lepto-hadronic model with  $p_e = 1.7$  and  $p_p = 1.7$  power-law index.

gether with a thin accretion disc including reflection (Markoff et al. 2001; Zhang et al. 2010; Kylafis & Reig 2018; Connors et al. 2019; Lucchini et al. 2022). However, compared to earlier works (e.g. Markoff et al. 2005), we can also better reproduce the significantly inverted radio-to-IR spectrum by introducing a decreasing particle acceleration efficiency along the jets (Lucchini et al. 2021). We see, however, in Table 3.3 that the parameter  $f_{pl}$  controlling this effect cannot be well-constrained by the data, and we can only set an upper-limit.

Apart from particle acceleration, we require significant electron heating of the thermal population (Sironi & Spitkovsky 2009; Gedalin et al. 2012; Plotnikov et al. 2013; Sironi et al. 2013; Sironi & Spitkovsky 2014; Melzani et al. 2014; Crumley et al. 2019) to reproduce both the optical and IR bands as jet synchrotron emission. In particular, we find that the scenario where optical emission originates from the jet base and the IR emission originates from the particle acceleration region  $z_{\text{diss}}$  is consistent with the data. An alternative scenario is that both the IR and the optical emission originate in a hot flow that consists of thermal and non-thermal electrons (Poutanen & Veledina 2014; Kosenkov et al. 2020b), a scenario that better describes the soft states

(Kosenkov & Veledina 2018). Further simultaneous IR-to-optical observations in the hard state would be able to test this scenario, as well as simultaneous polarisation measurements across the entire optical/IR band (however see e.g. Russell & Fender 2008 for measurements prior to the 2010 outburst).

In both the leptonic and lepto-hadronic scenarios the shape of the radio-to-X-ray spectrum of GX 339–4 looks identical and the radiative mechanisms are also the same. The spectral shape is determined primarily by the jet geometry and dynamics, which are similar between the scenarios. However, for the case of the lepto-hadronic models, where we assume equal number density of accelerated electrons and protons, we require much more power injected into the jet base than for the purely leptonic model, which is a well-known issue with hadronic models (see e.g. Pepe et al. 2015; Abeysekara et al. 2018; Kantzas et al. 2020).

To fit the optical emission with thermal synchrotron emission from the base of the jets while the accelerated particles fit the radio-to-IR, we require high electron temperature. This radiation leads to a curved IC spectrum in the soft X-rays, so another component is required to explain the hard power-law. If it can be confirmed that the optical emission is jet synchrotron (via polarisation for instance), then the need for a second component to fit the X-rays will be more robust. For this reason, we have added a simple thermal corona model, which together with reflection, can well account for the X-ray spectrum, but is otherwise independent of the jet parameters. In reality, these components should be linked, but it is well known that spectral information alone is often not enough to probe the detailed geometry of the corona, which is the case in our work here as well (see e.g. Del Santo et al. 2008; Droulans et al. 2010; Reig & Kylafis 2015, 2021; Kylafis & Reig 2018; Connors et al. 2019; Cao et al. 2021b).

When protons are accelerated, the hadronic interactions contribute with additional flux in the  $\gamma$ -ray regime of the spectrum. For the scenario with a hard proton power-law index of  $p_p = 1.7$ , producing significant TeV flux detectable by CTA would require a non-physical amount of power dissipated into proton acceleration. By constraining the non-thermal proton power to 5 per cent of the jet power, we see that the TeV flux does not exceed the CTA sensitivity (see Figure 3.5). A more typical power-law index of  $p_p = 2.2$  produces even less GeV and TeV flux. In addition, both of these models require strongly matter-dominated outflows even at their launching point ( $\sigma \lesssim 0.1$ ). Such a low magnetisation raises issues of physicality for these models, since the final bulk Lorentz factor of the flow is expected to be on the order of the initial magnetisation  $\sigma$  (Komissarov et al. 2007, 2009; Tchekhovskoy et al. 2008, 2009; Chatterjee et al. 2019). Specifically, BHXB jets consistently show at least mildly relativistic velocities of  $\Gamma \sim 2-3$  in several systems (Mirabel & Rodriguez 1994; Fender 2001; Fender et al. 2004; Casella et al. 2010; Miller-Jones et al. 2012). Such a low initial magnetisation would struggle to explain the bulk acceleration of the flow unless further energy is available by, e.g. thermal pressure. However, numerical simulations

show that a jet “sheath” forms where the originally Poynting-flux dominated “spine” interacts and entrains the surrounding disc wind, resulting in a region with much lower magnetisation (McKinney 2006; Móscibrodzka et al. 2016; Nakamura et al. 2018; Chatterjee et al. 2019). The instabilities that form along this boundary are expected to be sites of reconnection and particle acceleration (Rieger & Duffy 2004; Faganello et al. 2010; Rieger 2019; Sironi et al. 2021). Thus, although our approach is quite simplistic, it would be consistent with the emission occurring along this boundary as suggested by recent radio observations of AGN jets, such as M87 (Hada et al. 2016) or Cen A (Janssen et al. 2021), and GRMHD simulations (e.g. Móscibrodzka & Falcke 2013; Davelaar et al. 2018). Although BHXB jets cannot be resolved by current facilities, similar scenarios may apply to them since the systems are likely to be governed by the same physical laws (Heinz & Sunyaev 2003; Merloni et al. 2003; Falcke et al. 2004).

### 3.5.2 Particle distributions

In Figures 3.6 and 3.7 we plot the total distribution of the primary electrons and protons, respectively, integrated along the jets. The MJ-only distribution at the jet base dominates the lower energy regime, with its peak defined by the free parameter  $T_e$  (see Table 3.3), while the higher energy electrons originate mostly at the first particle acceleration region  $z_{\text{diss}}$ . The shifting of the thermal peak between the two shows the effect of the  $f_{\text{heat}}$  parameter. The fact that the slope is steeper than  $p_e = 2$  indicates that the synchrotron cooling break occurs below  $\sim 10^9$  eV.

In Figure 3.8 we plot the differential number density of the secondary pairs from pp and p $\gamma$  for the lepto-hadronic model with  $p_p = 2.2$ . We also include for comparison the total distribution of the primary pairs of the jets. We note that the secondary pairs from p $\gamma$  are synchrotron cooled, and hence their spectrum is flat. The excess of particles around  $\sim 10^{12}$  eV is responsible for the TeV flux of Figure 3.4.

Assuming a maximum value of  $f_{\text{sc}} = 0.01$ , we see that the compact jets of GX 339–4 can accelerate CRs up to 100 TeV. Consequently, if this is true and moreover the entire population of BHXBs can accelerate CRs up to 100 TeV, then BHXBs may contribute to the Galactic CR spectrum up to the knee depending on their total number (see also Cooper et al. 2020).

### 3.5.3 Non-thermal proton power

The uncomfortably high proton powers needed for lepto-hadronic jet models has been a topic of discussion for many years (see e.g. Böttcher et al. 2013; Zdziarski & Böttcher 2015; Liodakis & Petropoulou 2020; Kantzas et al. 2020). As discussed in Section 3.5.1, given what we see in AGN jet observations and simulations, we would expect proton acceleration to happen primarily at the interface between the spine and

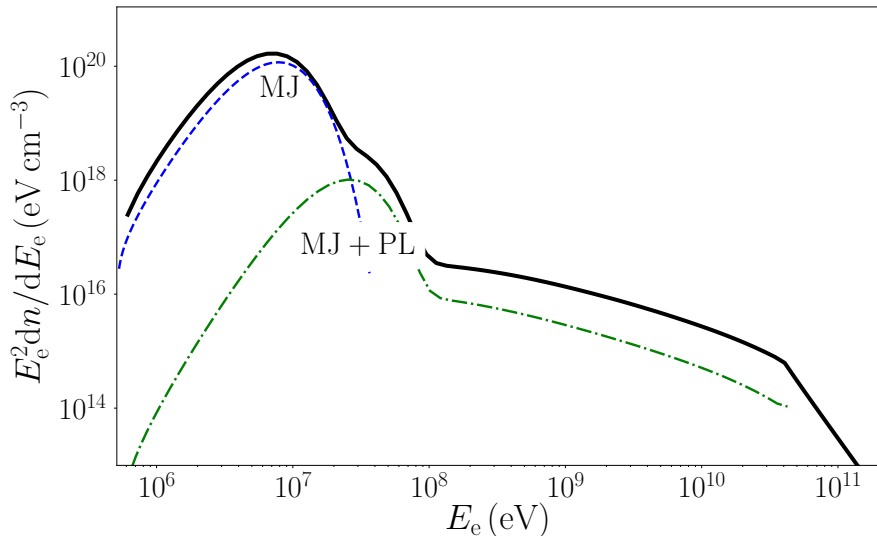


**Figure 3.6:** The total electron number density of the jets multiplied by the square of the electron energy for the leptonic model (solid black line) with  $p_e = 1.7$  and  $p_p = 1.7$  power-law index. We also show the contribution of the Maxwell-Jüttner distribution at the jet base (MJ; dashed blue line), and the contribution of the MJ plus the power-law tail of accelerated electrons (MJ+PL; dash-dotted green line) at the particle acceleration region  $z_{\text{diss}}$ .

the sheath of the jet, a region of limited volume (Rieger & Duffy 2019). In our current setup, as a first approximation, we can limit the volume where proton acceleration occurs by reducing the extent of this region with respect to the total jet length. In particular, similar to previous studies (Romero & Vila 2008; Vila & Romero 2010; Zhang et al. 2010; Pepe et al. 2015; Hoerbe et al. 2020), we terminate the proton acceleration at a distance  $10 z_{\text{diss}}$  from the region where acceleration initiates. As a consequence, we see that even for a hard power law index of  $p_p = 1.7$ , the TeV emission of GX 339–4 due to hadronic processes will not be detectable by CTA, but the energy budget remains within reasonable values.

A further way to constrain the total power of the accelerated protons is by increasing the minimum energy of the accelerated particles (Zdziarski & Böttcher 2015; Pepe et al. 2015). We nevertheless decide to use as the minimum energy for the accelerated leptons the peak of the MJ distribution and for the accelerated protons the rest mass energy (see Section 3.3), but will explore this in more detailed future work.

Recent high resolution magneto-hydrodynamic simulations have shown that jets can be significantly mass-loaded via instabilities at distances well beyond the launching point (Chatterjee et al. 2019). This progressive mass-loading could significantly



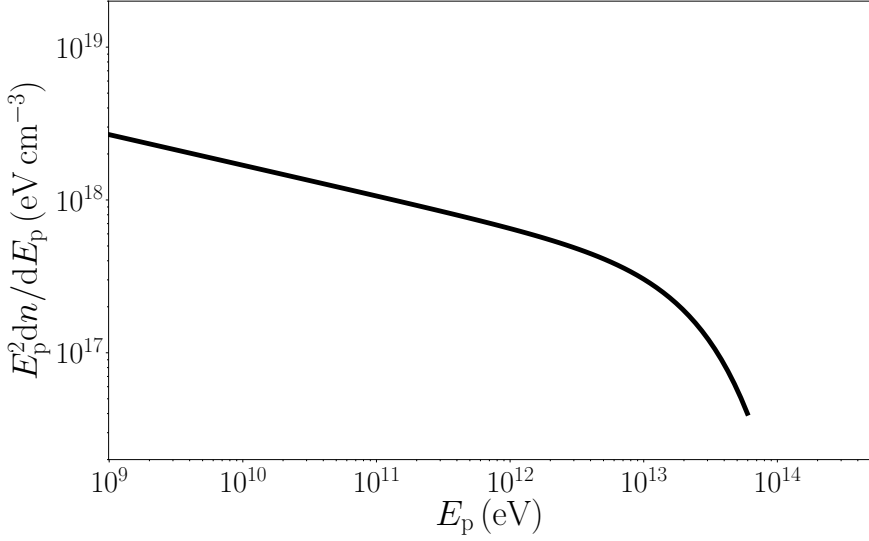


**Figure 3.7:** Similar to Figure 3.6 but for the population of protons for the lepto-hadronic model with  $p_e = 2.2$  and  $p_p = 2.2$  power-law indexes.

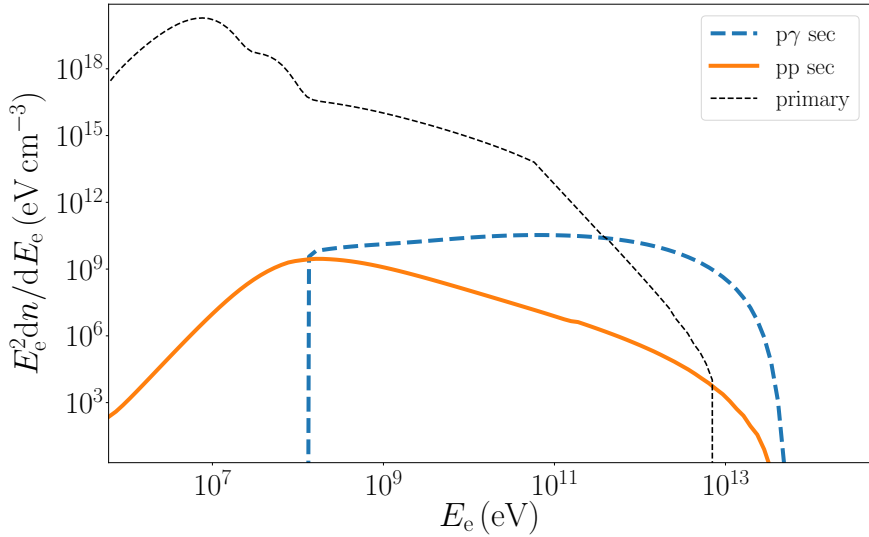


**Figure 3.8:** Similar to Figure 3.6 but for the secondary pairs of the lepto-hadronic model with  $p_e = 2.2$  and  $p_p = 2.2$ . We also plot the distribution of the primary electrons for comparison.

reduce the total proton power and make the hadronic models more viable, but this is a project we will pursue in the future.

### 3.5.4 $\gamma$ -ray attenuation on the optical/IR emission

In both lepto-hadronic models, the optical emission is produced in the jet base due to synchrotron emission from the thermal leptons. The GeV-to-TeV  $\gamma$ -ray emission on the other hand, is produced in the particle acceleration region and above, which is located at some distance of  $3000 r_g$  from the black hole, two orders of magnitude further away from the jet base. Moreover, the  $\gamma$ -ray is beamed away making it difficult for any attenuation on this optical emission. The IR emission of GX 339–4 is produced in the particle acceleration region where the  $\gamma$ -ray emission originates as well. We therefore examine any  $\gamma$ -ray attenuation on the IR emission.

We calculate the optical depth of a 3 TeV  $\gamma$ -ray that has the maximum likelihood to interact with the  $\sim 0.08$  eV IR emission using Equation 16 of Mastichiadis (2002):

$$\tau_{\gamma\gamma} = \frac{R_{\text{diss}}}{4\pi} \int \epsilon_{\text{ph}} n_{\text{ph}}(\epsilon_{\text{ph}}) \int d\Omega (1 - \cos\theta) \sigma_{\gamma\gamma} \approx 10^{-8}, \quad (3.6)$$

where  $\epsilon_{\text{ph}}$  is the target photon energy and  $n_{\text{ph}}$  is the target photon number density of the particle acceleration region. Such a small values indicates that the particle acceleration region is optically thin to TeV  $\gamma$ -rays.

### 3.5.5 $\gamma$ -rays from BHXBs

Despite the fact that GX 339–4 is considered a 'canonical' low-mass BHXB, it is also amongst the most distant ones. There are Galactic low-mass BHXBs that are as close as approximately 1 to 3 kpc, e.g. GRO J0422+32 (Webb et al. 2000; Gelino & Harrison 2003; Hynes 2005), XTE J1118+480 (Gelino et al. 2006; Hernández et al. 2008), XTE J1650–500 (Homan et al. 2006; Orosz et al. 2004), GRO J1655–40 (Hjellming & Rupen 1995; Shahbaz et al. 1999; Beer & Podsiadlowski 2002), GRS 1716–249 (Remillard & McClintock 2006), GS 2000+251 (Casares et al. 1995; Barret et al. 1996; Harlaftis et al. 1996), V404 Cyg (Miller-Jones et al. 2009), VLA J2130+12 (Kirsten et al. 2014; Tetarenko et al. 2016a), Swift J1357.2–0933 (Shahbaz et al. 2013; Torres et al. 2015), MAXI J1348–630 (Chauhan et al. 2020) and many more at unknown distances that might also be as low as 2–3 kpc (see Liu et al. 2007; Kreidberg et al. 2012; Tetarenko et al. 2016b).

For this reason we also check whether some BHXBs at a distance of 3 kpc with the same  $\gamma$ -ray luminosity and spectrum as GX 339–4 could be detected by CTA. Assuming that the jets in this putative source have identical properties to GX 339–4, the  $\gamma$ -ray flux of a nearer source scales as  $(d_{\text{GX 339-4}}/d_{\text{source}})^2 F_{\gamma}$ , where  $d_{\text{GX 339-4}}$  and  $d_{\text{source}}$  are the distances of GX 339–4 and the source, respectively, and  $F_{\gamma}$  is the  $\gamma$ -ray flux of GX 339–4. We plot this  $\gamma$ -ray flux in Figure 3.9 and compare it to the

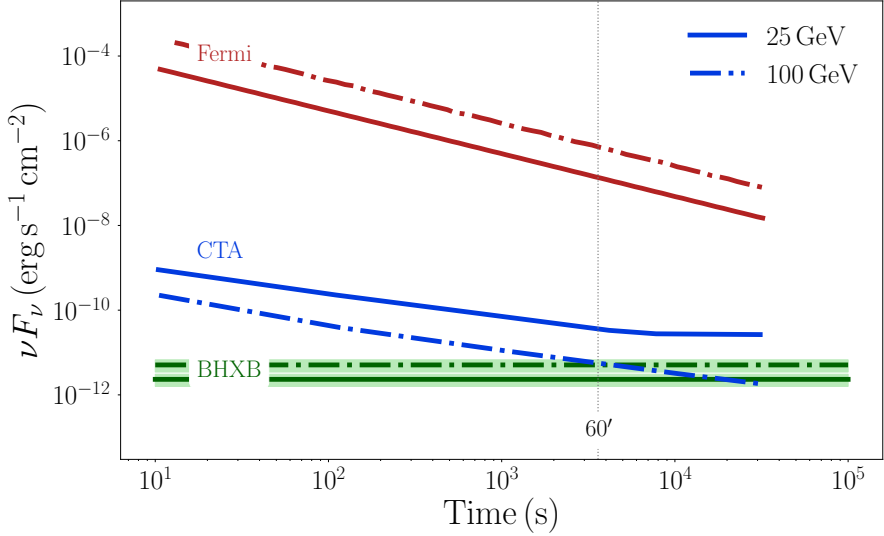


**Figure 3.9:** The  $\gamma$ -ray light curves in two energy bins as indicated in the legend. The horizontal green lines indicate the predicted flux of a BHXB with the same luminosity as GX 339–4 but located at a distance of 3 kpc instead. We assume that the accelerated particles follow a power-law with index  $p_e=1.7$  and  $p_p=1.7$ , and the emitted flux remains constant for one day. CTA can detect such a GeV emission within the first hour of the outburst, but *Fermi*/LAT is not sensitive enough to detect such an outburst.

simulated sensitivity of CTA for various energies, as a function of observation time.<sup>1</sup> The energy range we study here coincides with the energy range of *Fermi*/LAT which as we can see in Figure 3.9 is orders of magnitude less sensitive than CTA for short integration times. We assume that the  $\gamma$ -ray flux remains constant for up to one day and its uncertainty is of the order of 30 per cent. We see CTA is sensitive enough to detect the 100 GeV emission of a GX 339–4-like source at 3 kpc distance, with an exposure of approximately one hour, assuming the emission remains persistent for that long. Consequently, CTA should be able to detect GeV  $\gamma$ -rays from several future bright outbursts of nearby Galactic BHXBs assuming that the accelerated particles form hard spectra within the relativistic jets produced at peak hard/hard-intermediate states.

We finally examine a more specific example, in particular that of MAXI J1820+070, which is at 2.96 kpc (Gandhi et al. 2019; Atri et al. 2020). During its outburst in 2018, the source was monitored across the multi-wavelength spectrum, from radio to X-rays (Tucker et al. 2018). Here, we merely benchmark the spectral energy distribu-

<sup>1</sup><https://www.cta-observatory.org/science/ctao-performance/>

tion instead of optimising to determine the best fit, with the goal of illustrating the similarities and differences with our results on GX 339–4. We use the radio-to-X-ray spectrum, as presented by (Tetarenko et al. 2021). We set the black hole mass at  $8.5 M_{\odot}$  (Torres et al. 2020), the inclination angle at  $63^{\circ}$  and the injected jet power at 15 per cent of the Eddington luminosity (Atri et al. 2020). We take the same model parameters we found for the best fit of GX 339–4 for the case of  $p_e = p_p = 1.7$  and present the spectral energy distribution of the 2018 outburst in Figure 3.10 and 3.11. We see that the radio-to-X-ray spectrum is similar to the one of GX 339–4, namely the radio spectrum is due to non-thermal synchrotron radiation, the optical band is due to thermal synchrotron in agreement with Tetarenko et al. (2021) (although see Veledina et al. 2019 for further contributors), and the X-ray spectrum is due to a thermal corona. In contrast to GX 339–4, the  $p\gamma$  emission exceeds the CTA sensitivity in the sub-TeV regime. We further compare our predicted spectrum in Figure 3.11 to the upper limits set by Fermi/*LAT* and the Cherenkov telescopes MAGIC, VERITAS and H.E.S.S. (Hoang et al. 2019). We see that the predicted emission exceeds the upper limits of H.E.S.S. and marginally those of VERITAS, but it is worth mentioning that these upper limits are derived after 26.9 and 12.2 h, respectively (Hoang et al. 2019). We are unable to capture the timing signature of the TeV emission with the current version of our model, but we moreover do not know yet whether the high-energy emission of these sources is persistent for up to 20–30 h (Bodaghee et al. 2013). If MAXI J1820+070’s TeV emission persists for at least a couple of hours during its next outburst, it could then be a possible target-of-opportunity for CTA. Moreover, based on the population-synthesis results of Olejak et al. (2020) and on the recent X-ray observations of Hailey et al. (2018) and Mori et al. (2021), Cooper et al. (2020) estimated that a few thousands BHXBs may reside in the Galactic disc capable of accelerating protons to high energy (also see Fender et al. 2005). If these sources spend approximately 1 per cent of their outburst in the hard to hard-intermediate state (Tetarenko et al. 2016b), then CTA might be able to detect a few tens of BHXBs in its first years of operation.

In our current analysis, we assume equal number density of electrons and protons in the jets, similar to previous studies (Vila & Romero 2010; Connors et al. 2019). Following this assumption, we derive the jet kinetic power to be  $2 \times 10^{37} \text{ erg s}^{-1}$ . Tetarenko et al. (2021) though suggest that the jets of MAXI J1820+070 cannot be proton dominated and constrain the ratio of protons to positrons to be  $\sim 0.6$  otherwise the jet kinetic power, which they estimate to be  $6 \times 10^{37} \text{ erg s}^{-1}$ , may reach 18 times the accretion power. We aim to further study the impact of the pair-to-proton ratio to jet evolution and emission in a forthcoming work.

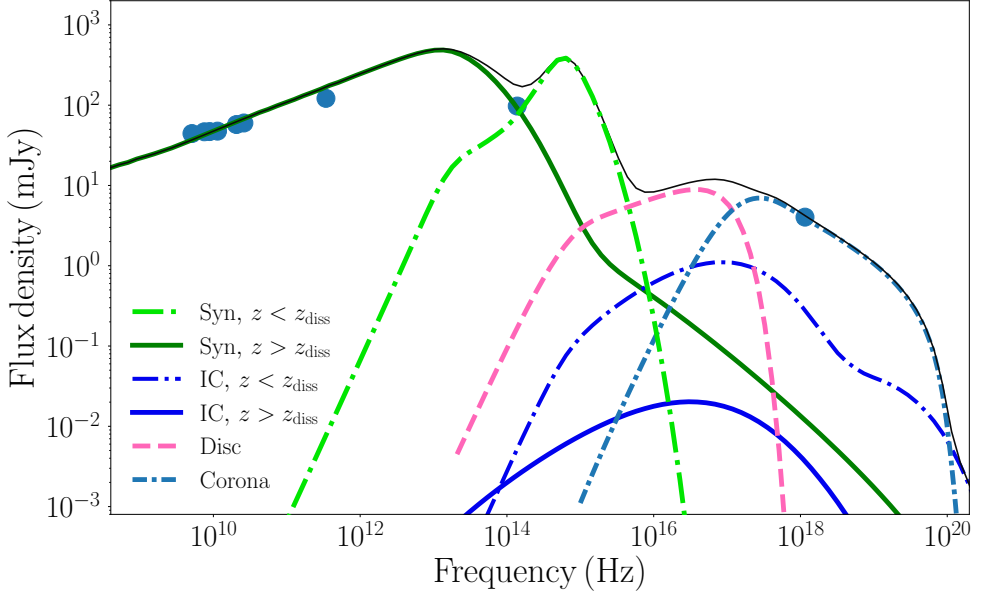


**Figure 3.10:** The predicted flux density based on the lepto-hadronic scenario with  $p_p=1.7$  for the 2018 outburst of MAXI J1820+070. We compare the total emitted spectrum to the data of Tetarenko et al. (2021). The rest of the components are the same as in Figure 3.1.

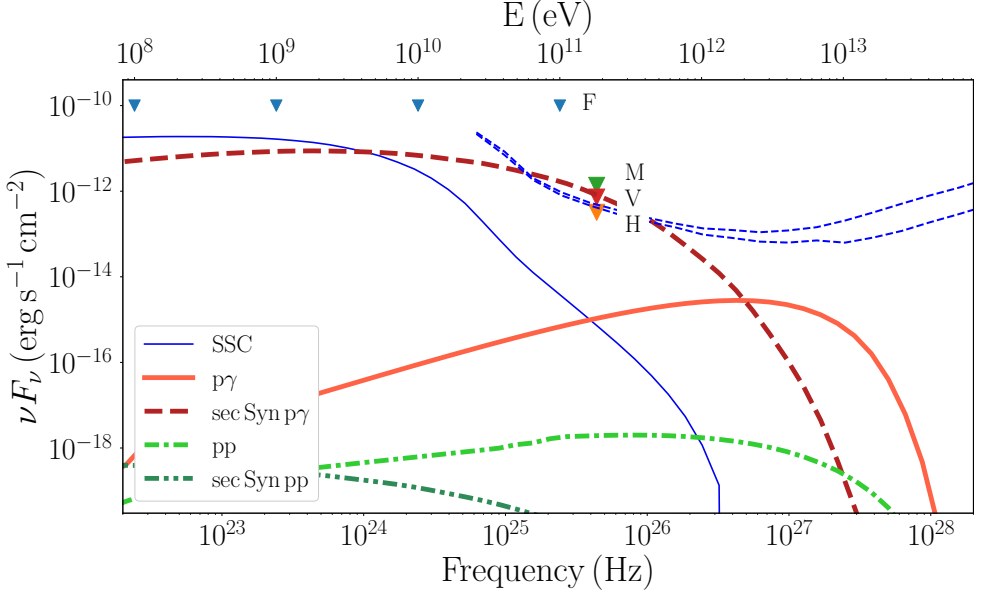


**Figure 3.11:** The spectral energy distribution based on the lepto-hadronic scenario with  $p_p=1.7$  for the 2018 outburst of MAXI J1820+070. We compare the total emitted spectrum to the upper limits of *Fermi*/LAT (F), MAGIC (M), VERITAS (V) and H.E.S.S. (H) from Hoang et al. (2019), and the predicted 50-hour sensitivity of the North and South site of CTA (from [www.cta-observatory.org](http://www.cta-observatory.org)). The rest of the components are the same as in Figure 3.4.

## 3.6 Summary and Conclusions

Astrophysical jets are ideal laboratories to understand the underlying physics of particle acceleration and the physical processes responsible for the non-thermal emission. It is still unclear whether BHXB jets can accelerate particles to high enough energy to shine in the  $\gamma$ -ray regime of the electromagnetic spectrum. Such emission strongly depends on the composition of the jets, which remains poorly constrained for either Galactic or extragalactic jets. A possible hadronic composition would support BHXB jets as candidate sources of Galactic CRs and shed light on this long-standing open question. Understanding the jet composition is clearly crucial not only for a better understanding of the non-thermal radiation and total power requirements, but also for our understanding of the jet launching and bulk acceleration properties.

To further understand the properties of Galactic jets and predict any TeV signature, we studied the ‘canonical’ low-mass BHXB GX 339–4 during the bright outburst of 2010. We presented the best fit of our jet model to the multiwavelength emission and found that the whole radio-to-GeV electromagnetic spectrum can be due to primary leptonic processes. To explain both the radio and the IR/Optical bands, we require a heating mechanism similar to what we see in PIC simulations (Sironi & Spitkovsky 2009, 2011; Crumley et al. 2019). We further found that the jets of GX 339–4 can accelerate protons to a non-thermal power law up to a few hundreds of TeV. Depending on the power-law index, we saw that the accelerated protons can produce a strong TeV emission via neutral pion decay and synchrotron radiation of secondary pairs. In the case of a hard power law of protons in particular, we found that the photomeson processes dominate the pp interactions and the synchrotron emission of secondary pairs dominates the sub-TeV band.

GX 339–4 is, however, a distant source, located at 8 kpc and the predicted TeV flux will not be strong enough to be detected by future  $\gamma$ -ray facilities, such as CTA. We rescaled the emitted spectrum to a distance of 3 kpc and compared it to the predicted timing sensitivity of CTA. We find that CTA would be able to detect such emission with an hour of integrated observations in the energy range above 100 GeV, which would be an indication that protons are accelerated into a hard power law. We further tested this scenario by bench-marking the electromagnetic spectrum of a nearby source, such as the newly discovered BHXB MAXI J1820+070. We found that this source might be a potential target-of-opportunity for future CTA observations to hint BHXBs as TeV sources and CR accelerators.

## Acknowledgements

We would like to thank K. Chatterjee for many fruitful conversations on jet physics and A. López-Oramas for the insightful discussion on  $\gamma$ -ray Astronomy. DK, SM and

ML are grateful for support from the Dutch Research Council (NWO) VICI grant (no. 639.043.513). CC acknowledges support from the Swedish Research Council (VR). R.M.T.C acknowledges support from NASA grant NNG08FD60C. This research made use of `ASTROPY` (<http://www.astropy.org>), a community-developed core `PYTHON` package for Astronomy (Astropy Collaboration et al. 2013; Price-Whelan et al. 2018), `MATPLOTLIB` (Hunter 2007), `NUMPY` (Oliphant 2006), `SCIPY` (Virtanen et al. 2020), `ISIS` functions (`ISISscripts`) provided by ECAP/Remeis observatory and MIT (<http://www.sternwarte.uni-erlangen.de/isis/>), and the CTA instrument response functions provided by the CTA Consortium and Observatory (see <https://www.cta-observatory.org/science/ctao-performance/> for more details).

## Data availability

All observational data in this paper are publicly available (see Table 3.1). The output of our model and the plotting scripts are available in Zenodo, at <https://dx.doi.org/>

## 3.A Proton characteristic timescales

In Figure 3.12 we show the characteristic cooling timescales of synchrotron, escape,  $p\bar{p}$  and  $p\gamma$  for the accelerated protons inside the jets, in comparison to the acceleration timescale. When any of the energy-loss timescales intersects the acceleration timescale we derive the maximum proton energy for every jet segment. The residence timescale is the one that defines the maximum proton energy inside the jets.

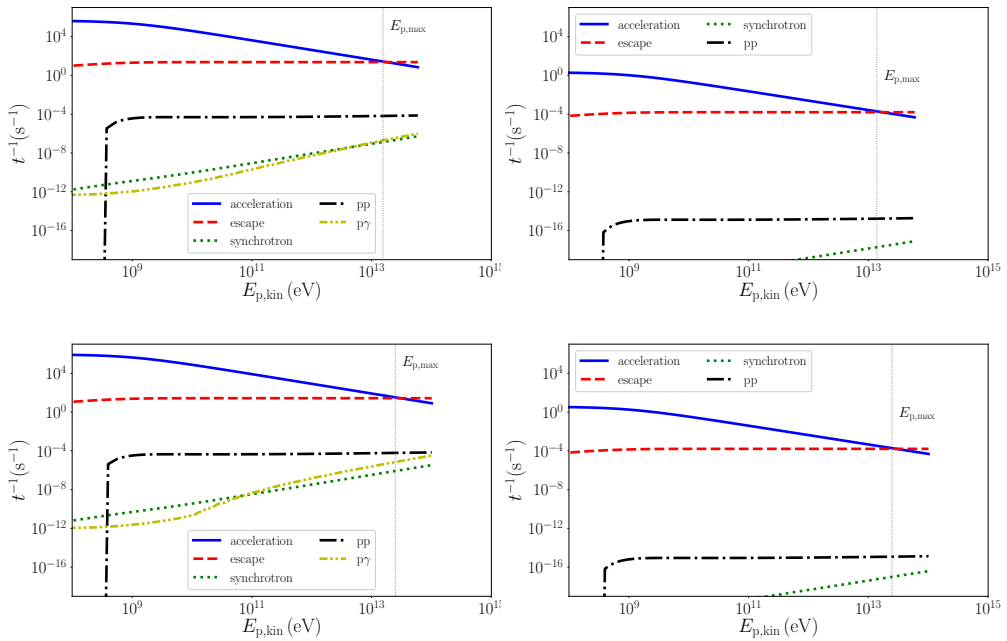


**Figure 3.12:** The inverse of the characteristic timescales for various physical processes in the jets as indicated by the legend versus the proton kinetic energy. The *top* plots correspond to a power-law index of  $p_p = 2.2$  and the *bottom* plots correspond to a power-law index of  $p_p = 1.7$ . The *left* plots correspond to the particle acceleration region and the *right* plots to the final jet segment. The vertical line in each plot shows the maximum energy.



## Exploring neutrino and cosmic ray production in X-ray binary jets using multi-wavelength case studies

D. Kantzas, S. Markoff, A. J. Cooper, D. Gaggero, M. Petropoulou & P. De La Torre Luque

*To be submitted to Monthly Notices of the Royal Astronomical Society*

### *Abstract*

For over a century, the identification of the high-energy cosmic ray (CR) sources remains one of the persistent mysteries in astroparticle physics. For the Galactic CRs with energy up to  $10^{15}$  eV in particular, supernova remnants (SNRs) have traditionally been thought to be the main candidate source. However, recent TeV  $\gamma$ -ray observations of HAWC, LHAASO and Tibet AS $_{\gamma}$  have questioned the SNR paradigm. Propagating CRs are deflected by the Galactic magnetic field, making it impossible for us to trace back their origin. For this reason,  $\gamma$ -rays and neutrinos produced via inelastic hadronic interactions are necessary to hint at the CR sources. In this work, we study the  $\gamma$ -ray and neutrino emission produced by CRs accelerated inside Galactic jets of stellar-mass black holes in X-ray binaries (BHXBs). We calculate the intrinsic neutrino emission of two prototypical BHXBs, Cygnus X-1 and GX 339-4, for which we have multiwavelength spectra. Based on these prototypical sources, we discuss the likelihood of the 35 known BHXBs to be efficient CR accelerators. Moreover, we calculate the potential contribution to the CR spectrum of a viable population of BHXBs that reside in the Galactic plane, but remain in X-ray quiescence. When these BHXBs go into outburst, they may accelerate particles to 100s of TeV that contribute to the diffuse  $\gamma$ -ray and neutrino spectra while propagating in the Galactic

medium. Using **HERMES**, an open-source code that calculates the hadronic processes along the line of sight, we discuss the contribution of BHXBs to the diffuse  $\gamma$ -ray and neutrino spectra, and compare this to their intrinsic  $\gamma$ -ray and neutrino emission. Finally, we discuss whether BHXBs can be significant sources of the observed spectrum of Galactic CRs.

## 4.1 Introduction

For more than a hundred years, the origin of cosmic rays (CRs) remains an unsolved mystery. CRs are accelerated atomic nuclei of extraterrestrial origin that populate a power law that covers more than ten orders of magnitude in energy. Energetic protons of Galactic origin dominate the low-energy regime of the CR spectrum that shows a break at around 1 PeV ( $10^{15}$  eV), known as the “knee”. The CR composition beyond the “knee” is not certain, but it is likely that the CR spectrum becomes dominated by heavier elements at the highest energy regime up to the “ankle” feature at around 1 EeV ( $10^{18}$  eV; Buitink et al. 2016). Beyond the “ankle”, different experiments favour different CR composition, and it is not clear yet whether CRs are proton or iron dominated (Abbasi et al. 2010; Abu-Zayyad et al. 2013; Aab et al. 2014).

The astrophysical sources capable of accelerating CRs up to (and beyond) 1 PeV are the so-called PeVatrons. Based on energetic arguments, supernovae (SNe) and young supernova remnants (SNRs) in particular, have so-far been considered the dominant candidate sources of Galactic CRs (Baade & Zwicky 1934; Ginzburg & Syrovatskii 1964; Hillas 1984; Blasi 2013). When CRs are accelerated in the SN/SNR shock front, they interact with the ambient medium to initiate inelastic collisions that will lead to the formation of secondary particles, such as  $\gamma$ -rays and neutrinos (Stephens & Badhwar 1981; Dermer 1986; Berezhinsky 1991; Mannheim 1993; Mannheim & Schlickeiser 1994; Rachen & Mészáros 1998; Aharonian & Atoyan 2000; Blattnig et al. 2000; Mücke et al. 2003). These secondary  $\gamma$ -rays carry energy that is approximately one tenth of the energy of the primary protons. If CRs were accelerated up to PeV energies, we would hence expect to observe SNe and SNRs up to ultra-high energies above 100 TeV. Current TeV observations however show that SNRs exhibit a softening or even a cutoff in the  $\gamma$ -ray spectrum before the  $\sim$  hundreds of TeV regime (Aharonian et al. 2006b, 2007a,b, 2009; Abramowski et al. 2011, 2014; Ackermann et al. 2013; Archambault et al. 2017). Such a spectral feature questions the SN paradigm, and hence theoretical and observational investigation into new candidate sources are ongoing.

Recent TeV  $\gamma$ -ray observations show that various other Galactic sources can accelerate particles up to TeV, and PeV energies. Clusters of young massive stars (Ackermann et al. 2011; Abramowski et al. 2012; Aharonian et al. 2019), pulsars (H.E.S.S. Collaboration et al. 2018b; MAGIC Collaboration et al. 2020), pulsar wind nebulae (Amenomori et al. 2019; López-Coto et al. 2022),  $\gamma$ -ray binaries (Aharonian et al. 2005; Hinton et al. 2008) are among the prime examples of capable sources. The latest observations of the Galactic plane from HAWC (Albert et al. 2020), LHAASO (Cao et al. 2021a) and Tibet-AS $_{\gamma}$  (Amenomori et al. 2021) found no association with SNRs and suggest the existence of numerous sources capable of producing  $\gamma$ -ray emission beyond 1 PeV with the aforementioned sources being in the list, as well as many of yet unknown nature.

The relativistic jets launched by stellar-mass black holes in X-ray binaries also shine up to  $\gamma$ -rays. Cygnus X-3 and Cygnus X-1 (Cyg X-1) are known to emit GeV radiation (Tavani et al. 2009; Sabatini et al. 2013; Malyshev et al. 2013; Zanin et al. 2016), but it remains unclear whether the origin of this emission is due to the acceleration of electrons (Zdziarski et al. 2014a) or protons (Pepe et al. 2015). There is no persistent TeV emission detected yet from these two sources (Albert et al. 2020, 2021), making it impossible to argue against or in favour of any proton acceleration in their jets. The well-known case of SS433 was moreover the first BH-candidate found to emit in the TeV regime with its jets to be potential acceleration sites (Abeysekara et al. 2018).

As expected in large-scale jets of Active Galactic Nuclei (AGN), when protons accelerate to high energies above a few PeV, they also produce astrophysical neutrinos and antineutrinos via inelastic collisions that carry energy of the order of 1 TeV–1 PeV (Murase et al. 2014; Petropoulou et al. 2015; Aartsen et al. 2018; Keivani et al. 2018). Astrophysical neutrinos are hence the smoking gun of CR acceleration. The current state-of-the-art neutrino detectors IceCube and ANTARES, in the South Pole and the Mediterranean Sea respectively, have not so far confirmed the Galactic origin of any neutrino to favour any particular source as a potential PeV accelerator (PeVatron; Aartsen et al. 2020). The diffuse neutrino observations seem to be isotropic, implying that extragalactic sources significantly contribute to the detected spectrum at these energies. The accumulated data after ten years of operation of the IceCube experiment, as well as the expected data from the next-generation facilities, such as KM3NeT/ARCA (Aiello et al. 2019) and IceCube-Gen2 (IceCube-Gen2 Collaboration et al. 2014; Aartsen et al. 2021), offer a unique opportunity to set new constraints on individual sources and allow for further understanding of the sources of high-energy CRs.

In this work, we revisit the idea of BHXBs being Galactic CR sources and hence potential neutrino sources. BHXBs have been suggested as neutrino sources in the past (Levinson & Waxman 2001; Romero et al. 2003; Romero & Orellana 2005; Torres et al. 2005; Bednarek et al. 2005; Romero & Vila 2008; Reynoso et al. 2008; Zhang et al. 2010; Carulli et al. 2021; Cooper et al. 2020) but were neglected for numerous years, mainly due to lack of  $\gamma$ -ray and neutrino observations. In this work, we tie the multiwavelength emission of BHXB jets to the dynamical properties of the acceleration site, and hence we can self-consistently predict the neutrino counterpart. We use, in particular, the multi-zone jet model of Kantzas et al. (2020, hereafter K20) that accounts for acceleration of both leptons and hadrons. The leptons accelerate to non-thermal energies to emit synchrotron radiation along the jets, being able to reproduce the flat-to-inverted radio spectra detected by multiple BHXBs (Blandford & Königl 1979; Hjellming & Johnston 1988; Falcke & Biermann 1995; Markoff et al. 2001, 2005; Lucchini et al. 2022). The accelerated protons interact inelastically with protons in the bulk flow and the jet radiation to produce secondary particles via in-

elastic proton-proton (pp) and proton-photon ( $p\gamma$ ) collisions that contribute to the high-energy regime of the spectrum. We further develop this particular jet model to account for the intrinsic neutrino counterpart due to the above processes.

The increasing number of newly discovered BHXBs, which may not be bright enough to be detected in the  $\gamma$ -ray regime, makes the BHXB population a viable candidate to contribute to the Galactic neutrino spectrum, and hence the CR spectrum. In particular, recent X-ray observations of the Galactic centre suggest the existence of hundreds-to-thousands of BHXBs in the pc-scale of the Galactic centre (Hailey et al. 2018; Mori et al. 2021). Based on these observations, Cooper et al. (2020, hereafter C20) suggest that of the order of a few thousands of BHXBs suffice to contribute significantly to the CR spectrum, and possibly dominate the spectrum slightly above the “knee”, before the transition to the extragalactic origin. In this work, we further investigate the contribution of BHXBs to the CR spectrum, utilising a physical jet model that we better constrain with the multiwavelength observations of BHXBs, such as Cyg X-1 (K20) and GX 339-4 (K22). In particular, we use the up-to-date BHXB WATCHDOG catalogue of Tetarenko et al. (2016b) to study the possibility of the intrinsic neutrino emission of these sources to contribute to the observed spectrum, and discuss the likelihood of future facilities, such as KM3NeT/ARCA, to be able to detect any Galactic neutrinos from BHXBs. We further study the contribution of these sources to the CR spectrum when the accelerated CRs escape the acceleration sites and propagate through the interstellar medium towards Earth. We finally discuss the interaction of the propagated CRs with the intergalactic medium to produce diffuse  $\gamma$ -rays and neutrinos.

In Section 4.2, we discuss the jet model we utilise to produce the intrinsic neutrino fluxes, that we present in Section 4.3 for the known BHXBs. In Section 4.4, we present our analysis for a population of 1000 BHXBs, in Section 4.5 we discuss the contribution of BHXBs to the CR spectrum, and in Section 4.6 we summarise our results and conclude.

## 4.2 Neutrinos from BHXB jets

In this work, we use a physical jet model based on work presented in Markoff et al. (2005) that explains the flat radio spectrum detected in BHXBs (see, e.g., Corbel & Fender 2002; Fender et al. 2000, 2009). In a multizone stratified jet, particles accelerate to non-thermal energies to emit in the multiwavelength spectrum from radio to X-rays (Blandford & Königl 1979; Falcke & Biermann 1995; Markoff et al. 2001, 2003, 2005; Corbel et al. 2013; Russell et al. 2019; Tetarenko et al. 2021; Cao et al. 2021b). The population of primary leptons accelerates along the jets into a power-law distribution in energies and emit non-thermal synchrotron radiation that is further upscattered to higher energies (Markoff et al. 2005; Lucchini et al. 2018,

2022). K20 included for the first time hadronic acceleration along the jets to account for the inelastic  $pp$  and  $p\gamma$  interactions that lead to the formation of secondary electrons/positrons and  $\gamma$ -rays. In this work, we further self-consistently calculate the neutrino distributions that form due to the above interactions, as we describe below.

### 4.2.1 Jet dynamics and particle acceleration

In this work, we use the multizone jet model as described in Markoff et al. (2005); Crumley et al. (2017) and K20, but we briefly discuss the basic assumptions here for consistency. In particular, during the so-called hard X-ray spectral state, BHXBs launch bipolar, mildly relativistic and collimated jets. We assume the jets are launched at some height from the black holes, assuming a thermal electron/positron and cold proton composition. We do not account for any particular jet launching mechanism, as both Blandford-Znajek (Blandford & Znajek 1977) and Blandford-Payne (Blandford & Payne 1982) are viable. We assume that the leptonic population of the jet base follows a Maxwell-Jüttner distribution that is characterized by its peak temperature. The two particle distributions share the same number density, which we calculate assuming particle-number conservation along the jets. Finally, we calculate the bulk velocity profile of the jets, as well as the magnetic energy density, by solving the 1D relativistic Bernoulli equation along the jet axis (Königl 1980; Crumley et al. 2017; Lucchini et al. 2022).

Whereas the particle distributions are thermal at the jet base and remain thermal for some distance from the launching point, we assume that a fraction of them accelerates in a power-law at some specific distance  $z_{\text{acc}}$  from the black hole. We assume that particles are accelerated up to some maximum energy that we calculate self-consistently by equating the acceleration timescale to the radiation loss timescales (Markoff et al. 2005). The power-law index of the non-thermal particles has been the subject of much research over decades, and it strongly depends on the nature of the acceleration site and the acceleration mechanism. Using a simple jet model we cannot capture the exact acceleration mechanism, we hence take the power-law index  $p$  to be a free parameter. We examine in particular two different cases, first assuming a soft power-law index of  $p = 2.2$ , and compare it to a harder one with  $p = 1.7$ . We choose these two more extreme values as they could represent different acceleration mechanisms, where the soft case may favour a diffusive shock acceleration (Drury 1983; Malkov & Drury 2001; Sironi & Spitkovsky 2009; Caprioli 2012; Caprioli & Spitkovsky 2014a; Park et al. 2015) and the hard case magnetic reconnection (Sironi & Spitkovsky 2014; Guo et al. 2014, 2016; however, see Petropoulou & Sironi 2018). Finally, we assume for simplicity that both electrons and protons accelerate into distributions with the same power-law index.

### 4.2.2 Lepto-Hadronic Processes

We refer the interested reader to Lucchini et al. (2022) for a detailed description of how we calculate the leptonic radiative processes; i.e., the cyclo-synchrotron emission of either thermal or non-thermal leptons, as well as inverse Compton scattering (ICS). In this work, we describe only the hadronic processes which are responsible for the neutrino counterpart and CR acceleration.

When protons accelerate to high energy, they can interact with the bulk flow and the associated radiation to initiate particle cascades that lead to the formation of secondary electrons/positrons,  $\gamma$ -rays and neutrinos (Rachen & Biermann 1993; Mannheim 1993; Mannheim & Schlickeiser 1994; Rachen & Mészáros 1998; Mücke et al. 2003). An alternative hadronic contribution to the electromagnetic spectrum is when accelerated protons emit synchrotron radiation (Aharonian 2002; Böttcher et al. 2013).

In this work, we self-consistently calculate the neutrino distributions as they emerge from the inelastic pp collisions following the semi-analytical formalism of Kelner et al. (2006). We account for both the bulk thermal protons of the flow and the cold protons of the stellar wind of the companion, where we find that the former is the dominant target population even for the case of high-mass BHXBs (K20). We use the cross-section of the pp interactions based on Kafexhiu et al. (2014):

$$\sigma_{pp}(T_p) = \left[ 30.7 - 0.96 \log \left( \frac{T_p}{T_{\text{thr}}} \right) + 0.18 \log^2 \left( \frac{T_p}{T_{\text{thr}}} \right) \right] \times \left[ 1 - \left( \frac{T_{\text{thr}}}{T_p} \right)^{1.9} \right]^3 \text{ mb}, \quad (4.1)$$

where  $T_p$  is the proton kinetic energy in the laboratory frame and  $T_{\text{thr}} = 2m_\pi + m_\pi^2/2m_p \simeq 0.2797 \text{ GeV}$  is the threshold for pp interaction to take place. The formalism of Kelner et al. (2006) leads directly to steady state distributions of secondary electrons/positrons,  $\gamma$ -rays and neutrinos; assuming that intermediate unstable charged muons and pions immediately decay without radiating. This is an accurate approximation as long as the maximum energy (or Lorentz factor  $\gamma_p$  in fact) of the initial accelerated protons fulfils the criterion (Böttcher et al. 2013):

$$\gamma_p \ll \begin{cases} 7.8 \times 10^{11}/B & \text{for pions} \\ 5.6 \times 10^{10}/B & \text{for muons,} \end{cases} \quad (4.2)$$

where  $B$  is the strength of the magnetic field in the jet rest frame in units of Gauss. In the case of BHXBs where the magnetic field does not exceed the  $10^5 \text{ G}$  at the particle acceleration region, and the maximum proton energy far beyond  $\sim \text{PeV}$  ( $\gamma_p \simeq 10^6$ ), we find that these two inequalities are always satisfied.

The accelerated protons in the jet can also interact with the intrinsic radiation in the jet flow, and in particular with the X-ray photons emitted as synchrotron

radiation of the primary electrons. We account for this inelastic  $p\gamma$  interactions that lead to the formation of secondary electrons/positrons,  $\gamma$ -rays and neutrinos. We follow the semi-analytical formalism of Kelner & Aharonian (2008). Similar to the  $pp$  interactions, we see that the synchrotron radiation of the charged muons and pions is insignificant.

In Section 4.3 we present the distributions of muon and electron neutrinos and anti-neutrinos from both  $pp$  and  $p\gamma$  interactions, and discuss the contribution of each distribution.

### 4.2.3 Electromagnetic spectrum

In this work, we only present the neutrino distributions from  $pp$  and  $p\gamma$ . We calculate the electromagnetic counterpart self-consistently, and use it to constrain the jet parameters and consequently the proton acceleration that leads to the  $pp$  and  $p\gamma$  interactions. We use the electromagnetic emission of the canonical high-mass BHXB Cyg X-1 (K20), and the canonical low-mass BHXB GX 339-4 (Kantzas et al. 2022, hereafter K22), as we show in Fig. 4.1 to produce representative neutrino distributions. As we discuss above, the different acceleration mechanisms may lead to different power-law indexes, so we choose to examine two different cases similar to K20 and K22. In particular, we study the case where the accelerated proton populate a soft power law with  $p = 2.2$ , and compare it to a harder power law with  $p = 1.7$ . The former case of  $p = 2.2$  explains well the flat-to-inverted radio spectrum, but recent results on modelling the spectral energy distribution of Cyg X-1 (see, e.g., Zdziarski et al. 2017; K20) suggest that a hard power law of accelerated electrons is necessary to explain the polarized emission in the MeV band as detected by *INTEGRAL* (Laurent et al. 2011; Jourdain et al. 2012; Rodriguez et al. 2015; Cangemi et al. 2021). Due to lack of similar observations on further sources, however, we examine both cases similar to K20 and K22.

## 4.3 Intrinsic neutrino emission

In this section, we present the further developments of the jet model to incorporate the intrinsic neutrino emission of both high-mass and low-mass BHXBs. For the former, we base our analysis on the case study of Cyg X-1 (K20), whereas for the latter, we base our analysis on the canonical source GX 339-4 (K22).

### 4.3.1 Neutrino emission from Cyg X-1

In Figure 4.2 we plot the integrated neutrino energy flux along the jets of Cyg X-1, for both muon neutrinos/antineutrinos (left), and electron neutrinos/antineutrinos (right). In all panels, we highlight the contribution of  $pp$  and  $p\gamma$  interactions to



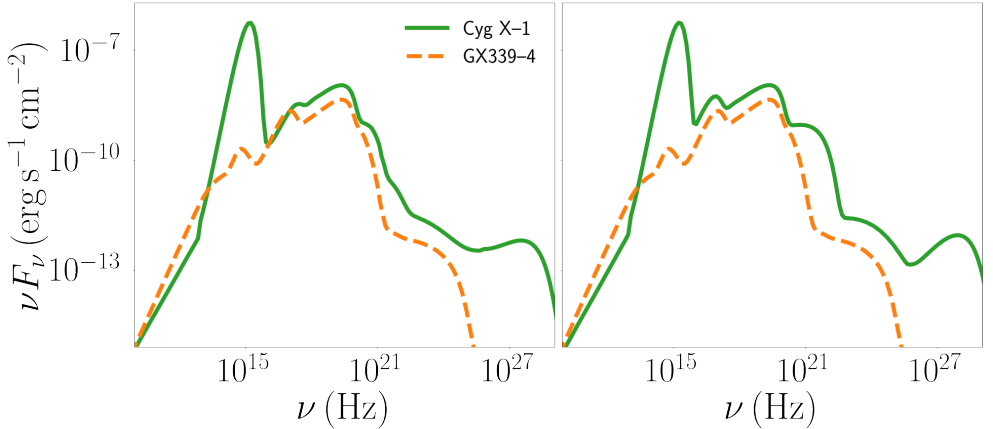


**Figure 4.1:** The predicted multiwavelength energy spectra of Cyg X-1 and GX 339-4 (see K20 and K22, respectively). In the *left* panel we show the soft case where the non-thermal particles accelerate in a power-law with index  $p = 2.2$ , and in the *right* panel we show the hard case where  $p = 1.7$ .

disentangle the contribution of each process in the GeV-PeV regime.

In all four panels, we see that the pp-initiated neutrinos form a power law that follows the parent power law of protons. In particular, they share the same slope that exceeds to some maximum energy that is approximately one tenth of the maximum proton energy. The p $\gamma$  neutrinos, on the other hand, form a distribution that peaks close to the maximum energy, which once again is approximately one tenth of the maximum proton energy. For the case of a hard power law of protons, the p $\gamma$  neutrinos can dominate the high-energy regime of the spectrum, whereas for the case of a soft power law, the p $\gamma$  neutrinos dominate in the cutoff of the spectrum.

In Figure 4.3, we plot the electron neutrino emission of Cyg X-1 for the two power-law slopes,  $p = 1.7$  (left) and  $p = 2.2$  (right). We compare the predicted intrinsic emission to the upper limits of the cascade-like events of IceCube after 7 yr of operation (Aartsen et al. 2019). The three different lines in both plots, correspond to the three different energy spectra as assumed by IceCube. We see that the predicted emission is below the sensitivity of IceCube by an order of magnitude, and hence the detection of any electron neutrino from Cyg X-1 is unlikely with the current generation of neutrino observatories, at least based on the typical hard state behaviour.

### 4.3.2 Neutrino emission from GX 339-4

In Figure 4.4, we show the total predicted electron neutrino and antineutrino emission of the jets of GX 339-4 during an outburst similar to the bright outburst in 2010. The produced neutrinos share the same properties as the parent particles. Similar to the case of Cyg X-1, the pp neutrinos dominate in the TeV regime, whereas the p $\gamma$

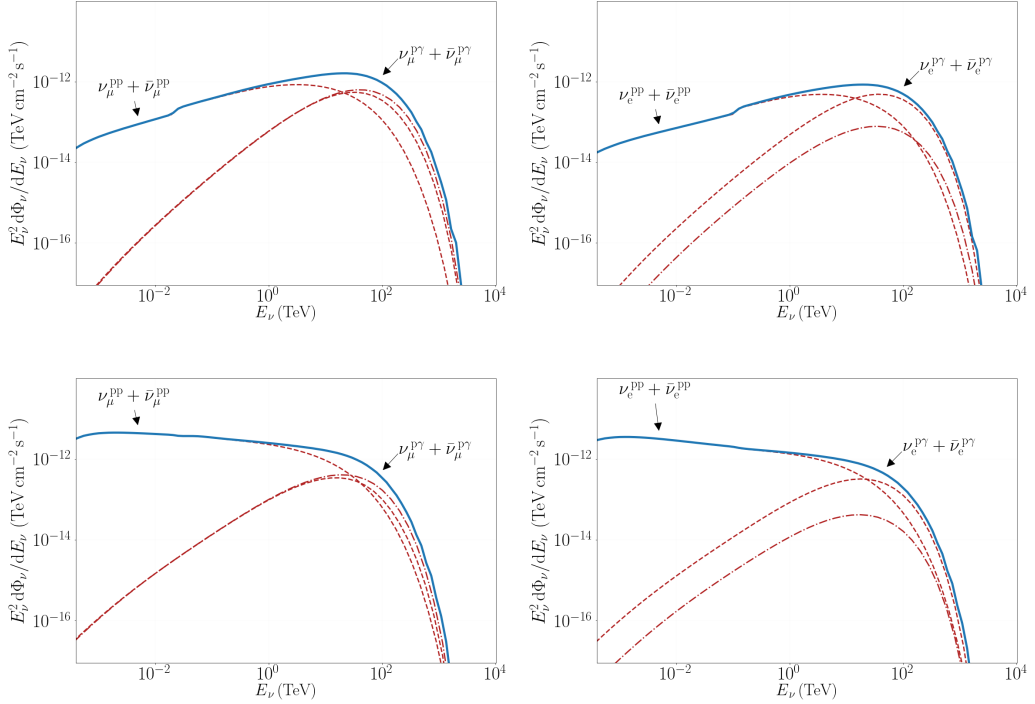


**Figure 4.2:** The intrinsic neutrino and antineutrino energy flux of the jet of Cyg X-1. In the *top* panels, the neutrinos originate in a hard power law of non-thermal protons with an index  $p = 1.7$ , and in the *bottom* panels, we assume  $p = 2.2$ . In the *left* plots, we show the distributions of muon neutrinos, and in the *right* plots, we show the electron neutrinos. The neutrinos from pp interactions dominate the low-energy regime of the spectrum, and the neutrinos from  $p\gamma$  interactions contribute in the maximum energy of the order of 100 TeV. For the secondaries of  $p\gamma$ , we plot the muon/electron neutrinos with dashed lines, and the muon/electron antineutrino with dash-dotted lines. The solid line is for the total neutrino/antineutrino spectrum.

neutrinos peak close to the maximum available energy around 100 TeV. The neutrino flux of GX 339-4 is too low to be detected, which is expected based on the estimated power of the jets.

We also compare the predicted neutrino flux to the upper limits as set by IceCube (Aartsen et al. 2019). We see that GX 339-4 is also incapable of producing enough electron neutrinos to be detected by IceCube.

### 4.3.3 Neutrino rates

The current neutrino detectors are not sensitive enough to detect a neutrino spectrum from a particular source and merely detect single events. We convert the neutrino

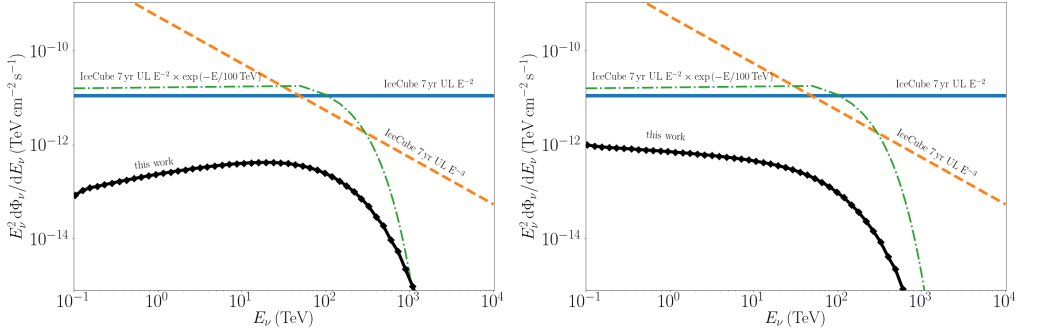


**Figure 4.3:** The total predicted  $\nu_e + \bar{\nu}_e$  flux of the jets of Cyg X-1 for a hard power-law of accelerated protons in the *left* ( $p = 1.7$ ) and for a soft power-law in the *right* ( $p = 2.2$ ). We compare the predicted neutrino flux to the IceCube upper limits of cascade-like events after 7 yr of operation (Aartsen et al. 2019) for the three different assumed spectra, as indicated in the plots.

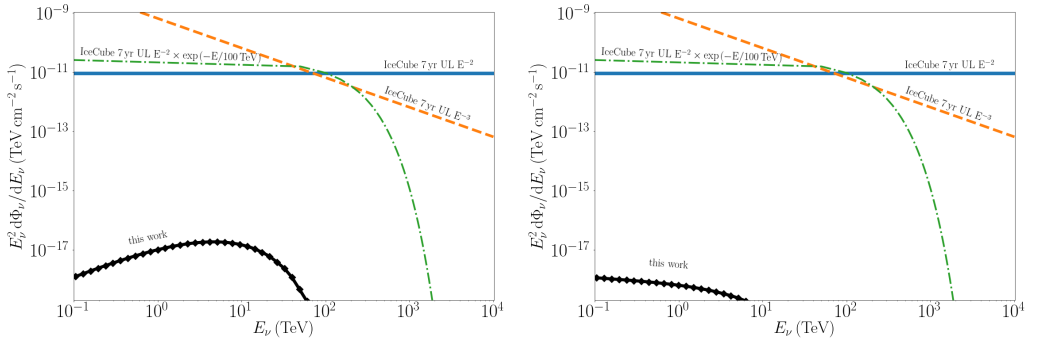


**Figure 4.4:** Similar to Figure 4.3 but for the case of GX 339-4.

spectra to rate of events

$$R = \int 4\pi \frac{d\Phi_\nu}{dE_\nu} A_{\text{eff}}(E_\nu) dE_\nu, \quad (4.3)$$

where  $d\Phi_\nu/dE_\nu$  is the neutrino differential flux,  $A_{\text{eff}}$  is the effective area of the detector, and we integrate between 0.1 TeV and 10 PeV. We use the effective areas of IceCube (Aartsen et al. 2013, 2019), ANTARES (Albert et al. 2017a) and the simulated effective area of KM3NeT/ARCA (Adrián-Martínez et al. 2016).

In Table 4.1, we show the event rates (per year) for the three different detectors. The number of track-like events for both IceCube and KM3NeT/ARCA is similar for the case of Cyg X-1 and around 1–1.3 neutrinos per year when the source launches jets for both  $p = 2.2$  and  $p = 1.7$  power-law slopes. The number of shower-like events

**Table 4.1:** The neutrino rate (per year) for Cyg X-1 and GX 339-4 for the various detectors, and for two different proton power-law slopes. It is worth mentioning that IceCube and KM3NeT/ARCA could detect of the order of one muon neutrino from Cyg X-1 if it launched relativistic jets for a year.

		soft proton power law ( $p = 2.2$ )			hard proton power law ( $p = 1.7$ )		
		IceCube	ANTARES	KM3NeT	IceCube	ANTARES	KM3NeT
Cyg X-1	$\nu_\mu + \bar{\nu}_\mu$	1.1	0.006	1.3	1.0	0.007	1.3
	$\nu_e + \bar{\nu}_e$	0.002	0.001	0.6	0.005	0.001	0.4
GX 339-4	$\nu_\mu + \bar{\nu}_\mu$	$7 \times 10^{-10}$	$3 \times 10^{-7}$	$3 \times 10^{-5}$	$6 \times 10^{-10}$	$3 \times 10^{-7}$	$3 \times 10^{-5}$
	$\nu_e + \bar{\nu}_e$	$3 \times 10^{-9}$	$3 \times 10^{-7}$	$1 \times 10^{-5}$	$3 \times 10^{-9}$	$3 \times 10^{-7}$	$1 \times 10^{-5}$

( $\nu_e$  and/or  $\bar{\nu}_e$ ) for IceCube is significantly reduced due to the effective area of the detector and the veto forced by the IceCube collaboration, namely the subtraction of the outer volume of the detector (Aartsen et al. 2013).

In agreement with what we expect from the neutrino distribution, we see that GX 339-4 cannot produce a significant rate of events for IceCube nor KM3NeT/ARCA.

#### 4.3.4 Contribution from all known BHXBs

Although we have now established that Cyg X-1 and GX 339-4 on their own cannot be detected as neutrino sources, it is interesting to examine whether the entire population of BHXBs together would be a significant contributor to the diffuse neutrino background. We utilise the most recent XRB catalogue of Tetarenko et al. (2016b) that includes all the BHXBs and BHXB-candidates detected until 2016. We use only those that are BHXBs or BHXB-candidates, and known to emit in radio bands described as jet emission. This is a conservative estimate because XRBs with neutron stars have been observed to launch jets that sometimes may be as powerful as BHXBs (see, e.g., van den Eijnden et al. 2018; Coriat et al. 2019). From the 70 sources in total presented there, we consider 31 for this analysis. From these sources, 4 are high-mass BHXBs, and 27 are low-mass BHXBs. We base the neutrino emission of the high-mass BHXBs on the results of the prototypical case of Cyg X-1 (K20), and for the rest of the sources on the prototypical case of GX 339-4 (K22) due to the lack of better quality simultaneous observations of BHXBs, but we rescale the distance, the mass of the black hole and the inclination. For numerous sources, the exact distance, the inclination and/or the mass of the black hole are not well constrained. In these cases, Tetarenko et al. (2016b) assumed fiducial values: a distance of 8 kpc, the mass of the

black hole equal to  $8 M_{\odot}$ , and an inclination angle of  $60^{\circ}$ . In this work, we adopt the same assumptions. We finally include four more low-mass BHBs/BHXB-candidates discovered after 2016 based on the Faulkes Telescopes project (Lewis et al. 2008). We show the exact values of these sources in Table 4.2 of Appendix 4.A.

In Figure 4.5, we sum the intrinsic  $\nu_{\mu} + \bar{\nu}_{\mu}$  emission from all 35 known BHBs assuming either a soft power law of accelerated protons with  $p = 2.2$  for every source, or a hard power law with  $p = 1.7$ . We further assume an average duty cycle of 1 per cent (Tetarenko et al. 2016b; C20; but also see Deegan et al. 2009 who suggest a few 0.1 per cent for the particular case of GRS 1915+105) to account for the fact that BHBs do not launch persistent jets, but they transit between different spectral states (Belloni 2010). For the unique case of Cyg X-1 in particular, we assume a duty cycle of 25 per cent because in the past ten years, it has spent 1/4th of its time in the jet-launching state (Cangemi et al. 2021). Comparing our results to the detected astrophysical neutrino signal of IceCube (Stettner 2019), we see that the known population of BHBs cannot contribute more than  $\sim 0.2$  per cent in the energy band around 40 TeV, assuming a hard proton power law. The contribution in the case of a soft power law of protons is even less than 0.1 per cent.

In Figure 4.6, we plot the differential  $\nu_{\mu} + \bar{\nu}_{\mu}$  energy flux at 1 TeV for the 35 known BHBs as a function of the declination angle  $\delta$ . We compare our predicted values to the 90% median sensitivity of IceCube (Aartsen et al. 2020) and the predicted sensitivity of KM3NeT/ARCA (Aiello et al. 2019) assuming that the flux scales as  $E_{\nu}^{-2}$  (solid lines) or  $E_{\nu}^{-3}$  (dashed line). We highlight the predicted emission of Cyg X-1 that, as we discuss above, is of the same order of magnitude as the sensitivity of IceCube and KM3NeT/ARCA, thus may be a good candidate source of Galactic neutrinos. We indicate the other high-mass BHBs V4641 Sgr, MWC 656 and Cyg X-3 that contribute significantly to the overall predicted spectrum, as we discuss in the Appendix 4.C. The other four low-mass BHBs we highlight are the sources Abbasi et al. (2022) discuss in their analysis. Finally, in Figure 4.6, we indicate the upper limits of those microquasars as derived by the IceCube collaboration (Aartsen et al. 2019; Abbasi et al. 2022) for track-like events that are in the list of sources we examine in this work. The above works present multiple upper limits based on different assumptions on the energy dependence of the neutrino flux. We show only the upper limits derived under the assumption of a neutrino flux that scales as  $E^{-2}$ , because in our two models we assume a proton power-law index close to 2, and hence the produced secondaries follow a similar distribution.

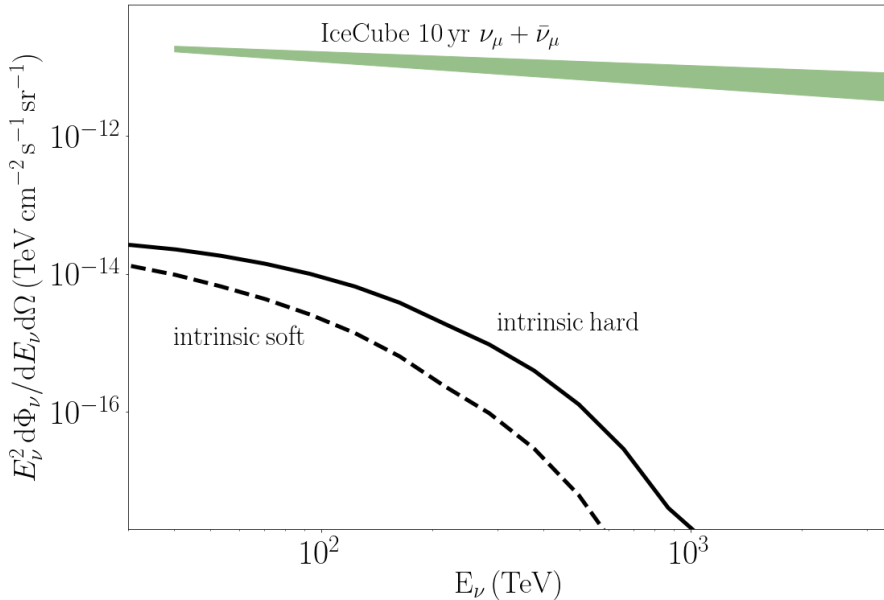


**Figure 4.5:** The predicted  $\nu_\mu + \bar{\nu}_\mu$  energy flux for the 35 known BHXBs assuming a soft power law of protons ( $p = 2.2$ ; dashed line) or a hard power law ( $p = 1.7$ ; solid line). We assume that the sources have a one-percent duty cycle, and also plot the astrophysical background as observed by IceCube in 10 yr (Stettner 2019) as a reference.

## 4.4 Diffuse secondary emission

### 4.4.1 BHXBs as CR sources

In the above, we calculated the intrinsic neutrino and  $\gamma$ -ray emission of 35 known BHXB jets. In this section, we use DRAGON2 (Evoli et al. 2017, 2018) to examine the contribution of a broader population of BHXBs to the CR spectrum. In particular, we assume the existence of 1000 Galactic sources that follow a spatial distribution similar to the observed distribution of pulsars (Lorimer et al. 2006), but we also account for a pc scale spike of sources close to the Galactic centre, as indicated by Mori et al. (2021). The spike of BHXBs around the Galactic centre peaks at 1 pc with a Full width half maximum of 10 pc. Based on the detected BHXBs so far, we assume that 90 per cent of them are low-mass and 10 per cent are high-mass BHXBs (Tetarenko et al. 2016b). Similar to our previous analysis, the BHXBs follow the behaviour of the prototypical source, therefore the jets of low BHXBs accelerate protons up to 100 TeV, and the high-mass sources accelerate protons up to 1 PeV.

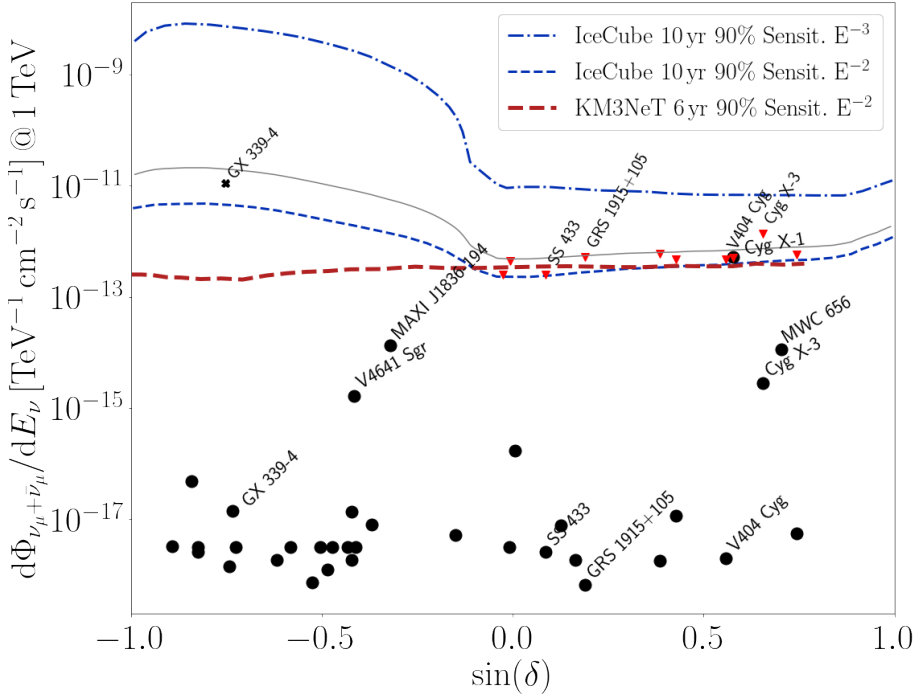


**Figure 4.6:** The predicted  $\nu_\mu + \bar{\nu}_\mu$  differential flux at 1 TeV for the 35 known BHXBs we study here versus the sin of their declination (Dec). We also show the 90 per cent median sensitivity of IceCube (dot-dashed blue line for  $E_\nu^{-3}$  and dashed blue line for  $E_\nu^{-2}$ ; Aartsen et al. 2020) and KM3NeT/ARCA (thick, dashed red line; Aiello et al. 2019) for reference for an energy flux that scales with energy. We note that we cannot directly compare to these sensitivity curves because in our work we assume an  $E_\nu^{-2.2}$  dependence. We hence plot the interpolated flux for  $E_\nu^{-2.2}$  with a thin solid gray line. The crosses (Aartsen et al. 2019) and the red triangles (Abbasi et al. 2022) correspond to the 90 per cent upper limits for  $E_\nu^{-2}$ .

Using DRAGON2, we inject CR protons which propagate in the Galactic plane in a 2D grid of radius 12 kpc and height 4 kpc. We only propagate the population of protons as we have not included heavier elements in our previous studies to be able to further constrain their spectral properties. We assume a constant spatial diffusion coefficient with  $D_0 = 2.7 \times 10^{28} \text{ cm}^2 \text{ s}^{-1}$ , an energy dependency of  $E^{-0.45}$  (Fornieri et al. 2020), and a Galactic magnetic field model based on Pshirkov et al. (2011).

In Fig. 4.7, we show the contribution of both low-mass and high-mass BHXBs to the overall CR spectrum. We see that 900 low-mass BHXBs can contribute up to 50 per cent of the spectrum at the TeV energy range. The contribution falls signifi-

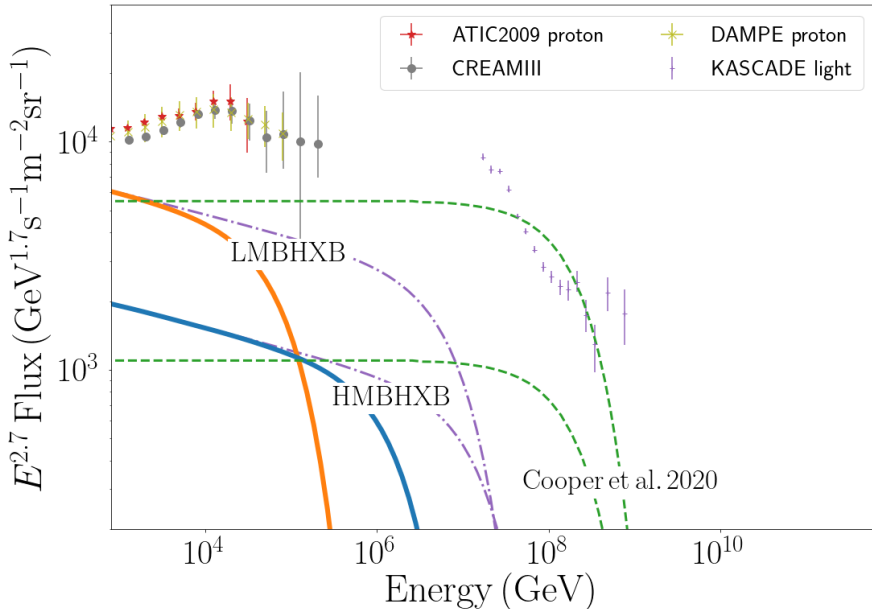


**Figure 4.7:** The contribution of a 1000 BHXBs to the CR spectrum calculated with DRAGON2. The population consists of 90 per cent low-mass BHXBs and 10 per cent of high-mass BHXBs. We assume that all the sources accelerate protons to a soft power law with an index  $p = 2.2$  up to some maximum energy that depends on whether it is a low-mass or a high-mass BHXBs. We compare our results to the observational constraints as shown in the legend, and we over-plot the “optimistic” (uppermost) and “pessimistic” (lowermost) scenarios of Cooper et al. 2020 for comparison. We show for comparison an extreme scenario (dash-dotted lines) where the particles follow similar power-laws in energy but with larger maximum energy of the order of  $10^7$  GeV. The observational data are as labelled from ATIC2009 (Chang et al. 2008), CREAMIII (Yoon et al. 2017), DAMPE (DAMPE collaboration et al. 2019) and KASCADE (Apel et al. 2011).

cantly though and at  $\sim 100$  TeV the spectrum drops exponentially. The 100 high-mass BHXBs cannot significantly contribute to the CR spectrum even though they allow for proton energy that is 10 times greater than the one of low-mass BHXBs. We moreover include the “optimistic” and the “pessimistic” scenarios of C20 for comparison, and we see that despite the similar contribution in the low-energy regime at around TeV, the approach we follow here leads to different maximum CR energy. Finally, we overplot an extreme scenario where we assume that the maximum energy of the CRs reaches values of the order of  $10^7$  GeV as particle acceleration theory allows for (see Section 4.5.4. Such a scenario is derived from the extreme values allowed from the best fits of K20 and K22.



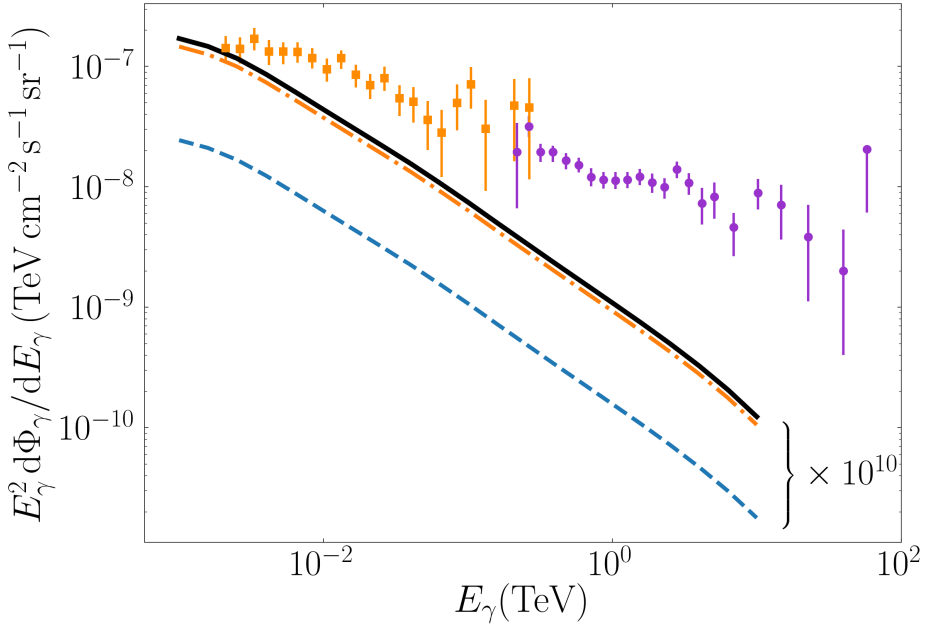


**Figure 4.8:** The diffuse  $\gamma$ -ray emission of CRs accelerated in BHXB jets as calculated with **HERMES** for Galactic latitudes within  $5^\circ$  from the Galactic centre. We plot the diffuse emission multiplied by a factor of  $10^{10}$  to better compare to the results of *Fermi*/LAT (squares; Abdollahi et al. 2020) and the H.E.S.S. collaboration (circles; H.E.S.S. Collaboration et al. 2018a).

#### 4.4.2 Diffuse gamma-ray and neutrino emission from BHXBs

After CR protons escape the acceleration site, they interact with the interstellar medium while propagating through the Galactic plane. To account for the inelastic collisions between the propagating protons and the interstellar medium, we utilise **HERMES**. **HERMES** a publicly available code designed to compute the emission originated from a variety of non-thermal processes including synchrotron and free-free radio emission, gamma-ray emission from bremsstrahlung and inverse-Compton scattering,  $\gamma$ -ray and neutrino emission from pion decay (Dundovic et al. 2021) In Figure 4.8, we plot the diffuse  $\gamma$ -ray emission when protons interact with atomic hydrogen based on the 21 cm line emission (dot-dashed orange line), and the molecular hydrogen based on the CO molecular gas (dashed blue line; Luque et al. 2022). We compare our results to the diffuse  $\gamma$ -ray spectrum of *Fermi*/LAT (Abdollahi et al. 2020) and the H.E.S.S. collaboration (H.E.S.S. Collaboration et al. 2018a). In Figure 4.9, we plot the diffuse neutrinos of the same processes and compare them to the astrophysical background as observed by IceCube (Stettner 2019).

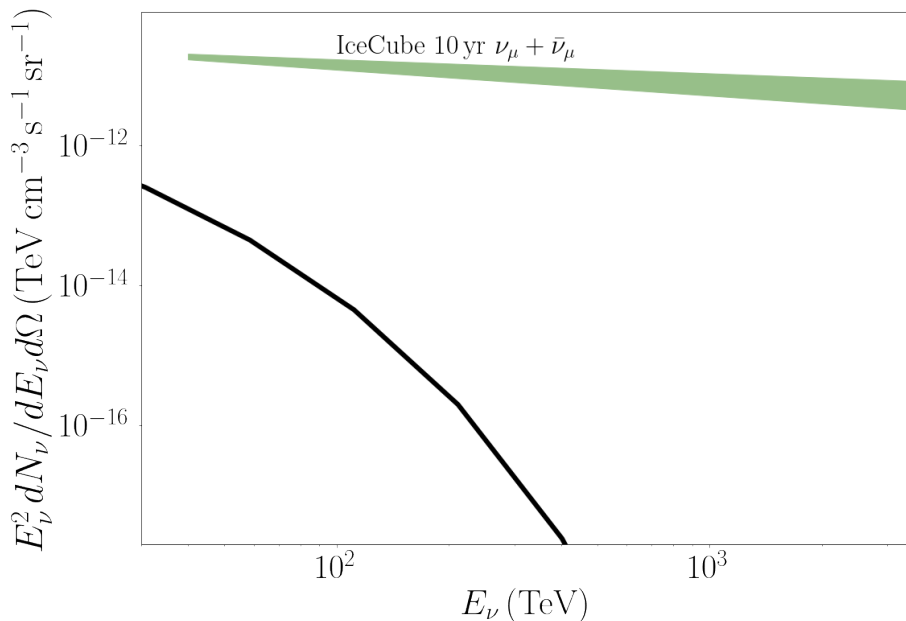


**Figure 4.9:** The diffuse neutrino emission of CRs accelerated in 1000 BHXB jets, while propagating in the Galactic plane. We also plot the diffuse neutrino emission of IceCube for comparison (Stettner 2019).

## 4.5 Discussion

### 4.5.1 Cyg X–1 and GX 339–4 as Galactic neutrino sources

Both ANTARES and IceCube have performed an in-depth analysis searching for point-like neutrino emission from Cyg X–1. ANTARES collaboration used 4 yr of data to set upper limits of the level of  $10^{-10}$   $\text{TeV cm}^{-2} \text{s}^{-1}$  assuming a neutrino flux that follows a single power law of the form  $E_\nu^{-2}$  (Albert et al. 2017b). They did not include Cyg X–1 in most recent studies because it did not show any TeV emission since 2016 (Aublin et al. 2019). The IceCube collaboration used 7 yr of data to set upper limits for Cyg X–1. Different assumptions for the energy dependence of the neutrino flux lead to different upper limits. For a single power-law that drops as  $E_\nu^{-2}$ , they set an upper limit of the order of  $10^{-11}$   $\text{TeV cm}^{-2} \text{s}^{-1}$  (Aartsen et al. 2019). They did not include Cyg X–1 in most recent studies because it is not included in the recent TeV catalogues (Aartsen et al. 2020). Both upper limits set by ANTARES and IceCube are above our predicted flux, which is of the order of  $10^{-12}$   $\text{TeV cm}^{-2} \text{s}^{-1}$ .

Recently, the IceCube collaboration released the updated upper limits for the Galactic BHXBs using 7.5 yr of data, where they set the 90 per cent upper limit of Cyg X-1 at  $0.5 \times 10^{-12} \text{ TeV}^{-1} \text{ cm}^{-2} \text{ s}^{-1}$ , a value very close to our predicted flux (Abbasi et al. 2022). We convert the IceCube flux to fluence by multiplying with 7.5 yr to obtain  $1.2 \times 10^{-4} \text{ TeV}^{-1} \text{ cm}^{-2}$ . The neutrino fluence of Cyg X-1 according to our prediction is  $2 \times 10^{-6} \text{ TeV}^{-1} \text{ cm}^{-2}$  assuming the neutrino production lasts for an orbital period of 6.5 days. This assumption allows us to derive the lower limit of the fluence. Despite accounting for the persistent jets Cyg X-1 launches (Rushton et al. 2012), it is difficult to identify any astrophysical neutrinos. This is in part because the TeV energy range in which we expect emission is dominated by atmospheric neutrinos (Aartsen et al. 2017a). It is also worth mentioning that Abbasi et al. (2022) assume an energy dependence of the neutrino flux with  $E_\nu^{-1.25}$ , which is significantly harder even compared to our hard power-law index of  $p = 1.7$ , inherited by the non-thermal protons. This difference in the energy dependence may relax the fact that our prediction is so close to the IceCube upper limits. In other words, if the IceCube collaboration uses a softer index, then the upper limits will increase.

In Table 4.1, we see the neutrino rate per year from the region of Cyg X-1. The muon neutrino rate after accounting for the effective area of IceCube and KM3NeT/ARCA are of the order of one neutrino per year, close to previous studies, such as Anchordoqui et al. 2014 where the authors used LS 5039 as a study case. If we account for the duty cycle of Cyg X-1, the neutrino rate may decrease fourfold, which is the duty cycle of Cyg X-1 the past 20 yr (Cangemi et al. 2021). Furthermore, we merely base our neutrino estimates on the steady-state emission of the jets of Cyg X-1 when the system was in the inferior conjunction, such that the companion star was behind the black-hole-jet system on the line of sight. A more detailed analysis, where the orbital attenuation of the non-thermal emission is properly accounted for, is outside the scope of this work (see, e.g., Vieyro & Romero 2012, for a neutrino prediction during a flaring state). Finally, when deriving the neutrino rate from Equation 4.3, we integrate in the energy range between 0.1 TeV and 1 PeV, thus we do not know the exact expected energy of the incoming neutrino(s). As aforementioned, the low-energy regime of the detected neutrino spectrum is dominated by the atmospheric background, therefore detectable astrophysical neutrinos from Cyg X-1 will occur in the energy range between  $\sim 10 \text{ TeV}$  and  $\sim 100 \text{ TeV}$ .

Due to the high number of outbursts and the plethora of observations, GX 339-4 has attracted the attention of the community and several previous works have predicted the neutrino emission based on different models and/or physical processes (see, e.g., Distefano et al. 2002; Zhang et al. 2010). The muon and electron neutrino spectra we present here, and consequently the neutrino rates, are intrinsically connected to the most up-to-date multiwavelength constraints of GX 339-4. This is because we compute the neutrino spectra while self-consistently constraining the overall electromagnetic emission (K22). We see that GX 339-4 likely fails to be a potential source

of Galactic neutrinos as we show in Figures 4.4 and 4.6, and based on the neutrino rates of Table 4.1.

### 4.5.2 BHXBs as Galactic neutrino sources

Comparing the total neutrino spectrum of the 35 known BHXBs to the astrophysical background of IceCube Stettner (2019), we see that BHXBs cannot contribute more than 0.1 per cent at 40 TeV if all the sources accelerated proton in a hard non-thermal power law with index  $p = 1.7$  (see Figure 4.5). The contribution of BHXBs significantly drops in larger energies where it eventually cuts off at approximately 1 PeV.

In Figure 4.6, we show the predicted neutrino differential energy flux at 1 TeV for the 35 known BHXBs. Indicated with the black dots, the majority of sources are more than 3 to 4 orders of magnitude below the sensitivity of IceCube (assuming an energy dependence of  $E_\nu^{-2}$ ), or the predicted sensitivity of KM3NeT/ARCA after 6 yr of operation. We compare the predicted emission of GX 339-4 to the upper limits of Aartsen et al. (2020), but as discussed above, this particular source is unlikely to emit any significant number of neutrinos to be detected by IceCube. Abbasi et al. (2022) discussed the likelihood of SS433, GRS 1915+105 and V404 Cyg to be Galactic neutrino sources. We see that none of these sources can produce a flux of neutrinos close to the sensitivities in this energy regime. We see on the other hand, that the 3 high-mass BHXBs, V4641 Sgr, MWC 656 and Cyg X-3 are capable of emitting a neutrino flux 100 times stronger than the majority of the sources, but still not enough to be detected by IceCube and KM3NeT/ARCA. The low-mass BHXB with the strongest neutrino flux is MAXI J1836-194, which launches a jet with an inclination angle between 5 and 15° (Russell et al. 2014) making it a good candidate source for further spectral analysis, in particular in the case of lepto-hadronic jets (see Lucchini et al. 2021, for a purely leptonic scenario).

Comparing our results to the recently derived upper limits of IceCube (Abbasi et al. 2022), we see that our prediction of Cyg X-1 is remarkably close to the upper limit. In Section 4.5.1 we discuss the implication of Cyg X-1 as a candidate neutrino source, but here we stress once more that the sensitivity curves and the upper limits we plot in Figure 4.6 are shown as reference alone and cannot accurately be directly compared. In particular, to derive the predicted differential fluxes we use the soft power-law of the accelerated protons ( $p = 2.2$ ), but the sensitivity curves refer to  $p = 2$  or  $p = 3$  cases. A more accurate comparison would require either to obtain the instrument sensitivity assuming  $E_\nu^{-2.2}$  or to interpolate between the two depicted sensitivities of  $E_\nu^{-2}$  and  $E_\nu^{-3}$ . For simplicity, we use the publicly available sensitivity curves of IceCube with blue lines, and with a thin solid gray line the interpolated sensitivity for  $p = 2.2$ . Comparing to this sensitivity curve, we see that Cyg X-1 is slightly below the threshold for detection.

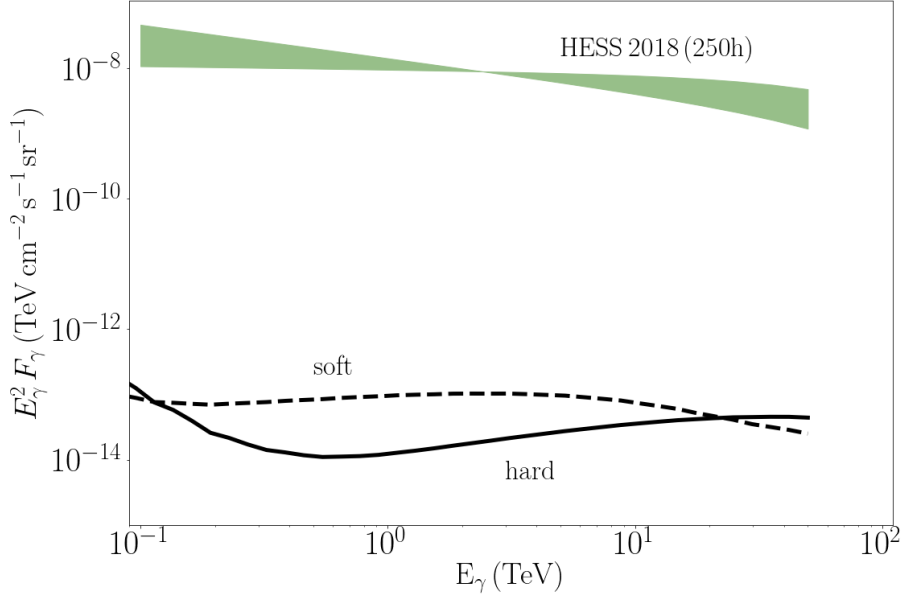


**Figure 4.10:** The overall intrinsic  $\gamma$ -ray emission of the 35 BHXBs of this work. We assume that the accelerated protons follow either a soft power-law of  $p = 2.2$  (dashed line) or a hard power-law of  $p = 1.7$  (solid line). We also plot the diffuse  $\gamma$ -ray emission detected after 250 hours by H.E.S.S. (H.E.S.S. Collaboration et al. 2018a) as a reference to our predicted  $\gamma$ -ray emission.

### 4.5.3 Gamma-ray emission counterpart

To ensure the  $\gamma$ -ray counterpart of the 35 BHXBs obeys the current observational constraints, we compare the overall GeV-to-TeV emission of these sources for the two different power-law indices to the observed flux (see Figure 4.10). The H.E.S.S. collaboration has detected the Galactic plane in the same energy range, we hence use these observations for the comparison. We use the result of the best fit of the observational data that is a power-law with an exponential cutoff at 100 TeV, a photon index of  $2.28 \pm 0.02_{\text{stat}} \pm 0.2_{\text{syst}}$ , and a normalisation at 1 TeV of  $1.2 \pm 0.04_{\text{stat}} \pm 0.2_{\text{syst}} \times 10^{-8} \text{ TeV cm}^{-2} \text{ s}^{-1} \text{ sr}^{-1}$  (H.E.S.S. Collaboration et al. 2018a). This diffuse  $\gamma$ -ray emission is from the inner 200 pc of the Galactic centre, but not all the sources we study here are located in this region. These observations, however, originate in a  $\gamma$ -ray bright region of the sky and hence we use them as an upper limit for the overall contribution of the so-far known BHXBs. We see that the predicted high-energy emission from the BHXBs is of the order of five orders of magnitude below the H.E.S.S. observations and thus do not violate the  $\gamma$ -ray constraints.

#### 4.5.4 BHXBs and the CR spectrum

Recent population synthesis results (see, e.g., Olejak et al. 2020), and in agreement with new X-ray observations of the Galactic centre, (Hailey et al. 2018; Mori et al. 2021) suggest it is likely that of the order of 1000 accreting BHXBs exist in the Galaxy capable of launching jets. Such systems may have faint radio jets currently in quiescence, or their outbursts may otherwise be obscured. In this work, we use DRAGON2 to find their likely contribution to the CR spectrum while properly accounting for propagation in the Galactic disc (see Figure 4.7). We find that BHXBs can contribute up to maximum 50 per cent in the low-energy regime of the spectrum close to TeV energies. This significant contribution is in broad agreement with the findings presented in C20 below the knee.

There are two notable differences between the CR contribution calculated in this work and the one in C20: the larger CR flux in the  $\sim$ TeV regime of the spectrum compared to the pessimistic model of C20, and the lack of contribution at higher energies. The first can be explained by the fact that a softer power law is assumed, resulting in the steeper slope observed in Figure 4.7. Secondly, we find in this work that multi-wavelength constraints for Cyg X-1 and GX 339-4 require a high-energy hadronic cut-off for accelerated protons at 100s TeV. Given this, we find that BHXBs cannot reproduce this prominent excess in the 100 PeV energy band that would distinguish them from other Galactic or extragalactic sources, as suggested by C20. Further multi-wavelength studies of BHXBs may aid in precluding BHXBs as sources of CRs above the knee. We discuss the hadronic particles acceleration in more detail below, specifically outlining the limitations to this work.

This maximum energy of accelerated CRs is an important parameter for the CR contribution, and also the neutrino spectrum. In this work, we assume that all the low-mass BHXBs follow the behaviour of the prototypical source GX 339-4 for which, based on the results of K22, protons get accelerated only up to  $\sim$  100 TeV. This maximum energy results by equating the acceleration timescale to the confinement timescale (Hillas 1984). For a Bohm-like acceleration where particles diffusively cross a shock front (diffusive shock acceleration; DSA, also known as first-order Fermi acceleration),  $t_{\text{acc}} \propto E_p/f_{sc}$ , where  $E_p$  is the proton energy and  $f_{sc}$  is the acceleration efficiency (Jokipii 1987; Aharonian 2002), and the confinement timescale  $t_{\text{esc}} \propto R_{\text{acc}}$ , where  $R_{\text{acc}}$  is the radius of the acceleration site.  $f_{sc}$  is the most impactful free parameter, whose exact value depends on the acceleration mechanism and is not well constrained yet. K22 set  $f_{sc} = 0.01$ , a value that allows for the primary electrons to reach high enough energy to radiate in the GeV regime through ICS without overshooting the *Fermi*/LAT upper limits (C20 assume  $f_{sc} = 0.1$ ). Similar to K22, we assume that the acceleration efficiency is the same for both primary electrons and protons because we do not have a more robust constraint for the  $f_{sc}$  of protons. Recent numerical simulations of particle acceleration though suggest that the efficiency

of electrons and protons may differ, and in fact the proton acceleration may be more efficient depending on the kinematic conditions of the acceleration site (Caprioli & Spitkovsky 2014a; Crumley et al. 2019). A more efficient proton acceleration would allow for protons to accelerate to energies beyond 100 TeV, and hence allowing for the BHXB population to contribute more significantly in the CR spectrum, as in C20.

The efficiency of the particle acceleration also depends on the magnetisation of the shock and its medium, as well as the obliquity of the system, which is defined as the orientation of the magnetic field lines regarding the shock front. In relativistic, magnetised media as we expect in the jets we examine here, when the magnetic field is almost aligned with the shock front, DSA is thought to be inefficient (Sironi et al. 2013). In that case in particular, the acceleration timescale based on particle-in-cell numerical simulations (PIC) is  $t_{\text{acc,pic}} = 4\gamma_p^2/\Gamma^2\omega_{pi}$  (Sironi et al. 2013). Here,  $\omega_{pi} = \sqrt{m_e/m_p}\omega_{pe}$  and  $\omega_{pe} = (4\pi e^2 n_e/\Gamma m_e)^{1/2}$  are the plasma frequencies for the protons and the electrons, respectively. In the plasma frequency,  $e$  is the elementary charge,  $n_e$  is the number density of the particles at the acceleration region, and  $\Gamma$  is its bulk Lorentz factor.

In Figure 4.11, we plot the inverse acceleration and escape timescale as a function of the proton energy  $(\gamma_p - 1)m_p c^2$ . The intersection of the two lines, indicates the maximum energy that protons can attain. In the top panel, we use the Bohm acceleration timescale, and in the bottom, we use the relativistic shock acceleration according to Sironi et al. (2013). In both panels of Figure 4.11, we show the exact timescales (solid line for escape, dashed line for Bohm acceleration, dot-dashed line for relativistic shock) and indicate the maximum energy with a black vertical line. We show the possible values of the maximum energy within the shaded regions that are within the  $1\sigma$  uncertainty of the free parameters (see Table 3 of K22) and for  $0.001 \leq f_{sc} \leq 0.1$ , where the former boundary indicates a relatively inefficient acceleration and the latter indicates an efficient particle acceleration. The exact dynamical values we use here correspond to the first particle acceleration region of the jet, but beyond that region, the maximum energy remains almost constant (see Figure 4 of C20). Overall, we see that protons can accelerate to a maximum energy that ranges between 400 GeV and 2.5 PeV, but due to lack of stronger evidence, we cannot further constrain it.

An alternative plausible acceleration mechanism which could be more efficient, is magnetic reconnection (Drenkhahn & Spruit 2002; Uzdensky 2011; Guo et al. 2014; Sironi & Spitkovsky 2014; Sironi et al. 2015; Kagan et al. 2015). The acceleration timescale of magnetic reconnection scales as  $t_{\text{rec}} \propto E_p$  and based on PIC simulations,  $t_{\text{rec}} = E_p/(0.1ecB)$ , where the factor 0.1 comes for the reconnection rate of the field lines  $r_{\text{rec}} = v_{in}/v_A$ . (Sironi & Spitkovsky 2014) In the case of a strongly magnetised medium, the Alfvén velocity  $v_A = c\sqrt{\sigma/(1+\sigma)} \simeq c$ , and hence the inflow velocity  $v_{in} \simeq 0.1c$ . The inflow velocity defines the electric field responsible for the acceleration  $E_{\text{rec}} \simeq 0.1B$  (Uzdensky 2011; Sironi & Spitkovsky 2014). Comparing the

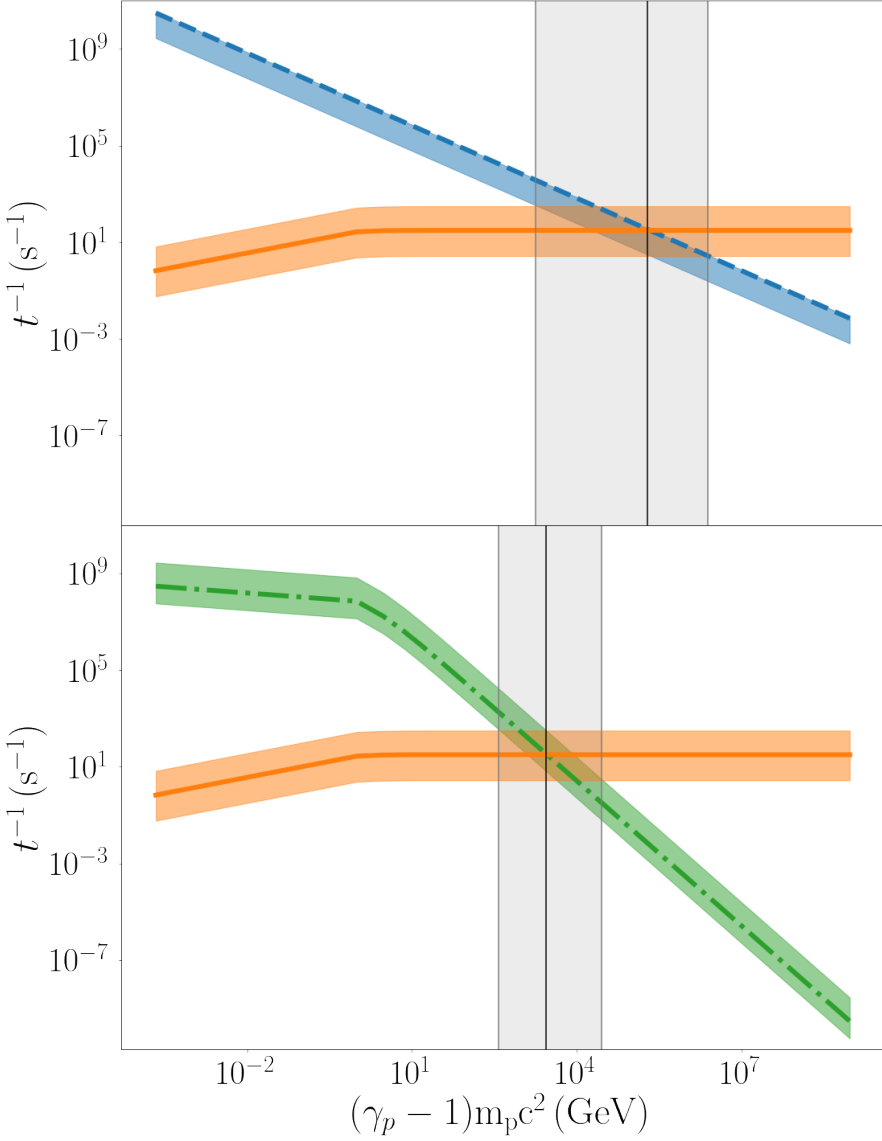


**Figure 4.11:** The acceleration and escape rates of CRs in low-mass BHXBs. When the two timescales are equal, the accelerated protons reach their maximum energy, as we show with the vertical black line. We show in both plots with a solid orange line the confinement timescale. In the *top* panel, we assume a Bohm-like, DSA-type acceleration such that  $\gamma_p \propto t$  (dashed line), and in the *bottom* we assume a relativistic shock acceleration where  $\gamma_p \propto t^{1/2}$  (dot-dashed line). The shaded regions show the range of the maximum energy within  $1\sigma$  uncertainty.



reconnection timescale to the Bohm acceleration timescale, we see that for  $f_{sc} \simeq 0.1$ , the two timescales are equal, if Bohm acceleration is very efficient. In strong magnetised regions, however, one has to consider the effect of the synchrotron radiation on the accelerated particles, and hence a more self-consistent treatment is necessary (Hakobyan et al. 2019; Petropoulou et al. 2019; Ripperda et al. 2022). Consequently, in the efficient acceleration regime of DSA, or in the case of magnetic reconnection where particles do not radiate away their energy immediately, it is likely for low-mass BHXBs jets to accelerate particles to slightly larger energies. If such a scenario is feasible for the majority of the Galactic low-mass BHXBs, then that would increase their contribution to the CR spectrum (Figure 4.7). In Appendix 4.D we show the maximum CR energy for the case of high-mass BHXBs based on K20.

It is also very likely that different BHXBs allow for different particle acceleration properties that may differ in each single outburst, but it is impossible to better constrain the acceleration properties of each individual source. In a future work, we aim to better connect the acceleration properties to the jet kinematics, especially in the case where jets are mass loaded due to their interaction with their ambient medium. Such a mass-loading scenario, might in fact also assist in solving one long-standing problem: how particles accelerate in jets without violating the energy reservoir (Kantzas et al., in prep). In this work, we try to capture the broader contribution of the population of BHXBs in the CR spectrum, using the prototypical sources GX 339–4 and Cyg X–1 to examine the whole population of BHXBs. For the case of high-mass BHXBs and based on the prototypical source Cyg X–1, the proton energy reaches values of the order of PeV (K20). C20 used first-principle estimates to calculate the maximum proton energy attained in BHXBs and found values of the order of  $10^{16}$  and  $10^{18}$ eV based on different assumptions for the fiducial jet parameters (see Figure 4 in C20; see also Romero & Vila 2008). Such a simplification allows for larger proton energies, but there is no constraint on the electromagnetic spectrum. Our approach, on the other hand, is in better agreement with the observed Cyg X–1 and GX 339–4 multi-wavelength emission constraints for the two prototypical sources. It is important to stress once more that the assumption that all the sources show the same behaviour may underestimate the contribution of the population of BHXBs to the CR spectrum, particularly above the knee. A more realistic scenario may allow for a contribution of BHXBs to the CR spectrum that is between our solution and that of C20 (see Figure 4.7).

Finally, we make the following assumptions about the BHXB population that result in deviations to the CR estimate by C20. First, we simplify the problem by assuming a duty cycle, according to which the low-mass BHXBs spend 1 per cent of their time in the so-called hard state based on the information we have so far from the 35 known sources (Tetarenko et al. 2016b, and references therein). For the case of high-mass BHXBs, we assume a duty cycle of 25 per cent, but this is a value that we can hardly constrain because the high-mass BHXBs we observe so far spend most of

their time in the so-called hard state (like the case of Cyg X-1; Grinberg et al. 2015; Cangemi et al. 2021). We further assume that the population of BHXBs is dominated (by 90 per cent) by low-mass sources based on the current observations, whereas C20 only calculate the CR contribution from low-mass BHXBs. It is likely, therefore, that we overestimate the number of low-mass BHXBs that contribute the CR contribution but do not accelerate protons at energies beyond 100 TeV.

#### 4.5.5 Diffuse gamma-ray and neutrino emission from BHXBs

Finding the  $\gamma$ -ray and neutrino sources that contribute to the diffuse emission is important to better constrain the population of sources that accelerate particles to energies of the order of PeV and beyond. H.E.S.S. and *Fermi*/LAT have detected a diffuse  $\gamma$ -ray emission along the Galactic plane whose origin is not clear yet (Abramowski et al. 2016). Such diffuse emission is a natural result of the inelastic interactions between accelerated CRs and the Galactic molecular gas. In this work, we aim to constrain the contribution of the accelerated protons in BHXB jets to this diffuse emission, as well as connect it to the diffuse neutrino emission. Using the publicly available code HERMES, we produce both the  $\gamma$ -ray and the neutrino spectra and compare them to the observational constraints (Figure 4.8 and Figure 4.9, respectively). We see that a population of 1000 BHXBs cannot contribute significantly to the  $\gamma$ -ray emission. Similar to the  $\gamma$ -ray emission, we see that the predicted emission is of the order of 100 below the IceCube observations in the  $\sim 10$  TeV regime.

Future imaging Cherenkov telescopes, such as the Cherenkov Telescope Array (Acharya et al. 2013), water Cherenkov telescopes, such as the Large High Altitude Air Shower Observatory - LHAASO (Bai et al. 2019), as well as cubic kilometer neutrino detectors, such as KM3NeT/ARCA (Adrián-Martínez et al. 2016) and IceCube-Gen2, which will be 5 times more sensitive than the current facilities (IceCube-Gen2 Collaboration et al. 2014; Aartsen et al. 2021), will play a crucial role in further constraining the diffuse emission, and hence lead to a better understanding of CR acceleration.

## 4.6 Summary and Conclusions

Despite the detailed studies over the years, we still do not fully understand the origin of the CRs. CRs that escape the accelerating site, are deflected due to the (extra-)Galactic magnetic field, making it hence impossible to pinpoint their sources. We can however use indirect, multi-messenger means to examine the CR acceleration in astrophysical sources by studying the intrinsic  $\gamma$ -rays and neutrinos produced, as well as the diffuse emission when accelerated CRs interact with the surrounding medium and/or radiation.

In this work, we use the lepto-hadronic, multi-zone jet model of K20, and further

develop it to include the neutrino distributions due to the inelastic pp and p $\gamma$  collisions (Kelner et al. 2006 and Kelner & Aharonian 2008, respectively). We first produce the intrinsic neutrino distributions for the two canonical BHXBs, namely the high-mass Cyg X-1, and the low-mass GX 339-4. We constrain the neutrino emission based on the work of K20 for Cyg X-1 and K22 for GX 339-4, who constrain the proton acceleration in the BHXB jets by reproducing the multiwavelength radio-to- $\gamma$ -ray spectrum. We expand our prediction on the intrinsic neutrino estimates for a list of 35 known BHXBs discovered so far. If the candidate source is a low-mass BHXBs, we use the study-case of GX 339-4, and if the source is high-mass, we use the canonical case of Cyg X-1. We find that Cyg X-1 is a good candidate neutrino source, and in fact, our predicted muon neutrino flux is close to the upper-limits of IceCube. Cubic km neutrino detectors, such as KM3NeT/ARCA in the Northern Hemisphere and IceCube-Gen2 in the Southern Hemisphere, will further test the case of Cyg X-1 in the next decade(s), especially when the source launches two relativistic jets. From the other 34 sources, only one more source (MAXI J1836-194) might warrant further, more detailed investigation.

Recent X-ray observations of the Galactic centre support the existence of hundred-to-thousand BHXBs in quiescence that we do not detect due to their duty cycle. In this work, we assume the existence of 1000 such sources distributed in the Galaxy capable of accelerating CRs following the behaviour of the two prototypical sources. When CRs escape the acceleration sites, they interact with the Galactic molecular gas while they propagate in the Galactic plane, to produce further  $\gamma$ -rays and neutrinos that contribute to the diffuse spectra we detect on Earth. To properly study the CR propagation we use DRAGON2 (Evoli et al. 2017, 2018), and to self-consistently calculate the  $\gamma$ -ray and neutrino counterparts, we use the publicly available code HERMES (Dundovic et al. 2021). These 1000 BHXBs are able to contribute up to some small fraction in the TeV regime of the CR spectrum, but whether they can contribute in the PeV regime strongly depends on the particle acceleration properties that are still poorly constrained. Finally, the exact number of the Galactic BHXBs is not well constrained but according to the early data release of the third catalogue (Gaia Collaboration et al. 2021; Gommel et al. 2022), which includes over 30 million stars, *Gaia* will be able to classify non-single stars and provide a more accurate number of BHXBs in quiescence, all candidate CR sources when they go into outbursts.

## Acknowledgements

DK and SM are supported by the Dutch Research Council (NWO) VICI grant (no. 639.043.513).

## Data availability

The neutrino upper limits and detector sensitivities used in this work are publicly available (see references above). The output of our model and the plotting scripts will be available in Zenodo.

### 4.A Detected BHXBs

In Table 4.2, we show the 35 Galactic BHXBs we examine in this work. We use the WATCHDOG catalogue of Tetarenko et al. (2016b) for the 31 sources that were detected before 2016. We include 4 more sources detected by the Faulkes Telescopes project (Lewis et al. 2008) after 2016. In the same table, we indicate whether the BHXBs is low- (L) or high-mass (H).

**Table 4.2:** The 35 known Galactic BHXBs we use in this work. The values of the Distance, the Mass of the black hole and the inclination are from the WATCHDOG catalogue (see Tetarenko et al. 2016b, and references therein) for the first 31 sources, but we use the updated values of Miller-Jones et al. (2021) for Cyg X-1. When the exact distance is unknown, Tetarenko et al. (2016b) assume 5 kpc, when the mass is unknown, they assume  $8 M_{\odot}$ , and when the inclination is unknown, they assume  $60^{\circ}$ . We indicate these values with italics. MAXI J1820+070 (Atri et al. 2020), MAXI J1348-630 (Belloni et al. 2020), MAXI J1535-571 (Chauhan et al. 2019) and MAXI J1828-249 (Oda et al. 2019) were detected after 2016 and are not in the WATCHDOG catalogue. The last column indicates the nature of the companion, where L is for low-mass and H is for high-mass.

Name	Dec (J2000)	RA (J2000)	Distance (kpc)	$M_{\text{BH}}$ ( $M_{\odot}$ )	Inclination (deg)	Companion
1A 0620-00	-00 20 44.72	06 22 44.503	1.06	6.6	51	L
XTE J1118+480	+48 02 12.6	11 18 10.80	1.7	7.3	75.0	L
SWIFT J1357.2-0933	-09 19 12.00	13 57 16.818	3.9	8.0	60.0	L
MAXI J1543-564	-56 24 48.35	15 43 17.336	5	8.0	60.0	L
XTE J1550-564	-56 28 35.0	15 50 58.78	4.4	10.4	67.4	L
4U 1630-472	-47 23 34.8	16 34 01.61	5	8.0	60.0	L
XTE J1650-500	-49 57 43.6	16 50 00.98	2.6	4.7	75.2	L
GRO J1655-40	-39 50 44.90	16 54 00.137	3.2	5.4	69	L
GX 339-4	-48 47 22.8	17 02 49.36	8	8.0	60.0	L
IGR J17091-3624	-36 24 24.	17 09 08.	5	8.0	60.0	L
GRS 1716-249	-25 01 03.4	17 19 36.93	2.4	8.0	60.0	L
XTE J1720-318	-31 45 01.25	17 19 58.994	5	8.0	60.0	L
1E 1740.7-2942	-29 44 42.6	17 43 54.83	5	8.0	60.0	L

Table 4.2: continued.

Name	Dec (J2000)	RA (J2000)	Distance (kpc)	$M_{\text{BH}}$ ( $M_{\odot}$ )	Inclination (deg)	Companion
Swift J174510.8-262411	-26 24 12.60	17 45 10.849	5	8.0	60.0	L
CXOGC J174540.0-290031	-29 00 31.0	17 45 40.03	8	8.0	60.0	L
H 1743-322	-32 14 00.60	17 46 15.608	10.4	8.0	60.0	L
XTE J1752-223	-22 20 32.782	17 52 15.095	3.5	9.6	60.0	L
Swift J1753.5-0127	-01 27 06.2	17 53 28.29	5	8.0	60.0	L
GRS 1758-258	-25 44 36.1	18 01 12.40	5	8.0	60.0	L
SAX J1819.3-2525 (V4641 Sgr)	-25 24 25.8	18 19 21.63	6.2	6.4	72.3	H
MAXI J1836-194	-19 19 12.1	18 35 43.43	5	8.0	9.5	L
XTE J1859+226	+22 39 29.4	18 58 41.58	8	10.8	60	L
XTE J1908+094	+09 23 04.90	19 08 53.077	6.5	8.0	60.0	L
SS 433	+04 58 57.9	19 11 49.57	5.5	8.0	60.0	L
GRS 1915+105	+10 56 44.8	19 15 11.55	8.6	12.4	70	L
4U 1956+350 (Cyg X-1)	+35 12 05.778	19 58 21.675	2.22	21.4	27.1	H
GS 2000+251	+25 14 11.3	20 02 49.58	2.7	8.4	60.0	L
GS 2023+338 (V404 Cyg)	+33 52 02.2	20 24 03.83	2.39	7.2	80.1	L
4U 2030+40 (Cyg X-3)	+40 57 27.9	20 32 25.78	8.3	2.4	43	H

Table 4.2: continued.

Name	Dec (J2000)	RA (J2000)	Distance (kpc)	$M_{\text{BH}}$ ( $M_{\odot}$ )	Inclination (deg)	Companion
MWC 656	+44 43 18.25	22 42 57.30	2.6	5.4	66	H
MAXI J1820+070	7.18563	275.091	2.96	9.2	63	L
MAXI J1348-630	-63.274	207.054	5.3	9.1	60	L
MAXI J1535-571	-57.23	233.832	4.1	10.4	45	L
MAXI J1828-249	-25.029	277.244	7.0	9.0	60	L

## 4.B Neutrino backgrounds

### 4.B.1 Atmospheric neutrino background

The spectrum of the lower neutrino energies is dominated by the so-called conventional atmospheric background, which is due to the decay of kaons and charged pions (Gaisser et al. 2016). The best fit of this flux is (Feyereisen et al. 2017):

$$\frac{d\Phi_\nu}{dE_\nu} = 2 \times 10^{-14} \left( \frac{E_\nu}{10 \text{ TeV}} \right)^{-3.7} \text{ GeV}^{-1} \text{ cm}^{-2} \text{ s}^{-1} \text{ sr}^{-1} \quad (4.4)$$

where the normalization is set by the 10 TeV  $\nu_\mu$  flux. The power-law index changes to 3.9 for neutrino energies higher than 1 PeV.

### 4.B.2 Astrophysical neutrino background

The total all-flavor neutrino and anti-neutrino astrophysical spectrum was studied by the IceCube collaboration (Aartsen et al. 2015) using both track-like (muon) and shower-like (electron) events in the TeV-PeV range, between 2009 (with the 59-string configuration) and 2012 (with the full 86-string configuration). It has recently been extended to 7.5 yr of operation and the unbroken power-law best fit of the flux for the 7.5 yr sample is (Schneider 2019):

$$\frac{d\Phi_{6\nu}}{dE_\nu} = 6.45_{-0.46}^{+1.46} \times 10^{-18} \left( \frac{E_\nu}{100 \text{ TeV}} \right)^{-(2.89_{-0.19}^{+0.20})}, \quad (4.5)$$

where the uncertainties correspond to the  $1\sigma$  confidence interval and the units are the same as Equation 4.4.

The total astrophysical muon neutrino and anti-neutrino flux was presented by the IceCube collaboration using track-like events in the neutrino energy range of 194 TeV and 7.8 PeV, between 2009 and 2015 (Aartsen et al. 2016). It has recently been updated to the almost 10-yr sample and the best fit flux is (Stettner 2019):

$$\frac{d\Phi_{\nu_\mu + \bar{\nu}_\mu}}{dE_\nu} = 1.44_{-0.24}^{+0.25} \times 10^{-18} \left( \frac{E_\nu}{100 \text{ TeV}} \right)^{-(2.28_{-0.09}^{+0.08})}, \quad (4.6)$$

with the same units as Equation 4.4.

### 4.B.3 Diffuse neutrino spectrum

Cosmic rays in the Galactic plane interact with their ambient medium producing a diffuse  $\gamma$ -ray emission (Ackermann et al. 2012; Abramowski et al. 2016). The  $\gamma$ -ray spectrum along the Galactic plane (Prodanović et al. 2007; Abdo et al. 2008) can be explained by a radial dependence of the diffusion of the CRs (Gaggero et al. 2015;



Luque et al. 2022). This model, referred to as  $\text{KRA}_\gamma$ , manages to reproduce the  $\gamma$ -ray spectrum as well as predicts the diffuse neutrino emission from the Galactic plane (Gaggero et al. 2015; Albert et al. 2018). The primary CR distribution is assumed to have an exponential cutoff at a certain energy.

Based on this model, IceCube and ANTARES released the upper limits at the 90 percent confidence level for the three-flavor neutrino flux (Adrián-Martínez et al. 2016; Aartsen et al. 2017b; Albert et al. 2018). According to IceCube the best fit is achieved with an exponential cutoff at 50 PeV ( $\text{KRA}_\gamma^{50}$ ), whereas according to ANTARES at 5 PeV ( $\text{KRA}_\gamma^5$ ).

## 4.C Contribution from individual sources

For the soft proton power law (upper panel of Figure 4.12), we see that the high-mass BHXBs Cyg X-1, MWC 656 (Aleksić et al. 2015), and SAX J1819.3-2525 (Orosz et al. 2001) are the sources that mainly contribute to the total neutrino spectrum (solid black line). For the hard proton power law (bottom panel of Figure 4.12), Cyg X-1 dominates the neutrino emission.

## 4.D Maximum CR energy from a high-mass BHXB

In Figure 4.13, we show the inverse of the acceleration and escape timescale similar to Figure 4.11 but for the case of a high-mass BHXB based on K20. Overall, the maximum CR energy ranges between 1 TeV and 10 PeV. See Section 4.5 for a more coherent discussion.

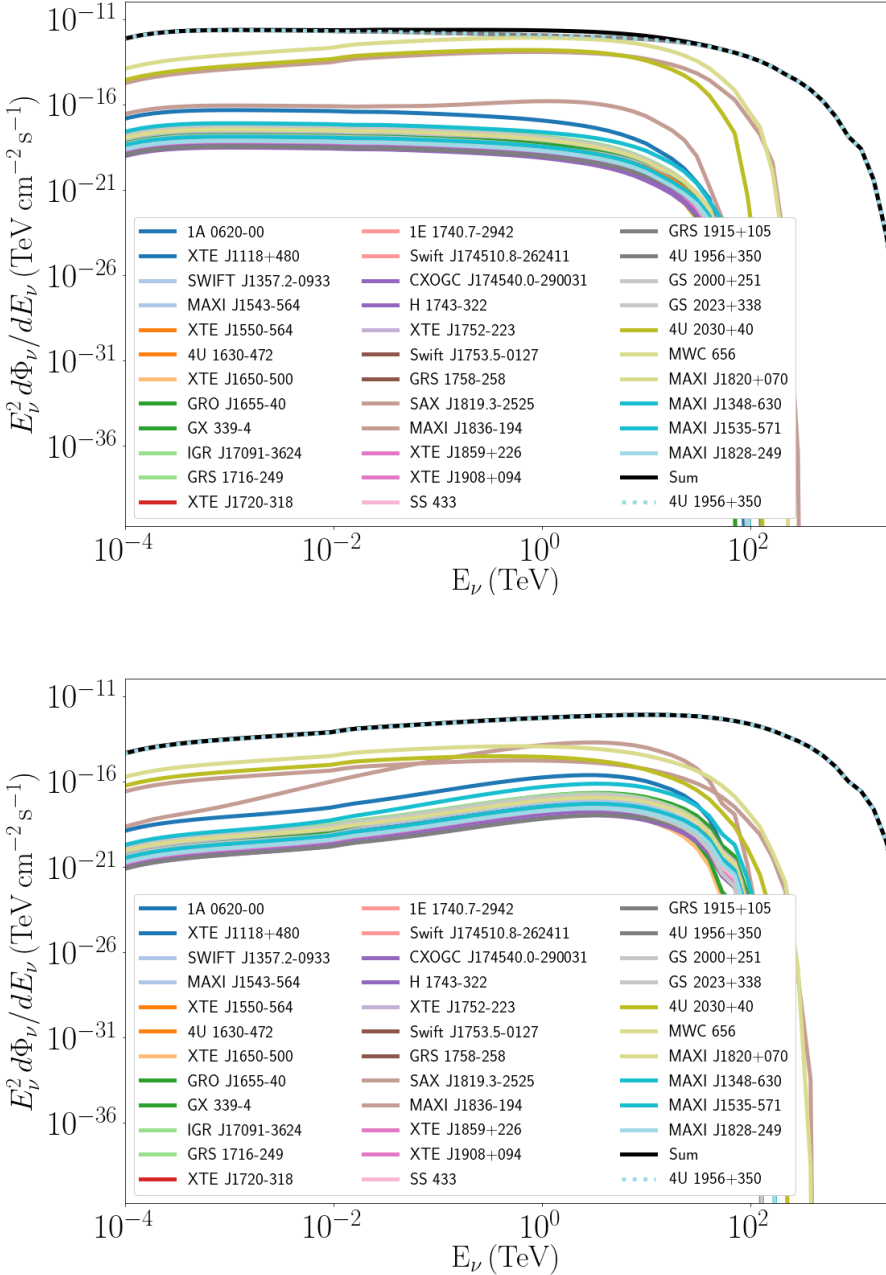


**Figure 4.12:** Contribution of all known sources to the total intrinsic  $\nu_\mu + \bar{\nu}_\mu$  spectrum, assuming a soft power law of accelerated protons ( $p = 2.2$ ) for the top figure and a hard ( $p = 1.7$ ) for the bottom figure.

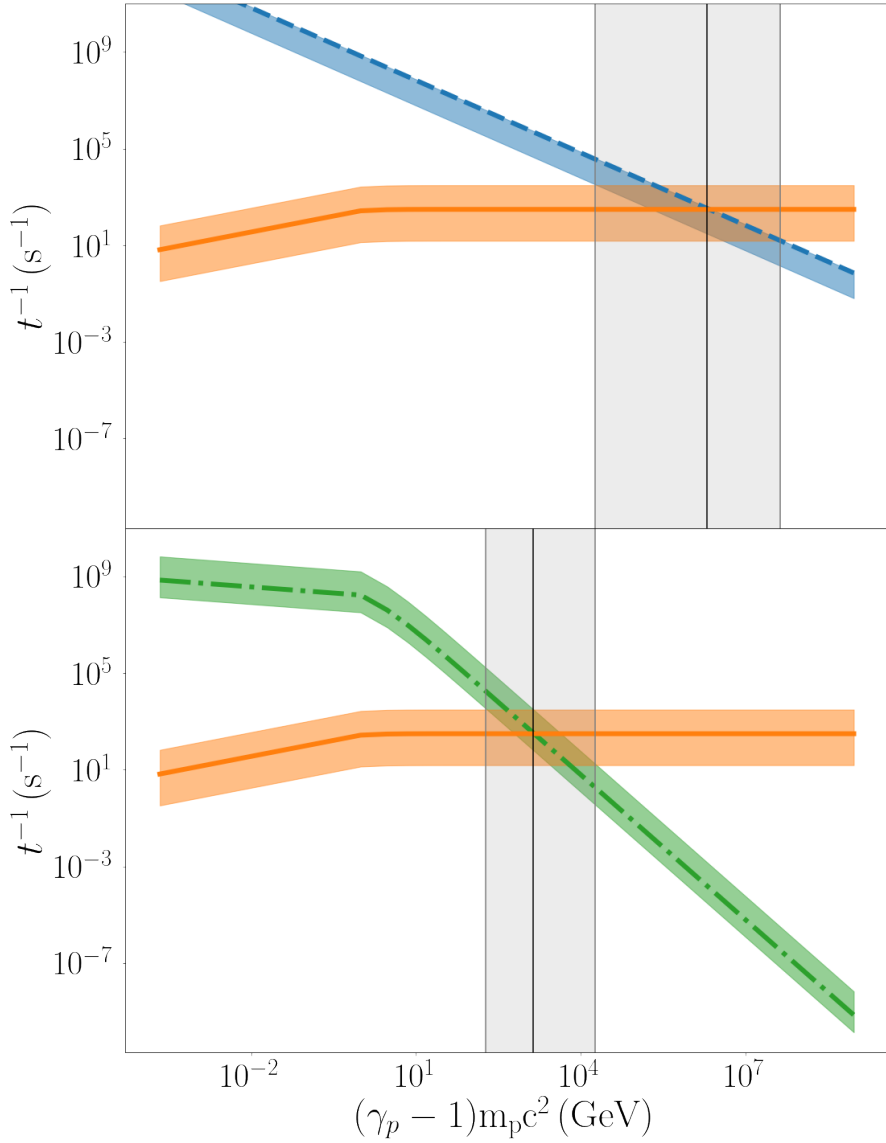


**Figure 4.13:** Similar to Figure 4.11 but for high-mass BHXBs. Both mechanisms allow for maximum proton energy between 1 TeV and 10 PeV.



## Exploring the role of composition and mass-loading on the properties of hadronic jets

D. Kantzas, S. Markoff, M. Lucchini, C. Ceccobello & K. Chatterjee

*Submitted to Monthly Notices of the Royal Astronomical Society*

### *Abstract*

Astrophysical jets are relativistic outflows that remain collimated for remarkable orders of magnitude. Jets that are connected to both supermassive black holes in the centre of galaxies and stellar-mass black holes harboured in X-ray binaries, are among the candidate sources of cosmic rays (CRs). Despite decades of research, the origin of CRs remains unclear, but jets are viable sites of particle acceleration. When CRs accelerate in astrophysical jets, they initiate particle cascades that form  $\gamma$ -rays and neutrinos. In the so-called hadronic scenario, the population of accelerated CRs requires a significant amount of energy to properly explain the spectral constraints similarly to a purely leptonic scenario. The amount of energy required, often exceeds the Eddington limit, or even the total energy available by the jets. The exact energy source for the accelerated protons is unclear, but due to energy conservation along the jets, it is believed to come from the jet itself in the form of dissipated magnetic or kinetic energy from the outflow. To address this hadronic energy issue and to self-consistently evolve the energy flux along the flows, we explore a novel treatment for including hadronic content, in which instabilities along the jet/wind border play a critical role. We discuss the impact of the different jet composition on the jet dynamics for a pair dominated and an electron-proton jet, and consequently the emitted spectrum, accounting for both leptonic and hadronic processes. Finally, we discuss the implications of this mass-loading scenario to address the proton energy issue.

## 5.1 Introduction

Accreting black holes can efficiently launch relativistic outflows, known as astrophysical jets, by converting gravitational energy to kinetic energy. Large-scale jets launched by supermassive black holes (SMBH) share some common physical laws to the small-scale jets launched by stellar-mass black holes in X-ray binaries (BHXBs; Heinz & Sunyaev 2003; Merloni et al. 2003; Falcke et al. 2004), and hence black hole jets appear to be scale invariant in some of their properties. For example, SMBHs with masses of the order of  $\sim 10^6 - 10^9 M_\odot$  power jets that remain collimated up to Mpc scales (Waggett et al. 1977), whereas BHXBs with mass of the order of a few solar masses display jets that remain collimated up to sub-pc scales (Mirabel & Rodriguez 1994). Galactic BHXBs are of particular importance because they transition between different jetted and non-jetted states over human-like timescales, giving us the chance to understand plasma evolution in extreme conditions and better probe jet physics (see, e.g., Markoff et al. 2001, 2003, 2005; Reig et al. 2003; Giannios et al. 2004; Maitra et al. 2009; Vila & Romero 2010; Zdziarski et al. 2014a; Connors et al. 2019; Lucchini et al. 2021).

The exact physical mechanism responsible for jet launching is not clear yet. On one hand, the Blandford-Znajek mechanism (Blandford & Znajek 1977) describes a way to extract the rotational energy of a spinning black hole and power relativistic jets that can be pair-plasma dominated (see, e.g., Broderick & Tchekhovskoy 2015; Parfrey et al. 2019). On the other hand, magnetic fields anchored in the accretion disc can launch baryon-dominated jets via the Blandford-Payne mechanism (Blandford & Payne 1982). The difference in jet composition from the two launching mechanisms would have an important impact on the interpretation of the spectral energy distribution (SED) observed from such black hole systems as well as the consideration of relativistic jets as candidate sources of cosmic rays (CRs).

CRs are charged particles that exhibit a large range of energies up to ultra-high energies of the order of  $10^{20}$  eV (The Pierre Auger Observatory et al. 2017; Abbasi et al. 2020). The detected CR spectrum shows two very prominent features, known as the “knee” and the “ankle” where the spectrum steepens and hardens, respectively. The “knee” is observed at  $10^{15}$  eV (PeV) and is likely to be the maximum energy that CR protons accelerated in Galactic sources can reach, but the identification of these particular sources remains a mystery despite the decades of studies. The “ankle”, located at  $\sim 10^{18}$  eV (EeV), is where extragalactic sources are thought to start dominating the spectrum. The exact CR composition is not clear and strongly depends on the particle energy. GeV CRs primarily consist of protons ( $\sim 99$  per cent; Shikaze et al. 2007), with electrons and positrons mainly contributing to the rest of the spectrum. It is likely that heavier elements/ions accelerated in Galactic sources start dominating the CR spectrum between the “knee” and the “ankle” (Aloisio et al. 2012), beyond which the composition is unclear (Abbasi et al. 2019; Yushkov et al.

2019; Corstanje et al. 2021).

Similar to large-scale jets of active galactic nuclei (AGN), which are among the dominant candidate sources of the extragalactic CRs (Protheroe & Kazanas 1983), recent studies suggest the small-scale jets of BHXBs as potential CR acceleration sites (Romero et al. 2003; Fender et al. 2005; Cooper et al. 2020). There are currently only a few tens of Galactic BHXBs detected in the Milky Way (Tetarenko et al. 2016b), but population-synthesis simulations (see, e.g., Olejak et al. 2020) suggest that a few thousand black holes likely reside in the Galactic disc, in agreement with the recent X-ray observations of the Galactic centre by Hailey et al. (2018) and Mori et al. (2021). Based on such observations, Cooper et al. (2020) proposed that a few thousand BHXBs are capable of contributing to the observed CR spectrum above the “knee”.

Whether or not BHXBs jets can indeed accelerate CRs up to the “knee”, and AGN jets beyond the “ankle”, strongly depends on two further issues: (1) can astrophysical jets, in general, accelerate particles to high energies, and (2) are astrophysical jets actually comprised of protons and/or heavier elements? On the former, observations of non-thermal emission from radio bands (see, e.g., Lister et al. 2016) up to GeV/TeV  $\gamma$ -rays from both SMBHs (see, e.g., Lister et al. 2009) and BHXBs (see, e.g., Zanin et al. 2016), suggest that both classes of jets can efficiently accelerate particles. Numerous numerical studies, moreover, suggest that jets can indeed be viable sites of particle acceleration either via shocks (Hillas 1984), or via magnetic reconnection (Drenkhahn & Spruit 2002; Guo et al. 2014; Sironi & Spitkovsky 2014; Matthews et al. 2020).

The jet composition however remains an open question. The two different proposed launching mechanisms mentioned above yield an entirely different jet content at the base that significantly alters not only the jet dynamics, but the emitted spectrum as well (Petropoulou et al. 2019). A pair-dominated jet would allow only for leptonic processes, such as synchrotron and inverse Compton scattering (ICS; Blumenthal & Gould 1970). A leptonic plus hadronic jet, on the other hand, allows for further non-thermal processes, when inelastic collisions occur between the accelerated protons and the cold flow or radiation (e.g., Mannheim 1993; Rachen & Biermann 1993; Mannheim & Schlickeiser 1994; Rachen & Mészáros 1998). Such hadronic processes can lead to the production of astrophysical neutrinos, but usually require a much larger jet energy budget than the leptonic ones, sometimes requiring super-Eddington jet powers (Böttcher et al. 2013; Liodakis & Petropoulou 2020). Such super-Eddington powers challenge the accretion paradigm (Zdziarski & Böttcher 2015), but they still seem feasible for relativistic AGN jets (Ghisellini et al. 2014).

Several BHXB jets, such as the peculiar case of SS433 or the prototypical Cygnus X–1, show evidence of baryonic jet content (Fabrika 2004 and Gallo et al. 2005; Heinz 2006, respectively). Both the compact objects of SS433 and Cygnus X–1 are accompanied by a high mass donor star that may be the source of the heavy composition through its stellar wind. There is evidence of baryon-loaded jets though, even in

the case of a low-mass companion, such as the black hole candidate 4U 1630–47, based on iron emission lines (Díaz Trigo et al. 2013). The cases of MAXI J1820+070 (Tetarenko et al. 2021; Zdziarski et al. 2022b), MAXI J1836–194 (Lucchini et al. 2021), XTE J1752–223, MAXI J1659–152, and XTE J1650–500 (Cao et al. 2021b) on the other hand, favour a jet composition of the order of a few to a few tens of pairs per proton based on energetic arguments.

The composition is also difficult to constrain in extragalactic jets. Circular polarisation measurements indicate that the jets of the blazar 3C 279 are pair-dominated (Liodakis et al. 2021), and energetic arguments of the radio galaxy 3C 120 are consistent with a pair-dominated jet (Zdziarski et al. 2022a). Celotti & Fabian (1993), on the other hand, based on very-large baseline interferometry and spectral arguments for numerous sources, support an electron-proton plasma. The blazar TXS 0506+056, finally, due to the correlation with the high-energy neutrino IceCube-170922A, supports a baryon content in its jets as well (Aartsen et al. 2018).

Currently, the state-of-the-art to model jet launching and dynamics in a more *a priori* way are high-resolution simulations that solve the magneto hydrodynamic equations in the general relativistic regime (GRMHD). Such simulations have furthered our understanding of the accretion-launching paradigm and have shown that a Poynting flux dominated outflow can convert a significant amount of its initial magnetic energy into kinetic to accelerate the bulk flow (McKinney 2006; Komissarov et al. 2007; Tchekhovskoy et al. 2008, 2009; Komissarov et al. 2009). The same simulations, have established that the accretion disc can significantly impact the spatial evolution of the jets not only at  $r_g$ -scale distances ( $r_g = GM_{\text{bh}}/c^2$ , where  $M_{\text{bh}}$  is the mass of the black hole), but also further out. In particular, Chatterjee et al. (2019, hereafter CLTM19) performed a series of high-resolution GRMHD simulations of strongly magnetised systems to better understand the loading of jets with matter from the wind of the accretion disc. When the jets propagate in a medium, pinch instabilities can occur in the interface between the jet and the ambient medium to give rise to eddies that eventually allow for matter to entrain the jet (Eichler 1993; Spruit et al. 1997; Begelman 1998; Giannios & Spruit 2006; CLTM19; Sironi et al. 2021). Such mass entrainment can significantly affect the jet kinematics and hence the non-thermal emission.

Such GRMHD simulations, though, usually make the ideal gas assumption and therefore cannot capture dissipative processes like particle acceleration self-consistently. Kinetic simulations of particles-in-cell (PIC), on the other hand, calculate the trajectories of individual particles based on first principles, allowing for a more detailed and comprehensive understanding of the relativistic outflows. Both GRMHD and PIC simulations, however, are very computational expensive, and they cannot easily be compared to observations through statistical methods that explore the full parameter phase space.

In this work, we develop a new treatment for incorporating mass-loading and thus



evolving compositions in jets, and apply it to a multi-zone jet model. This treatment is inspired by recent GRMHD simulations such as [CLTM19](#), to explore jet composition and its impact on the total jet power as well as its electromagnetic emission. In particular, we build on the multi-zone jet model developed by Markoff et al. (2005) that relies on the pioneering ideas of Blandford & Königl (1979), Hjellming & Johnston (1988), and Falcke & Biermann (1995). After many developments, the latest version of the model is **BHJet** (Lucchini et al. 2022), a multi-zone jet model that better connects the jet acceleration and jet physical quantities to the radiative output. For the first time, we connect the physically motivated model **BHJet** with hadronic acceleration, accounting for self-consistent energy conservation. We further present **HadJet**, a multi-zone, lepto-hadronic, mass-loaded jet model. In this work, we discuss the main physical properties of both models and how **HadJet** can be used to address the jet-power crisis of lepto-hadronic models.

The paper is structured as follows. In Section 5.2 we describe the semi-analytical calculations for the magnetically accelerated jet accounting for both leptonic and hadronic acceleration and radiative processes. We present the results of the above jet model in Section 5.3. In Section 5.4, we describe the details of the mass-loaded jet model (**HadJet**) and present the results in Section 5.5. Finally, in Section 5.6 we discuss the implication of our new models on the proton power issue and conclude in Section 5.7.

## 5.2 Magnetically accelerated steady-state jets

We assume two initially cold, Poynting flux dominated jets of either leptonic or lepto-hadronic content, that accelerate up to some maximum velocity because of magnetic energy dissipation (Vlahakis & Königl 2003; McKinney 2006; Komissarov et al. 2007). At the region where the bulk velocity reaches the maximum value (acceleration region henceforth, denoted by  $z_{\text{acc}}$ ), we further assume that energy is also dissipated to accelerate particles to non-thermal energies (Blandford & Rees 1974; Begelman et al. 1984). With our formalism, we cannot capture whether the magnetic energy dissipates immediately to particle acceleration (as in the case of magnetic reconnection) or if magnetic energy dissipates to kinetic energy first and this extra kinetic energy dissipates to particle acceleration through shocks (Bogovalov & Tsinganos 2005). We assume instead that the total energy of the jet is conserved at the particle acceleration region. From this point outwards along the jets, we assume a constant particle acceleration rate and discuss below how this assumption affects the evolution of both the jet velocity and magnetic field. In Table 5.1, we define all the parameters and their fiducial values (if applicable) that we use in this section.

### 5.2.1 Jet dynamical properties

Based on both semi-analytical and numerical calculations, the bulk jet Lorentz factor  $\gamma$  is expected to scale approximately as  $z^{1/2}$ , where  $z$  is the distance along the jet (Beskin & Nokhrina 2006; McKinney 2006). We parametrise the jet Lorentz factor as Lucchini et al. (2018) (and see also Potter & Cotter 2012)

$$\gamma(z \leq z_{\text{acc}}) = \gamma_0 + (\gamma_{\text{acc}} - \gamma_0) \frac{z^{1/2} - z_0^{1/2}}{z_{\text{acc}}^{1/2} - z_0^{1/2}}, \quad (5.1)$$

where  $\gamma_0$  is the initial Lorentz factor at the jet base and  $z_0$  is the distance of the jet base from the black hole and  $\gamma_{\text{acc}}$  is the maximum bulk Lorentz factor at  $z_{\text{diss}}$ . We assume that the jets launch initially with the speed of sound, which for a relativistic flow with adiabatic index  $4/3$  is equal to  $0.43c$ , or  $\gamma_0 = 1.11$  (Crumley et al. 2017).

The jets are thus set to be initially parabolic while they accelerate and become conical when they achieve  $\gamma_{\text{acc}}$  (Komissarov et al. 2009). We express the cross-sectional radius of the jet along the jet axis as

$$r = r_0 + (z - z_0) \tan(\theta), \quad (5.2)$$

where  $r_0$  is the radius of the jet base and  $\theta$  is the opening angle of the jets. Based on very long baseline interferometry observations and the Monitoring of jets in AGN with VLBA Experiments (MOJAVE; see, e.g., Pushkarev et al. 2009, 2017), we set the jet opening angle to be

$$\theta = \frac{0.15}{\gamma}. \quad (5.3)$$

While the number of particles along the jet is conserved, we express the number density of leptons as

$$n = n_0 \left( \frac{\gamma\beta}{\gamma_0\beta_0} \right)^{-1} \left( \frac{r}{r_0} \right)^{-2}, \quad (5.4)$$

where  $\beta$  is the jet velocity normalized to the speed of light and  $n_0$  is the initial number density. We calculate  $n_0$  by the power  $L_{\text{jet}}$  injected at the jet base in the comoving frame

$$L_{\text{jet}} = 2\beta_0\gamma_0 c\pi r_0^2 \omega_0 \quad (5.5)$$

where we account for two identical jets (hence the factor of 2), and  $n_0$  depends on  $L_{\text{jet}}$  and the initial conditions of the jet base as written out below. We write the jet enthalpy  $\omega$  as (Falcke & Biermann 1995; Crumley et al. 2017)

$$\omega = \rho c^2 + U_j + P_j = \rho c^2 + U_p + P_p + U_e + P_e + U_B + P_B, \quad (5.6)$$

where  $U_j = U_p + U_e + U_B$  is the total internal jet energy density and  $P_j = P_p + P_e + P_B$  is the total jet pressure. In the above equation,  $\rho$  is the jet mass density

$$\rho = n_p m_p + n_e m_e. \quad (5.7)$$

We express the number of protons in terms of the number of leptons as  $n_p = n_e/\eta_e$ , where  $n_{e/p}$  is the number density of leptons/protons, respectively, and  $\eta_e \geq 1$  is a free parameter that remains constant unless the jets are mass-loaded (see below).

For an ideal gas, we can write the pressure terms as

$$P_{e,p} = (\Gamma_{e,p} - 1) U_{e,p}, \quad (5.8)$$

where  $\Gamma_{e,p}$  is the adiabatic index. For the rest of the paper, we assume a relativistic pair content ( $\Gamma_e = 4/3$ ) at the jet base and a cold proton population ( $\Gamma_p = 5/3$ ) until the particle acceleration region (see below). For the pair temperatures we are interested in this work, the flow remains cold even if is dominated by pairs at the base. For  $U_B = P_B = B^2/8\pi$ , we write the jet enthalpy as

$$\omega = \rho c^2 + \Gamma_p U_p + \Gamma_e U_e + \frac{B^2}{4\pi}. \quad (5.9)$$

We define the specific enthalpy of the gas as

$$h = \frac{U_g + P_g}{\rho c^2} = \frac{\Gamma_p U_p + \Gamma_e U_e}{\rho c^2} \quad (5.10)$$

where we used Equation 5.8. We calculate  $U_{e,p}$  by computing the integral

$$U_{e,p} = \int \frac{dn_{e,p}}{d\varepsilon_{e,p}} \varepsilon_{e,p} m_{e,p} c^2 d\varepsilon_{e,p}. \quad (5.11)$$

where  $\varepsilon_{e,p}$  is the Lorentz factor of the particles, but we can also express the internal energy density in terms of the average total energy of the particles

$$U_{e,p} \simeq (\langle \varepsilon_{e,p} \rangle - 1) n_{e,p} m_{e,p} c^2, \quad (5.12)$$

where  $\langle \varepsilon_{e,p} \rangle$  is the average Lorentz factor of the pairs/protons of the jet segment (see below for calculation). This equation is more convenient than Equation 5.11 for the following discussion, however we note that it might not be accurate enough if a significant fraction of the leptons accelerate to non-thermal energies, in particular in a hard power law with slope  $< 2$ .

A useful parameter to characterise the jets is the magnetisation. We define the magnetisation of a flow as the Poynting flux over the total energy flux (Nokhrina et al. 2015)

$$\sigma = \frac{B^2}{4\pi(\rho c^2 + U_g + P_g)} \Rightarrow \quad (5.13)$$

$$\sigma = \frac{B^2}{4\pi\rho c^2(1+h)}. \quad (5.14)$$

When the flow is cold ( $h \ll 1$ ), the above definition reduces to the well-known expression of

$$\sigma_c \simeq \frac{B^2}{4\pi\rho c^2}. \quad (5.15)$$

We write the enthalpy of Equation 5.9 of a flow from Equations 5.10 and 5.14 as

$$\omega = \rho c^2(1+\sigma)(1+h). \quad (5.16)$$

We can plug this equation into Equation 5.5 to calculate the particle number density at the jet base

$$n_0 = \frac{L_{\text{jet}}}{2\beta_0\gamma_0 c\pi r_0^2 (m_p/\eta_e + m_e)c^2(1+\sigma_c)}. \quad (5.17)$$

We further use the relativistic Bernoulli's equation to express the conservation of energy flux along the jet axis (Königl 1980)

$$\gamma \frac{\omega}{\rho} = \text{constant}, \quad (5.18)$$

and from Equation 5.16

$$\mu = \gamma(1+\sigma)(1+h), \quad (5.19)$$

where  $\mu$  is the normalised total energy flux and is conserved along the jets (unless the jets entrain mass; see below). In a cold jet where the specific enthalpy  $h$  is negligible, Equation 5.19 simplifies to  $\mu \simeq \gamma(1+\sigma_c)$ . This is a very well-known equation to express the maximum jet Lorentz factor when the majority of the Poynting flux has been converted to kinetic energy ( $\gamma_{\text{max}} \simeq \mu$ ). In this work, we keep this term in our calculations because  $h$  is an estimate of the energy that the accelerated particles carry in each jet segment, and in numerous instances can dominate both the magnetisation and the jet Lorentz factor.

While the jets accelerate between the launching point and the acceleration region  $z_{\text{acc}}$ ,  $\mu$  remains constant. We write Equation 5.19 at the jet base and equate it to the acceleration region and solve for the initial magnetisation

$$\sigma_0 = \frac{\gamma_{\text{acc}}}{\gamma_0} (1 + \sigma_{\text{acc}}) \left( \frac{1 + h_{\text{acc}}}{1 + h_0} \right) - 1, \quad (5.20)$$

and in general for every  $z$  below the acceleration region

$$\sigma(z \leq z_{\text{acc}}) = \frac{\gamma_0}{\gamma} (1 + \sigma_0) \left( \frac{1 + h_0}{1 + h} \right) - 1, \quad (5.21)$$

or

$$\sigma(z \leq z_{\text{acc}}) = \frac{\gamma_{\text{acc}}}{\gamma} (1 + \sigma_{\text{acc}}) \left( \frac{1 + h_{\text{acc}}}{1 + h} \right) - 1. \quad (5.22)$$

With the magnetisation and the specific enthalpy at the acceleration region as free parameters ( $\sigma_{\text{acc}}$  and  $h_{\text{acc}}$ , respectively), we set the initial magnetisation  $\sigma_0$  required for the flow to be Poynting flux dominated and to carry enough energy to efficiently accelerate particles to non-thermal energies. In particular, we use  $\sigma_{\text{acc}}$  as a free parameter because this is the simplest way to force our semi-analytical model to have dissipated the majority of the magnetisation at the acceleration region, and we set  $h_{\text{acc}}$  from Equation 5.10 (see also the discussion on particle acceleration below). The initial specific enthalpy  $h_0$  is set by the free parameters at the jet base, and as we discuss below, it is negligible for the standard case of an initially cold jet that we study here (see subsection 5.3.1).

Above the acceleration region, we assume the toroidal component dominates the poloidal component of the magnetic fields similar to Blandford & Königl (1979), so

$$B(z > z_{\text{acc}}) = B_{\text{acc}} \left( \frac{z}{z_{\text{acc}}} \right)^{-1}, \quad (5.23)$$

where  $B_{\text{acc}}$  is the magnetic field strength at the acceleration region.

Based on Equation 5.14, we generalize the expression of  $\sigma$  for every  $z$  above the acceleration region

$$\sigma(z \geq z_{\text{acc}}) = \sigma_{\text{acc}} \frac{\rho_{\text{acc}}(1 + h_{\text{acc}})}{\rho(1 + h)} \left( \frac{z}{z_{\text{acc}}} \right)^{-2}. \quad (5.24)$$

## 5.2.2 The acceleration region and particle acceleration

We assume that the pairs at the jet base follow a Maxwell-Jüttner distribution (MJ; the relativistic regime of the Maxwell-Boltzmann distribution) with a peak energy  $k_B T_e$  that is a free parameter. The population of protons on the other hand is cold, making the flow cold at the launching point.

By the time the flow reaches the acceleration region the Poynting flux dominated flow has dissipated the magnetic energy thus the magnetisation has dropped to a value  $\sigma_{\text{acc}}$ . At the same region, we assume a constant fraction  $f_{\text{pl}} \sim 0.1$  of particles accelerates to a non-thermal power law between a minimum and a maximum energy. For the leptonic scenario, we assume that only pairs accelerate in a power law from an energy  $\varepsilon_{\text{min}} m_e c^2 = k_B T_e$  to some  $\varepsilon_{\text{max}}$  that we calculate self-consistently by equating the acceleration timescale  $4\varepsilon m_e c^2 / (3f_{\text{sc}} e c B)$  to the escape timescale (Jokipii 1987; Aharonian 2004). The acceleration efficiency  $f_{\text{sc}}$  depends on the particle acceleration mechanism, but we fix it at a value between 0.01 and 0.1 leading to a maximum electron energy of the order of GeV for the case of a BHXB. For the lepto-hadronic

scenario, we assume that protons accelerate as well in a power law from an  $\varepsilon_{\min} = 1$  to some  $\varepsilon_{\max}$  that we calculate by equating the acceleration timescale to the (lateral) escape timescale  $r/c$  of the jet segment and for the case of BHXBs it may attain values of the order of 100 TeV and above (Pepe et al. 2015; Kantzas et al. 2020, 2022). We constrain the non-thermal particle distributions by assuming that they extend up to the maximum energy, and then they drop exponentially

$$\frac{dn(\varepsilon)}{d\varepsilon} = K\varepsilon^{-p} \exp(-\varepsilon/\varepsilon_{\max}), \quad (5.25)$$

where  $n$  is the particle number density for any species,  $K$  is the normalisation, and the slope  $p$  of the power law depends on the particle acceleration mechanism, but we use it as a free parameter between 1.7 and 2.4, assuming it remains the same between electrons and protons.

Finally, we derive the average Lorentz factor for every species from the equation

$$\langle\varepsilon\rangle = \frac{\int \varepsilon \frac{dn}{d\varepsilon} d\varepsilon}{\int \frac{dn}{d\varepsilon} d\varepsilon}. \quad (5.26)$$

### 5.2.3 Jet evolution and particle acceleration

Beyond the acceleration region where particles accelerate to non-thermal energies as well, the specific enthalpy can become important because the average Lorentz factors of pairs and/or protons may have significantly increased (see Equation 5.10). We write the bulk Lorentz factor for every jet segment above the acceleration region for an outflow from Equation 5.19:

$$\gamma(z) = \gamma_{\text{acc}} \left( \frac{1 + h_{\text{acc}}}{1 + h} \right) \left( \frac{1 + \sigma_{\text{acc}}}{1 + \sigma} \right). \quad (5.27)$$

### 5.2.4 Radiative Processes

We suggest the interested readers to seek for further details on the radiative processes in Lucchini et al. (2022) for the leptonic processes, and in Kantzas et al. (2020) for the hadronic processes. We nevertheless briefly discuss the main processes here for completeness.

#### 5.2.4.1 Leptonic processes

The main three radiative processes of leptonic nature that we require in our analysis here are: synchrotron radiation, inverse Compton scattering (ICS) and pair production. In particular, the thermal pairs of the MJ distribution and the non-thermal

**Table 5.1:** The definition of the jet quantities we use in this work with their units, some fiducial values (if applicable), the equation number where we define the parameter or whether it is a free parameter. See Sections 5.2 and 5.4 for further information.

Parameter	Units	Fiducial value(s)	Definition	Equation
$z$	$r_g$	—	distance from the black hole along the jet axis	—
$z_0$	$r_g$	6	distance of the jet base from the black hole	—
$\gamma$	—	1 – 3	bulk Lorentz factor of the flow	5.1
$\gamma_0$	—	1.1	bulk Lorentz factor at the jet base	—
$r$	$r_g$	—	cross-sectional radius of the flow	5.2
$\theta$	rad	—	jet opening angle	5.3
$n$	$\text{cm}^{-3}$	—	jet (total) particle number density	5.4
$n_0$	$\text{cm}^{-3}$	—	jet number density at the jet base	5.17
$n_e$	$\text{cm}^{-3}$	—	jet pair number density	—
$n_p$	$\text{cm}^{-3}$	—	jet proton number density	—
$\rho$	$\text{g cm}^{-3}$	—	jet mass density	5.7
$\omega$	$\text{erg cm}^{-3}$	—	total jet enthalpy	5.9
$h$	—	—	jet specific enthalpy	5.10
$\sigma$	—	—	magnetisation of the flow	5.13
$\sigma_0$	—	1 – 100	magnetisation of the flow at the jet base	5.20
$\mu$	—	1 – 100	normalised total jet energy flux	5.19
$\langle \varepsilon_{e,p} \rangle$	—	1 – 100	particle average Lorentz factor	5.26
$z_{\text{acc}}$	$r_g$	$10^3$	location where jet acceleration reaches the max value	free parameter
$\gamma_{\text{acc}}$	—	3	maximum Lorentz factor of the flow at $z_{\text{acc}}$	free parameter
$r_0$	$r_g$	$10 - 10^2$	jet base radius	free parameter
$L_{\text{jet}}$	$L_{\text{Edd}}$	0.01	injected jet power at the jet base	free parameter
$\eta_e$	—	$1 - 10^6$	jet pair-to-proton content	free parameter
$\sigma_{\text{acc}}$	—	0.1	magnetisation of the flow at the acceleration region	free parameter
$k_B T_e$	keV	—	electron peak energy at the jet base	free parameter

power-law tail above the dissipation region, lose energy due to cyclo-synchrotron radiation (Blumenthal & Gould 1970; Rybicki & Lightman 2008). We only account for the average magnetic field strength of the particular jet segment and assume an isotropic distribution of pitch angles that we average over.

We further account for the ICS between the pairs and the radiation fields of the outflow (Blumenthal & Gould 1970; Rybicki & Lightman 2008). In particular, in this work we neglect any external photon field and only allow for ICS between the emitting pairs and the synchrotron photons (synchrotron self Compton; SSC). For the ICS processes, we account for the Klein-Nishina regime when necessary, and allow for multiple scatterings to better capture the evolution of the exponential cutoff. This particular process is the most computationally expensive amongst the leptonic ones, we hence choose to neglect it when the radiative output becomes  $10^4$  times smaller than the synchrotron counterpart for the particular segment.

The final process of leptonic nature we account for is the photon annihilation to pair production and vice versa (Coppi & Blandford 1990). These two processes are usually negligible, so we do not mention them unless we discuss their impact on the particle population or the spectrum (see, e.g., Connors et al. 2019).

#### 5.2.4.2 Hadronic Processes

We account for both proton-proton (pp) and proton-photon ( $p\gamma$ ) processes when accelerated protons interact with the cold protons of the flow and the jet radiation, respectively. In particular, we use the semi-analytical parametrisation of Kelner et al. (2006) for the pp interactions, and Kelner & Aharonian (2008) for the  $p\gamma$ . The above analysis provides the resulted distributions of secondary particles (pions that decay into muons, and the muons decay into neutrinos, pairs and  $\gamma$ -rays) and hence cannot account for any synchrotron radiation of muons and/or pions, but for the current systems we examine, we see that it is not required. We do however consider the cyclo-synchrotron radiation of secondary pairs due to the presence of the magnetic field.

In our particular analysis, we find that the synchrotron photons produced by the primary pairs act as the target for the  $p\gamma$  interactions. Based on this analysis, we can also produce the neutrino counterpart in a self-consistent manner (Kantzas et al. in prep).

### 5.3 Results for the steady-state jets

We first present the results of the analysis of the model where we do not account yet for any mass entrainment. In this flavour of the model, we try to better understand and constrain the number of leptons in the jets with respect to the number of protons  $\eta_e$ . We further present the jet dynamical properties and their correspond-



ing multiwavelength spectra before we compare them to ones when we account for mass-loading.

### 5.3.1 Specific enthalpy and particle acceleration

We can express Equation 5.10 as

$$h = \frac{\Gamma_e(\langle\varepsilon_e\rangle - 1) + \Gamma_p(\langle\varepsilon_p\rangle - 1) \frac{m_p/m_e}{\eta_e}}{1 + \frac{m_p/m_e}{\eta_e}}, \quad (5.28)$$

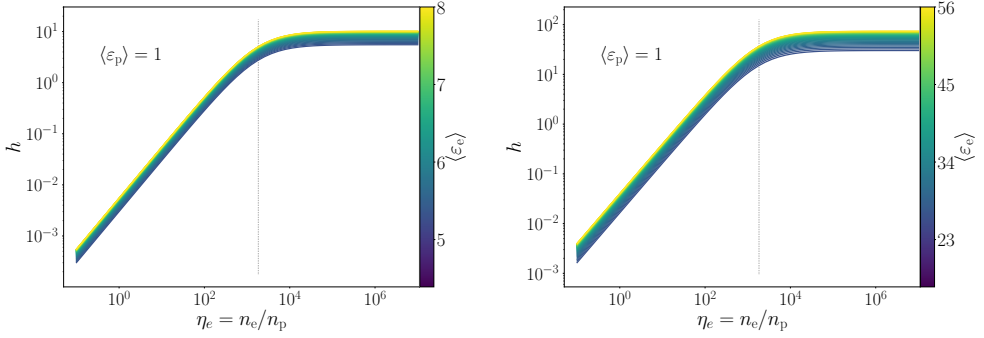
where we used Equations 5.7, (5.12), and  $n_p = n_e/\eta_e$ .

From the above equation, we see that the specific enthalpy depends merely on the ratio between pairs and protons. Moreover, we see that  $h$  strongly depends on any mechanism (acceleration or cooling) that would significantly change the average Lorentz factor of the particles.

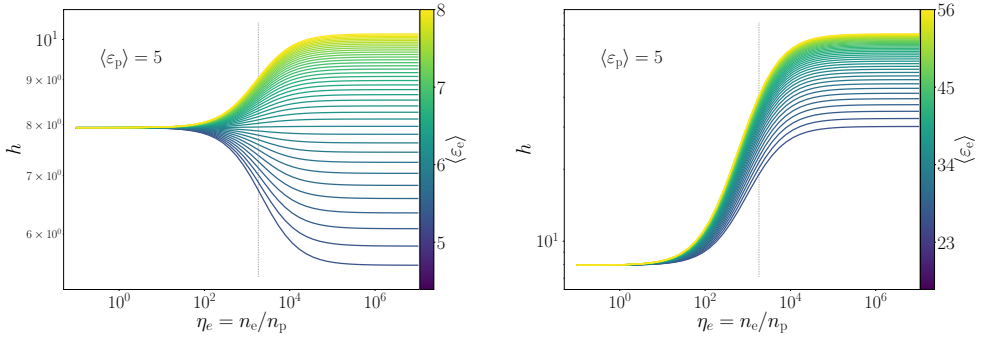
In Figure 5.1, we plot the specific enthalpy  $h$  as a function of the pair-to-proton ratio  $\eta_e$  for various values of  $\langle\varepsilon_e\rangle$  and  $\langle\varepsilon_p\rangle$ . Both  $\langle\varepsilon_e\rangle$  and  $\langle\varepsilon_p\rangle$  depend on the power law slope of the accelerated particles, as well as the minimum and the maximum particle energy. We let  $\eta_e$  to scale between a few and  $10^6$  although the latter values are extreme and perhaps not physically expected. A jet with more protons than leptons ( $\eta_e < 1$ ) would be positively charged and hence is unphysical. On the other hand, a very large number of pairs per proton would be difficult to explain the observed Lorentz factors on parsec scales (Ghisellini & Tavecchio 2010).

In the top left plot of Figure 5.1 where no protons accelerate at all, and in particular in the case of approximately equal amount of pairs and protons ( $\eta_e \sim 1$ ), we see that the specific enthalpy is significantly smaller than unity ( $\eta_e \ll 1$ ). This is in agreement with the initial setups of GRMHD simulations where the specific enthalpy is usually neglected (McKinney 2006; Komissarov et al. 2007). In the other regime, where the flow is dominated by pairs ( $\eta_e \gtrsim 10^3$ ), we see that  $h \sim \Gamma_e \langle\varepsilon_e\rangle$  (Equation 5.28). In the top right plot of Figure 5.1 where we assume  $\varepsilon_{e,\min} = 10$ , we see a similar evolution of  $\eta_e$ . The main difference is that  $\langle\varepsilon_e\rangle$  goes to larger values, hence  $h$  goes to larger values as well. From both plots, we see that for a purely leptonic flow, the specific enthalpy is not negligible and in fact, it can be as important as the magnetisation and the kinetic energy in the evolution of the jets (as discussed below).

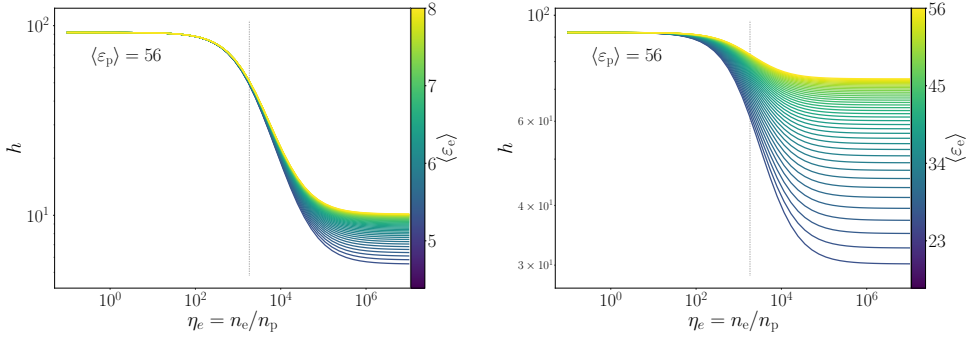
In the middle plots of Figure 5.1, where protons accelerate in a similar power law as the accelerated pairs, we see a significantly different evolution of  $\eta_e$  for different jet content. In particular, in the case where  $\varepsilon_{e,\min} = 1$  and  $\varepsilon_{p,\min} = 1$  (middle left plot), we see that for an equal pair-to-proton jet content ( $\eta_e = 1$ ),  $h$  is driven by the accelerated protons and in fact,  $h \sim \Gamma_p \langle\varepsilon_p\rangle$  (see Equation 5.28). In the regime of a purely leptonic flow ( $\eta_e \gg 1$ ), we see that  $h \sim \Gamma_e \langle\varepsilon_e\rangle$  and depending on whether



(a) Purely leptonic acceleration with  $\varepsilon_{e,\min} = 1.5$ . (b) Purely leptonic acceleration with  $\varepsilon_{e,\min} = 10$ .



(c) Leptohadronic acceleration with  $\varepsilon_{e,\min} = 1.5$ . (d) Leptohadronic acceleration with  $\varepsilon_{e,\min} = 10$ .



(e) Efficient hadronic, and leptonic acceleration with  $\varepsilon_{e,\min} = 1.5$ .

(f) Efficient hadronic, and leptonic acceleration with  $\varepsilon_{e,\min} = 10$ .

**Figure 5.1:** The jet specific enthalpy  $h$  as a function of the jet content  $\eta_e = n_e/n_p$ . In all plots, we assume a soft non-thermal power law with  $p = 2.2$ . The average Lorentz factor of each species is indicated in each panel. The vertical lines correspond to  $\eta_e = m_p/m_e$ . Note the different y-axis ranges.

$\langle \varepsilon_e \rangle > \langle \varepsilon_p \rangle$  or  $\langle \varepsilon_e \rangle < \langle \varepsilon_p \rangle$ ,  $h$  will increase or decrease, respectively. In the right-hand-side of the middle subplots of Figure 5.1, we get larger values of  $\langle \varepsilon_e \rangle$  because of the larger value of  $\varepsilon_{e,\min}$  (for the particular  $p = 2.2$ ), and hence the specific enthalpy may attain significantly larger values, reaching values of the order of  $\Gamma_e \langle \varepsilon_e \rangle$ .

In the bottom plots of Figure 5.1 where protons accelerate in a power law from a  $\varepsilon_{p,\min} = 10$ , we see that a flow of  $\eta_e \sim 1$  has a significant fraction of energy in the specific enthalpy because  $h \sim \Gamma_p \langle \varepsilon_p \rangle \sim 90$ . In the purely leptonic regime ( $\eta_e \gg 1$ ), we see that  $h$  can drop to values smaller than 10 depending on the average Lorentz factor of the pairs. In the case where pairs accelerate in a power law from a high energy as  $10 m_e c^2$  (right-hand-side plot of the lowermost panels of Figure 5.1), the energy content in the specific enthalpy remains significant for both  $\eta_e \sim 1$  and  $\eta_e \sim 10^6$ .

From Figure 5.1, we overall see that the specific enthalpy of a flow that accelerates particles can be important in the evolution of the flow (see also discussion below). In the case where only pairs accelerate in the jets and for an equal amount of electrons-to-protons as is commonly assumed in GRMHD (left-hand-side of the uppermost subplots, and in particular in the case of one), we see that the specific enthalpy is indeed negligible ( $h \ll 1$ ). In any other case where both pairs and protons accelerate in the jets, and regardless of the jet content (either pair-dominated or equal pair-to-proton content), the specific enthalpy of the flow might be of the order of a few-to-tens, and hence it is important for the evolution of the flow (see also discussion of CLTM19).

In Appendix 5.A we discuss the evolution of  $h$  in the case of a hard power law of accelerated particles with  $p = 1.7$  power law index. Such hard values, resulting from efficient particle acceleration e.g., in magnetic reconnecting regions (Sironi et al. 2015; Ball et al. 2018), lead to even larger values of  $h$  of the order of thousands. Such large values of  $h$  along with large bulk Lorentz factors as observed in relativistic outflows in AGN and GRBs, would lead to significantly larger values of total energy flux  $\mu$  compared to those in the literature (Komissarov et al. 2007, 2009).

### 5.3.2 Total energy flux evolution for steady state jets

In Figure 5.2, we plot the evolution of  $\mu$  along the jets with the different components: magnetisation ( $\sigma$ ), bulk Lorentz factor ( $\gamma$ ) and specific enthalpy ( $h$ ). In the left plots of Figure 5.2, we assume a jet content of equal number of leptons and protons ( $\eta_e = 1$ ) and in the right plots we assume a pair-dominated outflow ( $\eta_e = 10000$ ). In the top subplots, we assume that only leptons accelerate to non-thermal energies, whereas in the bottom subplots, we assume that hadrons accelerate as well in a power law with the same index.

In the top left subplot, where we assume one lepton per proton and account only for leptonic acceleration with  $\langle \varepsilon_e \rangle = 6$ , we see that the initial magnetisation of the outflow converts to bulk kinetic energy whereas the magnetisation drops to  $\sigma_{\text{acc}} = 0.1$  (a free parameter). The specific enthalpy starts as negligible at the cold jet base ( $h_0 \ll$

$10^{-2}$ ) and remains insignificant for the jet evolution above the particle acceleration region  $z_{\text{acc}}$ . This particular jet evolution resembles of the physical quantities GRMHD simulations account for, and in fact, is the only regime that **BHJet** can probe self-consistently, while here we can further explore the jet kinematics (Lucchini et al. 2022).

In the top right subplot, where we assume a pair-dominated jet ( $\eta_e \gg 1$ ) that accelerates only leptons, we see that the initial magnetisation converts almost equally to bulk kinetic energy and internal energy ( $h$  is now comparable to  $\gamma$ ). The initial specific enthalpy at the jet base is larger compared to the previous case and based on Equation 5.19, we see that also  $\mu$  has significantly increased (see also Section 5.3.1).

In the bottom left subplot of Figure 5.2 where we account for hadronic acceleration with  $\langle \varepsilon_p \rangle = 4$ , we see that the initial magnetisation dissipates almost equally to kinetic and internal energy. The initial specific enthalpy is negligible at the cold jet base but when particles accelerate at the acceleration region,  $h$  increases to values comparable to  $\gamma$ . Finally, in the bottom right subplot where the jet is pair-dominated, we see that the specific enthalpy at the jet base is of the order of 1 but still much smaller than the initial magnetisation.

In Figure 5.2, according to the approach we follow here,  $h$  can overall be significant for the jet evolution depending on the hadronic acceleration and the jet content. The former, in particular, strongly depends on the jet properties, but we cannot capture this non-linear behaviour of the jet evolution, its effect on the particle acceleration and the consequent feedback of particle acceleration back to the jet evolution without significantly increasing the computational cost of the model. However, we can still investigate the jet properties to gain a better insight on jet physics.

In Appendix 5.B we present a more detailed series of jet evolution for various jet quantities and different average particle Lorentz factors. Overall, we find that for many physical scenarios, the specific enthalpy becomes important for the jet evolution, especially in the case where hadrons accelerate in the jets as well, and for pair-dominated outflows (see also Section 5.3.1).

### 5.3.3 Electromagnetic spectrum of steady state jets

We plot in Figure 5.3 the multiwavelength spectra that correspond to the four different models of Figure 5.2. In particular, in the top subplots we plot the purely leptonic scenarios, whereas in the bottom we plot the lepto-hadronic models. For the left plots, we assume one proton per electron ( $\eta_e = 1$ ), whereas on the right plot we examine the extreme case of  $\eta_e = 10^4$ .

For all four subplots, we assume a quite “warm” MJ distribution of leptons with  $k_B T_e = 1000$  keV, an initial jet-radius of  $10 r_g$  in which we inject some power equal to  $10^{-2} L_{\text{Edd}}$  for the leptonic models, and  $10^{-3}$  for the lepto-hadronic ones. The particle acceleration that happens at  $1000 r_g$  leads to a power-law of particles with

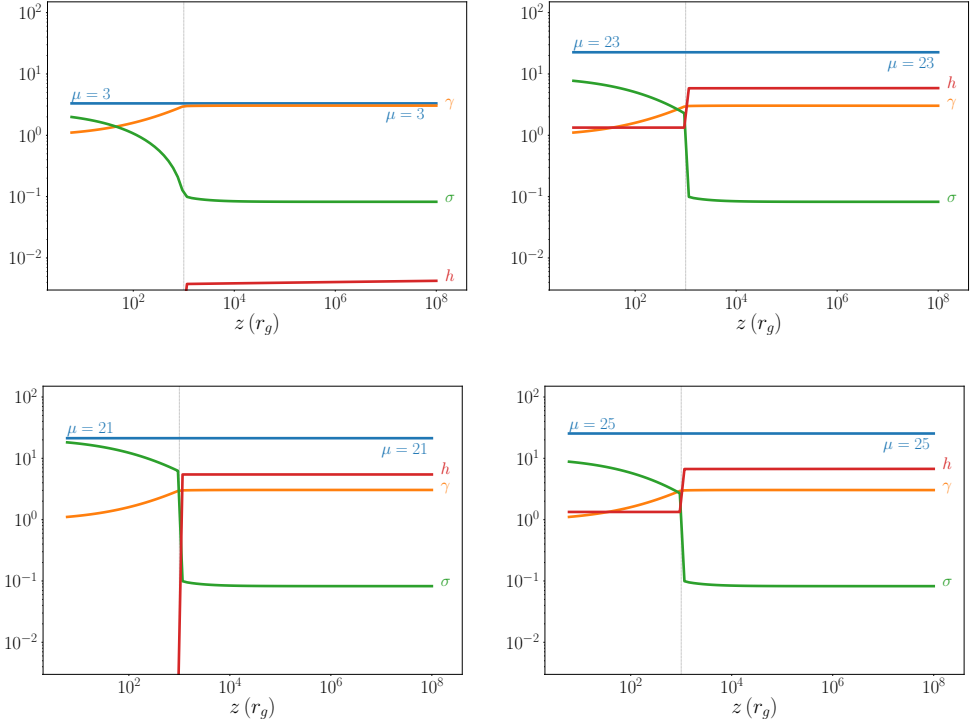


**Figure 5.2:** The energy jet components;  $\gamma$  (the bulk Lorentz factor),  $\sigma$  (the magnetisation), and  $h$  (the specific enthalpy) that follow the relation  $\mu = \gamma(1 + \sigma)(1 + h)$  (Equation 5.19). In all plots we use  $z_0 = 6 r_g$ ,  $z_{\text{acc}} = 10^3 r_g$ ,  $\gamma_{\text{acc}} = 3$ ,  $\sigma_{\text{acc}} = 0.1$  and  $\langle \varepsilon_e \rangle = 6$  (see Table 5.1 for definitions). We show a pair/proton flow with  $\eta_e = 1$  in the *left* column and a pair-dominated flow with  $\eta_e = 10000$  in the *right* column. In the *top* panels, we only account for leptonic acceleration and in the *bottom* panels, we consider hadronic acceleration as well with  $\langle \varepsilon_p \rangle = 4$ .

an index of 2.2. In all subplots, we show the contribution to the spectrum of the jet segments before the dissipation region (yellow-shaded) and above (blue-shaded). For the lepto-hadronic model of the bottom subplots, we include the hadronic contribution as green-shaded. Finally, the densely dashed line shows the synchrotron contribution, whereas the loosely dashed line corresponds to the ICS.

In the top left subplot of Figure 5.3, we see the thermal part dominates in the UV and X-ray bands, whereas the outer jets dominate in the radio bands via synchrotron radiation, and in the GeV with ICS. In the case where we assume an increased ratio of pairs (top right subplot), for the same initial conditions we see a similar picture that is increased to larger, but perhaps unphysical luminosities because the initial number density has increased (see Equation 5.17).

In the lepto-hadronic cases of the bottom subplots of Figure 5.3, we see that

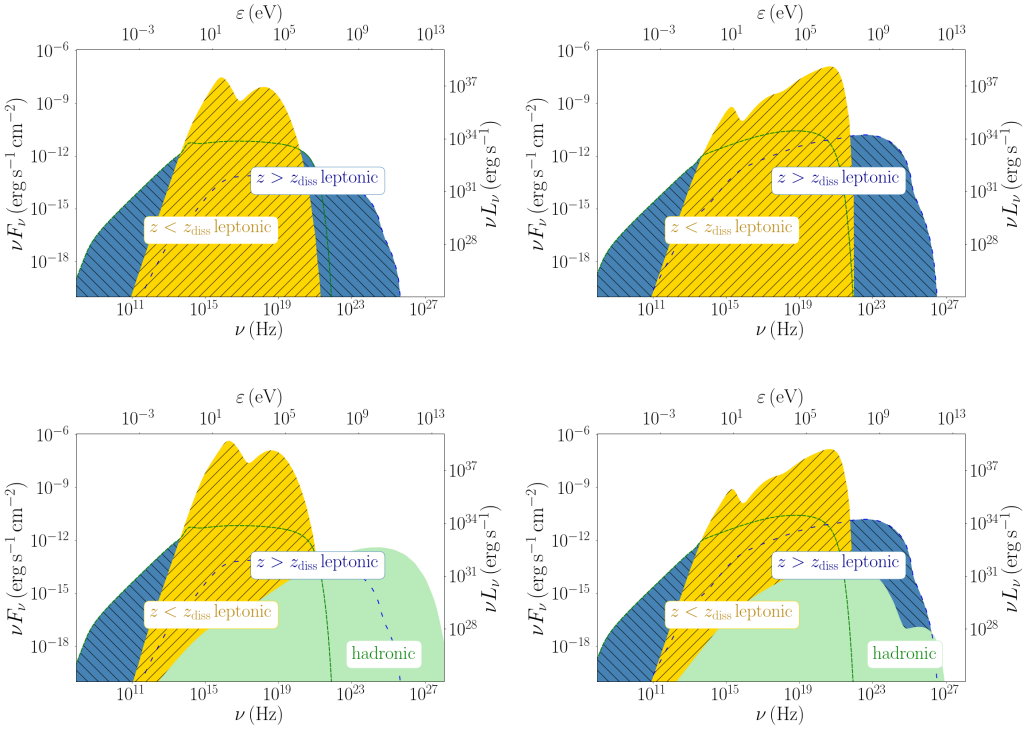


**Figure 5.3:** The predicted spectral energy distributions for the four models of Figure 5.2. In the *top* subplots, we only account for leptonic acceleration, and in the *bottom* ones, we consider both leptonic and hadronic. In the two *left* plots, we assume one proton per electron ( $\eta_e = 1$ ) and in the *right* ones we assume  $\eta_e = 10^4$ . In all four subplots, we use  $k_B T_e = 1000$  keV, and  $z_{\text{diss}} = 1000 r_g$  for a  $10 M_\odot$  BHXB at 3 kpc. We also assume  $L_{\text{jet}} = 2 \times 10^{-2} L_{\text{Edd}}$  for the leptonic scenarios and  $L_{\text{jet}} = 2 \times 10^{-3} L_{\text{Edd}}$  for the hadronic. The aforementioned values lead to  $\langle \epsilon_e \rangle = 5$ . We highlight the contribution of the jet-segments before the dissipation region (yellow shaded) and that of the jet-segments above the dissipation region (blue shaded). We show the synchrotron emission with densely dashed green line, and the contribution of the ICS with loosely dashed blue line. Finally, the green shaded region is the hadronic contribution where we include both neutral pion decay and the synchrotron radiation of the secondary electrons.

the pair content may significantly affect the SED, and in particular the high-energy part. For the case of one proton per lepton, we see that the GeV-to-TeV spectrum first drops exponentially due to the synchrotron emission of the primary pairs, but later increases due to the hadronic contribution of the  $p\gamma$  interactions. The ICS contribution in this particular case is well below the hadronic contribution (loosely dashed line). In the pair-dominated jet of the right-hand subplot, we see that the increased number of pairs leads to a stronger GeV-to-TeV flux that dominates over the hadronic contribution.

**Table 5.2:** The fixed and the free (fitted) parameters that drive the mass-loading jet dynamics. See Section 5.4 for further information.

Parameter	Fiducial value(s)	Definition	Status
$\gamma_0$	1.11	bulk Lorentz factor at the jet base $z_0$	fixed
$\sigma_0$	10 – 50	magnetisation of the flow at the jet base	free
$k_B T_e$ (keV)	1000	electron peak energy at the jet base	free
$\gamma_{\text{acc}}$	2 – 10	bulk Lorentz factor at $z_{\text{acc}}$	free
$h_{\text{acc}}$	$h_0^a$	jet specific enthalpy at $z_{\text{acc}}$	fixed
$f_\rho$	10	jet mass density increase factor	fixed
$z_{\text{diss}} (r_g)^b$	100	region where the mass entrainment initiates	free
$z_{\text{load, end}}/z_{\text{diss}}$	100	region where the mass entrainment finishes	fixed

<sup>a</sup>calculated by the temperature of the electrons at the jet base (see Equation 5.10),

<sup>b</sup>same as  $z_{\text{acc}}$  and  $z_{\text{diss}}$ .

## 5.4 Mass loaded jets

High-resolution GRMHD simulations of accreting black holes that launch jets suggest that a significant portion of the wind from the accretion disc might end up in the jet via entrainment. While the jets accelerate in a dense surrounding medium, they are subject to lateral pressure from the wind of the accretion disc that forces the jet to wobble. Overall, the jets remain stable up to a distance where the flow starts to become superfast. Beyond this region, the jet becomes more susceptible to instabilities forming at the interface between the flow and the ambient medium. In particular, magnetic pinch instabilities lead to the formation of eddies that trap matter from the wind and drive it inwards through the jet-wind interface, allowing for mass entrainment (Mignone et al. 2013; Gourgouliatos & Komissarov 2018; Bodo et al. 2021). Without such eddies, significant mass entrainment into the jet from the external medium may not be possible due to the jet’s strong magnetic field. Previous numerical simulations led to the conclusion that pinch instabilities do not survive to large distances from the black hole (Moll et al. 2008; Granot et al. 2011; Porth & Komissarov 2015), but that might actually depend on the continuous collimation by the disk wind (CLTM19).

Pinch instabilities form close the black hole, at the jet-wind interface, almost independently of the initial magnetisation of the jet, as long as it starts out Poynting flux dominated. Pinch instabilities dissipate magnetic energy to heat and increases the specific enthalpy of the jet (see, e.g., Eichler 1993; Bowman et al. 1996; Spruit et al. 1997; Begelman 1998; Giannios & Spruit 2006; Bromberg & Tchekhovskoy 2015). Interest-

ingly, two properties of the jet shown in CLTM19 change at distances  $\sim 10^2 - 10^3 r_g$ : (1) the toroidal component of the magnetic field starts to dominate over the poloidal component, and (2) the jet speed becomes larger than the local magnetosonic speed. While toroidal field-dominance is required for the initiation of the pinch instabilities, it is not clear if the superfast speed of the jet is necessary to aggravate the instability enough to trigger mass loading. Following the results of CLTM19, we connect this region to the first particle acceleration region of jets as originally proposed by (Markoff et al. 2005; Polko et al. 2014). This region is responsible for the spectral break between the optically thin and optically thick synchrotron emission of non-thermal particles, detected in numerous BHXBs (Markoff et al. 2001; Corbel & Fender 2002; Fender et al. 2000, 2009; Gandhi et al. 2011) and can perhaps be associated with the “blazar zone” invoked by single-zone models (see, e.g., Marscher et al. 2008; Murase et al. 2018). We hence link the region where the mass-loading initiates (or more precisely, becomes important) because of instabilities explicitly to the region where non-thermal particle acceleration occurs.

In this work, we parametrise the fiducial model B10 of CLTM19 to derive a semi-analytical formalism that connects the mass loading region to the particle acceleration region, and study its impact on the emitted electromagnetic spectrum by studying both the leptonic and the hadronic processes we discussed above. We assume that the mass loading initiates at distance  $z_{\text{diss}}$  and at a distance of  $100 z_{\text{diss}}$  the total jet mass density has increased by a factor of  $f_\rho = 10$ . In Figure 5.4 we plot the mass density of a mass loaded jet (solid line) and compare it to a non-loaded steady state jet, assuming one proton per lepton.

CLTM19 confirm that the magnetic energy converts to kinetic energy, accelerating the jets similar to previous works (McKinney 2006; Komissarov et al. 2007, 2009). When matter is entrained by the jets, further magnetic energy is dissipated to heat up the jet, and the inertia of the entrained gas slows down the jet. The mass entrainment leads to a decrease in the total (specific) energy flux  $\mu$  along the jets up to the distance where the mass loading stops. In this work, we choose to force the mass loading to stop at a distance of  $100 z_{\text{diss}}$  because we suspect that the jets above a distance of the order of  $10^5 r_g$  are not yet in steady state at the end of the simulation.  $\mu$  should be conserved for the rest of the jets hence, the jets start to re-accelerate while both the magnetisation and the specific enthalpy decrease. We show the resulting energy components ( $\gamma$ ,  $\sigma$ , and  $h$ ) of the B10 model of CLTM19 in Figure 5.5 with dashed lines, and below, we discuss the way we parametrise these quantities.

### 5.4.1 Mass loading region

In this section, we present the parametrisation of the values of  $\sigma$ ,  $\gamma$  and  $h$  of the mass loading region of the B10 model of CLTM19. In particular, we fit a polynomial to the CLTM19 profiles along the jet between  $10 z_{\text{diss}} = 1000 r_g$  and  $z_{\text{load, end}} = 10^4 r_g$ ,



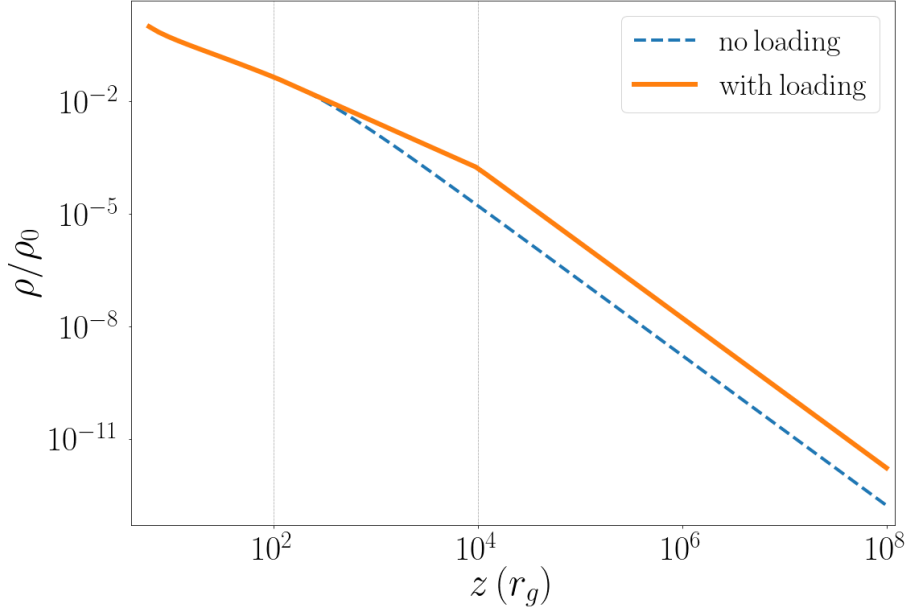


**Figure 5.4:** The mass density profile of a mass loaded jet (solid line) compared to a steady state jet without mass loading (dashed line). Both profiles are normalized to the initial mass density at the jet base. The mass loading initiates at a distance  $z_{\text{diss}}$  and at  $100 z_{\text{diss}}$  the mass density has increased by a factor of 10 compared to a non-loading, steady-state jet.

and the coefficients of the polynomials for the three quantities are:

$$\log_{10}(\sigma) = 0.62 x^5 - 3.01 x^4 + 4.60 x^3 - 2.50 x^2 + 0.24 x + 0.56, \quad (5.29)$$

$$\log_{10}(\gamma) = -0.28 x^6 + 1.41 x^5 - 2.21 x^4 + 0.85 x^3 + 0.26 x^2 - 0.08 x + 0.39, \quad (5.30)$$

$$\log_{10}(h) = 0.47 x^5 - 1.90 x^4 + 1.10 x^3 + 2.48 x^2 - 1.17 x - 1.83, \quad (5.31)$$

where  $x = \log_{10}(z/z_{\text{diss}})$  and  $1 \leq x \leq \log_{10}(z_{\text{diss}}/z_{\text{load, end}})$ .

We connect the jet base to the mass-loading region assuming that the specific enthalpy is constant to its initial value at the jet base as we calculate it with Equation 5.10. We assume that the flow is launched at a speed equal to the speed of sound (see Equation 5.1) and reaches a value  $\gamma_{\text{acc}}$ , which is a free parameter, following a logarithmic dependence. In Table 5.2, we show the parameters of the mass-loading jet model, indicating whether they are fixed or fitted parameters.

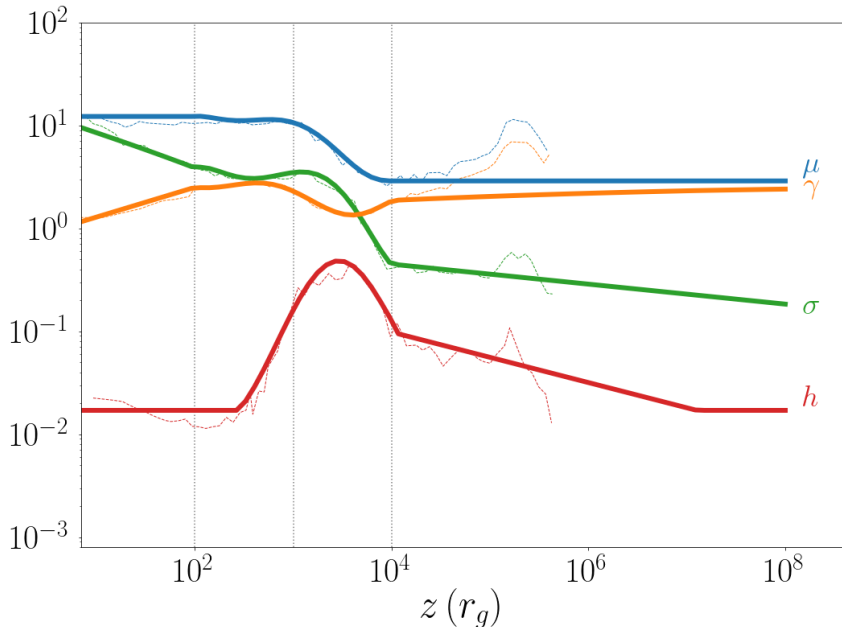


**Figure 5.5:** The energy flux components of a mass loaded jet, where  $\mu$  is the ratio between the total energy flux and the rest-mass flux,  $\gamma$  is the bulk Lorentz factor,  $\sigma$  is the magnetisation, and  $h$  is the specific enthalpy. The mass entrainment occurs between  $10^2$  and  $10^4 r_g$  (vertical lines), but the entrained matter becomes comparable to the mass of the jet at a distance of  $10^3 r_g$  (middle vertical line). Finally, we over-plot with dashed lines the fiducial model B10 of CLTM19 on which we base our analysis (see Section 5.4).

### 5.4.2 Jet segments beyond the mass loading region

To better constrain the profile of  $\sigma$  and  $h$  beyond the mass-loading region, we fit a first order polynomial between  $10^4$  and  $10^5 r_g$ , with coefficients:

$$\log_{10}(\sigma) = -0.10x - 0.18, \quad (5.32)$$

$$\log_{10}(h) = -0.25x - 0.58, \quad (5.33)$$

where  $x$  is the same as above.

Having derived the values of  $\mu$ ,  $\sigma$  and  $h$ , we calculate the bulk Lorentz factor for every jet segment above the  $z_{\text{diss}}$

$$\gamma(z \geq z_{\text{diss}}) = \frac{\mu}{\sigma + h + 1}. \quad (5.34)$$

In Figure 5.5, we show the global picture of a mass loaded jet as described above.

### 5.4.3 Particle acceleration and mass loaded jets

At the location where matter is entrained into the jets, particles start to accelerate to non-thermal energy as well. Based on the definition of  $h$ , we solve for the energy density of the protons

$$U_p = \frac{h\rho c^2 - \Gamma_e U_e}{\Gamma_p}, \quad (5.35)$$

where we calculate  $U_e$  from Equation 5.11 for an MJ+non-thermal power-law distribution of electrons with a fixed ratio of thermal to non-thermal electrons, and a fixed power-law slope  $p$ . We finally, derive the normalisation of the non-thermal protons

$$K_p = \frac{U_p}{m_p c^2 \int \varepsilon^{-p+1} \exp(-\varepsilon/\varepsilon_{\max}) d\varepsilon}, \quad (5.36)$$

where

$$\frac{dn_p}{d\varepsilon} = K_p \varepsilon^{-p} \exp(-\varepsilon/\varepsilon_{\max}). \quad (5.37)$$

Following the above approach, we manage to self-consistently connect the mass-loading that leads to an increase in the specific enthalpy  $h$  to the electromagnetic radiation due to the proton acceleration.

## 5.5 Results for mass-loaded jets

### 5.5.1 Total energy flux evolution for mass-loaded jets

In Figure 5.6, we present the energy components for two different mass-loaded jets following the prescription of Section 5.4. We assume that both jets are Poynting flux dominated at the jet base with an initial magnetisation of  $\sigma_0 = 30$  and accelerate to a bulk Lorentz factor of  $\gamma_{\text{acc}} = 3$ . In the left plot, we assume one electron per proton at the jet base of temperature  $k_B T_e = 500$  keV, and in the right, we assume a pair-dominated jet of  $\eta_e = 1000$  with  $k_B T_e = 50$  keV. In the particular case of the pair-dominated jets, the specific enthalpy reaches values that are comparable to the bulk Lorentz factor and the magnetisation, especially at the loading region (see also Equation 5.28). Despite the initially pair-dominated jet base, the matter that entrains the jets is in approximately equal number of electrons and protons because the most likely composition of an accretion disc wind is a neutral gas of electrons and protons. The jet composition hence changes from pair-dominated at the regions before the loading to almost equal number of protons and pairs (Anglés-Castillo et al. 2020).

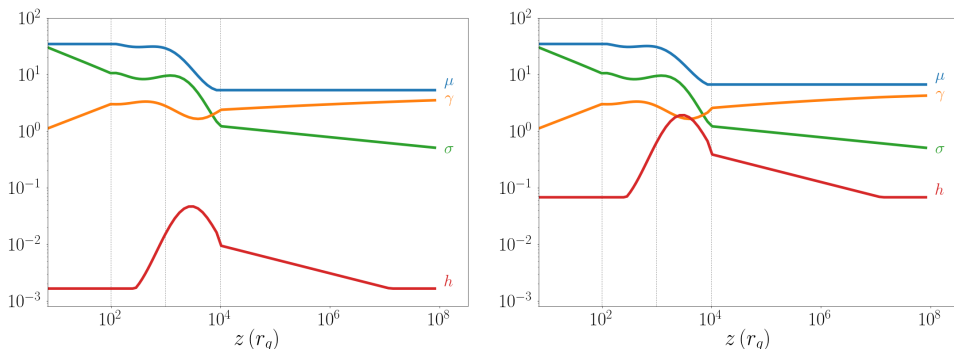


**Figure 5.6:** Similar to Figure 5.5, but for: *left* an initial lepton temperature at the jet base of  $k_b T_e = 500$  keV and one electron per proton ( $\eta_e = 1$ ), and in the *right*  $k_b T_e = 50$  keV for a pair-dominated jet ( $\eta_e = 1000$ ). Both scenarios are for an initial magnetisation of  $\sigma_0 = 30$  and  $\gamma_{\text{acc}} = 3$ . The increased pair content of the right subplot leads to an increased initial specific enthalpy of the jets.

In the right subplot of Figure 5.6, we see that the increased number of pairs at the jet base leads to an increase in  $h$ . In the extreme case where  $\eta_e \gg 1000$ , the peak of the profile of  $h$  may lead to an artificial and unphysical increase in  $\mu$  in the loading region. In Appendix 5.C we discuss how we constrain the increase in  $h$  to avoid such an artificial mass loss.

### 5.5.2 Electromagnetic spectra of steady state mass-loaded jets

In Figure 5.7, we plot in the left the predicted SED of the fiducial mass-loaded jet model based on the dynamical quantities that we show in Figure 5.5. We further assume a jet base of radius  $10 r_g$ , an electron temperature of 500 keV at the jet base, an injected jet power of  $10^{-3} L_{\text{Edd}}$  and the power-law slope of the accelerated particles  $p = 2.2$  for both leptons and protons. Similar to above, we show the contribution of the leptonic emission of the jet segments before the dissipation/loading region, the leptonic contribution from the dissipation/loading region and beyond, and the hadronic contribution that is due to  $p\gamma$ . In the right subplot, we show the spectrum of a non-loaded jet with similar initial conditions. The main differences are in the jet emission from the jet base (yellow-shaded region) and the hadronic contribution. The jet-base emission is higher in the non-loaded case due to the magnetisation profile we assume here that leads to greater values for the first few jet segments up to the acceleration region (see, e.g., Figure 5.2).

In Figure 5.8 we plot the SEDs that correspond to the two models of Figure 5.6, where we account for mass loading at a distance  $100 r_g$  and assume the injected jet power to be  $2 \times 10^{-2}$  and  $2 \times 10^{-5} L_{\text{Edd}}$  for the left and right subplots, respectively.

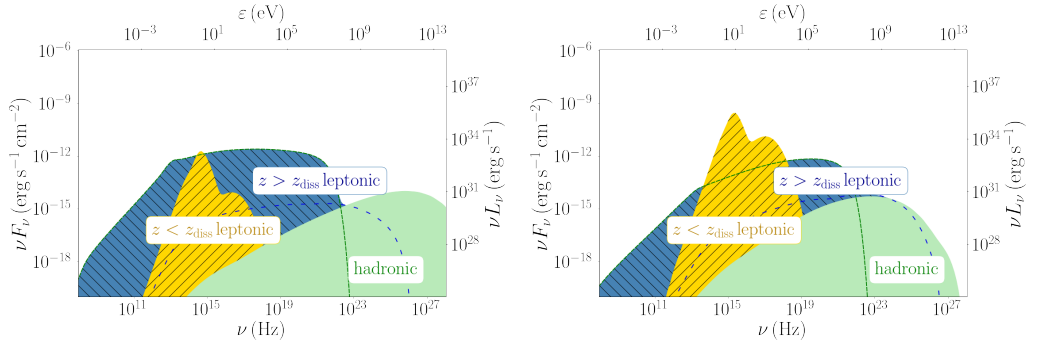


**Figure 5.7:** *Left:* The predicted spectral energy distribution of a mass-loaded jet that corresponds to the dynamical quantities of Figure 5.5 for a  $10 M_{\odot}$  BHXB at 3 kpc. We assume a jet base of 500 keV and radius of  $10 r_g$ . We show the contribution of the jet-segments before the mass loading (yellow shaded region), and the contribution of the mass-loaded segments of both leptonic (blue-shaded) and hadronic (green-shaded). The hadronic contributes includes both the neutral pion decay and the synchrotron radiation of the secondary electrons/positrons. *Right:* Similar to the left, but for a non-loaded jet with similar initial conditions.

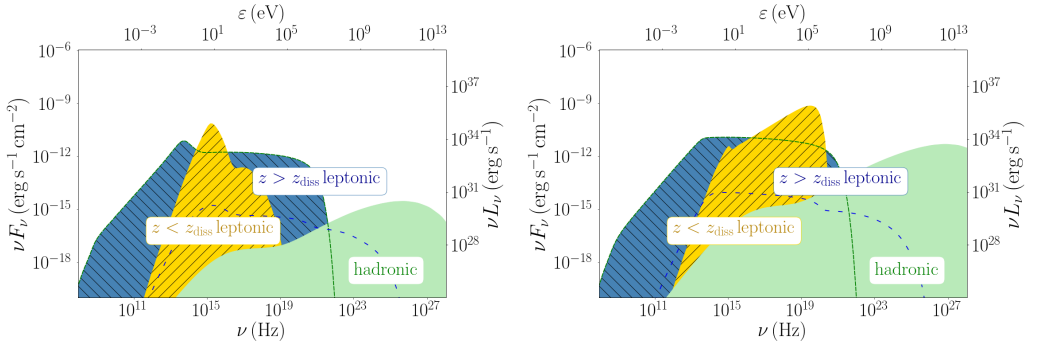


**Figure 5.8:** Similar to Figure 5.7 but for the mass-loaded jets that correspond to the dynamical quantities of Figure 5.6. The overall spectral distribution can significantly change under the assumption of a pair-dominated jet ( $\eta_e = 1000$ ) in the *right* plot.

## 5.6 Discussion

### 5.6.1 Steady state jets

In the first part of this work, we present the analytical jet model that includes the specific enthalpy in the jet kinematics and the spatial evolution.

### 5.6.1.1 Specific enthalpy, particle acceleration and jet evolution

The specific enthalpy  $h$  is a good estimate of whether a jet is cold or hot, with values of  $h \ll 1 + \sigma$  to indicate a cold flow, and values of  $h \gtrsim 1 + \sigma$  to indicate a hot flow. Astrophysical jets launched by black holes are overall considered cold and strongly magnetised. The majority of semi-analytical models that focus on the radiative output rather than the detailed description of the jets, neglect the specific enthalpy for simplicity (Markoff et al. 2005; Bosch-Ramon et al. 2006; Vila et al. 2012; Zdziarski et al. 2014a). When particles accelerate though, and in particular in the case where these accelerated particles carry a significant fraction of the jet energy, the specific enthalpy increases. As we show in Figure 5.1, the exact value of the specific enthalpy may get values that can easily compare to the bulk Lorentz factor (values of the order of 1 and  $\sim 10$ ) and/or the jet magnetisation (values greater than unity for a magnetised outflow). The exact value of  $h$  strongly depends on three aspects: the matter composition of the jet, the efficiency of the leptonic acceleration, and whether hadrons accelerate as well or not.

**Leptonic acceleration** In the case where only leptons accelerate inside the jets, we expect the average Lorentz factor to increase as the acceleration efficiency increases (top panels of Figure 5.1) and hence the specific enthalpy to increase as well, according to Equation 5.28. The total specific enthalpy however depends on the jet composition as well. When a jet is of one electron per proton ( $\eta_e = 1$ ), the values of  $h$  are  $\sim 0.01$  regardless of the exact average Lorentz factor of the electrons (as long as the average Lorentz factor of the leptons remains less than  $m_p/m_e \simeq 1836$ ). This is the typical scenario that current GRMHD and semi-analytical jet models consider when studying the exact jet evolution, both in space and time. As we mention above though, based on observations of both extragalactic and Galactic jets, it is very likely that jets are pair-dominated (or at least the scenario of one proton per electron is disfavoured in some cases). Such a jet content leads to an increase in the specific enthalpy compared to the case of  $\eta_e = 1$  (see Equation 5.28). The specific enthalpy hence of a jet that is pair-dominated at launching may contribute significantly to the spatial evolution of the jet, and the more relativistic (or warmer) the distribution of pairs, the larger the impact of  $h$  on the jet evolution. A pair dominated jet in fact requires specific enthalpy that can be two to three orders of magnitude larger than the jet case of an equal number of electrons and protons (see, e.g., top plots of Figure 5.1). Consequently, to achieve bulk flow acceleration up to the same bulk Lorentz factor, a pair-dominated jet, also requires a larger value of magnetisation at the jet base if energy flux is conserved along the jet.

**Lepto-hadronic acceleration** The energy content of the particles can further increase when jets accelerate both leptons and hadrons to non-thermal energies. In fact,

the more efficient the particle acceleration, the larger the specific enthalpy, which may get values of the order of  $\Gamma_p \langle \varepsilon_p \rangle$ , regardless of the jet content, as long as  $\eta_e \leq m_p/m_e$  (Figure 5.1). It is hard to predict the exact value of the specific enthalpy in a jet that efficiently accelerates particles, but overall, it may get values equal to or even exceed that of the bulk Lorentz factor and/or the magnetisation, that would mean that the outflow converts to particle dominated instead. We thus suggest that the specific enthalpy should be treated with extra care.

### 5.6.1.2 Specific enthalpy and spectral energy distribution

The SED of the steady jets strongly depends not only on the hadronic acceleration (or lack of it), but also on the jet content. The most important difference is in the GeV-to-TeV spectrum. A pair dominated jet is characterised by the ICS and any contribution from the hadronic processes is suppressed. In the case of a jet with equal number of protons and pairs, and accounting for an efficient hadronic acceleration, the hadronic component dominates in the GeV/TeV bands via the neutral pion decay, which has a distinguishable shape than that of ICS in the Klein-Nishina regime.

The IR-to-X-ray spectrum of BHXBs may be contaminated by different components, such as the companion star and/or the accretion disc. In the case of a pair-dominated jet, though, the X-ray spectrum shows the multiple Compton scatterings due to the increased electron density that can potentially replicate the role of the theoretical corona (Markoff et al. 2005, 2015; Lucchini et al. 2021; Cao et al. 2021b). Such an X-ray signature can prove a useful tool to distinguish between different jet compositions, especially with the next-generation X-ray telescopes, such as for instance the Imaging X-ray Polarimetry Explorer (IXPE; Weisskopf et al. 2016), the Advanced Telescope for High-energy Astrophysics (Athena; Nandra et al. 2013) and the Advanced X-ray Imaging Satellite (AXIS; Mushotzky et al. 2019).

### 5.6.2 Mass-loaded jets – HadJet

The initial jet composition at the jet base significantly alters the specific enthalpy of the jet along its axis, even if we assume that at the mass-loading region the jet converts to a pair-proton outflow. We see, in particular, that a pair-proton jet base with a thermal pair distribution that peaks at some energy of the order of 500 keV, which is a reasonable value for BHXBs, resulting in insignificant specific enthalpy compared to the rest energy components, namely the magnetisation and the kinetic (see, e.g., the left subplot of Figure 5.6). If the jet base, on the other hand, is pair-dominated, then similar to our discussion above, the initial specific enthalpy at the jet base is increased and thus its effect on the jet dynamical evolution might be more important because the energy content carried by particles might be similar to the bulk kinetic energy (see, e.g, the right subplot of Figure 5.6).

The initial conditions at the jet base have a significant impact on the electromagnetic spectrum that is our tool to distinguish between the different scenarios. For the two different scenarios we study here, where the one shows a pair-proton jet base and the other a pair dominated jet base, there are two prominent differences in the multiwavelength SEDs. The most important one is in the GeV/TeV regime, where the larger specific enthalpy of the initially pair-dominated jet base allows for more energy to be dissipated to protons. The increased energy available for non-thermal proton acceleration allows for a stronger TeV flux, which is dominated by the neutral pion decay due to  $p\gamma$  interactions. Such TeV flux, depending on the distance of the BHXB (see, e.g., Kantzas et al. 2022) might be significant to be detected by current TeV facilities, such as the Large High Altitude Air Shower Observatory (LHAASO) or future  $\gamma$ -ray facilities, such as the Cherenkov Telescope Array (CTA). The fact that an initially pair dominated jet can potentially lead to a stronger TeV flux may sound counterintuitive, but in fact it is natural in our treatment due to the assumption that the mass loading is linked with energy dissipation into particle acceleration. The increase in the specific enthalpy depends on the initial conditions of the jet launching, and in this work we base our formalism on one specific setup of GRMHD simulations. A different setup is very likely to lead to less efficient heating of the jets, the specific enthalpy nevertheless will still increase due to energy dissipation (see discussion of CLTM19). To explore the full range of possible physical scenarios with GRMHD simulations is currently too computationally expensive. We can however examine semi-analytically how the impact on the jet kinematics depends on the level of dissipation by replacing the heating parameter  $f_{\text{heat}}$  (that was used in previous work to estimate the heating of the thermal particles at the particle acceleration region; see, e.g., discussion in Lucchini et al. 2021) with the fraction of the magnetic energy that is additionally allowed to go into energising particles. With such a parameterisation,  $h$  will increase by a factor  $f_{\text{heat}}\sigma$  along the jet, whereas the magnetisation will be reduced as  $(1 - f_{\text{heat}})\sigma$ . We show in Figure 5.9 the impact of this free parameter in the energy components. To avoid a steep increase in  $h$  that looks like a step-function, we use a function  $\tanh^2(z/z_{\text{diss}})$ , instead. The underlying model is that of the left-hand panel of Figure 5.6 where we assume a “hot” jet base (500 keV) and one proton per electron.

A further spectral difference between a pair-proton and a pair-dominated jet base is in the lower energy regime of the spectrum, and in particular, in the UV-to-X-ray spectrum. For the same initial magnetisation and injected power, the number density of the pairs at the pair-dominated jet base is enhanced (see, e.g., Equation 5.17) resulting in increased Compton scatterings that lead to a significant difference in the  $\sim 1 - 100$  keV range. The X-ray spectrum in particular shows a hard spectral index ( $\nu F_\nu \propto \nu^{-\alpha+1}$ , with  $\alpha < 1$ ; see right-hand plot in Figure 5.8) that is similar to the expected output of a thermal corona (Sunyaev & Titarchuk 1980; Haardt & Maraschi 1993; Titarchuk 1994; Narayan & Yi 1994; Magdziarz & Zdziarski 1995).



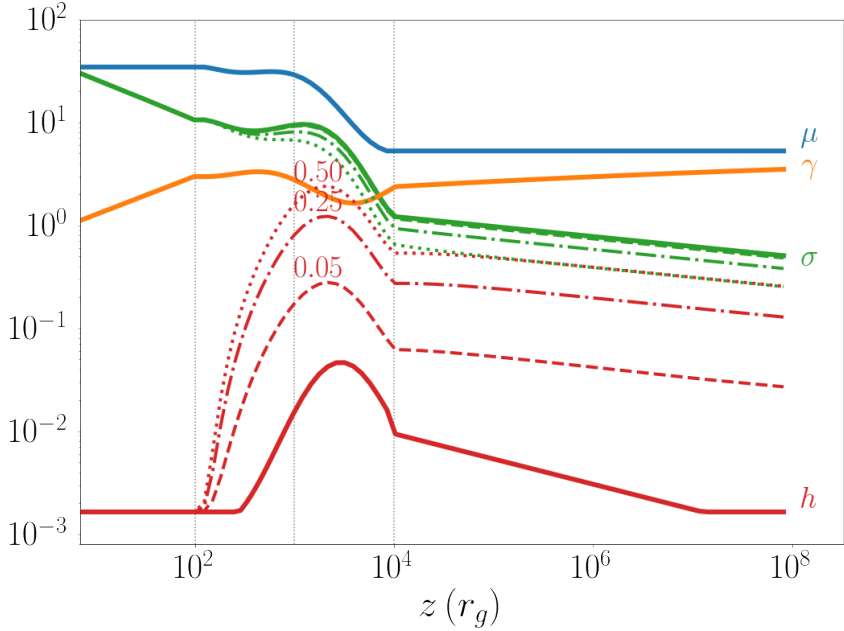


**Figure 5.9:** Similar to the left sub-plot of Figure 5.6, but with different  $f_{\text{heat}}$  parameters as shown in the plot. The  $f_{\text{heat}}$  parameter expresses the fraction of the magnetic energy that is allocated to the specific enthalpy to allow a further exploration of dissipation beyond our single GRMHD-based parameterisation.

### 5.6.3 Total proton energy

With the conserved, mass-loading jet model we develop here, we are able to constrain the total energy that is allocated to the protons and is used to accelerate them to non-thermal energies. In that way, the total energy carried by the accelerated protons never exceeds the available energy of the jets that has been a major issue in the past (Böttcher et al. 2013; Zdziarski & Böttcher 2015; Lioudakis & Petropoulou 2020; Kantzas et al. 2022). In Figure 5.10, we plot the specific enthalpy of the protons  $\Gamma_p U_p / \rho c^2$  divided by  $\mu$  as a function of the total jet enthalpy  $h$ . This quantity expresses the fraction of the total energy flux of the jet that is used by the accelerated protons, and we show its dependence on  $h$  for different average electron Lorentz factors, as indicated by the colour-map. Regardless of the average electron energy  $\langle \varepsilon_e \rangle$ , the protons can hardly carry more than  $\sim 10$  per cent of the total energy in the jets because higher fractions would require specific enthalpy  $h$  of the order of a few or above (upper-right corner of the plot) resulting in strongly magnetised flows ( $\sigma \gtrsim \gamma h$ ). Moreover, for particular values of  $\langle \varepsilon_e \rangle$  (see the blue lines for instance that

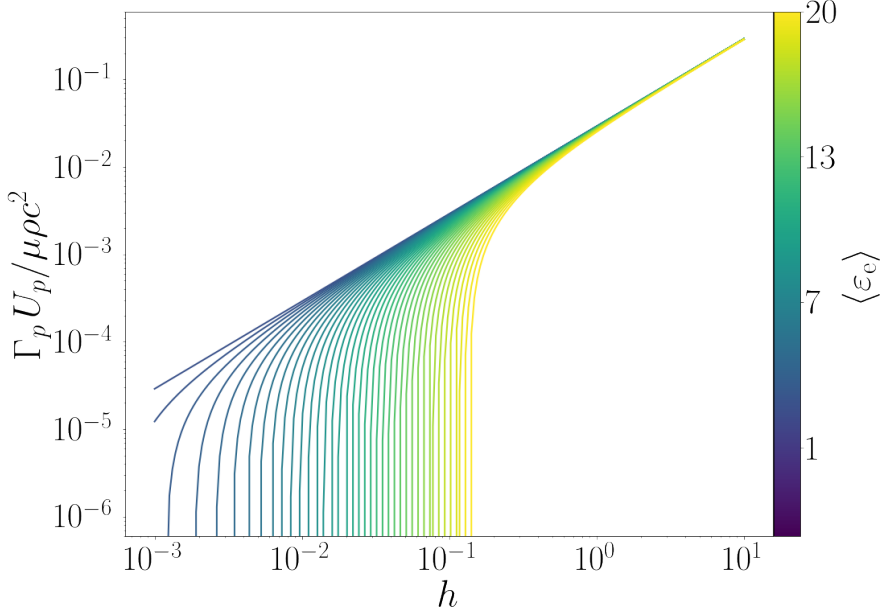


**Figure 5.10:** The specific enthalpy of the protons  $\Gamma_p U_p / \rho c^2$  divided by  $\mu$  shows the total energy that is allocated to protons with respect to the total available jet energy, as a function of the jet specific enthalpy  $h$ . We plot the proton energy density for a number of different electron energy densities that correspond to different values of  $\langle \varepsilon_e \rangle$  as shown in the colour-map, and we use  $\eta_e = 10$ .

correspond to values of the order of 1 to 5), the protons can only be accelerated if the total specific enthalpy  $h$  is greater than some critical value  $h > h_{\text{crit}}$  where

$$h_{\text{crit}} = \frac{(\langle \varepsilon_e \rangle - 1)\Gamma_e}{1 + \frac{m_p/m_e}{\eta_e}}, \quad (5.38)$$

hence the cutoffs for different  $\langle \varepsilon_e \rangle$  at small values of  $h$ . In this particular figure, we use  $\eta_e = 10$ , but as we show in Appendix 5.D for smaller (larger) values of  $\eta_e$  the only difference is that the cutoffs are located to smaller (larger) values of  $h$ .

From Figure 5.10, we see that the energy of the accelerated protons never exceeds that of the jet because the specific enthalpy of the non-thermal protons is always less than the total normalised energy flux ( $\Gamma_p U_p / \rho c^2 < \mu$ ).

## 5.7 Summary and Conclusions

Relativistic jets are efficient CR accelerators, but we still do not fully understand the particle acceleration mechanism. To fully interpret the jet kinematics, and how they relate to particle acceleration, we need to better understand how to link the observed spectra emitted by jetted sources over more than ten orders of magnitude in photon frequency to the jet physical properties. Currently uncertainties about the composition as well as a lack of conserved dynamical models have contributed to a degeneracy between leptonic and lepto-hadronic models.

To break this degeneracy, we have developed a new multi-zone approach that links the jet composition to the jet dynamics. The total energy flux along the jet is conserved, where magnetic energy can be dissipated into both kinetic and gas enthalpy via particle acceleration. This new approach makes clear the key role that the specific enthalpy  $h$  can have on the evolution and exchange of energy along the jet. In particular the enthalpy should be explicitly taken into account in models where: i) electrons accelerate to large average energies, ii) protons accelerate in the jets as well, and/or iii) when the jet is pair-dominated, as suggested for numerous Galactic and extragalactic jets launched by black holes.

When protons are accelerated into a non-thermal power law, the energy requirement often exceeds the total energy that can be provided by the jet and/or the accretion energy onto the black hole, potentially violating energy conservation. We have developed a new model **HadJet** based on our earlier lepto-hadronic work, that now conserves energy and includes a prescription for proton entrainment. By allowing the jets to entrain protons over a range of distance, as seen to occur in GRMHD simulations via eddies forming at the jet/accretion disc interface ([CLTM19](#)), we demonstrate a new method to avoid the “hadronic power” problem in a more self-consistent approach. In a future work, we plan to further explore the impact of mass loading on the multiwavelength emission of both BHXB jets and AGN jets.

## Acknowledgements

DK and SM are supported by the Netherlands Organisation for Scientific Research (NWO) VICI grant (no. 639.043.513).

## Data availability

No new data were generated or analysed in support of this research.

## 5.A Specific enthalpy for a hard power law of accelerated particles

In Figure 5.11 we plot the evolution of  $h$  for different jet composition. See Section 5.3.1 for a detailed description of the subplots. In this figure, we show the evolution of  $h$  assuming that the particles accelerate in a harder power law with an index of  $p = 1.7$  compared to  $p = 2.2$  we discuss in the main text.

In the top subplots, we notice a similar behaviour to Figure 5.1 but  $h$  goes to larger values for the case of a pair-dominated jet ( $h \sim \Gamma_e \langle \varepsilon_e \rangle$ ) according to Equation 5.28).

In the case where protons accelerate as well,  $h$  can attain values as large as  $\sim 2000$  for a particle acceleration with  $\varepsilon_{e,\min} = \varepsilon_{p,\min} = 10$  as we show in the lowermost subplots. This value is significantly larger than the expected values of  $\gamma$  of the bulk flow and in combination with the case where  $\sigma$  takes large values to lead to hard power laws of particles (Sironi et al. 2015, 2021; Ball et al. 2018), we see that the equation  $\mu \simeq \gamma(\sigma + 1)$  would not be a good approximation for the bulk Lorentz factor anymore (McKinney 2006; Komissarov et al. 2007, 2009; Beskin 2010).

## 5.B All energy components plots

In Figures 5.12–5.15, we show the evolution of  $\mu$  along the jet for different values of  $h$ . In particular, for all subplots of Figures 5.12–5.15, we assume that the accelerated particles follow a power law with an index of  $p=2.2$ . The outflow launches at a distance of  $6 r_g$  from the black hole and the particle acceleration initiates at  $10^3 r_g$ . While the jets accelerate at some maximum Lorentz factor  $\varepsilon_{\text{acc}} = 3$ , we assume that the magnetisation at this region has dropped to  $\sigma_{\text{acc}} = 0.1$ . For every subplot, we assume  $\eta_e = 10$  (top left),  $\eta_e = 100$  (top right),  $\eta_e = 10^3$  (bottom left) and  $\eta_e = 10^4$  (bottom right) constant along the outflow.

In Figure 5.12, we plot the jet evolution assuming only leptonic acceleration with an average Lorentz factor of  $\langle \varepsilon_e \rangle = 6$ . In agreement with Figure 5.1, we see that while the pair content increases in the jets, the specific enthalpy increases accordingly, and hence the total  $\mu$  increases. In the cases of  $\eta_e = 10^3$  and  $10^4$ , in particular, we see that the specific enthalpy  $h$  has values comparable or even larger than the bulk Lorentz factor of the jet flow.

In Figure 5.13, we plot a purely leptonic acceleration similar to Figure 5.12 but assuming  $\langle \varepsilon_e \rangle = 32$  instead. The pair-dominated jets where  $\eta_e = 10^3$  and  $10^4$  (bottom subplots), indicate that an efficient acceleration mechanism would lead to high values of  $h$ , which for the case of  $\eta_e = 10^4$  the overall value of  $\mu$  is of the order of 100, a much higher value than commonly found in the literature.

In Figures 5.14 and 5.15, we further account for hadronic acceleration with  $\langle \varepsilon_p \rangle = 4$ . In the cases where the jets are pair-dominated, to obtain the specific enthalpy  $h$

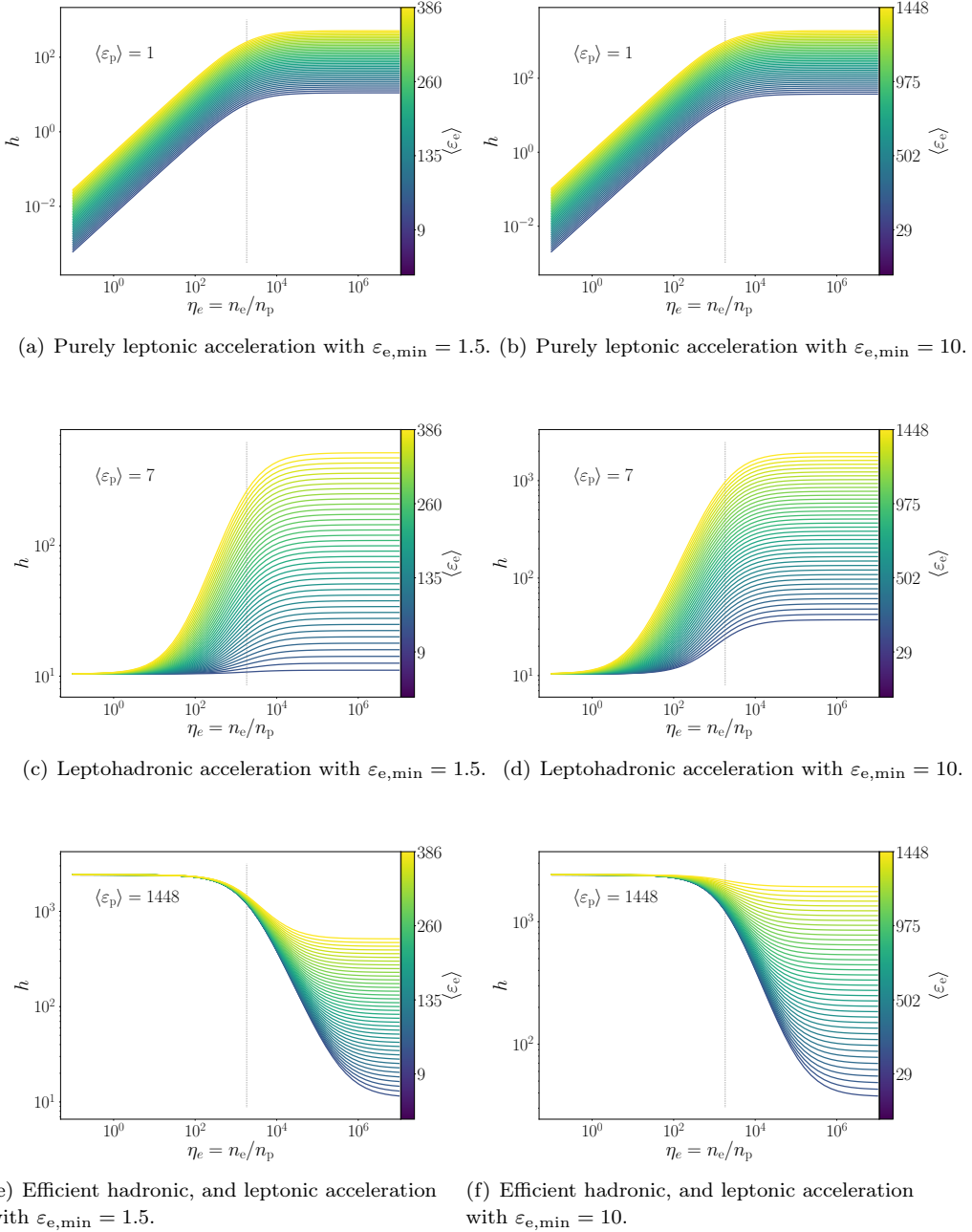


**Figure 5.11:** The jet specific enthalpy  $h$  as a function of the jet content  $\eta_e = n_e/n_p$ . In all plots, we assume  $p = 1.7$ . The average Lorentz factor of each species is indicated in each panel. The vertical lines correspond to  $\eta_e = m_p/m_e$ . Note the different y-axis ranges.

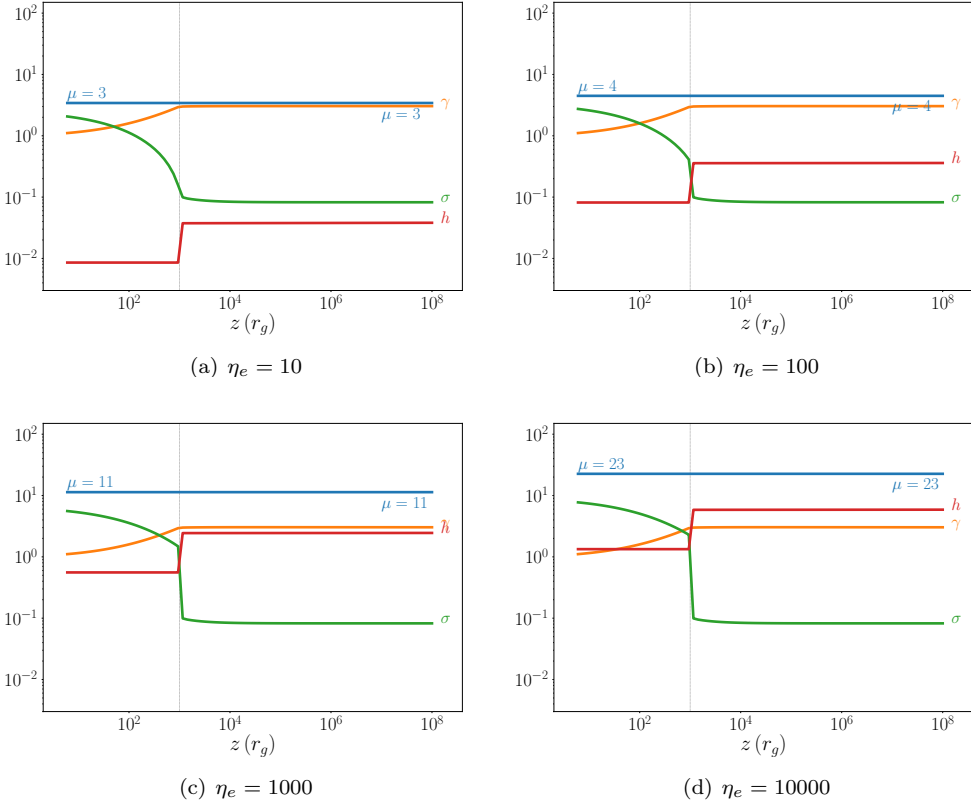


**Figure 5.12:** The evolution of the different energy components  $\gamma$ ,  $\sigma$  and  $h$  as indicated in each panel, and the total  $\mu$  based on Equation 5.19. We assume only leptonic acceleration with  $\langle \varepsilon_e \rangle = 6$ . The jet content is shown in each sub-caption.

calculated at the particle acceleration region, we require a jet base that is Poynting flux dominated with a magnetisation of the order of 50 – 100.

## 5.C Artificial mass loss

In Figure 5.16 we show how the increase in the specific enthalpy  $h$  in the mass-loading region may lead to a non-physical increase in  $\mu$  that would mean mass loss instead. Such an artificial mass loss is due to the fact that we assume a hot flow and/or a pair dominated jet base with  $\eta_e \gg 1000$ . To avoid such a condition, we first calculate the value of  $\mu$  from the 5<sup>th</sup> order polynomial

$$\log_{10}(\mu) = 0.22 x^5 - 0.72 x^4 + 0.45 x^3 + 0.10 x^2 - 0.093 x + 1.03, \quad (5.39)$$

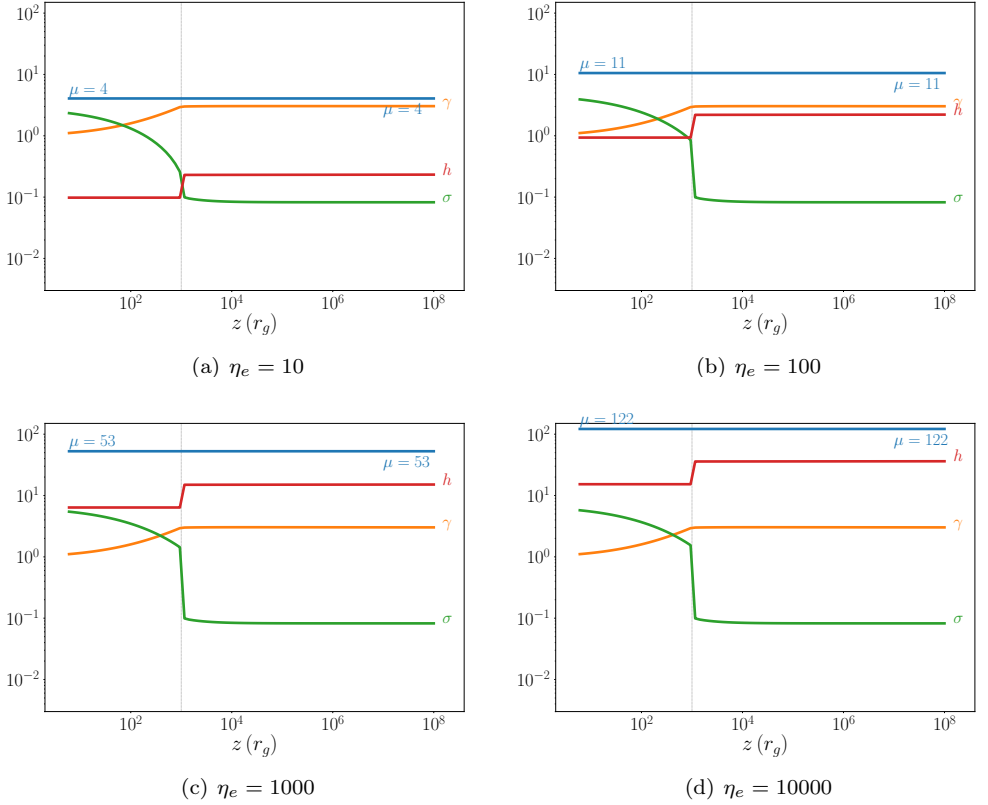


**Figure 5.13:** Same as Figure 5.12 but for  $\langle \varepsilon_e \rangle = 32$ .

based on the results of CLTM19, and then we calculate  $h$  from the equation  $h = \mu/\gamma - (\sigma + 1)$ , where the values of  $\gamma$  and  $\sigma$  are from Equations 5.30 and 5.29, respectively. In the above equation,  $x$  is the same as in Section 5.4.

In Figure 5.17, we plot the scenario where the specific enthalpy is particularly increased due to a hot jet base ( $k_B T_e = 20.000$  keV). The above assumption allows us to constrain the artificial mass loss once more (right subplot).

Finally, in Figure 5.18 we plot the scenario where the artificial mass loss is due to a combination of a large Lorentz factor ( $\gamma_{\text{acc}} = 10$ ) and the profile of  $h$  from Equation 5.31. The above assumption allows forcing a mass-loading scenario.

## 5.D Proton power

In Figure 5.19, we plot the fraction of the energy that is allocated to proton acceleration with respect to the total available energy flux of the jet  $\mu$ . We plot this quantity

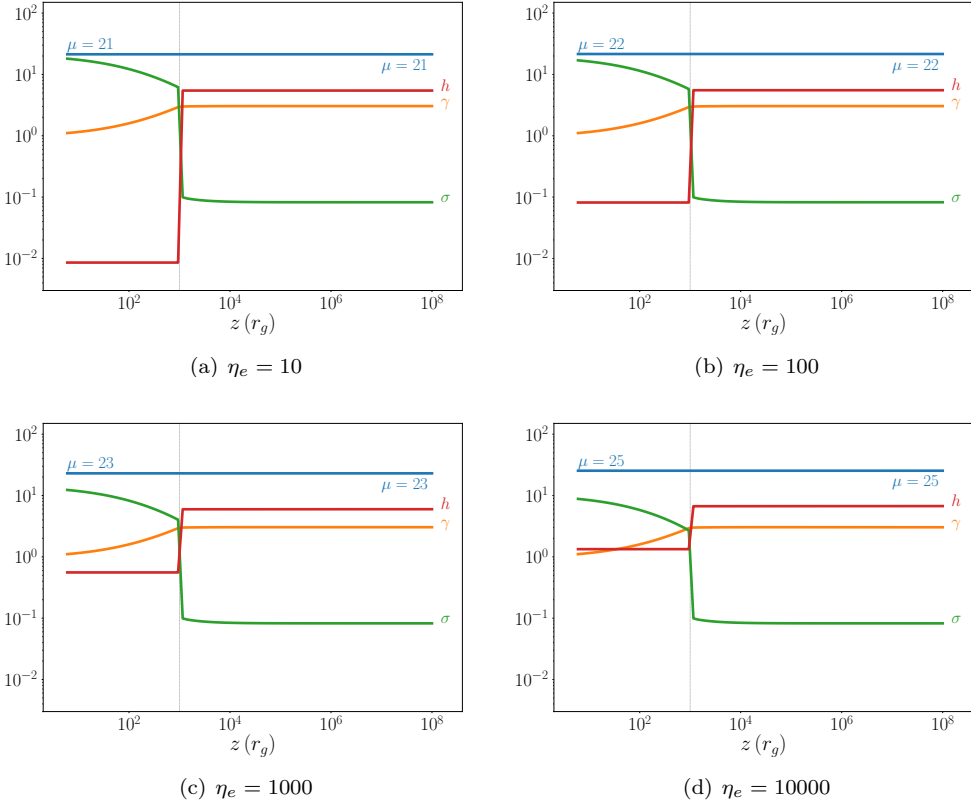


**Figure 5.14:** Same as Figure 5.12 but for  $\langle \varepsilon_e \rangle = 6$ . We further account for hadronic acceleration with  $\langle \varepsilon_p \rangle = 4$ .

versus the total specific enthalpy of the jet  $h$  for different average Lorentz factors  $\langle \varepsilon_e \rangle$  of the electrons. In the main text, we included the case where  $\eta_e = 10$  and here we plot the cases where  $\eta_e = 1$  (*left*) and  $\eta_e = 100$  (*right*), for completeness. See Section 5.6.3 for further discussion.



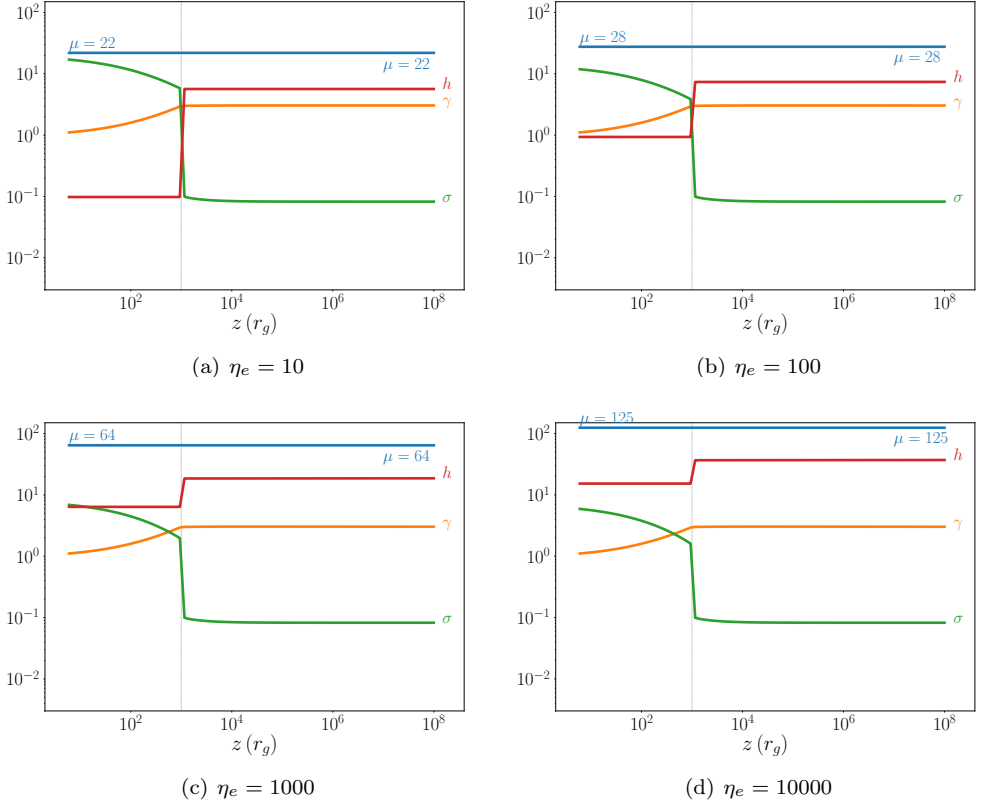


**Figure 5.15:** Same as Figure 5.14 but for  $\langle \varepsilon_e \rangle = 32$  and  $\langle \varepsilon_p \rangle = 4$ .

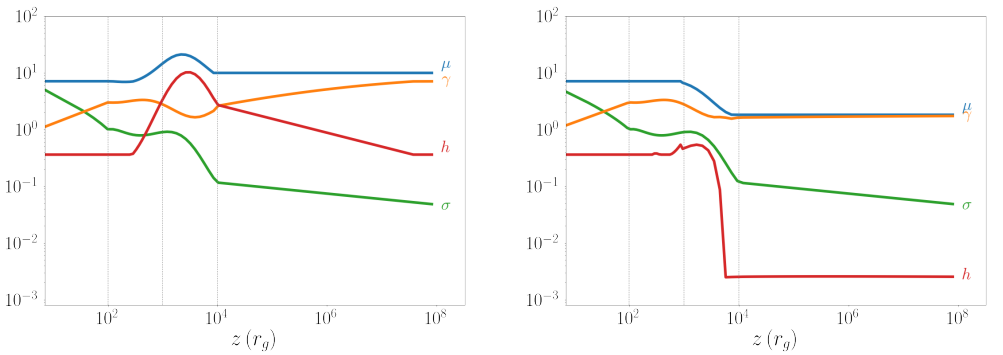


**Figure 5.16:** The jet energy components similar to Figure 5.6 but for the case of a jet base with  $\eta_e = 10^5$ . Following the description of Section 5.4, the particular profile of  $h$  leads to an artificial increase in  $\mu$  that would mean mass loss instead, which is unphysical (*left*). Using the profile of  $\mu$  from Equation 5.39, we constrain  $h$  to follow the mass-loading scenario (*right*). The initial magnetisation is  $\sigma_0 = 5$  and the Lorentz factor at the dissipation region is  $\gamma_{\text{acc}} = 3$ .

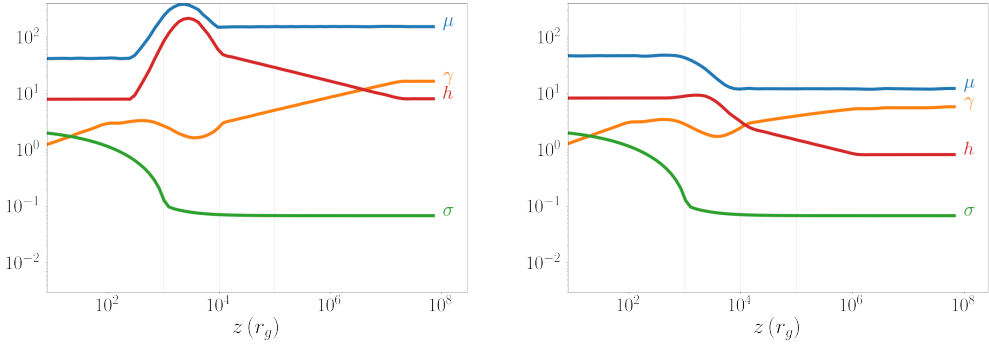


**Figure 5.17:** Similar to Figure 5.16 but for the case of a hot jet base with  $k_B T_e = 20.000 \text{ keV}$ ,  $\eta_e = 100$  and  $\sigma_0 = 30$ .

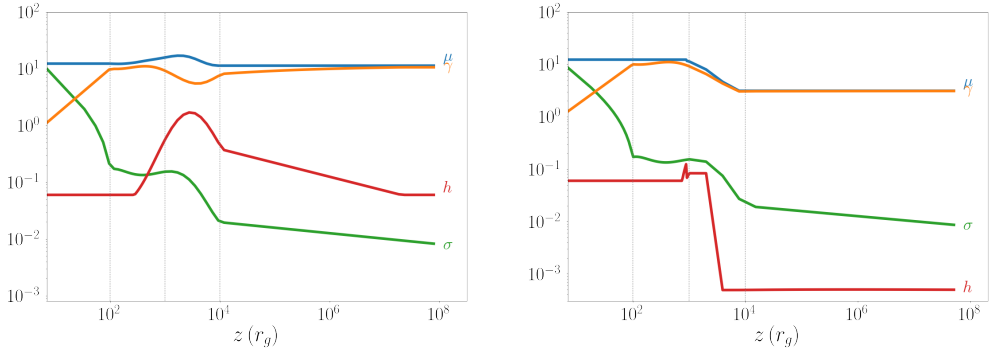


**Figure 5.18:** Similar to Figure 5.16 but for the case of  $\gamma_{\text{acc}} = 10$ ,  $\sigma_0 = 10$  and  $\eta_e = 10^4$ .

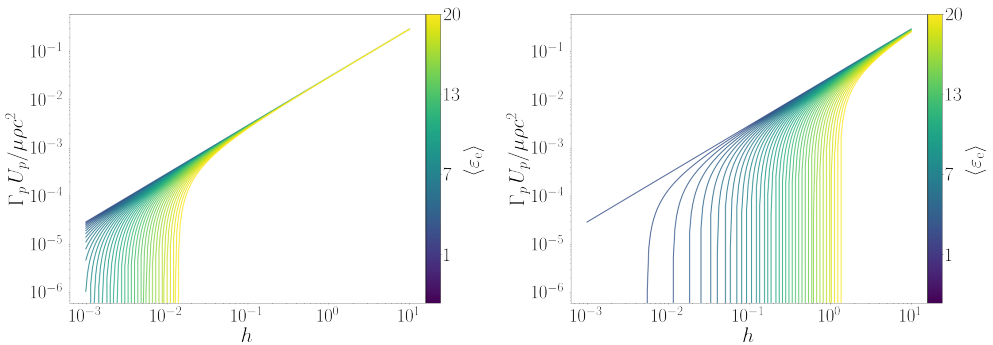


**Figure 5.19:** The specific enthalpy of the protons  $\Gamma_p U_p / \rho c^2$  divided by  $\mu$  shows the total energy that is allocated to protons with respect to the total available jet energy, as a function of the jet specific enthalpy  $h$ . We plot the proton energy density for a number of different electron energy densities that correspond to different values of  $\langle \epsilon_e \rangle$  as shown in the colour-map, and we use  $\eta_e = 1$  in the *left*, and  $\eta_e = 100$  in the *right*.

## Bibliography

- Aab, A., Abreu, P., Aglietta, M., et al. 2014, *Phys. Rev. D*, 90, 122005
- Aartsen, M., Ackermann, M., Adams, J., et al. 2018, *Science*, 361, 1378
- Aartsen, M. G., Abbasi, R., Abdou, Y., et al. 2013, *Science*, 342, 1242856
- Aartsen, M. G., Abbasi, R., Ackermann, M., et al. 2021, *J. Phys. G: Nucl. Part. Phys.*, 48, 060501
- Aartsen, M. G., Abraham, K., Ackermann, M., et al. 2016, *ApJ*, 833, 3
- Aartsen, M. G., Abraham, K., Ackermann, M., et al. 2017a, *ApJ*, 835, 151
- Aartsen, M. G., Abraham, K., Ackermann, M., et al. 2015, *ApJ*, 809, 98
- Aartsen, M. G., Ackermann, M., Adams, J., et al. 2020, *Phys. Rev. Lett.*, 124, 051103
- Aartsen, M. G., Ackermann, M., Adams, J., et al. 2019, *ApJ*, 886, 12
- Aartsen, M. G., Ackermann, M., Adams, J., et al. 2017b, *ApJ*, 849, 67
- Abbasi, R., Abdou, Y., Abu-Zayyad, T., et al. 2013, *Astroparticle Physics*, 44, 40
- Abbasi, R., Ackermann, M., Adams, J., et al. 2022, *ApJ Letters*, 930, L24
- Abbasi, R. U., Abe, M., Abu-Zayyad, T., et al. 2020, *ApJ*, 898, L28
- Abbasi, R. U., Abe, M., Abu-Zayyad, T., et al. 2019, *Phys. Rev. D*, 99, 022002
- Abbasi, R. U., Abe, M., Abu-Zayyad, T., et al. 2018, *ApJ*, 867, L27
- Abbasi, R. U., Abu-Zayyad, T., Al-Seady, M., et al. 2010, *Phys. Rev. Lett.*, 104, 161101
- Abbasi, R. U., Abu-Zayyad, T., Allen, M., et al. 2008, *Phys. Rev. Lett.*, 100, 101101
- Abbott, R., Abbott, T. D., Abraham, S., et al. 2021, *Phys. Rev. X*, 11, 021053
- Abdalla, H., Aharonian, F., Benkhali, F. A., et al. 2021, *ApJ*, 917, 6
- Abdo, A., Allen, B., Aune, T., et al. 2008, *ApJ*, 688
- Abdo, A. A., Ackermann, M., Ajello, M., et al. 2009, *ApJ*, 708, 1254
- Abdo, A. A., Ackermann, M., Ajello, M., et al. 2010, *ApJ*, 720, 272
- Abdollahi, S., Acero, F., Ackermann, M., et al. 2020, *ApJ Supplement Series*, 247, 33

- Abeysekara, A., Albert, A., Alfaro, R., et al. 2018, *Nature*, 562, 82
- Abeysekara, A., Albert, A., Alfaro, R., et al. 2017, *ApJ*, 843, 40
- Abeysekara, A., Alfaro, R., Alvarez, C., et al. 2013, *Astroparticle Physics*, 50-52, 26
- Abeysekara, A. U., Albert, A., Alfaro, R., et al. 2020, *Phys. Rev. Lett.*, 124, 021102
- Abramowski, A., Acero, F., Aharonian, F., et al. 2012, *A&A*, 537, A114
- Abramowski, A., Acero, F., Aharonian, F., et al. 2011, *A&A*, 531, A81
- Abramowski, A., Aharonian, F., Benkhali, F. A., et al. 2014, *MNRAS*, 439, 2828
- Abramowski, A., Fiasson, A., Krayzel, F., et al. 2016, *Nature*, 531, 476
- Abu-Zayyad, T., Aida, R., Allen, M., et al. 2013, *ApJ*, 768, L1
- Acharya, B., Actis, M., Aghajani, T., et al. 2013, *Astroparticle Physics*, 43, 3
- Achterberg, A. 1983, *A&A*, 119, 274
- Ackermann, M., Ajello, M., Allafort, A., et al. 2013, *Science*, 339, 807
- Ackermann, M., Ajello, M., Allafort, A., et al. 2011, *Science*, 334, 1103
- Ackermann, M., Ajello, M., Allafort, A., et al. 2012, *ApJ*, 755, 164
- Ackermann, M., Ajello, M., Atwood, W. B., et al. 2012, *ApJ*, 750, 3
- Ackermann, M., Ajello, M., Baldini, L., et al. 2018, *ApJ*, 237, 32
- Actis, M., Agnetta, G., Aharonian, F., et al. 2011, *Experimental Astronomy*, 32, 193
- Adrián-Martínez, S., Ageron, M., Aharonian, F., et al. 2016, *J. Phys. G: Nucl. Part. Phys.*, 43, 084001
- Adriani, O., Akaike, Y., Asano, K., et al. 2019, *Phys. Rev. Lett.*, 122, 181102
- Adriani, O., Akaike, Y., Asano, K., et al. 2018, *Phys. Rev. Lett.*, 120, 261102
- Adriani, O., Barbarino, G. C., Bazilevskaya, G. A., et al. 2013, *Phys. Rev. Lett.*, 111, 081102
- Adriani, O., Barbarino, G. C., Bazilevskaya, G. A., et al. 2010, *Phys. Rev. Lett.*, 105, 121101
- Adriani, O., Barbarino, G. C., Bazilevskaya, G. A., et al. 2011, *Science*, 332, 69
- Adriani, O., Barbarino, G. C., Bazilevskaya, G. A., et al. 2014, *ApJ*, 791, 93
- Adrián-Martínez, S., Albert, A., André, M., et al. 2016, *Physics Letters B*, 760, 143
- Aguilar, M., Aisa, D., Alpat, B., et al. 2015a, *Phys. Rev. Lett.*, 114, 171103
- Aguilar, M., Aisa, D., Alpat, B., et al. 2014a, *Phys. Rev. Lett.*, 113, 221102
- Aguilar, M., Aisa, D., Alpat, B., et al. 2015b, *Phys. Rev. Lett.*, 115, 211101
- Aguilar, M., Aisa, D., Alvino, A., et al. 2014b, *Phys. Rev. Lett.*, 113, 121102
- Aguilar, M., Alberti, G., Alpat, B., et al. 2013, *Phys. Rev. Lett.*, 110, 141102
- Aguilar, M., Ali Cavasonza, L., Alpat, B., et al. 2016, *Phys. Rev. Lett.*, 117, 091103
- Aharonian, F. 2000, *New Astronomy*, 5, 377
- Aharonian, F. 2002, *MNRAS*, 332, 215
- Aharonian, F., Akhperjanian, A., Barrio, J., et al. 1999, *A&A*, 342, 69
- Aharonian, F., Akhperjanian, A. G., Aye, K.-M., et al. 2005, *Science*, 309, 746
- Aharonian, F., Akhperjanian, A. G., Barres de Almeida, U., et al. 2008a, *Phys. Rev. Lett.*, 101, 261104
- Aharonian, F., Akhperjanian, A. G., Bazer-Bachi, A. R., et al. 2007a, *ApJ*, 661, 236

- Aharonian, F., Akhperjanian, A. G., Bazer-Bachi, A. R., et al. 2006a, *A&A*, 457, 899
- Aharonian, F., Akhperjanian, A. G., Bazer-Bachi, A. R., et al. 2007b, *A&A*, 464, 235
- Aharonian, F., Akhperjanian, A. G., Bazer-Bachi, A. R., et al. 2006b, *A&A*, 449, 223
- Aharonian, F., Akhperjanian, A. G., de Almeida, U. B., et al. 2009, *ApJ*, 692, 1500
- Aharonian, F., Buckley, J., Kifune, T., & Sinnis, G. 2008b, *Rep. Prog. Phys.*, 71, 096901
- Aharonian, F., Yang, R., & de Oña Wilhelmi, E. 2019, *Nature Astronomy*, 3, 561
- Aharonian, F. A. 2004, *Very high energy cosmic gamma radiation: a crucial window on the extreme Universe* (World Scientific)
- Aharonian, F. A. & Atoyan, A. M. 2000, arXiv:0009009
- Aharonian, F. A., Belyanin, A. A., Derishev, E. V., Kocharovskiy, V. V., & Kocharovskiy, V. V. 2002, *Phys. Rev. D*, 66, 023005
- Ahn, H. S., Allison, P., Bagliesi, M. G., et al. 2009, *ApJ*, 707, 593
- Ahnen, M. L., Ansoldi, S., Antonelli, L., et al. 2017a, *MNRAS*, 472, 3474
- Ahnen, M. L., Ansoldi, S., Antonelli, L. A., et al. 2017b, *MNRAS*, 472, 2956
- Aiello, S., Akrame, S., Ameli, F., et al. 2019, *Astroparticle Physics*, 111, 100
- Ajello, M., Angioni, R., Axelsson, M., et al. 2020, *ApJ*, 892, 105
- Ajello, M., Mauro, M. D., Paliya, V. S., & Garrappa, S. 2020, *ApJ*, 894, 88
- Albert, A., Alfaro, R., Alvarez, C., et al. 2021, *ApJ Letters*, 912, L4
- Albert, A., Alfaro, R., Alvarez, C., et al. 2020, *ApJ*, 905, 76
- Albert, A., André, M., Anghinolfi, M., et al. 2017a, *Phys. Rev. D*, 96, 082001
- Albert, A., André, M., Anghinolfi, M., et al. 2018, *ApJ*, 868, L20
- Albert, A., André, M., Anton, G., et al. 2017b, *J. Cosmology Astropart. Phys.*, 2017, 019
- Albert, J., Aliu, E., Anderhub, H., et al. 2007, *A&A*, 474, 937
- Aleksić, J., Ansoldi, S., Antonelli, L. A., et al. 2015, *A&A*, 576, A36
- Aloisio, R., Berezhinsky, V., & Gazizov, A. 2012, *Astroparticle Physics*, 39-40, 129
- Alves Batista, R. & Silk, J. 2017, *Phys. Rev. D*, 96, 103003
- Amato, E. & Blasi, P. 2005, *MNRAS: Letters*, 364, L76
- Amato, E. & Blasi, P. 2006, *MNRAS*, 371, 1251
- Amato, E. & Blasi, P. 2009, *MNRAS*, 392, 1591
- Ambrosone, A., Chianese, M., Fiorillo, D. F. G., et al. 2021, *MNRAS*, 503, 4032
- Amenomori, M., Ayabe, S., Cao, P. Y., et al. 1999, *ApJ*, 525, L93
- Amenomori, M., Bao, Y. W., Bi, X. J., et al. 2021, *Phys. Rev. Lett.*, 126, 141101
- Amenomori, M., Bao, Y. W., Bi, X. J., et al. 2019, *Phys. Rev. Lett.*, 123, 051101
- Anchordoqui, L. A., Goldberg, H., Paul, T. C., da Silva, L. H. M., & Vlcek, B. J. 2014, *Phys. Rev. D*, 90, 123010
- Anglés-Castillo, A., Perucho, M., Martí, J. M., & Laing, R. A. 2020, *MNRAS*, 500, 1512
- Apel, W., Arteaga-Velázquez, J., Bekk, K., et al. 2013, *Astroparticle Physics*, 47, 54
- Apel, W. D., Arteaga-Velázquez, J. C., Bekk, K., et al. 2011, *Phys. Rev. Lett.*, 107,

- 171104
- Archambault, S., Archer, A., Benbow, W., et al. 2017, *ApJ*, 836, 23
- Astropy Collaboration, Robitaille, T. P., Tollerud, E. J., et al. 2013, *A&A*, 558, A33
- Atkins, R., Benbow, W., Berley, D., et al. 2003, *ApJ*, 595, 803
- Atkins, R., Benbow, W., Berley, D., et al. 2005, *Phys. Rev. Lett.*, 95, 251103
- Atkins, R., Benbow, W., Berley, D., et al. 2000, *Nucl. Instrum. Methods A*, 449, 478
- Atri, P., Miller-Jones, J. C. A., Bahramian, A., et al. 2020, *MNRAS: Letters*, 493, L81
- Aublin, J., Illuminati, G., & Navas, S. 2019, arXiv:1908.08248
- Axford, W. 1969, in *Invited Papers (Springer)*, 155–203
- Axford, W. I., Leer, E., & Skadron, G. 1977, *International Cosmic Ray Conference*, 11, 132
- Baade, W. & Minkowski, R. 1954, *ApJ*, 119, 215
- Baade, W. & Zwicky, F. 1934, *Proceedings of the National Academy of Sciences*, 20, 259
- Bai, X., Bi, B. Y., Bi, X. J., et al. 2019, arXiv:1905.02773
- Baixeras, C. 2003, *Nucl. Phys. B Proc. Suppl.*, 114, 247
- Ball, D., Sironi, L., & Özel, F. 2018, *ApJ*, 862, 80
- Band, D., Matteson, J., Ford, L., et al. 1993, *ApJ*, 413, 281
- Barrau, A., Bazer-Bachi, R., Beyer, E., et al. 1998, *Nucl. Instrum. Methods A*, 416, 278
- Barret, D., McClintock, J. E., & Grindlay, J. E. 1996, *ApJ*, 473, 963
- Bartoli, B., Bernardini, P., Bi, X. J., et al. 2014, *ApJ*, 790, 152
- Bartoli, B., Bernardini, P., Bi, X. J., et al. 2015, *ApJ*, 809, 90
- Basak, R., Zdziarski, A. A., Parker, M., & Islam, N. 2017, *MNRAS*, 472, 4220
- Becker, P. A., Le, T., & Dermer, C. D. 2006, *ApJ*, 647, 539
- Bednarek, W., Burgio, G., & Montaruli, T. 2005, *New Astronomy Reviews*, 49, 1
- Beer, M. E. & Podsiadlowski, P. 2002, *MNRAS*, 331, 351
- Begelman, M. C. 1998, *ApJ*, 493, 291
- Begelman, M. C., Blandford, R. D., & Rees, M. J. 1984, *Rev. Mod. Phys.*, 56, 255
- Bell, A. R. 1978a, *MNRAS*, 182, 147
- Bell, A. R. 1978b, *MNRAS*, 182, 443
- Bell, A. R. 2004, *MNRAS*, 353, 550
- Belloni, T., ed. 2010, *Lecture Notes in Physics*, Berlin Springer Verlag, Vol. 794, *The Jet Paradigm*
- Belloni, T., Méndez, M., van der Klis, M., Lewin, W. H. G., & Dieters, S. 1999, *ApJ*, 519, L159
- Belloni, T., Parolin, I., Del Santo, M., et al. 2006, *MNRAS*, 367, 1113
- Belloni, T. M., Zhang, L., Kylafis, N. D., Reig, P., & Altamirano, D. 2020, *MNRAS*, 496, 4366
- Beloborodov, A. M. 2017, *ApJ*, 850, 141

- Berezhko, E. G. & Ellison, D. C. 1999, *ApJ*, 526, 385
- Berezinsky, V. 1991, *Nucl. Phys. B Proc. Suppl.*, 19, 375
- Berezinsky, V. 2013, *EPJ Web of Conferences*, 53, 01003
- Beskin, V. S. 2010, *Physics-Uspekhi*, 53, 1199
- Beskin, V. S. & Nokhrina, E. E. 2006, *MNRAS*, 367, 375
- Bethe, H. & Heitler, W. 1934, *Proceedings of the Royal Society of London. Series A*, 146, 83
- Bhattacharya, D. & van den Heuvel, E. P. J. 1991, *Phys. Rep.*, 203, 1
- Binns, W. R., Garrard, T. L., Israel, M. H., et al. 1988, *ApJ*, 324, 1106
- Bird, D., Corbata, S., Dai, H., et al. 1993, *Phys. Rev. Lett.*, 71, 3401
- Bird, D. J., Corbato, S. C., Dai, H. Y., et al. 1995, *ApJ*, 441, 144
- Biskamp, D. 1996, *Ap&SS*, 242, 165
- Blandford, R. & Königl, A. 1979, *ApJ*, 232, 34
- Blandford, R. D. & Levinson, A. 1995, *ApJ*, 441, 79
- Blandford, R. D. & Ostriker, J. P. 1978, *ApJ*, 221, L29
- Blandford, R. D. & Payne, D. G. 1982, *MNRAS*, 199, 883
- Blandford, R. D. & Rees, M. J. 1974, *MNRAS*, 169, 395
- Blandford, R. D. & Znajek, R. L. 1977, *MNRAS*, 179, 433
- Blasi, P. 2013, *Nuclear Physics B Proceedings Supplements*, 239, 140
- Blasi, P., Amato, E., & Caprioli, D. 2007a, *MNRAS*, 375, 1471
- Blasi, P., Gabici, S., & Brunetti, G. 2007b, *International Journal of Modern Physics A*, 22, 681
- Blattnig, S. R., Swaminathan, S. R., Kruger, A. T., Ngom, M., & Norbury, J. W. 2000, *Phys. Rev. D*, 62, 094030
- Blumenthal, G. R. 1970, *Phys. Rev. D*, 1, 1596
- Blumenthal, G. R. & Gould, R. J. 1970, *Reviews of Modern Physics*, 42, 237
- Bodaghee, A., Tomsick, J. A., Pottschmidt, K., et al. 2013, *ApJ*, 775, 98
- Bodo, G., Mamatsashvili, G., Rossi, P., & Mignone, A. 2021, *MNRAS*, 510, 2391
- Bogovalov, S. & Tsinganos, K. 2005, *MNRAS*, 357, 918
- Bolton, C. T. 1972, *Nature*, 235, 271
- Borione, A., Covault, C., Cronin, J., et al. 1994, *Nucl. Instrum. Methods A*, 346, 329
- Bosch-Ramon, V., Khangulyan, D., & Aharonian, F. 2008, *A&A*, 489, L21
- Bosch-Ramon, V., Romero, G. E., & Paredes, J. M. 2006, *A&A*, 447, 263
- Böttcher, M. & Dermer, C. D. 2005, *ApJ Letters*, 634, L81
- Böttcher, M., Reimer, A., Sweeney, K., & Prakash, A. 2013, *ApJ*, 768, 54
- Böttcher, M. & Schlickeiser, R. 1997, *A&A*, 325, 866
- Bowman, M., Leahy, J. p., & Komissarov, S. S. 1996, *MNRAS*, 279, 899
- Broderick, A. E. & Tchekhovskoy, A. 2015, *ApJ*, 809, 97
- Bromberg, O. & Tchekhovskoy, A. 2015, *MNRAS*, 456, 1739
- Brown, A., Vallenari, A., Prusti, T., et al. 2018, *A&A*, 616, A1
- Buitink, S., Corstanje, A., Falcke, H., et al. 2016, *Nature*, 531, 70

## BIBLIOGRAPHY

---

- Buxton, M. M., Bailyn, C. D., Capelo, H. L., et al. 2012, *AJ*, 143, 130
- Callanan, P. J., Charles, P. A., Honey, W. B., & Thorstensen, J. R. 1992, *MNRAS*, 259, 395
- Cangemi, F., Beuchert, T., Siegert, T., et al. 2021, *A&A*, 650, A93
- Cao, Z. 2010, *Chinese Physics C*, 34, 249
- Cao, Z., Aharonian, F. A., An, Q., et al. 2021a, *Nature*, 594, 33
- Cao, Z., Lucchini, M., Markoff, S., Connors, R. M. T., & Grinberg, V. 2021b, *MNRAS*, 509, 2517
- Caprioli, D. 2012, *J. Cosmology Astropart. Phys.*, 2012, 038
- Caprioli, D. & Spitkovsky, A. 2013, *ApJ*, 765, L20
- Caprioli, D. & Spitkovsky, A. 2014a, *ApJ*, 783, 91
- Caprioli, D. & Spitkovsky, A. 2014b, *ApJ*, 794, 46
- Caprioli, D. & Spitkovsky, A. 2014c, *ApJ*, 794, 47
- Carulli, A. M., Reynoso, M. M., & Romero, G. E. 2021, *Astroparticle Physics*, 128, 102557
- Casares, J., Charles, P. A., & Marsh, T. R. 1995, *MNRAS*, 277, L45
- Casella, P., Maccarone, T. J., O'Brien, K., et al. 2010, *MNRAS: Letters*, 404, L21
- Cawley, M. F., Fegan, D., Harris, K., et al. 1990, *Experimental Astronomy*, 1, 173
- Celotti, A. & Fabian, A. C. 1993, *MNRAS*, 264, 228
- Celotti, A., Ghisellini, G., & Chiaberge, M. 2001, *MNRAS*, 321, L1
- Cendes, Y., Eftekhari, T., Berger, E., & Polinsky, E. 2021, *ApJ*, 908, 125
- cenko, S. B., Krimm, H. A., Horesh, A., et al. 2012, *ApJ*, 753, 77
- Cerutti, B., Werner, G. R., Uzdensky, D. A., & Begelman, M. C. 2014, *ApJ*, 782, 104
- Chang, J., Adams, J., Ahn, H., et al. 2008, *Nature*, 456, 362
- Chang, J., Ambrosi, G., An, Q., et al. 2017, *Astroparticle Physics*, 95, 6
- Chatterjee, K., Liska, M., Tchekhovskoy, A., & Markoff, S. B. 2019, *MNRAS*, 490, 2200
- Chauhan, J., Miller-Jones, J. C. A., Anderson, G. E., et al. 2019, *MNRAS: Letters*, 488, L129
- Chauhan, J., Miller-Jones, J. C. A., Raja, W., et al. 2020, *MNRAS: Letters*, 501, L60
- Chauvin, M., Florén, H. G., Friis, M., et al. 2018a, *Nature Astronomy*, 2, 652
- Chauvin, M., Florén, H.-G., Jackson, M., et al. 2018b, *MNRAS: Letters*, 483, L138
- Chodorowski, M. J., Zdziarski, A. A., & Sikora, M. 1992, *ApJ*, 400, 181
- Cobb, B. E., Bailyn, C. D., van Dokkum, P. G., & Natarajan, P. 2006, *ApJ*, 645, L113
- Comisso, L. & Sironi, L. 2018, *Phys. Rev. Lett.*, 121, 255101
- Connors, R., Markoff, S., Nowak, M., et al. 2016, *MNRAS*, 466, 4121
- Connors, R. M. T., van Eijnatten, D., Markoff, S., et al. 2019, *MNRAS*, 485, 3696
- Cooper, A. J., Gaggero, D., Markoff, S., & Zhang, S. 2020, *MNRAS*, 493, 3212
- Coppi, P. & Blandford, R. 1990, *MNRAS*, 245, 453
- Corbel, S., Aussel, H., Broderick, J. W., et al. 2013, *MNRAS: Letters*, 431, L107



- Corbel, S., Coriat, M., Brocksopp, C., et al. 2012, *MNRAS*, 428, 2500
- Corbel, S. & Fender, R. P. 2002, *ApJ*, 573, L35
- Corbel, S., Fender, R. P., Tzioumis, A. K., et al. 2000, *A&A*, 359, 251
- Corbel, S., Nowak, M. A., Fender, R. P., Tzioumis, A. K., & Markoff, S. 2003, *A&A*, 400, 1007
- Coriat, M., Fender, R. P., Tasse, C., et al. 2019, *MNRAS*, 484, 1672
- Corstanje, A., Buitink, S., Falcke, H., et al. 2021, *Phys. Rev. D*, 103, 102006
- Cowley, A. P., Schmidtke, P. C., Hutchings, J. B., & Crampton, D. 2002, *ApJ*, 123, 1741
- Crumley, P., Caprioli, D., Markoff, S., & Spitkovsky, A. 2019, *MNRAS*, 485, 5105
- Crumley, P., Ceccobello, C., Connors, R. M. T., & Cavecchi, Y. 2017, *A&A*, 601, A87
- Curtis, H. D. 1918, *Publications of Lick Observatory*, 13, 9
- DAMPE Collaboration, Ambrosi, G., An, Q., et al. 2017, *Nature*, 552, 63
- DAMPE collaboration, An, Q., Asfandiyarov, R., et al. 2019, *Science advances*, 5, eaax3793
- Davelaar, J., Móscibrodzka, M., Bronzwaer, T., & Falcke, H. 2018, *A&A*, 612, A34
- De Colle, F. & Lu, W. 2020, *New Astronomy Reviews*, 89, 101538
- Deegan, P., Combet, C., & Wynn, G. A. 2009, *MNRAS*, 400, 1337
- Del Santo, M., Malzac, J., Jourdain, E., Belloni, T., & Ubertini, P. 2008, *MNRAS*, 390, 227
- Dermer, C. D. 1986, *A&A*, 157, 223
- Dermer, C. D. & Schlickeiser, R. 1993, *ApJ*, 416, 458
- Díaz Trigo, M., Miller-Jones, J. C., Migliari, S., Broderick, J. W., & Tzioumis, T. 2013, *Nature*, 504, 260
- Dimitrakoudis, S., Mastichiadis, A., Protheroe, R. J., & Reimer, A. 2012, *A&A*, 546, A120
- Distefano, C., Guetta, D., Waxman, E., & Levinson, A. 2002, *ApJ*, 575, 378
- Dmitruk, P., Matthaeus, W. H., & Seenu, N. 2004, *ApJ*, 617, 667
- Domček, V., Vink, J., Hernández Santisteban, J. V., DeLaney, T., & Zhou, P. 2021, *MNRAS*, 502, 1026
- Drenkhahn, G. & Spruit, H. C. 2002, *A&A*, 391, 1141
- Droulans, R., Belmont, R., Malzac, J., & Jourdain, E. 2010, *ApJ*, 717, 1022
- Drury, L. O. 1983, *Rep. Prog. Phys.*, 46, 973
- Drury, L. O. 2012, *Astroparticle Physics*, 39-40, 52
- Dundovic, A., Evoli, C., Gaggero, D., & Grasso, D. 2021, *A&A*, 653, A18
- Duro, R., Dauser, T., Grinberg, V., et al. 2016, *A&A*, 589, A14
- Dzielałak, M. A., Zdziarski, A. A., Szanecki, M., et al. 2019, *MNRAS*, 485, 3845
- Eichler, D. 1993, *ApJ*, 419, 111
- Eichmann, B., Rachen, J., Merten, L., van Vliet, A., & Tjus, J. B. 2018, *J. Cosmology Astropart. Phys.*, 2018, 036
- Ellison, D. C., Jones, F. C., & Reynolds, S. P. 1990, *ApJ*, 360, 702

## BIBLIOGRAPHY

---

- Evoli, C. 2018, *The Cosmic-Ray Energy Spectrum*
- Evoli, C., Gaggero, D., Grasso, D., & Maccione, L. 2008, *J. Cosmology Astropart. Phys.*, 2008, 018
- Evoli, C., Gaggero, D., Vittino, A., et al. 2017, *J. Cosmology Astropart. Phys.*, 2017, 015
- Evoli, C., Gaggero, D., Vittino, A., et al. 2018, *J. Cosmology Astropart. Phys.*, 2018, 006
- Fabian, A. 2012, *ARA&A*, 50, 455
- Fabian, A. C., Rees, M. J., Stella, L., & White, N. E. 1989, *MNRAS*, 238, 729
- Fabrika, S. 2004, *Astrophys. Space Phys. Reviews*, 12, 1
- Faganello, M., Pegoraro, F., Califano, F., & Marradi, L. 2010, *Physics of Plasmas*, 17, 062102
- Falcke, H. & Biermann, P. L. 1995, *A&A*, 293, 665
- Falcke, H., Körding, E., & Markoff, S. 2004, *A&A*, 414, 895
- Farrar, G. R. & Gruzinov, A. 2009, *ApJ*, 693, 329
- Felten, J. E. 1967, *ApJ*, 72, 796
- Fender, R. P. 2001, *MNRAS*, 322, 31
- Fender, R. P., Belloni, T. M., & Gallo, E. 2004, *MNRAS*, 355, 1105
- Fender, R. P., Homan, J., & Belloni, T. M. 2009, *MNRAS*, 396, 1370
- Fender, R. P., Maccarone, T. J., & van Kesteren, Z. 2005, *MNRAS*, 360, 1085
- Fender, R. P., Pooley, G. G., Durouchoux, P., Tilanus, R. P. J., & Brocksopp, C. 2000, *MNRAS*, 312, 853
- Fender, R. P., Stirling, A., Spencer, R., et al. 2006, *MNRAS*, 369, 603
- Fermi, E. 1949, *Phys. Rev.*, 75, 1169
- Fernández-Barral, A., Blanch, O., de Oña Wilhemi, E., et al. 2017, *ICRC2017*, 301, 734
- Feyereisen, M. R., Tamborra, I., & Ando, S. 2017, *J. Cosmology Astropart. Phys.*, 2017, 057
- Fields, B. D. & Prodanović, T. 2010, *ApJ*, 722, L199
- Fletcher, R., Gaisser, T., Lipari, P., & Stanev, T. 1994, *Physical Review D*, 50, 5710
- Fokker, A. D. 1914, *Annalen der Physik*, 348, 810
- Foreman-Mackey, D., Hogg, D. W., Lang, D., & Goodman, J. 2013, *PASP*, 125, 306
- Fornieri, O., Gaggero, D., & Grasso, D. 2020, *JCAP*, 2020, 009
- Forot, M., Laurent, P., Grenier, I. A., Gouiffès, C., & Lebrun, F. 2008, *ApJ*, 688, L29
- Frank, J., King, A., King, B., & Raine, D. 2002, *Accretion Power in Astrophysics*, *Accretion Power in Astrophysics* (Cambridge University Press)
- Fürst, F., Nowak, M. A., Tomsick, J. A., et al. 2015, *ApJ*, 808, 122
- Gabici, S. & Aharonian, F. A. 2014, *MNRAS: Letters*, 445, L70
- Gaggero, D., Grasso, D., Marinelli, A., Urbano, A., & Valli, M. 2015, *ApJ*, 815, L25
- Gaia Collaboration, Brown, A. G. A., Vallenari, A., et al. 2021, *A&A*, 649, A1
- Gaisser, T. K., Engel, R., & Resconi, E. 2016, *Cosmic rays and particle physics*

- (Cambridge University Press)
- Gallo, E., Fender, R., Kaiser, C., et al. 2005, *Nature*, 436, 819
- Gandhi, P., Blain, A. W., Russell, D. M., et al. 2011, *ApJ*, 740, L13
- Gandhi, P., Rao, A., Johnson, M. A. C., Paice, J. A., & Maccarone, T. J. 2019, *MNRAS*, 485, 2642
- García, J. A., Steiner, J. F., McClintock, J. E., et al. 2015, *ApJ*, 813, 84
- García, J. A., Tomsick, J. A., Sridhar, N., et al. 2019, *ApJ*, 885, 48
- Garcia-Munoz, M., Mason, G. M., & Simpson, J. A. 1975, *ApJ*, 202, 265
- Gedalin, M., Smolik, E., Spitkovsky, A., & Balikhin, M. 2012, *EPL (Europhysics Letters)*, 97, 35002
- Gelino, D. M., Balman, Ş., Kızıloğlu, U., et al. 2006, *ApJ*, 642, 438
- Gelino, D. M. & Harrison, T. E. 2003, *ApJ*, 599, 1254
- Génolini, Y., Boudaud, M., Batista, P.-I., et al. 2019, *Phys. Rev. D*, 99, 123028
- Georganopoulos, M., Aharonian, F. A., & Kirk, J. G. 2002, *A&A*, 388, L25
- Georganopoulos, M., Perlman, E. S., Kazanas, D., & McEnery, J. 2006, *ApJ*, 653, L5
- Ghisellini, G. 2013, *Radiative Processes in High Energy Astrophysics* (Springer International Publishing)
- Ghisellini, G. & Tavecchio, F. 2010, *MNRAS: Letters*, 409, L79
- Ghisellini, G., Tavecchio, F., Foschini, L., et al. 2010, *MNRAS*, 402, 497
- Ghisellini, G., Tavecchio, F., & Ghirlanda, G. 2009, *MNRAS*, 399, 2041
- Ghisellini, G., Tavecchio, F., Maraschi, L., Celotti, A., & Sbarrato, T. 2014, *Nature*, 515, 376
- Giannios, D. 2010, *MNRAS: Letters*, 408, L46
- Giannios, D., Kylafis, N. D., & Psaltis, D. 2004, *A&A*, 425, 163
- Giannios, D. & Spruit, H. C. 2006, *A&A*, 450, 887
- Gies, D. R., Bolton, C. T., Blake, R. M., et al. 2008, *ApJ*, 678, 1237
- Ginzburg, V. L. & Syrovatskii, S. I. 1964, *The Origin of Cosmic Rays* (Elsevier)
- Gomel, R., Mazeh, T., Faigler, S., et al. 2022, *arXiv:2206.06032*
- Gould, R. J. & Schröder, G. 1966, *Phys. Rev. Lett.*, 16, 252
- Gourgouliatos, K. N. & Komissarov, S. S. 2018, *Nature Astronomy*, 2, 167
- Granot, J., Komissarov, S. S., & Spitkovsky, A. 2011, *MNRAS*, 411, 1323
- Greisen, K. 1966, *Phys. Rev. Lett.*, 16, 748
- Grinberg, Leutenegger, M. A., Hell, N., et al. 2015, *A&A*, 576, A117
- Grinberg, V., Hell, N., Pottschmidt, K., et al. 2013, *A&A*, 554, A88
- Guépin, C., Kotera, K., Barausse, E., Fang, K., & Murase, K. 2018, *A&A*, 616, A179
- Guo, F., Li, H., Daughton, W., & Liu, Y.-H. 2014, *Phys. Rev. Lett.*, 113, 155005
- Guo, F., Li, X., Li, H., et al. 2016, *ApJ*, 818, L9
- Gurnett, D. A., Kurth, W. S., Burlaga, L. F., & Ness, N. F. 2013, *Science*, 341, 1489
- Haardt, F. & Maraschi, L. 1993, *ApJ*, 413, 507
- Hada, K., Kino, M., Doi, A., et al. 2016, *ApJ*, 817, 131
- Hailey, C. J., Mori, K., Bauer, F. E., et al. 2018, *Nature*, 556, 70

- Hakobyan, H., Philippov, A., & Spitkovsky, A. 2019, *ApJ*, 877, 53
- Hanson, M. M., Still, M. D., & Fender, R. P. 2000, *ApJ*, 541, 308
- Harlaftis, E. T., Horne, K., & Filippenko, A. V. 1996, *PASP*, 108, 762
- Harrison, F. A., Craig, W. W., Christensen, F. E., et al. 2013, *ApJ*, 770, 103
- Heida, M., Jonker, P. G., Torres, M. A. P., & Chiavassa, A. 2017, *ApJ*, 846, 132
- Heinz, S. 2006, *ApJ*, 636, 316
- Heinz, S. & Sunyaev, R. 2002, *A&A*, 390, 751
- Heinz, S. & Sunyaev, R. A. 2003, *MNRAS*, 343, L59
- Hernández, J. I. G., Rebolo, R., Israelian, G., et al. 2008, *ApJ*, 679, 732
- HESS, Abramowski, A., Aharonian, F., et al. 2014, *MNRAS*, 439, 2828
- Hess, V. 1912, arXiv:1808.02927
- H.E.S.S. Collaboration, Abdalla, H., Abramowski, A., et al. 2018a, *A&A*, 612, A9
- H.E.S.S. Collaboration, Abdalla, H., Aharonian, F., et al. 2018b, *A&A*, 620, A66
- Hillas, A. M. 1984, *Annual review of A&A*, 22, 425
- Hillas, A. M. 1985, 19th International Cosmic Ray Conference, 3, 445
- Hillwig, T. C., Gies, D. R., Huang, W., et al. 2004, *ApJ*, 615, 422
- Hinton, J. 2004, *New Astronomy Reviews*, 48, 331, 2nd VERITAS Symposium on the Astrophysics of Extragalactic Sources
- Hinton, J. & Collaboration, S. 2022, arXiv:2111.13158, ICRC2021, 23
- Hinton, J. & Hofmann, W. 2009, *Annual Review of A&A*, 47, 523
- Hinton, J. & Ruiz-Velasco, E. 2020, *J. Phys.: Conf. Ser.*, 1468, 012096
- Hinton, J. A., Skilton, J. L., Funk, S., et al. 2008, *ApJ*, 690, L101
- Hirata, K., Kajita, T., Koshiba, M., et al. 1987, *Phys. Rev. Lett.*, 58, 1490
- Hjellming, R. & Johnston, K. 1988, *ApJ*, 328, 600
- Hjellming, R. & Rupen, M. 1995, *Nature*, 375, 464
- Hoang, J., Molina, E., López, M., et al. 2019, arXiv:1908.06958
- Hoerbe, M. R., Morris, P. J., Cotter, G., & Becker Tjus, J. 2020, *MNRAS*, 496, 2885
- Hofmann, W., Collaboration, H., et al. 2001, in *International Cosmic Ray Conference*, Vol. 7, 2785
- Holder, J., Acciari, V. A., Aliu, E., et al. 2008, *AIP Conference Proceedings*, 1085, 657
- Homan, J., Buxton, M., Markoff, S., et al. 2005, *ApJ*, 624, 295
- Homan, J., Wijnands, R., Kong, A., et al. 2006, *MNRAS*, 366, 235
- Houck, J. C. & Denicola, L. A. 2000, in *Manset N., Veillet C., Crabtree D., eds, ASP Conf. Ser. Vol. 216, Astronomical Data Analysis Software and Systems IX. Astron. Soc. Pac., San Francisco*, 591
- Hümmer, S., Baerwald, P., & Winter, W. 2012, *Phys. Rev. Lett.*, 108, 231101
- Hümmer, S., Rüger, M., Spanier, F., & Winter, W. 2010, *ApJ*, 721, 630
- Hunter, J. D. 2007, *Computing in Science & Engineering*, 9, 90
- Hynes, R. I. 2005, *ApJ*, 623, 1026
- Hynes, R. I., Steeghs, D., Casares, J., Charles, P. A., & O'Brien, K. 2003, *ApJ*, 583,

L95

- Hynes, R. I., Steeghs, D., Casares, J., Charles, P. A., & O'Brien, K. 2004, *ApJ*, 609, 317
- IceCube-Gen2 Collaboration, Aartsen, M. G., Ackermann, M., et al. 2014, [arXiv:1412.5106](https://arxiv.org/abs/1412.5106)
- Illarionov, A. F. & Sunyaev, R. A. 1975, *A&A*, 39, 185
- Janssen, M., Falcke, H., Kadler, M., et al. 2021, *Nature Astronomy*, 5, 1017
- Jokipii, J. 1987, *ApJ*, 313, 842
- Jourdain, E., Roques, J., Chauvin, M., & Clark, D. 2012, *ApJ*, 761, 27
- Kafexhiu, E., Aharonian, F., Taylor, A., & Vila, G. 2014, *Physical Review D*, 90, 123014
- Kagan, D., Sironi, L., Cerutti, B., & Giannios, D. 2015, *Space Sci. Rev.*, 191, 545
- Kalmykov, N., Ostapchenko, S., & Pavlov, A. 1997, *Nucl. Phys. B Proc. Suppl.*, 52, 17
- Kantzas, D., Markoff, S., Beuchert, T., et al. 2020, *MNRAS*, 500, 2112
- Kantzas, D., Markoff, S., Lucchini, M., et al. 2022, *MNRAS*, 510, 5187
- Kara, E., Steiner, J. F., Fabian, A. C., et al. 2019, *Nature*, 565, 198
- Kashti, T. & Waxman, E. 2005, *Phys. Rev. Lett.*, 95, 181101
- Kaufman Bernadó, M. M. and Romero, G. E. & Mirabel, I. F. 2002, *A&A*, 385, L10
- Kawai, H. et al. 2008, *Nucl. Phys. B Proc. Suppl.*, 175-176, 221
- Keivani, A., Murase, K., Petropoulou, M., et al. 2018, *ApJ*, 864, 84
- Kelner, S. & Aharonian, F. 2008, *Physical Review D*, 78, 034013
- Kelner, S., Aharonian, F. A., & Bugayov, V. 2006, *Physical Review D*, 74, 034018
- Khiali, B., de Gouveia Dal Pino, E. d., & del Valle, M. V. 2015, *MNRAS*, 449, 34
- Kirsten, F., Vlemmings, W., Freire, P., et al. 2014, *A&A*, 565, A43
- Klein, O. & Nishina, Y. 1929, *Zeitschrift für Physik*, 52, 853
- Komissarov, S. S., Barkov, M. V., Vlahakis, N., & Königl, A. 2007, *MNRAS*, 380, 51
- Komissarov, S. S., Vlahakis, N., Königl, A., & Barkov, M. V. 2009, *MNRAS*, 394, 1182
- Königl, A. 1980, *The Physics of Fluids*, 23, 1083
- Kosenkov, I. A. & Veledina, A. 2018, *MNRAS*, 478, 4710
- Kosenkov, I. A., Veledina, A., Berdyugin, A. V., et al. 2020a, *MNRAS*, 496, L96
- Kosenkov, I. A., Veledina, A., Suleimanov, V. F., & Poutanen, J. 2020b, *A&A*, 638, A127
- Kotera, K. & Olinto, A. V. 2011, *Annual Review of Astronomy and Astrophysics*, 49, 119
- Kotera, K. & Silk, J. 2016, *ApJ*, 823, L29
- Kouveliotou, C., Meegan, C. A., Fishman, G. J., et al. 1993, *ApJ*, 413, L101
- Kreidberg, L., Bailyn, C. D., Farr, W. M., & Kalogera, V. 2012, *ApJ*, 757, 36
- Kulikov, G. & Khristiansen, G. 1959, *Sov. Phys. JETP*, 35, 441
- Kumar, P. & Zhang, B. 2015, *Physics Reports*, 561, 1

- Kylafis, N. D. & Reig, P. 2018, *A&A*, 614, L5
- Laurent, P., Rodriguez, J., Wilms, J., et al. 2011, *Science*, 332, 438
- Lawrence, M. A., Reid, R. J. O., & Watson, A. A. 1991, *J. Phys. G: Nucl. Part. Phys.*, 17, 733
- Lazarian, A., Vlahos, L., Kowal, G., et al. 2012, *Space science reviews*, 173, 557
- Lebrun, F., Leray, J. P., Lavocat, P., et al. 2003, *A&A*, 411, L141
- Lefa, E., Kelner, S. R., & Aharonian, F. A. 2012, *ApJ*, 753, 176
- Levinson, A. & Blandford, R. 1995, *ApJ*, 449, 86
- Levinson, A. & Eichler, D. 1993, *ApJ*, 418, 386
- Levinson, A. & Waxman, E. 2001, *Phys. Rev. Lett.*, 87, 171101
- Lewis, F., Russell, D. M., Fender, R. P., Roche, P., & Clark, J. S. 2008, arXiv:0811.2336
- Linsley, J. 1963, *Phys. Rev. Lett.*, 10, 146
- Liodakis, I., Blinov, D., Potter, S. B., & Rieger, F. M. 2021, *MNRAS: Letters*, 509, L21
- Liodakis, I. & Petropoulou, M. 2020, *ApJ*, 893, L20
- Lipari, P., Lusignoli, M., & Meloni, D. 2007, *Phys. Rev. D*, 75, 123005
- Liska, M., Hesp, C., Tchekhovskoy, A., et al. 2017, *MNRAS: Letters*, 474, L81
- Liska, M., Tchekhovskoy, A., & Quataert, E. 2020, *MNRAS*, 494, 3656
- Lister, M. L., Aller, M., Aller, H., et al. 2013, *AJ*, 146, 120
- Lister, M. L., Aller, M. F., Aller, H. D., et al. 2016, *AJ*, 152, 12
- Lister, M. L., Homan, D. C., Kadler, M., et al. 2009, *ApJ*, 696, L22
- Liu, Q. Z., van Paradijs, J., & van den Heuvel, E. P. J. 2007, *A&A*, 469, 807
- Liu, R.-Y., Rieger, F., & Aharonian, F. 2017, *ApJ*, 842, 39
- Longair, M. S. 2011, *High energy astrophysics* (Cambridge university press)
- López-Coto, R., de Oña Wilhelmi, E., Aharonian, F., Amato, E., & Hinton, J. 2022, *Nature Astronomy*, 1
- Lorenz, E. 2004, *New Astronomy Reviews*, 48, 339, 2nd VERITAS Symposium on the Astrophysics of Extragalactic Sources
- Lorimer, D. R., Faulkner, A. J., Lyne, A. G., et al. 2006, *MNRAS*, 372, 777
- Lucchini, M., Ceccobello, C., Markoff, S., et al. 2022, *MNRAS* *subm.*
- Lucchini, M., Krauss, F., & Markoff, S. 2019, *MNRAS*, 489, 1633
- Lucchini, M., Markoff, S., Crumley, P., Krauß, F., & Connors, R. M. T. 2018, *MNRAS*, 482, 4798
- Lucchini, M., Russell, T. D., Markoff, S. B., et al. 2021, *MNRAS*, 501, 5910
- Luque, P. D. I. T., Gaggero, D., Grasso, D., et al. 2022, arXiv:2203.15759
- Lynn, J. W., Quataert, E., Chandran, B. D. G., & Parrish, I. J. 2014, *ApJ*, 791, 71
- Magdziarz, P. & Zdziarski, A. A. 1995, *MNRAS*, 273, 837
- MAGIC Collaboration, Acciari, V. A., Ansoldi, S., et al. 2020, *A&A*, 643, L14
- Mahmoud, R. D., Done, C., & De Marco, B. 2019, *MNRAS*, 486, 2137
- Maitra, D., Markoff, S., Brocksopp, C., et al. 2009, *MNRAS*, 398, 1638

- Maitra, D., Miller, J. M., Markoff, S., & King, A. 2011, *ApJ*, 735, 107
- Malkov, M. & Drury, L. O. 2001, *Rep. Prog. Phys.*, 64, 429
- Malkov, M. A. 1997, *ApJ*, 485, 638
- Malyshev, D., Zdziarski, A. A., & Chernyakova, M. 2013, *MNRAS*, 434, 2380
- Mannheim, K. 1993, *A&A*, 269, 67
- Mannheim, K. & Schlickeiser, R. 1994, *A&A*, 286, 983
- Maraschi, L., Ghisellini, G., & Celotti, A. 1992, *ApJ*, 397, L5
- Marcowith, A., Henri, G., & Pelletier, G. 1995, *MNRAS*, 277, 681
- Margutti, R., Milisavljevic, D., Soderberg, A. M., et al. 2014, *ApJ*, 797, 107
- Markert, T. H., Canizares, C. R., Clark, G. W., et al. 1973, *ApJ*, 184, L67
- Markoff, S., Falcke, H., & Fender, R. 2001, *A&A*, 372, L25
- Markoff, S., Nowak, M., Corbel, S., Fender, R., & Falcke, H. 2003, *A&A*, 397, 645
- Markoff, S., Nowak, M., Young, A., et al. 2008, *ApJ*, 681, 905
- Markoff, S. & Nowak, M. A. 2004, *ApJ*, 609, 972
- Markoff, S., Nowak, M. A., Gallo, E., et al. 2015, *ApJ*, 812, L25
- Markoff, S., Nowak, M. A., & Wilms, J. 2005, *ApJ*, 635, 1203
- Marscher, A. P., Jorstad, S. G., D’Arcangelo, F. D., et al. 2008, *Nature*, 452, 966
- Mastichiadis, A. 2002, in *Relativistic Flows in Astrophysics*, ed. A. W. Guthmann, M. Georganopoulos, K. Manolakou, & A. Marcowith (Berlin, Heidelberg: Springer Berlin Heidelberg), 1–23
- Mastichiadis, A. & Kirk, J. G. 1995, *A&A*, 295, 613
- Mastichiadis, A. & Kirk, J. G. 2002, *PASA*, 19, 138
- Mastroserio, G., Ingram, A., & van der Klis, M. 2019, *MNRAS*, 488, 348
- Matthews, J. H., Bell, A. R., & Blundell, K. M. 2020, *New Astronomy Reviews*, 89, 101543
- McClintock, J., Remillard, R., Lewin, W., & Van Der Klis, M. 2006, ed. WHG Lewin, M van der Klis, Cambridge Univ, 71
- McKinney, J. C. 2006, *MNRAS*, 368, 1561
- McMullin, J. P., Waters, B., Schiebel, D., Young, W., & Golap, K. 2007, in *Astronomical Society of the Pacific Conference Series*, Vol. 376, *Astronomical Data Analysis Software and Systems XVI*, ed. R. A. Shaw, F. Hill, & D. J. Bell (*Astronomical Society of the Pacific Conference Series*), 127
- Melzani, M., Walder, R., Folini, D., Winisdoerffer, C., & Favre, J. M. 2014, *A&A*, 570, A112
- Merloni, A., Heinz, S., & Di Matteo, T. 2003, *MNRAS*, 345, 1057
- Mészáros, P. 2002, *Annual Review of Astronomy and Astrophysics*, 40, 137
- Mészáros, P. 2006, *Rep. Prog. Phys.*, 69, 2259
- Metzger, B. D., Giannios, D., & Horiuchi, S. 2011, *MNRAS*, 415, 2495
- Meurs, E. J. A. & van den Heuvel, E. P. J. 1989, *A&A*, 226, 88
- Mignone, A., Striani, E., Tavani, M., & Ferrari, A. 2013, *MNRAS*, 436, 1102
- Miller, J. M., Wojdowski, P., Schulz, N., et al. 2005, *ApJ*, 620, 398

## BIBLIOGRAPHY

---

- Miller-Jones, J. C. A., Bahramian, A., Orosz, J. A., et al. 2021, *Science*, 371, 1046
- Miller-Jones, J. C. A., Jonker, P. G., Dhawan, V., et al. 2009, *ApJ*, 706, L230
- Miller-Jones, J. C. A., Moin, A., Tingay, S. J., et al. 2012, *MNRAS: Letters*, 419, L49
- Mioduszewski, A. J., Rupen, M. P., Hjellming, R. M., Pooley, G. G., & Waltman, E. B. 2001, *ApJ*, 553, 766
- Mirabel, I. & Rodriguez, L. 1994, *Nature*, 371, 46
- Mitsuda, K., Inoue, H., Koyama, K., et al. 1984, *PASJ*, 36, 741
- Moll, R., Spruit, H. C., & Obergaulinger, M. 2008, *A&A*, 492, 621
- Mori, K., Hailey, C. J., Schutt, T. Y. E., et al. 2021, *ApJ*, 921, 148
- Morlino, G. & Caprioli, D. 2012, *A&A*, 538, A81
- Morrison, P. 1958, *Il Nuovo Cimento (1955-1965)*, 7, 858
- Móscibrodzka, M. & Falcke, H. 2013, *A&A*, 559, L3
- Móscibrodzka, M., Falcke, H., & Shiokawa, H. 2016, *A&A*, 586, A38
- Motta, S., Belloni, T., & Homan, J. 2009, *MNRAS*, 400, 1603
- Muñoz Darias, T., Casares, J., & Martínez-Pais, I. G. 2008, *MNRAS*, 385, 2205
- Mücke, A., Protheroe, R., Engel, R., Rachen, J., & Stanev, T. 2003, *Astroparticle Physics*, 18, 593
- Muñoz-Darias, T., Jiménez-Ibarra, F., Panizo-Espinar, G., et al. 2019, *ApJ*, 879, L4
- Murase, K., Ahlers, M., & Lacki, B. C. 2013, *Phys. Rev. D*, 88, 121301
- Murase, K., Dermer, C. D., Takami, H., & Migliori, G. 2012, *ApJ*, 749, 63
- Murase, K., Inoue, Y., & Dermer, C. D. 2014, *Phys. Rev. D*, 90, 023007
- Murase, K. & Ioka, K. 2013, *Phys. Rev. Lett.*, 111, 121102
- Murase, K., Oikonomou, F., & Petropoulou, M. 2018, *ApJ*, 865, 124
- Mushotzky, R., Aird, J., Barger, A. J., et al. 2019, in *Bulletin of the American Astronomical Society*, Vol. 51, 107
- Nakamura, M., Asada, K., Hada, K., et al. 2018, *ApJ*, 868, 146
- Nandra, K., Barret, D., Barcons, X., et al. 2013, *arXiv:1306.2307*
- Narayan, R., Igumenshchev, I. V., & Abramowicz, M. A. 2003, *PASJ*, 55, L69
- Narayan, R. & Yi, I. 1994, *arXiv:9403052*
- Neilsen, J. & Lee, J. C. 2009, *Nature*, 458, 481
- Nokhrina, E. E., Beskin, V. S., Kovalev, Y. Y., & Zheltoukhov, A. A. 2015, *MNRAS*, 447, 2726
- Nowak, M. A., Wilms, J., & Dove, J. B. 2002, *MNRAS*, 332, 856
- Oda, S., Shidatsu, M., Nakahira, S., et al. 2019, *PASJ*, 71, 108
- Olejak, A., Belczynski, K., Bulik, T., & Sobolewska, M. 2020, *A&A*, 638, A94
- Oliphant, T. E. 2006, *A guide to NumPy*, Vol. 1 (Trelgol Publishing USA)
- Orosz, J. A., Kuulkers, E., van der Klis, M., et al. 2001, *ApJ*, 555, 489
- Orosz, J. A., McClintock, J. E., Aufdenberg, J. P., et al. 2011, *ApJ*, 742, 84
- Orosz, J. A., McClintock, J. E., Remillard, R. A., & Corbel, S. 2004, *ApJ*, 616, 376
- Ostapchenko, S. 2011, *Phys. Rev. D*, 83, 014018
- Parfrey, K., Philippov, A., & Cerutti, B. 2019, *Phys. Rev. Lett.*, 122, 035101



- Park, J., Caprioli, D., & Spitkovsky, A. 2015, *Phys. Rev. Lett.*, 114, 085003
- Parker, M. L., Tomsick, J. A., Kennea, J. A., et al. 2016, *ApJ*, 821, L6
- Parker, M. L., Tomsick, J. A., Miller, J. M., et al. 2015, *ApJ*, 808, 9
- Patnaude, D. J., Vink, J., Laming, J. M., & Fesen, R. A. 2011, *ApJ*, 729, L28
- Penzias, A. A. & Wilson, R. W. 1965, *ApJ*, 142, 419
- Pepe, C., Vila, G. S., & Romero, G. E. 2015, *A&A*, 584, A95
- Peretti, E., Blasi, P., Aharonian, F., & Morlino, G. 2019, *MNRAS*, 487, 168
- Peretti, E., Blasi, P., Aharonian, F., Morlino, G., & Cristofari, P. 2020, *MNRAS*, 493, 5880
- Perkins, J. S., Badran, H. M., Blaylock, G., et al. 2006, *ApJ*, 644, 148
- Perrone, L. 2020, *J. Phys.: Conf. Ser.*, 1342, 012018
- Perucho, M. 2020, *MNRAS*, 494, L22
- Petropoulou, M., Dimitrakoudis, S., Padovani, P., Mastichiadis, A., & Resconi, E. 2015, *MNRAS*, 448, 2412
- Petropoulou, M., Giannios, D., & Dimitrakoudis, S. 2014, *MNRAS*, 445, 570
- Petropoulou, M., Giannios, D., & Sironi, L. 2016, *MNRAS*, 462, 3325
- Petropoulou, M. & Mastichiadis, A. 2015, *MNRAS*, 447, 36
- Petropoulou, M. & Sironi, L. 2018, *MNRAS*, 481, 5687
- Petropoulou, M., Sironi, L., Spitkovsky, A., & Giannios, D. 2019, *ApJ*, 880, 37
- Petrosian, V. 2012, *Space science reviews*, 173, 535
- Pfahl, E., Rappaport, S., & Podsiadlowski, P. 2003, *ApJ*, 597, 1036
- Pian, E., Mazzali, P., Masetti, N., et al. 2006, *Nature*, 442, 1011
- Picozza, P., Galper, A., Castellini, G., et al. 2007, *Astroparticle Physics*, 27, 296
- Pierog, T. & Werner, K. 2008, *Phys. Rev. Lett.*, 101, 171101
- Piran, T. 1999, *Physics Reports*, 314, 575
- Piran, T. 2005, *Rev. Mod. Phys.*, 76, 1143
- Planck, V. 1917, *Sitzungsberichte der Preussischen Akademie der Wissenschaften zu Berlin*
- Plotkin, R. M., Markoff, S., Kelly, B. C., Körding, E., & Anderson, S. F. 2011, *MNRAS*, 419, 267
- Plotnikov, I., Pelletier, G., & Lemoine, M. 2013, *MNRAS*, 430, 1280
- Plotnikov, I., Pelletier, G., & Lemoine, M. 2011, *A&A*, 532, A68
- Polko, P., Meier, D. L., & Markoff, S. 2014, *MNRAS*, 438, 959
- Ponti, G., Fender, R. P., Begelman, M. C., et al. 2012, *MNRAS: Letters*, 422, L11
- Porth, O. & Komissarov, S. S. 2015, *MNRAS*, 452, 1089
- Potter, W. J. & Cotter, G. 2012, *MNRAS*, 429, 1189
- Poutanen, J. & Veledina, A. 2014, *Space Sci. Rev.*, 183, 61–85
- Price-Whelan, A. M., Sipőcz, B. M., Günther, H. M., et al. 2018, *AJ*, 156, 123
- Prodanović, T., Fields, B. D., & Beacom, J. F. 2007, *Astroparticle Physics*, 27, 10
- Protheroe, R. J. & Kazanas, D. 1983, *ApJ*, 265, 620
- Pryadko, J. M. & Petrosian, V. 1997, *ApJ*, 482, 774

## BIBLIOGRAPHY

---

- Pshirkov, M. S., Tinyakov, P. G., Kronberg, P. P., & Newton-McGee, K. J. 2011, *ApJ*, 738, 192
- Ptuskin, V. 2012, *Astroparticle Physics*, 39-40, 44
- Ptuskin, V., Zirakashvili, V., & Seo, E.-S. 2010, *ApJ*, 718, 31
- Punch, M., Akerlof, C. W., Cawley, M. F., et al. 1992, *Nature*, 358, 477
- Pushkarev, A. B., Kovalev, Y. Y., Lister, M. L., & Savolainen, T. 2009, *A&A*, 507, L33
- Pushkarev, A. B., Kovalev, Y. Y., Lister, M. L., & Savolainen, T. 2017, *MNRAS*, 468, 4992
- Rachen, J. P. & Biermann, P. L. 1993, *A&A*, 272, 161
- Rachen, J. P. & Mészáros, P. 1998, *Phys. Rev. D*, 58, 123005
- Rahoui, F., Lee, J. C., Heinz, S., et al. 2011, *ApJ*, 736, 63
- Raymond, J. C., Vink, J., Helder, E. A., & de Laat, A. 2011, *ApJ*, 731, L14
- Reid, M. J., McClintock, J. E., Narayan, R., et al. 2011, *ApJ*, 742, 83
- Reig, P. & Kylafis, N. D. 2015, *A&A*, 584, A109
- Reig, P. & Kylafis, N. D. 2021, *A&A*, 646, A112
- Reig, P., Kylafis, N. D., & Giannios, D. 2003, *A&A*, 403, L15
- Remillard, R. A. & McClintock, J. E. 2006, *ARA&A*, 44, 49
- Reynoso, M. M., Romero, G. E., & Christiansen, H. R. 2008, *MNRAS*, 387, 1745
- Rhoads, J. E. 1999, *ApJ*, 525, 737
- Rieger, F. M. 2019, *Galaxies*, 7, 78
- Rieger, F. M., Bosch-Ramon, V., & Duffy, P. 2007, in *The Multi-Messenger Approach to High-Energy Gamma-Ray Sources*, ed. J. M. Paredes, O. Reimer, & D. F. Torres (Dordrecht: Springer Netherlands), 119–125
- Rieger, F. M. & Duffy, P. 2004, *ApJ*, 617, 155
- Rieger, F. M. & Duffy, P. 2019, *ApJ*, 886, L26
- Rieger, F. M. & Mannheim, K. 2000, *Astron. Astrophys*, 353, 473
- Ripperda, B., Liska, M., Chatterjee, K., et al. 2022, *ApJ Letters*, 924, L32
- Riquelme, M. A. & Spitkovsky, A. 2011, *ApJ*, 733, 63
- Rodrigues, X., Biehl, D., Boncioli, D., & Taylor, A. 2019, *Astroparticle Physics*, 106, 10
- Rodrigues, X., Fedynitch, A., Gao, S., Boncioli, D., & Winter, W. 2018, *ApJ*, 854, 54
- Rodriguez, J., Grinberg, V., Laurent, P., et al. 2015, *ApJ*, 807, 17
- Romero, Vieyro, F. L., & Chaty, S. 2014, *A&A*, 562, L7
- Romero, G. E., Boettcher, M., Markoff, S., & Tavecchio, F. 2017, *Space Sci. Rev.*, 207, 5
- Romero, G. E. & Orellana, M. 2005, *A&A*, 439, 237
- Romero, G. E., Torres, D. F., Bernadó, M. K., & Mirabel, I. 2003, *A&A*, 410, L1
- Romero, G. E. & Vila, G. S. 2008, *A&A*, 485, 623
- Roth, M. A., Krumholz, M. R., Crocker, R. M., & Celli, S. 2021, *Nature*, 597, 341
- Rushton, A., Miller-Jones, J., Campana, R., et al. 2012, *MNRAS*, 419, 3194

- Rushton, A. P., Miller-Jones, J. C. A., Curran, P. A., et al. 2017, *MNRAS*, 468, 2788
- Russell, D. M. & Fender, R. P. 2008, *MNRAS*, 387, 713
- Russell, D. M., Fender, R. P., Hynes, R. I., et al. 2006, *MNRAS*, 371, 1334
- Russell, T. D., Lucchini, M., Tetarenko, A. J., et al. 2020, *MNRAS*, 498, 5772
- Russell, T. D., Soria, R., Motch, C., et al. 2014, *MNRAS*, 439, 1381
- Russell, T. D., Tetarenko, A. J., Miller-Jones, J. C. A., et al. 2019, *ApJ*, 883, 198
- Rybicki, G. B. & Lightman, A. P. 2008, *Radiative processes in astrophysics* (John Wiley & Sons)
- Sabatini, S., Tavani, M., Coppi, P., et al. 2013, *ApJ*, 766, 83
- Sari, R., Piran, T., & Halpern, J. 1999, *ApJ*, 519, L17
- Schneider, A. 2019, arXiv:1907.11266
- Sell, P. H., Heinz, S., Richards, E., et al. 2014, *MNRAS*, 446, 3579
- Shahbaz, T., Russell, D. M., Zurita, C., et al. 2013, *MNRAS*, 434, 2696
- Shahbaz, T., van der Hooft, F., Casares, J., Charles, P. A., & van Paradijs, J. 1999, *MNRAS*, 306, 89
- Shakura, N. I. & Sunyaev, R. A. 1973, *A&A*, 24, 337
- Shaposhnikov, N. & Titarchuk, L. 2009, *ApJ*, 699, 453
- Shidatsu, M., Ueda, Y., Tazaki, F., et al. 2011, *PASJ*, 63, S785
- Shikaze, Y., Haino, S., Abe, K., et al. 2007, *Astroparticle Physics*, 28, 154
- Sironi, L., Giannios, D., & Petropoulou, M. 2016, *MNRAS*, 462, 48
- Sironi, L., Petropoulou, M., & Giannios, D. 2015, *MNRAS*, 450, 183
- Sironi, L., Rowan, M. E., & Narayan, R. 2021, *ApJ*, 907, L44
- Sironi, L. & Spitkovsky, A. 2009, *ApJ*, 698, 1523
- Sironi, L. & Spitkovsky, A. 2011, *ApJ*, 726, 75
- Sironi, L. & Spitkovsky, A. 2014, *ApJ*, 783, L21
- Sironi, L., Spitkovsky, A., & Arons, J. 2013, *ApJ*, 771, 54
- Sjöstrand, T., Mrenna, S., & Skands, P. 2006, *JHEP*, 2006, 026
- Soderberg, A. M., Berger, E., Kasliwal, M., et al. 2006, *ApJ*, 650, 261
- Soderberg, A. M., Brunthaler, A., Nakar, E., Chevalier, R. A., & Bietenholz, M. F. 2010, *ApJ*, 725, 922
- Spruit, H., Daigne, F., & Drenkhahn, G. 2001, *A&A*, 369, 694
- Spruit, H. C., Foglizzo, T., & Stehle, R. 1997, *MNRAS*, 288, 333
- Stecker, F. W. 1968, *Phys. Rev. Lett.*, 21, 1016
- Stein, R., Velzen, S. v., Kowalski, M., et al. 2021, *Nature Astronomy*, 5, 510
- Stephens, S. & Badhwar, G. 1981, *Astrophysics and Space Science*, 76, 213
- Stettner, J. 2019, arXiv:1908.09551
- Stirling, A. M., Spencer, R., De La Force, C., et al. 2001, *MNRAS*, 327, 1273
- Stone, E. C., Cummings, A. C., Heikkila, B. C., & Lal, N. 2019, *Nature Astronomy*, 3, 1013
- Stone, E. C., Frandsen, A., Mewaldt, R., et al. 1998, *Space Science Reviews*, 86, 1
- Strong, A. & Moskalenko, I. 2001, *Advances in Space Research*, 27, 717

## BIBLIOGRAPHY

---

- Strüder, L., Briel, U., Dennerl, K., et al. 2001, *A&A*, 365, L18
- Sunyaev, R. A. & Titarchuk, L. G. 1980, *A&A*, 86, 121
- Szostek, A. & Zdziarski, A. A. 2007, *MNRAS*, 375, 793
- Takami, H., Kyutoku, K., & Ioka, K. 2014, *Phys. Rev. D*, 89, 063006
- Tamborra, I. & Ando, S. 2015, *J. Cosmology Astropart. Phys.*, 2015, 036
- Tamborra, I., Ando, S., & Murase, K. 2014, *J. Cosmology Astropart. Phys.*, 2014, 043
- Tanimori, T., Sakurazawa, K., Dazeley, S. A., et al. 1998, *ApJ*, 492, L33
- Tauris, T. M. & van den Heuvel, E. P. J. 2006, in *Compact stellar X-ray sources*, Vol. 39 (Cambridge University Press), 623–665
- Tavani, M., Bulgarelli, A., Piano, G., et al. 2009, *Nature*, 462, 620
- Tavecchio, F., Maraschi, L., & Ghisellini, G. 1998, *ApJ*, 509, 608
- Tchekhovskoy, A., McKinney, J. C., & Narayan, R. 2008, *MNRAS*, 388, 551
- Tchekhovskoy, A., McKinney, J. C., & Narayan, R. 2009, *ApJ*, 699, 1789
- Tchekhovskoy, A., Narayan, R., & McKinney, J. C. 2011, *MNRAS: Letters*, 418, L79
- Tetarenko, A., Casella, P., Miller-Jones, J., et al. 2019, *MNRAS*, 484, 2987
- Tetarenko, A. J., Casella, P., Miller-Jones, J. C. A., et al. 2021, *MNRAS*, 504, 3862
- Tetarenko, B. E., Bahramian, A., Arnason, R. M., et al. 2016a, *ApJ*, 825, 10
- Tetarenko, B. E., Dubus, G., Marcel, G., Done, C., & Clavel, M. 2020, *MNRAS*, 495, 3666
- Tetarenko, B. E., Sivakoff, G. R., Heinke, C. O., & Gladstone, J. C. 2016b, *ApJ Supplement Series*, 222, 15
- The EHT MWL Science Working Group, Algaba, J., Anczarski, J., et al. 2021, *ApJ letters*, 911, L11
- The LIGO Scientific Collaboration, The Virgo Collaboration, The KAGRA Collaboration, et al. 2021, *arXiv:2111.03606*
- The Pierre Auger Collaboration et al. 2015, *Nucl. Instrum. Methods A*, 798, 172
- The Pierre Auger Observatory, Aab, A., Abreu, P., et al. 2017, *Science*, 357, 1266
- Tinyakov, P., de Almeida, R., Abbasi, R., et al. 2021, *PoS, ICRC2021*, 375
- Titarchuk, L. 1994, *ApJ*, 434, 570
- Tomsick, J. A., Nowak, M. A., Parker, M., et al. 2013, *ApJ*, 780, 78
- Torres, D. F., Romero, G. E., & Mirabel, F. 2005, *Chinese Astron. Astrophys.*, 5, 183
- Torres, M. A. P., Casares, J., Jiménez-Ibarra, F., et al. 2020, *ApJ*, 893, L37
- Torres, M. A. P., Jonker, P. G., Miller-Jones, J. C. A., et al. 2015, *MNRAS*, 450, 4292
- Tucker, M. A., Shappee, B. J., Holoiën, T. W., et al. 2018, *ApJ*, 867, L9
- Uttley, P. 2017, in *The X-ray Universe 2017*, ed. J.-U. Ness & S. Migliari, 230
- Uttley, P., Wilkinson, T., Cassatella, P., et al. 2011, *MNRAS: Letters*, 414, L60
- Uzdensky, D. A. 2011, *Space Sci. Rev.*, 160, 45
- Vacanti, G., Cawley, M., Colombo, E., et al. 1991, *ApJ*, 377, 467
- van den Eijnden, J., Degenaar, N., Russell, T., et al. 2018, *Nature*, 562, 233
- van den Eijnden, J., Degenaar, N., Russell, T. D., et al. 2021, *MNRAS*, 507, 3899

- Vassiliev, V. V., Carter-Lewis, D. A., Hillas, A. M., et al. 1999, arXiv:10.48550
- Veledina, A., Berdyugin, A. V., Kosenkov, I. A., et al. 2019, *A&A*, 623, A75
- Verner, D. A., Ferland, G. J., Korista, K. T., & Yakovlev, D. G. 1996, *ApJ*, 465, 487
- Vieyro, F. L. & Romero, G. E. 2012, *A&A*, 542, A7
- Vila, Romero, G. E., & Casco, N. A. 2012, *A&A*, 538, A97
- Vila, G. S. & Romero, G. E. 2010, *MNRAS*, 403, 1457
- Vilhu, O., Hakala, P., Hannikainen, D. C., McCollough, M., & Koljonen, K. 2009, *A&A*, 501, 679
- Vink, J. 2004, *ASR*, 33, 356
- Vink, J. 2006, in *ESA Special Publication*, Vol. 604, *The X-ray Universe 2005*, ed. A. Wilson, 319
- Vink, J. 2008, *ApJ*, 689, 231
- Vink, J. 2012, *A&A Review*, 20, 1
- Virtanen, P., Gommers, R., Oliphant, T. E., et al. 2020, *Nature Methods*, 17, 261
- Vladimirov, A., Digel, S., Jóhannesson, G., et al. 2011, *Computer Physics Communications*, 182, 1156
- Vlahakis, N. & Konigl, A. 2003, *ApJ*, 596, 1080
- Völk, H. J., Berezhko, E. G., & Ksenofontov, L. T. 2003, *A&A*, 409, 563
- Völk, H. & Atoyan, A. 1999, *Astroparticle Physics*, 11, 73
- Waggett, P., Warner, P., & Baldwin, J. 1977, *MNRAS*, 181, 465
- Walter, R. & Xu, M. 2017, *A&A*, 603, A8
- Wang, X.-Y. & Liu, R.-Y. 2016, *Phys. Rev. D*, 93, 083005
- Waxman, E. 1995, *Phys. Rev. Lett.*, 75, 386
- Webb, N. A., Naylor, T., Ioannou, Z., Charles, P. A., & Shahbaz, T. 2000, *MNRAS*, 317, 528
- Webster, B. L. & Murdin, P. 1972, *Nature*, 235, 37
- Weekes, T., Badran, H., Biller, S., et al. 2002, *Astroparticle Physics*, 17, 221
- Weekes, T., Cawley, M. F., Fegan, D., et al. 1989, *ApJ*, 342, 379
- Weisskopf, M. C., Ramsey, B., O'Dell, S., et al. 2016, in *Society of Photo-Optical Instrumentation Engineers (SPIE) Conference Series*, Vol. 9905, *Space Telescopes and Instrumentation 2016: Ultraviolet to Gamma Ray*, ed. J.-W. A. den Herder, T. Takahashi, & M. Bautz, 990517
- Werner, G. R., Uzdensky, D. A., Cerutti, B., Nalewajko, K., & Begelman, M. C. 2015, *ApJ*, 816, L8
- Wik, D. R., Hornstrup, A., Molendi, S., et al. 2014, *ApJ*, 792, 48
- Wilms, J., Allen, A., & McCray, R. 2000, *ApJ*, 542, 914
- Wilms, J., Nowak, M. A., Pottschmidt, K., Pooley, G. G., & Fritz, S. 2006, *A&A*, 447, 245
- Wulf, T. 1909, *Physikalische Zeitschrift*, 11, 2
- Yoon, Y. S., Ahn, H. S., Allison, P. S., et al. 2011, *ApJ*, 728, 122
- Yoon, Y. S., Anderson, T., Barrau, A., et al. 2017, *ApJ*, 839, 5

## BIBLIOGRAPHY

---

- Yungelson, L. R., Lasota, J. P., Nelemans, G., et al. 2006, *A&A*, 454, 559
- Yushkov, A., Collaboration, P. A., et al. 2019, *ICRC*, 358, 482
- Zanin, R., Fernández-Barral, A., de Oña Wilhelmi, E., et al. 2016, *A&A*, 596, A55
- Zatsepin, G. T. & Kuzn'ın, V. A. 1966, *Soviet Journal of Experimental and Theoretical Physics Letters*, 4, 78
- Zauderer, B. A., Berger, E., Soderberg, A. M., et al. 2011, *Nature*, 476, 425
- Zdziarski, A. A. & Böttcher, M. 2015, *MNRAS: Letters*, 450, L21
- Zdziarski, A. A., Gierlinski, M., Mikołajewska, J., et al. 2004, *MNRAS*, 351, 791
- Zdziarski, A. A., Lubiński, P., & Sikora, M. 2012, *MNRAS*, 423, 663
- Zdziarski, A. A., Malyshev, D., Chernyakova, M., & Pooley, G. G. 2017, *MNRAS*, 471, 3657
- Zdziarski, A. A., Phuravhathu, D. G., Sikora, M., Böttcher, M., & Chibueze, J. O. 2022a, *ApJ Letters*, 928, L9
- Zdziarski, A. A., Pjanka, P., Sikora, M., & Stawarz, Ł. 2014a, *MNRAS*, 442, 3243
- Zdziarski, A. A., Stawarz, Ł., Pjanka, P., & Sikora, M. 2014b, *MNRAS*, 440, 2238
- Zdziarski, A. A., Tetarenko, A. J., & Sikora, M. 2022b, *ApJ*, 925, 189
- Zhang, J., Xu, B., & Lu, J. 2014, *ApJ*, 788, 143
- Zhang, J. F., Feng, Y. G., Lei, M. C., Tang, Y. Y., & Tian, Y. P. 2010, *MNRAS*, 407, 2468
- Ziółkowski, J. 2014, *MNRAS*, 440, L61

## Contribution from co-authors

The position in the author list reflects the importance of the contribution of each co-author.

**Chapter 2:** [A new lepto-hadronic model applied to the first simultaneous multi-wavelength data set for Cygnus X-1](#)

**D. Kantzas**, S. Markoff, T. Beuchert, M. Lucchini, A. Chhotray, C. Ceccobello, A. J. Tetarenko, J. C. A. Miller-Jones, M. Bremer, J. A. Garcia, V. Grinberg, P. Uttley & J. Wilms

*Monthly Notices of the Royal Astronomical Society, 2021, 500, 2, 2112–2126*

**Chapter 3:** [The prototype X-ray binary GX 339-4: using TeV  \$\gamma\$ -rays to assess LMXBs as Galactic cosmic ray accelerators](#)

**D. Kantzas**, S. Markoff, M. Lucchini, C. Ceccobello, V. Grinberg, R. M. T. Connors & P. Uttley

*Monthly Notices of the Royal Astronomical Society, 2022, 510, 4, 5187–5198*

**Chapter 4:** [Exploring neutrino and cosmic ray production in X-ray binary jets using multi-wavelength case studies](#)

**D. Kantzas**, S. Markoff, A. Cooper, D. Gaggero, M. Petropoulou & P. De La Torre Luque

*To be submitted to Monthly Notices of the Royal Astronomical Society*

**Chapter 5:** Exploring the role of composition and mass-loading on the properties of hadronic jets

**D. Kantzas**, S. Markoff, M. Lucchini, C. Ceccobello & K. Chatterjee

*Submitted to Monthly Notices of the Royal Astronomical Society*



### First-author articles

1. **Kantzas, D.**, Markoff, S., Beuchert, T., Lucchini, M., Chhotray, A, Ceccobello, C., Tetarenko, A.J., Miller-Jones, J.C.A., Bremer, Garcia, M,J.A., Grinberg, V., Uttley, P., & Wilms, J., 2021, Monthly Notices of the Royal Astronomical Society, 500(2), pp.2112-2126. (**Chapter 2**) *A new lepto-hadronic model applied to the first simultaneous multiwavelength data set for Cygnus X-1*
2. **Kantzas, D.**, Markoff, S., Lucchini, M., Ceccobello, C., Grinberg, G., Connors, R.M.T. & Uttley, P., 2022, Monthly Notices of the Royal Astronomical Society, 510(4), pp.5187-5198. (**Chapter 3**) *The prototype X-ray binary GX 339-4: using TeV  $\gamma$ -ray s to assess LMXBs as Galactic cosmic ray accelerators*

### Co-authored articles

1. Connors, R.M., van Eijnatten, D., Markoff, S., Ceccobello, C., Grinberg, V., Heil, L., **Kantzas, D.**, Lucchini, M. & Crumley, P., 2019, Monthly Notices of the Royal Astronomical Society, 485(3), pp.3696-3714. *Combining timing characteristics with physical broad-band spectral modelling of black hole X-ray binary GX 339-4*

### Conference proceedings

1. **Kantzas, D.**, Markoff, S., Lucchini, M. & Ceccobello, C., 2021. *Black-hole X-ray binaries in the new era of multi-messenger Astronomy*

2. López-Oramas, A., Bulgarelli, A., Chaty, S., Chernyakova, M., Gnatyk, R., Hnatyk, B., **Kantzas, D.**, Markoff, S., McKeague, S., Mereghetti, S. & Mestre, E., 2021, arXiv preprint arXiv:2108.03911.  
*Prospects for Galactic transient sources detection with the Cherenkov Telescope Array*

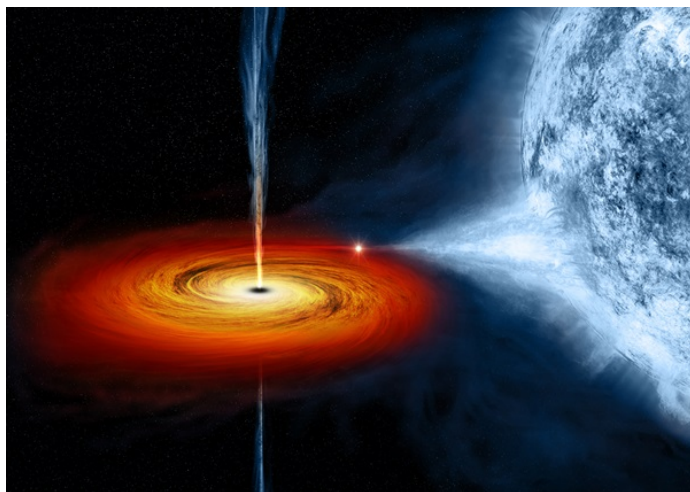
## Samenvatting

Sinds the ontdekking van kosmische straling (KS) in het begin van de 20e eeuw, zijn de hoog-energetisch astrofysische wetenschappers actief op zoek naar hun oorsprong. KS bestaat uit geladen deeltjes die we op Aarde detecteren met ofwel aarde- of ruimte-gebaseerde faciliteiten. Ze geven een spectrum dat meerdere ordes van grootte in energie dekt van circa onder de 1 GeV ( $10^9$  eV<sup>1</sup>) tot 100 EeV ( $10^{20}$  eV). KS met energieën tot  $\sim 10^{18}$  eV zijn versneld in Galactische bronnen, met protonen die het spectrum domineren tot  $10^{15}$  eV (PeV), en KS die in de meest energetische regime liggen van het spectrum worden versneld in extra-galactische bronnen. Wanneer KS hun versnellings-bron ontsnappen en zich door het interstellair/intergalactisch medium verplaatsen, worden ze afgebogen door magnetische velden die ze treffen onderweg naar Aarde. Een directe identificatie van de KS bron is daarom uitdagend, en indirecte middelen zijn noodzakelijk. Wanneer energetische KS interageren met het omringende medium door proton-proton (pp) of met de omringende straling door fotomeson ( $p\gamma$ ) interacties, initiëren ze een cascade van deeltjes dat leidt tot de formatie van secundaire deeltjes genaamd pionen en muonen. Deze secundaire deeltjes zijn instabiel en vervallen vrijwel onmiddellijk naar verdere secundaire deeltjes, zoals elektronen, positronen, gammastraling, neutrino's en anti-neutrino's. De resulterende gammastraling en neutrino's/anti-neutrino's zijn van groot belang omdat ze (bijna) vrij kunnen propageren zonder af te buigen, en we kunnen daarom hun detectie op Aarde gebruiken om de bronnen te lokaliseren. Een betrouwbare detectie van gammastraling en neutrino's van een bepaalde astrofysische bron zou wijzen op de oorsprong van KS.

In dit proefschrift, focussen we op een bepaalde kandidaat bron van KS versnelling in ons sterrenstelsel - de relativistische uitstroom gelanceerd door stellair-massa zwarte gaten met accretie in röntgendubbelsterren. Röntgendubbelsterren bestaan uit een compact object, zoals een neutronen ster of een zwart gat, die rondom een

---

<sup>1</sup>Een elektron volt (eV) is de kinetische energie die een elektron krijgt vanuit rust als het wordt versneld in een elektrisch spanningsverschil van 1 Volt in vacuüm, wat gelijk staat aan  $1.6 \times 10^{-19}$  J.



**Figuur A:** Illustratie van de hoge-massa röntgendubbelster Cyg X-1. Het centraal zwart gat toont accretie van materie door een accretieschijf dat wordt gevoed door de stellaire wind van de begeleidende ster, en lanceert twee gecollimeerde relativistische uitstromen bekend als jets. Deze systemen, voornamelijk de jets, kunnen mogelijk deeltjes versnellen dat leidt tot de emissie van niet-thermische emissie gedetecteerd in gammastraling. Afbeelding credit: NASA/Weiss.

baan draaien met een begeleidende ster. Een zwart gat röntgendubbelster (ZGRD) heeft een massa tussen een enkel tot ongeveer 20 zonne-massa eenheden, en er is accretie van de massa van de begeleidende ster naar het zwart gat. Gedurende geschikte condities, die momenteel nog ter discussie zijn, lanceert het zwart gat twee relativistische uitstromen, bekend als jets (zie Figuur A). Vergelijkbare jets, maar op veel grotere schaal, worden gelanceerd door de kernen van actieve sterrenstelsels. Er wordt van de jets van actieve sterrenstelsels en van een ZGRD gedacht dat ze dezelfde fysische wetten volgen, en het begrijpen van ZGRDs zal dus ook inzicht geven in actieve sterrenstelsels.

Astrofysische jets schijnen over het gehele elektromagnetisch spectrum van lage-energie radio straling tot de ultra-hoge energie van  $10^9 - 10^{12}$  eV gammastraling (GeV en TeV, respectievelijk). Deze multi-golflengte straling is het resultaat van een efficiënte deeltjes versneller die energieën van PeV kan overschrijden. Het exacte fysische mechanisme dat verantwoordelijk is voor deze straling is niet volledig begrepen, hoewel er twee leidende theorieën zijn: de eerste theorie is gebaseerd op het efficiënt versnellen van enkel leptonen, d.w.z., elektronen en positronen. In dit scenario, stralen de jets via synchrotronstraling als een resultaat van de magnetische velden in de jets, en via inelastische botsingen tussen leptonen en enkele foton velden. Dit laatste proces, bekend als het inverse Compton-effect, leidt tot de formatie van GeV en TeV straling met een spectrum die moeilijk te onderscheiden is van de  $pp$  en  $p\gamma$  processen die hierboven zijn vermeld. De tweede theorie betreft hadronische deeltjes zoals pro-

---

tonen, wanneer deze deeltjes worden versneld in jets produceren ze gammastraling en neutrino's via inelastische  $pp$  en  $p\gamma$  interacties.

Huidige neutrino detectoren zijn niet sensitief om een voldoende aantal neutrino's van bepaalde bronnen te ontvangen voor het ontwikkelen van een neutrino spectrum. Ondanks dat GeV en TeV gammastraling afkomstig van ZGRDs zijn gedetecteerd in de afgelopen twee decennia, is er een duidelijk gebrek aan neutrino detecties. Cyg X-1, Cyg X-3 en SS433 zijn enkele voorbeelden van ZGRDs die jets lanceren en bijdragen aan het geobserveerde non-thermisch spectrum. Als deze straling een hadronische oorsprong kent, zijn deze systemen mogelijk kandidaat bronnen voor astrofysische neutrino's, en daarom ook voor Galactische KS bronnen. In dit proefschrift verkennen we of ZGRDs Galactische KS versnellers zijn en berekenen we hun potentiële bijdrage aan het gehele KS spectrum.

In Hoofdstuk 2, presenteren we een nieuw lepton-hadron, multi-zone jet model, aannemend dat proton KS even efficiënt versneld worden als leptonen met dezelfde fysische eigenschappen. We vergelijken dit nieuw ontwikkeld jet model met de eerste simultaan radio-tot-röntgenstraling data die een volle omlooptijd omspannt van de hoge-massa ZGRD Cyg X-1. Om de jet kinematica en de resulterende bijdrage van hadronische versnellers aan het uitgezonden spectrum beter vast te leggen, gebruiken we statistische middelen om de parameters met de beste fits van ons model te vinden. Daarnaast, houden we rekening met de polarisatie observaties in röntgenstraling en de gemiddelde emissie in GeV, gedetecteerd voor Cyg X-1 in de eerste jaren van operatie van gammastraling satelliet, *Fermi*/LAT.

In Hoofdstuk 3, passen we hetzelfde lepton-hadron model toe aan de lage-massa ZGRD GX 339-4 om te bepalen of lage-massa ZGRDs KS kunnen versnellen naar energieën die vergelijkbaar zijn met die geobserveerd in Cyg X-1. We gebruiken quasi-simultaan radio-tot-röntgenstraling data om de beste fits te vinden van zowel een pure lepton als een lepton-hadron jet scenario. Met statistische middelen, vinden we de parameters met de beste fits van ons model om verder de dynamische eigenschappen van de jets te beperken. Nadat de jet kinematica zijn beperkt, voorspellen we de gammastraling emissie van GX 339-4, met een focus op het TeV regime waar verwacht wordt dat CTA de gevoeligheid van huidige gammastraling faciliteiten overtreft, zoals de ruimte-gebaseerde *Fermi*/LAT, en de aarde-gebaseerde faciliteiten H.E.S.S., MAGIC en VERITAS. We concluderen dat GX 339-4 niet een doelwit met kansen is voor CTA omdat de locatie te ver weg is, op een afstand van 8 kpc. Echter vinden we dat CTA lage-massa ZGRDs zal detecteren met een locatie dicht bij Aarde (binnen afstanden van 3 kpc), mits deze ZGRDs worden geobserveerd tijdens een lumineuze uitbarstingsfase vergelijkbaar met GX 339-4.

De hadronische versnelling in de jets van ZGRDs kunnen verder worden ondersteund in de potentiële detectie van een neutrino, zoals wordt besproken in Hoofdstuk 4. Om de mogelijkheid van een detectie van een neutrino van deze twee bronnen te voorspellen, berekenen we zelf-consistent de verwachte neutrino flux gebaseerd op

de elektromagnetische beperkingen die we hebben gezet met onze beste fits. We vinden dat GX 339–4 er niet in slaagt een voldoende aantal neutrino's te produceren binnen een redelijke tijdschaal van een enkele decennia. In tegenstelling tot GX 339–4, kan Cyg X–1 een orde van één muon neutrino produceren die gedetecteerd kan worden met zowel de huidige neutrino detector IceCube observatorium op de Zuidpool, als de toekomstige  $\text{km}^3$  detectoren zoals KM3NeT/ARCA in de Middellandse Zee. Gebaseerd op onze resultaten van deze twee ZGRDs, onderzoeken we de contributie van de overige 33 bekende ZGRDs die tot nu toe zijn ontdekt, echter vinden we dat er geen andere bron is die aannemelijke contributie kan leveren als een neutrino bron in de aankomende jaren. Het aantal gedetecteerde bronnen is echter relatief klein in vergelijking met de voorspellingen van populatie synthese modellen van stellaire evolutie. We onderzoeken daarom of een populatie van een groter aantal ZGRDs in het Galactisch vlak kan bijdragen aan het KS spectrum geobserveerd op Aarde en aan het diffuse gammastraling en neutrino emissie. Door grondige studie van de voortbeweging van versnelde KS door het Galactisch medium en hun effecten op de uitgestraalde emissie, gebruiken we allernieuwste numerieke simulaties, zoals DRAGON2 en HERMES. Ondanks de in-significante contributie van deze bronnen op de diffuse gammastraling en neutrino spectra, vinden we dat deze bronnen gecombineerd waarschijnlijk een contributie tot 30 procent kunnen leveren op het KS spectrum in het TeV bereik. Toekomstige observaties en voorspellingen van het aantal ZGRDs in het sterrenstelsel met hoge kwaliteit observaties, zoals uitgevoerd door e.g., Gaia, kunnen bijdragen aan het versterken van onze conclusies.

Gedurende het modelleren van het spectrum met het hadronisch scenario, zijn we een bekend probleem tegen gekomen: het vermogen van de hadronische versnelling overschrijdt het vermogen voorraad van het systeem, tenminste met de simpelste aannames. Om dit probleem te adresseren, introduceren we in Hoofdstuk 5 een nieuw multi-zone jet model dat het verkrijgen van massa langs de schede van de jet meerekent. Na hun lancering, bewegen jets door een omringend medium, en hun eigenschappen (e.g., temperatuur, deeltjes dichtheid en snelheid) kunnen significant verschillen van de een op andere bron. De interactie tussen de magnetische relativistische jet en het omringende medium kan zich tot een instabiliteit ontwikkelen op het raakvlak tussen de twee stromen, die omringende materie meevoert in de jets. Zulke condities zijn goed bestudeerd met nieuwe algemene relativiteit magnetohydrodynamische (ARMHD) simulaties die laten zien dat niet enkel het laden van massa significant is, maar ook kan leiden tot het opwarmen van de jet inhoud. Zulke ARMHD simulaties zijn echter relatief computationeel duur en vereisen vaak weken-tot-maanden om tot gedetailleerde resultaten te komen. Om tot snellere berekeningen te komen en voor directe vergelijkingen met observationele beperkingen, ontwikkelen we een semi-analytisch jet model dat een tweetal van gedomineerde jet basis aanneemt en significant baryonen laden in de buitenste gebieden van de jet. Het meegesleepte materie bestaat uit beide protonen en elektronen, en de geladen protonen zijn versneld

---

tot hoge-energieën, die navolgend lepton-hadron interacties toelaten. In een gedetailleerde analyse, laten we zien dat massa-geladen jets significante gammastraling emissie toelaten zonder dat de voorraad vermogen wordt geschonden. Met dit nieuw ontwikkeld jet model, kunnen we het multigolflengte spectrum van bronnen met een jet bestuderen om de lang bestaande KS bronnen te identificeren.





## Summary

Since the discovery of cosmic rays (CRs) at the beginning of the 20th century, the high-energy astrophysical community has actively been searching for their origin. CRs are charged particles that we detect on Earth with either ground-based or space-based facilities. They populate a spectrum that covers multiple orders of magnitude in energy from approximately below 1 GeV ( $10^9$  eV<sup>1</sup>) up to 100 EeV ( $10^{20}$  eV). CRs with energy up to  $\sim 10^{18}$  eV are accelerated in Galactic sources, with protons dominating the spectrum up to  $10^{15}$  eV (PeV), and CRs that populate the most energetic regime of the spectrum get accelerated in extragalactic sources. When CRs escape their acceleration sites and travel the interstellar/intergalactic medium, they are deflected by the magnetic fields they encounter on their way to Earth. Hence, the direct identification of CR sources is challenging, and indirect means are necessary. When energetic CRs interact with the ambient medium through proton-proton (pp) or their surrounding radiation through photomeson ( $p\gamma$ ) interactions, they initiate particle cascades that lead to the formation of secondary particles called pions and muons. These secondary particles are unstable and decay almost immediately to further secondary particles, such as electrons, positrons,  $\gamma$ -rays, neutrinos and antineutrinos. The resulting  $\gamma$ -rays and neutrinos/antineutrinos are of great importance because they can (almost) freely propagate without deflection, and we can therefore use their detection on Earth to localise their sources. A reliable detection of  $\gamma$ -rays and neutrinos from a specific astrophysical source would hint at the origin of CRs.

In this thesis, we focus on one particular candidate source for CR acceleration within our Galaxy – the relativistic outflows launched by stellar-mass accreting black holes in X-ray binary systems. X-ray binaries (XRBs) harbour a compact object, such as a neutron star or a black hole, orbiting a companion star. The black hole in X-ray binaries (BHXBs) has mass between a few and approximately 20 solar mass units, and accretes matter from the companion star. During suitable conditions, the details

---

<sup>1</sup>One electron volt (eV) is the kinetic energy an electron gains from rest when accelerated in an electric voltage difference of 1 Volt in vacuum, and is equal to  $1.6 \times 10^{-19}$  J.

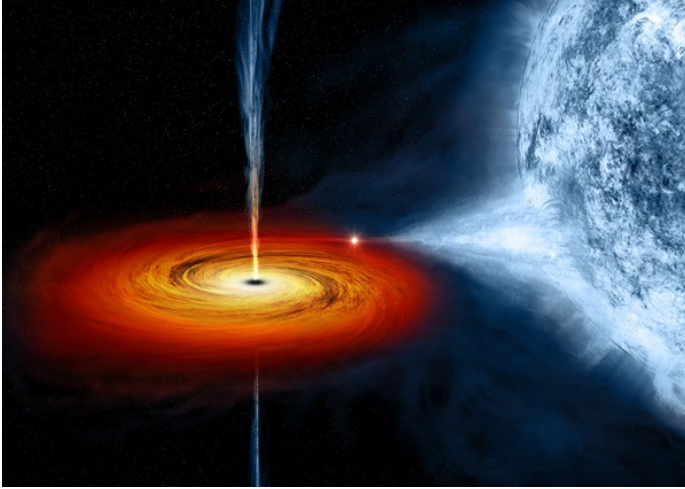


**Figure A:** Illustration of the high-mass X-ray binary Cyg X-1. The central black hole accretes matter through an accretion disc that is fed by the stellar wind of the companion star, and launches two collimated relativistic outflows known as jets. These systems, particularly the jets, may be particle acceleration sites that lead to the emission of non-thermal radiation detected in  $\gamma$ -rays. Image Credit: NASA/Weiss.

of which are still debated, the black hole launches two relativistic outflows, known as jets (see Figure A). Similar jets, but on much larger scales, are launched by the cores of active galactic nuclei (AGN). AGN jets and BHXB jets are thought to follow the same physical laws, and therefore improving our understanding of BHXRBs can also provide useful insights into AGN.

Astrophysical jets shine across the entire electromagnetic spectrum from the low-energy radio bands to the ultra-high energy of  $10^9 - 10^{12}$  eV  $\gamma$ -rays (GeV and TeV, respectively). This multiwavelength radiation is the result of an efficient particle acceleration to energies that can exceed PeV. The exact physical mechanisms responsible for this radiation are not fully understood, however there are two main leading theories: the first theory is based on the efficient acceleration of only leptons, i.e., electrons and positron. In this scenario, the jets then shine via synchrotron radiation as a result of magnetic fields within the jets, and via inelastic collisions between the leptons and some photon fields. This latter process, known as inverse Compton scattering, can lead to the formation of GeV and TeV radiation which has a spectrum that is difficult to distinguish from the pp and  $p\gamma$  processes mentioned above. The second theory concerns hadronic particles such as protons, when these particles are accelerated in the jets they produce  $\gamma$ -rays and neutrinos via inelastic pp and  $p\gamma$  interactions.

Current neutrino detectors are not sensitive enough to select a sufficient number of neutrinos from particular sources to produce a neutrino spectrum. Though GeV

---

and TeV  $\gamma$ -rays have been detected from BHXBs in the last two decades, there has been a distinct lack of neutrino detections. Cyg X-1, Cyg X-3 and SS433 are just a few examples of BHXBs that launch jets that viably contribute to the observed non-thermal spectrum. If this radiation is of hadronic origin, then these systems may be candidate sources for astrophysical neutrinos, and thus Galactic CR sources. In this thesis, we explore whether BHXBs are Galactic CR accelerators and calculate their potential contribution to the overall CR spectrum.

In Chapter 2, we present a new lepto-hadronic, multi-zone jet model, assuming that proton CRs are accelerated as efficiently as the leptons sharing the same physical properties. We compare this newly-developed jet model to the first simultaneous radio-to-X-ray data set spanning a full orbital period of the high-mass BHXB, Cyg X-1. To better capture the jet kinematics and the resulting contribution of hadronic acceleration to the emitted spectrum, we use statistical means to find the best-fit parameters of our model. Additionally, we account for the polarisation measurements in the X-ray band and the average GeV emission detected by Cyg X-1 in the first years of operation of the  $\gamma$ -ray satellite, *Fermi*/LAT. We compare our results to a purely leptonic scenario where protons are not accelerated to non-thermal energies, to determine the differences in the dynamical jet quantities (e.g., magnetic field, particle number density, jet radius) in the leptonic and hadronic scenarios. We conclude that if future TeV telescopes such as the Cherenkov Telescope Array (CTA) detect any TeV emission from the jets in Cyg X-1, then this radiation will most likely be of hadronic origin, indicating that Cyg X-1 is a CR source.

In Chapter 3, we apply the same lepto-hadronic model to the low-mass BHXB GX 339-4 in order to determine whether low-mass BHXBs can accelerate CRs to energies similar to those observed in Cyg X-1. We use quasi-simultaneous radio-to-X-ray data to find the best fits of both a purely leptonic and a lepto-hadronic jet scenario. Using statistical means, we find the best-fit parameters of our model to further constrain the dynamical quantities of the jets. Having constrained the jet kinematics, we then predict the  $\gamma$ -ray emission of GX 339-4, focusing on the TeV regime where CTA is expected to surpass the sensitivity of current  $\gamma$ -ray facilities, such as the space-based *Fermi*/LAT, and the ground-based facilities H.E.S.S., MAGIC and VERITAS. We conclude that GX 339-4 is not a target-of-opportunity for CTA because it is located too far away, at a distance of 8 kpc. However, we find that CTA will be able to detect low-mass BHXBs that are located closer to Earth (within distances of 3 kpc), provided that these BHXBs are observed during a bright outburst phase similarly to GX 339-4.

The hadronic acceleration in BHXB jets can be further supported in the potential detection of a neutrino counterpart as we discuss in Chapter 4. To estimate the possibility of detecting any neutrinos from these two sources, we self-consistently calculate the expected neutrino fluxes based on the electromagnetic constraints we have set with our best-fits. We find that GX 339-4 fails to produce a countable number

of neutrinos within reasonable timescales of a couple of decades. Unlike GX 339–4, Cyg X–1 can produce of the order of one muon neutrino that can be detected by the current state-of-the-art neutrino detectors of the IceCube observatory in the South Pole, as well as by future  $\text{km}^3$  detectors such as KM3NeT/ARCA in the Mediterranean Sea. Based on our results for these two BHXBs, we examine the contribution of the remaining 33 known BHXBs discovered so far, but we find that no other source can likely contribute as a neutrino source in the following years. The number of detected sources, however, is relatively small compared to the predictions of population synthesis models of stellar evolution. We therefore examine if a population of more numerous BHXBs in the Galactic plane can contribute to the CR spectrum detected on Earth, as well as the diffuse  $\gamma$ -ray and neutrino emissions. To thoroughly study the propagation of the accelerated CRs along the Galactic medium, as well as its effect on the emitted radiation, we use state-of-the-art numerical simulations, such as DRAGON2 and HERMES. Despite the insignificant contribution of these sources to the diffuse  $\gamma$ -ray and neutrino spectra, we find that all these sources combined can likely contribute up to 30 per cent of the CR spectrum in the TeV regime. Future observations and estimates on the number of BHXBs in the Galaxy with high quality observations, such those performed by e.g., Gaia, may help to strengthen our conclusions.

During the spectral modelling with the hadronic scenario, we encountered a well-known problem: the power implied by the hadronic acceleration exceeded the power budget of the system, at least when using the simplest assumptions. To address this problem, in Chapter 5, we introduce a new multi-zone jet model that accounts for mass loading along the jet sheath. Following their launch, jets propagate through a surrounding ambient medium, the properties (e.g., temperature, particle density and velocity) can differ significantly between sources. The interaction of the magnetised relativistic jets and the ambient medium can lead to the development of instabilities at the interface between the two flows, which allow ambient matter to be entrained in the jets. Such conditions are well studied by state-of-the-art general relativity magnetohydrodynamic (GRMHD) simulations that have shown that the mass loading may not only be significant, but may also lead to heating of the jet content. Such GRMHD simulations however are relatively computational expensive and often require weeks-to-months to achieve detailed results. To allow for faster calculations and direct comparison to observational constraints, we developed a semi-analytical jet model that assumes a pair-dominated jet base and significant baryon loading in the outer regions of the jets. The entrained matter consists of both protons and electrons, and the loaded protons are accelerated to high-energies, allowing for subsequent lepto-hadronic interactions. In a detailed analysis, we show that mass-loaded jets allow for significant  $\gamma$ -ray emission without violating the energy budget. With this newly developed jet model, we intend to study the multiwavelength spectra of jetted sources in order to identify long-lasting CR sources.

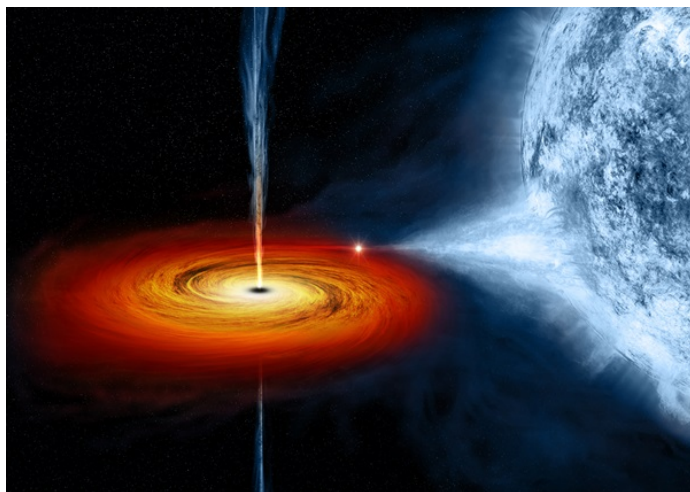
## Περίληψη

Από την ανακάλυψη της κοσμικής ακτινοβολίας στις αρχές του 20ού αιώνα, η κοινότητα αστροφυσικής υψηλών ενεργειών αναζητά την προέλευσή της. Οι κοσμικές ακτίνες (ΚΑ) αποτελούνται από φορτισμένα σωματίδια τα οποία παρατηρούμε στη Γη είτε με επίγειους ανιχνευτές είτε με ανιχνευτές στο διάστημα. Οι ΚΑ παρουσιάζουν ένα φάσμα το οποίο καλύπτει το εύρος ενεργειών μεταξύ περίπου 1 GeV ( $10^9$  eV<sup>1</sup>) μέχρι και 100 EeV ( $10^{20}$  eV). Οι ΚΑ ενέργειας μέχρι περίπου  $\sim 10^{18}$  eV προέρχονται από πηγές εντός του Γαλαξία μας, με τα σχετικιστικά πρωτόνια να κυριαρχούν το φάσμα μέχρι περίπου  $10^{15}$  eV (PeV), και οι ΚΑ μεγαλύτερης ενέργειας επιταχύνονται σε εξωγαλαξιακές πηγές. Όταν οι ΚΑ δραπετεύουν των επιταχυντών τους και ταξιδεύουν στο διαστρικό και διαγαλαξιακό μέσο, διαθλώνται λόγω των μαγνητικών πεδίων που συναντούν στη διαδρομή τους προς τη Γη και δεν ταξιδεύουν σε ευθεία τροχιά. Η άμεση ταυτοποίηση των πηγών των ΚΑ επομένως είναι δύσκολη και έμμεσοι τρόποι παρατήρησης χρειάζονται.

Όταν οι ΚΑ αλληλεπιδρούν με τα σωματίδια του περιβάλλοντα χώρου μέσω σκέδασης πρωτονίου-πρωτονίου (pp) ή με την περιβάλλουσα ακτινοβολία μέσω φωτομεσονικών αλληλεπιδράσεων (pγ), εκκινούν καταωνισμό σωματιδίων οι οποίοι οδηγούν στη δημιουργία δευτερογενών σωματιδίων όπως πιονίων και μιονίων. Αυτά τα δευτερογενή σωματίδια είναι ασταθή και διασπώνται σχεδόν ακαριαία σε περαιτέρω σωματίδια όπως ηλεκτρόνια, ποζιτρόνια, ακτίνες γ, νετρίνα και αντινετρίνα. Τα παραχθέντα νετρίνα και οι ακτίνες γ είναι πολύ μεγάλης σημασίας επειδή μπορούν να ταξιδέψουν (σχεδόν) ανεμπόδιστα χωρίς να σκεδαστούν και μπορούν επομένως να χρησιμεύσουν για την ταυτοποίηση των πηγών των ΚΑ.

Σε αυτή τη διατριβή, εστιάζουμε σε μια συγκεκριμένη υποψήφια πηγή ΚΑ εντός του Γαλαξία μας - τις σχετικιστικές εκροές που παράγονται από αστρικές μελανές οπές που εντοπίζονται σε διπλά συστήματα ακτίνων X. Τα συστήματα ακτίνων X φιλοξενούν ένα συμπαγές αντικείμενο, όπως ένας αστέρας νετρονίων ή μια αστική μελανή οπή, και έναν συνοδό αστέρα. Η μελανή οπή αυτών των συστημάτων έχει μάζα μεταξύ μερικών και

<sup>1</sup>Ένα eV (από το ηλεκτρονιοβόλτ) είναι η κινητική ενέργεια ενός ηλεκτρονίου όταν επιταχυνθεί σε διαφορά δυναμικού ενός Volt στο κενό, και είναι ίσο με  $1.6 \times 10^{-19}$  J.



**Σχήμα Α΄:** Καλλιτεχνική απεικόνιση του διπλού αστρικού συστήματος ακτίνων X, Κύκνος X-1. Η κεντρική μελανή οπή προσροφά μάζα μέσω του δίσκου προσαύξησης, ο οποίος τροφοδοτείται από τον αστρικό άνεμο του συνοδού αστέρα. Η μελανή οπή εκτοξεύει δυο σχετικιστικές και πολύ εστιασμένες εκροές, γνωστές ως πίδακες. Αυτά τα συστήματα, και πιο συγκεκριμένα οι πίδακες, είναι πιθανοί επιταχυντές σωματιδίων τα οποία παράγουν ακτινοβολία που μπορεί να παρατηρηθεί στις ακτίνες γ. Πηγή: NASA/Weiss.

περίπου 20 ηλιακών μαζών, και προσροφά μάζα από το συνοδό αστέρα. Υπό κατάλληλες συνθήκες, οι λεπτομέρειες των οποίων είναι ακόμα υπό μελέτη, η μελανή οπή εκτοξεύει δυο σχετικιστικές εκροές, γνωστές ως πίδακες (Σχήμα Α΄). Παρόμοιοι πίδακες αλλά σε πολύ μεγαλύτερη κλίμακα, εκτοξεύονται από τους πυρήνες ενεργών γαλαξιών (ΕΓΠ). Οι πίδακες που εκτοξεύονται από τις παραπάνω μελανές οπές θεωρείται ότι ακολουθούν τους ίδιους φυσικούς νόμους, και επομένως η καλύτερη κατανόηση των πιδάκων από αστικές μελανές οπές μπορούν να βοηθήσουν στην περαιτέρω κατανόηση των πιδάκων από ΕΓΠ.

Οι αστροφυσικοί πίδακες λάμπουν σε ολόκληρο το ηλεκτρομαγνητικό φάσμα από τα ραδιοκύματα μέχρι τις ακτίνες γ ενέργειας  $10^9 - 10^{12}$  eV (GeV και TeV, αντίστοιχα). Αυτή η πολυκυματική ακτινοβολία είναι το αποτέλεσμα μιας αποδοτικής επιτάχυνσης σωματιδίων σε ενέργειες που μπορούν να φτάσουν τα PeV. Ο ακριβής μηχανισμός επιτάχυνσης δεν είναι πλήρως κατανοητός, παρόλα αυτά υπάρχουν δυο κύριες θεωρίες: η πρώτη θεωρία βασίζεται στην επιτάχυνση λεπτονίων, δηλαδή ηλεκτρονίων και ποζιτρονίων. Σε αυτό το σενάριο, οι πίδακες λάμπουν λόγω ακτινοβολίας σύγχροτρον, και λόγω σχεδιάσεων μεταξύ των λεπτονίων και της ακτινοβολίας. Αυτή η τελευταία διαδικασία, γνωστή ως ανίστροφος σχεδιασμός Compton, μπορεί να οδηγήσει σε ακτινοβολία της τάξης των GeV και TeV, η οποία μπορεί να είναι δύσκολο να διαχωριστεί από την ακτινοβολία που παράγεται λόγω pp και pγ αλληλεπιδράσεων όπως προαναφέρθηκαν. Η δεύτερη θεωρία περιλαμβάνει την επιτάχυνση αδρονίων, κυρίως πρωτονίων, τα οποία

---

όταν επιταχύνονται οδηγούν σε ανελαστικές αλληλεπιδράσεις  $pp$  και  $p\gamma$ .

Οι ήδη υπάρχοντες ανιχνευτές νετρίνων δεν είναι αρκετά ευαίσθητοι να συλλέξουν έναν επαρκές αριθμό νετρίνων από μεμονωμένες πηγές. Ακτίνες  $\gamma$  ενέργειας GeV και TeV από την άλλη, έχουν παρατηρηθεί από συστήματα ακτίνων X με μελανή οπή (black hole X-ray binaries - BHXBs) τις τελευταίες δυο δεκαετίες. Ο Κύκνος X-1, ο Κύκνος X-3 και το σύστημα SS433 είναι μονάχα μερικά παραδείγματα πηγών που εκτοξεύουν πίδακες ικανοί να συνδράμουν στην παρατηρήσιμη ακτινοβολία. Εάν αυτή η ακτινοβολία είναι αδρονικής προέλευσης τότε αυτά τα συστήματα μπορεί να είναι υποψήφιες πηγές αστροφυσικών νετρίνων και ΚΑ. Σε αυτή τη διατριβή, μελετάμε εάν τα BHXBs μπορούν να συνδράμουν εν δυνάμει στο φάσμα των ΚΑ.

Στο Κεφάλαιο 2, παρουσιάζουμε ένα νέο λεπτο-αδρονικό μοντέλο ενός πίδακα που αποτελείται από πολλές ζώνες, υποθέτοντας ότι πρωτόνια ΚΑ επιταχύνονται εξίσου αποδοτικά με τα λεπτόνια. Συγκρίνουμε αυτό το νέο μοντέλο με τις πρώτες ταυτόχρονες παρατηρήσεις μεταξύ ραδιοκυμάτων και ακτίνων X από το σύστημα Κύκνος X-1 που ο συνοδός αστέρας είναι μεγάλης μάζας. Για να καταλάβουμε καλύτερα την κινηματική του πίδακα και τη συνεισφορά των επιταχυμένων πρωτονίων στο ηλεκτρομαγνητικό φάσμα, χρησιμοποιούμε στατιστικές μεθόδους να βρούμε τις καλύτερες δυνατές παραμέτρους του μοντέλου μας. Επιπλέον, λαμβάνουμε υπόψη τις μετρήσεις πόλωσης στο εύρος των ακτίνων X, καθώς και τη μέση ακτινοβολία ακτίνων GeV από τα πρώτα χρόνια λειτουργίας του τηλεσκοπίου ακτίνων  $\gamma$ , *Fermi*. Συγκρίνουμε τα αποτελέσματά μας μεταξύ ενός καθαρά λεπτονικού και ενός λεπτο-αδρονικού μοντέλου για να καταλάβουμε τις διαφορές των δυναμικών ποσοτήτων των πιδάκων (ένταση μαγνητικού πεδίου, αριθμητική πυκνότητα σωματιδίων, ακτίνα πίδακα κ.α.). Καταλήγουμε ότι εάν μελλοντικά τηλεσκόπια ακτίνων TeV όπως το σύστημα τηλεσκοπίων Τσερένκοφ (Cherenkov Telescope Array - CTA), εντοπίσουν ακτινοβολία ενέργειας TeV από τον Κύκνο X-1 τότε η πιο πιθανή προέλευση αυτής της ακτινοβολίας είναι λόγω επιτάχυνσης των πρωτονίων, και συνεπώς ο Κύκνος X-1 είναι υποψήφια πηγή ΚΑ.

Στο Κεφάλαιο 3, εφαρμόζουμε το λεπτο-αδρονικό μοντέλο σε ένα BHXB με συνοδό αστέρα μικρής μάζας, το σύστημα GX 339-4, με σκοπό να μελετήσουμε εάν αυτά τα συστήματα μπορούν να επιταχύνουν ΚΑ σε ενέργειες αντίστοιχες με αυτές του συστήματος του Κύκνου X-1. Χρησιμοποιούμε τις σχεδόν-ταυτόχρονες παρατηρήσεις από τα ραδιοκύματα έως τις ακτίνες X για να βρούμε τις καλύτερες δυνατές παραμέτρους ενός καθαρά λεπτονικού και ενός λεπτο-αδρονικού μοντέλου. Με τη χρήση στατιστικών μεθόδων, μπορούμε να περιορίσουμε τις παραμέτρους του μοντέλου μας που σχετίζονται με τις δυναμικές ποσότητες των πιδάκων. Με αυτόν τον τρόπο καταφέρνουμε να προβλέψουμε την ακτινοβολία  $\gamma$  από το σύστημα GX 339-4 εστιάζοντας στις ακτίνες  $\gamma$  ενέργειας TeV όπου το CTA θα είναι πολύ πιο ευαίσθητο από τα προϋπάρχοντα τηλεσκόπια όπως το *Fermi*, H.E.S.S, MAGIC και VERITAS. Καταλήγουμε ότι το σύστημα GX 339-4 δεν αποτελεί καλό στόχο για το CTA λόγω της μεγάλης απόστασής του από τη Γη, η οποία εκτιμάται στα 8 kpc. Παρόλα αυτά, βρίσκουμε ότι το CTA θα μπορεί να εντοπίσει BHXB με συνοδό μικρής μάζας εάν αυτά βρίσκονται σε απόσταση μικρότερη

των 3 kpc και είναι όσο λαμπρά όσο το σύστημα GX 339-4 .

Η αδρονική επιτάχυνση σε αστροφυσικούς πίδακες μπορεί να υποστηριχθεί περαιτέρω μέσω μιας εν δυνάμει παρατήρησης ενός νετρίνου, όπως συζητάμε στο Κεφάλαιο 4. Για να εκτιμήσουμε την πιθανότητα εντοπισμού ενός νετρίνου από τις δυο προαναφερθείσες πηγές, υπολογίζουμε αυτοσυνεπώς τη ροή νετρίνων που αντιστοιχεί στην ηλεκτρομαγνητική ακτινοβολία που έχουμε υπολογίσει παραπάνω. Βρίσκουμε ότι το σύστημα GX 339-4 , αποτυγχάνει να παράξει ένα μετρήσιμο αριθμό νετρίνων σε χρονικό διάστημα μιας με δύο δεκαετιών. Αντίθετα, ο Κύκνος X-1 μπορεί να παράξει τάξη μεγέθους ενός μιονικού νετρίνου το οποίο μπορεί να εντοπισθεί από τα σύγχρονα παρατηρητήρια νετρίνων όπως το IceCube στο Νότιο Πόλο, καθώς και τον μελλοντικό ανιχνευτή ενός κυβικού χιλιομέτρου KM3NeT στη Μεσόγειο. Βάσει των αποτελεσμάτων για αυτές τις δυο πηγές, ερευνούμε τη συνεισφορά των υπόλοιπων 33 BHXBs που έχουν εντοπισθεί μέχρι σήμερα, αλλά βρίσκουμε ότι καμία άλλη πηγή δεν μπορεί να συνδράμει ως πηγή νετρίνων. Ο αριθμός των ήδη εντοπισμένων πηγών παρόλα αυτά είναι αρκετά μικρός σε σχέση με αυτόν που εκτιμάται ότι πραγματικά υπάρχει στο γαλαξιακό επίπεδο. Για να μελετήσουμε διεξοδικά την προώθηση των ΚΑ που επιταχύνονται σε αυτές τις πηγές, καθώς και τη συνεισφορά τους στο φάσμα των ΚΑ και των νετρίνων, χρησιμοποιούμε τους αριθμητικούς προσομοιωτές DRAGON2 και HERMES. Παρά την αμελητέα συνεισφορά αυτών των συστημάτων στη διάχυτη ακτινοβολία  $\gamma$ , βρίσκουμε ότι μπορούν να συνεισφέρουν έως και 30 τοις εκατό στο φάσμα των ΚΑ στο εύρος ενεργειών 1–100 TeV. Μελλοντικές παρατηρήσεις και εκτιμήσεις για τον αριθμό των BHXBs στο Γαλαξία μας, όπως αυτές από το τηλεσκόπιο Gaia, θα μπορούσαν να ενισχύσουν τα συμπεράσματά μας.

Κατά τη μοντελοποίηση με τη χρήση του αδρονικού σεναρίου, αντιμετωπίσαμε ένα γνωστό πρόβλημα: η ισχύς που χρειάζεται για την αδρονική επιτάχυνση πολλές φορές είναι περισσότερη από το ενεργειακό ντεπόζιτο της πηγής, τουλάχιστον σύμφωνα με τις πιο απλές υποθέσεις. Για να επιλύσουμε αυτό το ζήτημα, στο Κεφάλαιο 5, παρουσιάζουμε ένα νέο μοντέλο πίδακα το οποίο λαμβάνει υπόψη το φόρτωμα μάζας κατά μήκος του πίδακα. Ύστερα από την εκτόξευση, οι πίδακες προωθούνται στον περιβάλλοντα χώρο τους, οι συνθήκες του οποίου (για παράδειγμα, η θερμοκρασία, η αριθμητική πυκνότητα και η ταχύτητα) μπορεί να διαφέρουν σημαντικά από πηγή σε πηγή. Η αλληλεπίδραση των μαγνητισμένων πίδακων και του περιβάλλοντα χώρου μπορεί να οδηγήσει στη δημιουργία ασταθειών μεταξύ των δυο ρευστών, οι οποίες επιτρέπουν μάζα από τον περιβάλλοντα χώρο να εισχωρήσει στους πίδακες. Τέτοιες συνθήκες είναι καλά μελετημένες από μαγνητοϋδροδυναμικές προσομοιώσεις με γενική σχετικότητα (ΓΣΜΥΔ) οι οποίες έχουν δείξει ότι η φόρτωση μάζας όχι μόνο είναι σημαντική αλλά μπορεί να οδηγήσει και στη θέρμανση του πίδακα. Τέτοιες ΓΣΜΥΔ προσομοιώσεις παρόλα αυτά, απαιτούν σχετικά αρκετή υπολογιστική ισχύς και αρκετές εβδομάδες με μήνες για να ολοκληρωθούν. Για να επιτύχουμε γρηγορότερους υπολογισμούς και άμεση σύγκριση με τα παρατηρησιακά δεδομένα, αναπτύξαμε ένα ημι-αναλυτικό μοντέλο το οποίο υποθέτει έναν πίδακα που αποτελείται από ζεύγη ηλεκτρονίων-ποζιτρονίων στη βάση του και φορτώνει περαιτέρω βαρυονική μάζα στα εξωτερικά στρώματα. Η επιπρόσθετη μάζα αποτελείται από πρω-



---

τόνια και ηλεκτρόνια, τα οποία επιταχύνονται σε υψηλές ενέργειες και επιτρέπουν σε ανελαστικές αλληλεπιδράσεις. Σε μια αναλυτική μελέτη, δείχνουμε ότι οι πίδακες με επιπρόσθετη μάζα επιτρέπουν για ακτινοβολία  $\gamma$  χωρίς να απαιτείται παραπάνω ισχύς από τη διαθέσιμη. Με αυτό το νέο μοντέλο, σκοπεύουμε να αναλύσουμε τα ηλεκτρομαγνητικά φάσματα πηγών με πίδακες με σκοπό να ταυτοποιήσουμε τις πηγές των ΚΑ που τόσο καιρό αναζητούμε.



## Acknowledgements

These five years of my PhD life have been unique, mainly thanks to a number of people. First of all, I would like to thank my supervisor Sera for letting me work on such a special topic. Cosmic rays, neutrinos, jets and black holes are some subjects very close to my heart. I'm very happy that 20 years after your PhD you decided to go back to the hadronic interactions and pick me to work on them. I'm also really grateful because with your unique way of pushing me to do things, you allowed me to develop to the person I'm right now and fulfil a number of achievements I never considered myself capable of. I didn't manage to follow you in the US for a trip that was cancelled multiple times due to Covid, but I'm really looking forward to future occasions (meals, drinks and scientific discussions) like those we had in Athens!

I owe a special thanks to Jacco, my co-supervisor. When we met first time in Crete in 2016, I had wished to be able to travel to Amsterdam someday (also thanks to the discussions I had with Alexandros, one of your former students). A few years later, I managed to become a member of your group, where I had the chance to meet and talk to wonderful people. Also thank you for the time you spent when I was TAing your course, astroparticle physics. It was so much fun!

The day of my defence, there are two wonderful people right next to me, Alex and Ariane, Ariane and Alex. In chronological order, when I met you Alex, you were still a master student working on a super interesting topic that eventually became kind of a chapter in my thesis. When I met you, I knew you would be successful and indeed, you continued for your PhD in API where we had the chance to spend some wonderful time together. We spent countless hours talking about neutrinos, academia, stress, job applications, but most importantly, I really enjoyed every single time we played football together and drinking beers afterwards to "recover". Ariane, especially the last year of our PhDs you have been of great support with all these conversations we had during breaks. I really enjoyed all the meetings we joined together, either the GRAPPA retreats or the Dutch astroparticle meetings. Also thanks to you (and a number of GRAPPA folks), I was better introduced to the "dark" side of astrophysics

that is calling me now. Most importantly, all this excitement in your words about Anncy and LAPTh made me not only to accept this challenge but also to look forward to getting there.

In these five years, I had the chance to collaborate and interact with many great people and in fact, I had the chance to share the office with some of them. Of course Leon and Wanga, you only joined the group recently, but I'm glad we shared the office this one year and had the chance to get to know you better. I'm sure you'll do great in your PhDs and I'm looking forward to seeing your results (especially any hadronic implementation in the GRMHD simulations). Doosoo, I'm glad I had the chance to meet and interact with you all these years because you taught me so many things about Korea and the US from your unique perspective. Atul, I had told you multiple times that you are like an older brother to me and I'm super happy for all these hours we spend late at work talking about science, India, Greece and the DynaMo! I'm sorry you didn't manage to enjoy the Dutch/Belgian beers in the beginning (I still remember your face drinking the "sweet" beer in Belgium), but perhaps you'll get to like them now with Eveline. Matteo and Koushik, what a great time we had together! It was so much fun to talk about computers, gaming, agnjet and complain about the Dutch food and weather with you Matteo. I still remember the first few months of my PhD that I would consume up to 2-3 hours of your day to talk about agnjet, and not only you wouldn't complain, but you also came to my place to build my computer just for a plate of pasta (for which I'm super glad you liked, as you had said). I'm also very happy I got the chance to become your witness at your wedding with Tam. I'm looking forward to more future meetings like the one we had in Athens. Koushik, or actually Kompton with K, needless to say what an important person you've been in my life all these years. The evening you had all the hundred offers and we spend late at office was perhaps one of the highlights of my PhD. We need to go to Scotland again to refill this bottle but please no more expired beers! Finally, we may have not shared office but Gibwa, you are a great person and I'm very glad I had the chance to meet you. I'm so indebted because you've been my personal editor from the very first moment to the very very very last one!

Speaking of Scotland, the reason Kompton and I went to Scotland was thanks to you, Vlad. And in fact, numerous things in my life were thanks to you. I will remember forever the first time we talked to each other in your office - you, Kompton and I. An unknown word - fragrance - allowed me to make a new friend with whom we travelled from the Netherlands to Belgium, the UK, Slovakia and Greece. Thank you for everything, Vlad! When I think of API, you are the first person to come to mind.

As a member of API, I had the chance to meet some great people. When Ylva was picking us up from the hotel during the interviews, I had no idea what was coming next. I'm super happy I had the chance to meet this generation of people such as Manos, Macla, Alice, Kaustubh, Alicia, Mathieu, Claire, Nina, and Rachel. I owe

---

some special thanks to Manos, who introduced me to all these amazing people. I'm very happy for you and "agapi"! Alice, you are a brilliant person, one of the very few to call a real friend. When I joined API, I had the chance to join along with some several great folks. Eva, Deniz, Vatsal, Kelly, Sarah, and Eleanor. Eva you are a great person and I'm very grateful we shared all these amazing moments together. If I had to pick a highlight, that would have been the evening after the race! Or the Latin dance lessons during the first Christmas party... I'm not sure. Deniz, speaking about politics and science with you was always so much fun. Regarding the "next-generation" of APIs, David, Kenzie, Ben, Lieke, Frank, Arkadip, Pushpita, Annelotte, Iris, Nick, Dante, Yves, Floris, I'm happy I met you guys. David and Floris, it was great to play football next to you guys, even though you were killing us. Arkadip, I hope you liked Athens, it was so much fun to hang out with you. I'm very happy for having you as a student Iris and then seeing you getting a PhD position at API.

I may have only been an unofficial member of GRAPPA, but I'm very glad for all these wonderful people I met all these years. Daniele, Bradley, Marco, Adam, Camila, Oscar, James, Pablo, Sam, Pipa, Jaco, Dmitry, Emanuele, Amael, Banafsheh, Dion, Fabian, Geert, Gimmy, Noemi and Udipta, thank you guys for sharing all these great moments with me!

All these years have been easier thanks to few people. Our great secretaries, Milena, Susan, Rene and Jirina have been there to solve any issues I may have encountered. In principle, you are in the support team as well, Martin, but the real support you offer is usually at Oerknal. Thanks for all the support! Also, you have been the best volleyball teammate, I will surely miss it.

There are a few more people that have contributed all these years with their own, unique way. For instance, it was such a pleasure to work on SEPs with you Monika. It was such a pity Covid ruined my trip to Prague but I'm still looking forward to visiting you there. Hui, I owe you my apologies instead because you have been the first person to work on my model. I'm sorry you had to go through such a horribly commented model but I'm also very thankful for all the discussion we had during lunch breaks the past few months. David and Amber, we lived together for almost 4 years (minus some Covid months). Sharing some feta-spinach-pie with you was as great as all these countless discussions we had late at night about... everything, more or less. Thank you very much guys especially for all the support the last year! You are great and the best roommates ever, for sure.

Ίσως συγγνώμη αντί για ευχαριστώ οφείλω και σε μερικούς ανθρώπους από Ελλάδα. Για παράδειγμα, με όλη αυτή την γκρίνια που έχετε ακούσει Κολλίντζας, Ζαφείρης, Ιατρόπουλος, Ζάνα, θα έπρεπε να μου είχατε κόψει και την καλημέρα αλλά αντιθέτως εσείς είστε πάντα εκεί να μου συμπαραστέκεστε. Σας ευχαριστώ πολύ, είμαι πραγματικά τυχερός που σας έχω στη ζωή μου. Επίσης, Γιουτζίν, τώρα που το σκέφτομαι το θεωρώ αστείο αλλά επί τέσσερα χρόνια όλες μας οι κουβέντες ήταν για τις ίδιες δυσκολίες που αντιμετοπίζαμε απλά άλλαζε η χώρα, τα ονόματα των ανθρώπων γύρω μας, ο τίτλος

του θέματος... κατά τ' άλλα ήταν σαν δυο παράλληλες ζωές. Ένα τεράστιο ευχαριστώ οφείλω και στην ψυχοαναλυτική ομάδα: Δώρα, Στεφανία και Ιουλία.

Δεν έχω καταλάβει γιατί πάντα αφήνουμε στο τέλος την οικογένεια, αλλά φτάνοντας στο τέλος, ένα τεράστιο ευχαριστώ σε όλη την οικογένεια. Πρώτα από όλα στους γονείς μου Κώστα και Ελένη, ελπίζω αυτο το βιβλίο να είναι ένα μικρό ευχαριστώ για τους κόπους σας όλων αυτών των χρόνων. Στους γονείς της Μάρως, Γιάννη και Νάσια, που ήταν και είναι και σαν δικοί μου γονείς πάνω από μια δεκαετία τώρα. Στα αδέρφια μου, όλα, ευχαριστώ για όλη την υποστήριξη στο Δημητράκη όλα αυτά τα χρόνια με το δικό σας ιδιαίτερο τρόπο. Τέλος, όχι μόνο αυτά τα τελευταία πέντε χρόνια αλλά και πολλά περισσότερα νωρίτερα, θα ήταν ανιαρά χωρίς την παρουσία ενός ανθρώπου που πάντα με υποστηρίζει, με σπρώχνει και με αγαπάει, τη Μάρω.

Dimitris,  
August 2022